

AD-A125 592

EFFECT OF SPALL ON THE CHARACTERISTICS OF EXPLOSIVE
GROUND MOTION(U) APPLIED RESEARCH ASSOCIATES INC
ALBUQUERQUE NM D H MERKLE ET AL 10 SEP 82

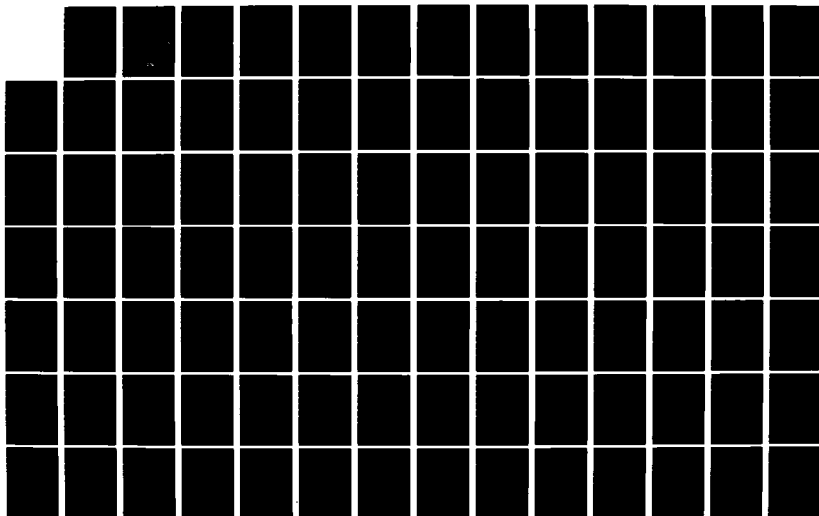
1/3

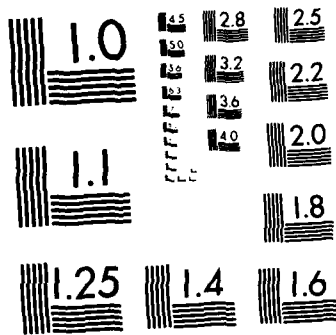
UNCLASSIFIED

AFOSR-TR-83-0060 F49620-81-C-0066

F/G 18/3

NL

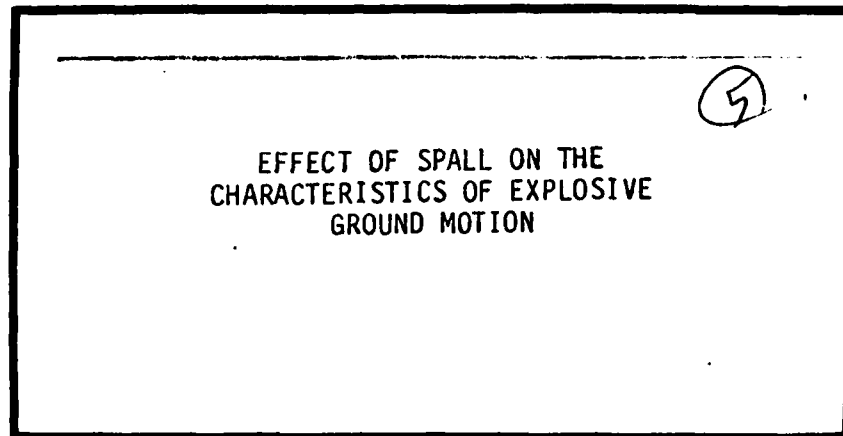




MICROCOPY RESOLUTION TEST CHART
NATIONAL BUREAU OF STANDARDS-1963-A

51 ✓

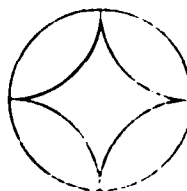
AD A125592



DTIC
MAR 14 1983
H
4-2

Approved for public release;
distribution is unlimited.

DTIC FILE COPY



**APPLIED
RESEARCH
ASSOCIATES, INC.**
Engineering and Applied Science

AIR FORCE OFFICE OF SCIENTIFIC RESEARCH (AFSC)
NOTICE OF TRANSMITTAL TO DTIC
This technical report has been reviewed and is
approved for release under AFM 190-12.
Distribution is unlimited.
MATTHEW J. MILLER
Chief, Technical Information Division

UNCLASSIFIED

(5)
EFFECT OF SPALL ON THE
CHARACTERISTICS OF EXPLOSIVE
GROUND MOTION

Douglas H. Merkle
Harry E. Auld
William C. Dass
James C. Partch
Peter T. Dzwilewski

Applied Research Associates, Inc.
2101 San Pedro NE, Suite A
Albuquerque, New Mexico 87110

10 September 1982

Final Report for Period 1 May 1981 - 30 April 1982

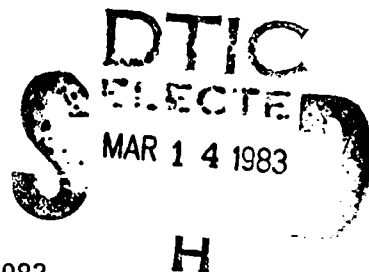
Contract No. F49620-81-C-0066

This work sponsored by the Air Force Office of
Scientific Research under

Program Element 61102F
Project 2309
Task A1

Prepared for

Director of Physics
Air Force Office of Scientific Research
Bolling AFB, D.C. 20332



APPLIED RESEARCH ASSOCIATES, INC.

REPORT DOCUMENTATION PAGE		READ INSTRUCTIONS BEFORE COMPLETING FORM
1. REPORT NUMBER AFOSR-TR- 83 - 0060	2. GOVT ACCESSION NO. AD-A125592	3. RECIPIENT'S CATALOG NUMBER
4. TITLE (and Subtitle) Effect of Spall on the Characteristics of Explosive Ground Motion		5. TYPE OF REPORT & PERIOD COVERED Final Report for period 1 May 1981 - 30 April 1982
		6. PERFORMING ORG. REPORT NUMBER
7. AUTHOR(s) Douglas H. Merkle James C. Partch Harry E. Auld Peter T. Dzwilewski William C. Dass		8. CONTRACT OR GRANT NUMBER(s) F49620-81-C-0066
9. PERFORMING ORGANIZATION NAME AND ADDRESS Applied Research Associates, Inc. 2101 San Pedro NE, Suite A Albuquerque, New Mexico 87110		10. PROGRAM ELEMENT, PROJECT, TASK AREA & WORK UNIT NUMBERS PE 61102F Project 2309, Task A1
11. CONTROLLING OFFICE NAME AND ADDRESS Director of Physics Air Force Office of Scientific Research Attn: NP, Bldg. 410, Bolling AFB, D.C. 20302		12. REPORT DATE 10 September 1982
		13. NUMBER OF PAGES 226
14. MONITORING AGENCY NAME & ADDRESS (if different from Controlling Office)		15. SECURITY CLASS. (of this report) Unclassified
		15a. DECLASSIFICATION/DOWNGRADING SCHEDULE
16. DISTRIBUTION STATEMENT (of this Report) Approved for public release; distribution unlimited.		
17. DISTRIBUTION STATEMENT (of the abstract entered in Block 20, if different from Report)		
18. SUPPLEMENTARY NOTES		
19. KEY WORDS (Continue on reverse side if necessary and identify by block number) Spall Pore Air Effect Ground Motion Nuclear Weapons Effects Negative Airblast Pressure		
20. ABSTRACT (Continue on reverse side if necessary and identify by block number) (U) An empirical technique is developed for predicting the vertical and horizontal extent of spall in soil or rock due to near-surface chemical or nuclear explosions. One-dimensional numerical analyses are presented describing multiple spalls in a tensilely weak, hysteretic material with a free surface. Theoretical analyses of the pore air effect are presented. They show that a fundamental understanding of soil spall requires an effective stress approach.		

PREFACE

The research reported herein was funded by the Air Force Office of Scientific Research (AFOSR), to address problems relating to explosion-induced spall in geologic materials of common concern to both AFOSR and the Air Force Weapons Laboratory (AFWL).

The authors are indebted to Capt. Brian Stump and Drs. Robert Reinke and Eric Rinehart of AFWL, and to Mr. Bill Best of AFOSR for numerous discussions during the course of the research, which helped to better define the mechanisms of spall in soil, and to identify the principal physical quantities which control these mechanisms.

Accession For	
NTIS GRA&I	<input checked="checked" type="checkbox"/>
DTIC TAB	<input type="checkbox"/>
Unannounced	<input type="checkbox"/>
Justification	
By	
Distribution/	
Availability Codes	
Dist	Avail and/or Special
A	



TABLE OF CONTENTS

<u>Section</u>	<u>Title</u>	<u>Page</u>
I	Purpose and Scope	1
II	Introduction	5
III	Numerical Studies of Spall Under Explosive Loading	6
	A. Purpose of the Calculations	6
	B. Computer Code Description	7
	C. Description of Calculational Set-Up	7
	D. Discussion of Results	10
IV	The Pore Air Effect	16
	A. Introduction	16
	B. Previous Investigations	18
	1. Hampton (1964)	18
	2. Zernow, et al (1973)	20
	3. Ullrich (1978)	24
	4. Morrison (1979a)	26
	5. Morrison (1979b)	27
	6. Rosenblatt, Orphal and Hassig (1979)	28
	7. Morrison, Berglund and Kelly (1979)	30
	8. Merkle (1980)	32
	9. Labreche (1980)	33
	10. Morrison, et al (1981)	34
	11. Rosenblatt, Hassig and Orphal (1982)	35
	C. Simple Discrete Models	36
	D. General Equations	37
V	Prediction of Negative Airblast Overpressures from Near-Surface Explosions	39
VI	Review of Spall Data from HE and NE Detonations	42
VII	Prediction of Spall Region for Near-Surface Detonations	51
	A. Introduction	51
	B. Spall Associated with High Explosive Detonations	52
	C. Spall Associated with Nuclear Detonations	53
VIII	Summary and Conclusions	55

<u>Appendices</u>	<u>Title</u>	<u>Page</u>
A	Isothermal Fluid Diffusion Through a Rigid Porous Medium	58
B	Transient Linear Pore Air Diffusion in a Vented Layer	60
C	Transient Linear Pore Air Diffusion in an Unvented Layer	69
D	Adiabatic Fluid Diffusion Through a Rigid Porous Medium	74
E	Propagation Velocity in Spalled Soil	76
F	Three-Dimensional Adiabatic Fluid Diffusion Through a Rigid, Porous, Isotropic Medium	79
G	Transient Linear Pore Air Diffusion in a Vented Layer Subjected to Surface Airblast Loading Having a Negative Phase	85
H	A Simple Piston Model for the Pore Air Effect	90
I	A Simple Dynamic Piston Model for the Pore Air Effect	97
J	Solution of a Fourth Order Algebraic Equation	113
K	Solution of a Fourth Order Linear Ordinary Differential Equation with Constant Coefficients	127
L	Numerical Solution of the Characteristic Equation	130
M	General Equations for the Pore Air Effect	135
References		141
Tables		145
Figures		158

LIST OF TABLES

<u>Number</u>	<u>Title</u>	<u>Page</u>
3.1	One-Dimensional Calculations	146
4.1	Summary of Peak Pore Air Pressure Below the Surface of Sand During Exposure to a 100 PSI Shock in an 8-Inch Shock Tube	147
4.2	Calculated Linear Diffusion Parameters for Zernow's 8-Inch Shock Tube Vented Samples	148
4.3	Calculated Peak Pore Air Pressure and Time of Occurrence for Zernow's 8-Inch Vented Samples	149
4.4	Adjusted Linear Diffusion Parameters for Zernow's 8-Inch Shock Tube Vented Samples	150
4.5	Calculated Peak Pore Air Pressure and Time of Occurrence for Zernow's 8-Inch Vented Samples, Using Adjusted Linear Diffusion Parameters	151
4.6	Adjusted Linear Diffusion Parameters for 8-Inch Shock Tube Unvented Samples	152
4.7	Calculated Peak Pore Air Pressure and Time of Occurrence for 8-Inch Unvented Samples Using Adjusted Linear Diffusion Parameters	153
5.1	Scaled Airblast Parameters, Large Yield Pacific Nuclear Data (10 kt - 10 mt)	154
6.1	Experimental Spall Data from Near-Surface Detonations	155
6.2	Maximum Scaled Radius of Spall, \bar{R}_S , for Various Explosive Charge Configurations	157

LIST OF FIGURES

<u>Number</u>	<u>Title</u>	<u>Page</u>
3.1	One-Dimensional Analysis of Explosive Spall Problems	159
3.2	One-Dimensional (Uniaxial Strain) Spall Calculations	160
3.3	Application of Gravity to Grid with Dynamic Relaxation	161
3.4	In Situ (Gravity) Stress and Pressure Distribution	162
3.5	Transmitting Boundary with Incident Velocity	163
3.6	Characteristic Planes for Two Boundary Conditions	164
3.7	Calculation 1--No Tensile Failure ($\rho_{MIN} = -100$ MPa)	165
3.8	Spall and No Spall Time History Comparisons at Depth = 0.5 M	166
3.9	Soil-Rock Boundary Behavior	167
3.10	Grid Snapshots of Incident Compressional Pulse at Time = 25 MS	168
3.11	Calculated Dwell Time for Depth = 5 M	169
3.12	Spall Plane Formation	170
4.1	Dynamic Pore Pressure Isochrones for a Vented Sample; $\beta = 0.463$	171
4.2	Dynamic Pore Pressure Isochrones for a Vented Sample; $\beta = 0.639$	174
4.3	Dynamic Pore Pressure Isochrones for a Vented Sample; $\beta = 0.279$	177
4.4	Dynamic Pore Pressure Response in a Vented Sample; $\beta = 0.463$	180
4.5	Dynamic Pore Pressure Response in a Vented Sample; $\beta = 0.639$	182
4.6	Dynamic Pore Pressure Response in a Vented Sample; $\beta = 0.279$	183

<u>Number</u>	<u>Title</u>	<u>Page</u>
4.7	Dynamic Pore Pressure Isochrones for a Vented Sample; $\beta = 2.31$	185
4.8	Dynamic Pore Pressure Isochrones for a Vented Sample; $\beta = 3.19$	188
4.9	Dynamic Pore Pressure Isochrones for a Vented Sample; $\beta = 1.39$	194
4.10	Dynamic Pore Pressure Response in a Vented Sample; $\beta = 2.31$	197
4.11	Dynamic Pore Pressure Response in a Vented Sample; $\beta = 3.19$	199
4.12	Dynamic Pore Pressure Response in a Vented Sample; $\beta = 1.39$	200
4.13	Dynamic Pore Pressure Isochrones for an Unvented Sample; $\beta = 9.25$	202
4.14	Dynamic Pore Pressure Isochrones for an Unvented Sample; $\beta = 12.77$	205
4.15	Dynamic Pore Pressure Isochrones for an Unvented Sample; $\beta = 5.56$	208
4.16	Dynamic Pore Pressure Response in an Unvented Sample; $\beta = 9.25$	211
4.17	Dynamic Pore Pressure Response in an Unvented Sample; $\beta = 12.77$	213
4.18	Dynamic Pore Pressure Response in an Unvented Sample; $\beta = 5.56$	214
5.1	Peak Negative Airblast Overpressure Versus Scaled Range, High Explosive	216
5.2	Peak Negative Airblast Overpressure Versus Scaled Range, Nuclear	217
5.3	Peak Negative Airblast Overpressure Versus Scaled Range, High Explosive and Nuclear	218
6.1	Sketch of Typical Spall Regions and Nomenclature	219
6.2	Estimated Extent of Spall, PHG I-07	220

<u>Number</u>	<u>Title</u>	<u>Page</u>
6.3	Typical Vertical Velocity Rejoin Amplitude, PRE-MINE THROW IV	221
6.4	Summary of Vertical Velocity Rejoin Amplitude Versus Scaled Range, PRE-MINE THROW IV	222
6.5	Scaled Maximum Radius of Spall at $z = 0.5$ m Versus Depth to the Second Layer	223
6.6	Maximum Depth of Spall Versus Depth to the Second Layer	224
6.7	Maximum Depth of Spall Versus Yield	225
7.1	Spall in the Negative Airblast Wing Region	226

SECTION I

Purpose and Scope

The purpose of the spall research described herein is defined in the Statement of Work for Air Force Office of Scientific Research Contract Number F49620-81-C-0066, viz:

1. Perform Analytical Studies and Finite Difference Calculations.

Formulate and perform one- and two-dimensional analytical studies and calculations to obtain insight into spall mechanisms and important material parameters. Include variations in wave type (e.g. reflected P and S waves, horizontally traveling P and S waves, etc.), tensile failure criteria (e.g., maximum principal tension, hydrostatic tension, extensional strain) and tensile strength. Include variations in material strength if this parameter appears to be important in spall phenomena.

2. Develop a Spall Prediction Technique. Using the results of Task 1, plus previous field data analysis, develop a method for predicting spall characteristics in both single and multiburst near-surface experiments. The prediction technique shall include the prediction of spall radius, depth, initial conditions, and post-spall behavior, all as a function of yield, height of burst, geology and material properties. The extension of the method for prediction of spall for high yield nuclear bursts shall be included.

As the research progressed, two things became clear:

1. Soil spall data from both chemical and nuclear explosive tests is limited in quantity and quality; and

2. A fundamental understanding of soil spall requires an effective stress approach, which explicitly treats both the soil skeleton stress-strain response and the transient effect of flowing pore fluid.

Consequently, relatively more attention was given to soil tensile stress-strain behavior, and also particularly to the pore air effect than originally planned, and somewhat less effort was spent on numerical calculations (because satisfactory material models were not available). The empirical analysis of single burst, near-surface explosion-induced soil and rock spall was exhaustive, and led to the single-burst prediction technique presented herein. However, the volume of test data for multiple burst spall is so small, and the material behavior influence so strong, that a multiple burst spall prediction technique requires a combined empirical and theoretical approach, and must await further research.

Section III of this report describes the theoretical basis and results of one-dimensional finite difference calculations of vertical wave propagation in a tensilely weak, hysteretic material with a free surface, using the computer program STEALTH 1D. Multiple spall features are predicted by these total stress calculations, which demonstrate the ability of STEALTH 1D to both include gravity in propagation problems, and to predict spall in tensilely weak material with given stress-strain behavior.

Section IV reviews previous tests and analyses of the pore air effect, and presents several new analyses which show that pore air expansion and pore air flow are not separate spall mechanisms, but rather two related aspects of the same mechanism. Nonlinear differential equations are derived in a series of appendices, for both isothermal and adiabatic

transient pore air flow through a rigid, porous, isotropic solid. Finite difference approximations to the above differential equations are also developed, some in a pseudo-linear form simple enough for even hand computation. Two simple, discrete-element models of the pore air effect are constructed and analyzed, one without and the other with mass. Because these models are linear, their response can be represented in closed form, which permits parametric studies. Both models exhibit rapid, undrained response (compression) to a suddenly applied constant surface fluid pressure, followed by gradual recovery (expansion) of the soil skeleton as additional pressurized fluid flows into the pore spaces. The model with mass is a fourth order model, in the sense that its closed form analysis requires the solution of a fourth order, linear, ordinary differential equation with constant coefficients. This involves the solution of a fourth order algebraic equation, with one root several orders of magnitude larger than the rest. Although the closed form solution of this equation was tedious, it was pursued because it provides considerable insight into the two principal modes of physical behavior of real soil, viz. undrained (composite) behavior and drained (separate) behavior of the two phases, and their relative rates of volumetric deformation. Finally, a general set of coupled, nonlinear, second order partial differential equations is derived which simultaneously describe both the propagation and diffusion phenomena which comprise the pore air effect. These equations are general enough to accommodate any soil effective stress-strain-strength relationship. Although written for one-dimensional motion, they can readily be generalized for two- or three-dimensional motion.

Sections V, VI and VII comprise an integrated, sequential treatment of explosion-induced negative (gage) airblast pressure for both chemical and nuclear near-surface bursts; an empirical analysis of all available soil and rock spall data from single, near-surface explosions, both chemical and nuclear; and an empirically-based predictive method for soil and rock spall from single, near-surface explosions, both chemical and nuclear.

SECTION II

Introduction

The study of near-surface explosion induced soil spall is basically a study of dynamic soil stress-strain behavior, and requires explicit recognition of the particulate, multiphase nature of soil. This does not mean that total stress approaches are not useful, but rather that their basis and interpretation are rooted in the concept of effective stress. Thus the finite difference calculations in Section III, and the empirical analyses in Sections VI and VII use a total stress approach, but the analyses of the pore air effect in Section IV use an effective stress approach, and help explain the results presented in the other sections.

Much work remains to be done to develop a reasonably thorough understanding of soil spall and its effect on near-surface explosion induced ground motions. Much of that work is of a calculational nature, involving parametric studies using the equations developed herein, and comparing the calculated results with the results of predictions made using empirical techniques also developed herein. From this point on the further development of spall calculation and empirical prediction techniques can best proceed in tandem.

SECTION III

Numerical Studies of Spall Under Explosive Loading

A. Purpose of the Calculations

Mathematical simulation and prediction of explosive events in soil require adequate treatment of tensile (spall) phenomena. Spallation, whether caused by layering effects, wave interaction with the ground surface, or some other phenomena, will significantly affect measured ground motions (especially at later times) and therefore should be modeled in a calculation. In order to illustrate the generation of spall and examine the effect of varying physical parameters such as tensile strength, a series of one-dimensional finite difference calculations was performed for this study.

Figure 3.1 shows two situations which may lead to spall. In Figure 3.1a, shock waves produced by an explosion at or above the earth's surface are propagated much faster in an underlying layer of rock than in the surface layer of soil. As a result, a compressive headwave moves upward into the undisturbed soil. The angle from the vertical (θ) at which this wave propagates may be estimated as:

$$\theta = \arcsin (C_s/C_r) \quad (3.1)$$

where C_s and C_r are the confined wavespeeds in soil and rock, respectively. In a situation where the lower layer has a much higher wavespeed than the upper one (i.e., a high impedance mismatch), the headwave will travel nearly vertically. Because of this, a one-dimensional, uniaxial idealization is appropriate, as shown in Figure 3.1c. Such a 1-D

calculational model of spall may also be adequate for the case of a buried burst, as shown in Figure 3.1b. Here the primary waves move vertically through undisturbed soil and reflect off the ground surface as tensile waves which cause spall.

The one-dimensional model used for these calculations (Figure 3.1c) may be considered to be an adequate simplification for studying many real cases of spall. It is true, however, that certain occurrences of spall can be accurately simulated only in two or three dimensions. Such cases require more sophisticated treatment of tensile behavior and geometric factors.

B. Computer Code Description

There are many one-, two-, and three-dimensional finite difference wave propagation codes currently available. The particular code chosen to perform this set of calculations was STEALTH [Hofmann (1978)]. STEALTH 1-D, 2-D, and 3-D are a set of "user-oriented" codes, and have been applied to many different kinds of dynamic problems.

STEALTH is attractive for studying spall because of its ability to accept different constitutive relationships and to allow the user to impose a wide variety of boundary conditions. The generality of STEALTH, although it requires a very large code, is also one of its strong points. For example, a purely mechanical spall model worked in one-dimension could be broadened to include pore fluid effects and still be implemented in STEALTH 1-D or 2-D, sparing any further development necessitated by code differences.

C. Description of Calculational Set-Up

The calculations for this study were performed under uniaxial strain

conditions. A 27 meter grid, consisting of 160 zones was used, as shown in Figure 3.2. The idealized site has a layered geology with 12 m of "soil" over 15 m of "rock". Actually, the soil is simply a bilinear, hysteretic material with an unloading wave speed (1122 m/s) equal to twice the loading wave speed (561 m/s). The rock is modeled elastically with equal loading and unloading speeds (2960 m/s). A P_{min} (minimum bulk stress) criterion was used to establish the soil spall-threshold. Because of the one-dimensional nature of the calculations, this is equivalent to a vertical principal stress cutoff criterion. The tensile cutoff (P_{min}) was varied for the soil, but the rock was not allowed to fail in tension. Neither material was allowed to fail in shear.

Gravity is an important part of any spall situation because it creates the lg dwell signatures which are a primary identifier of spall in data records. In-situ gravity stresses were established in the STEALTH grid by applying a body force equivalent to lg over the entire grid with a rigid boundary at the bottom. The resultant oscillations were then numerically damped (in STEALTH, this is known as "dynamic relaxation"). Within 100 ms a static condition was achieved. Figure 3.3 shows grid velocities at various depths during this relaxation phase. All information concerning the grid was saved at 200 ms and subsequent calculations were restarted from this time. Figure 3.4 shows the in-situ geostatic stresses in the grid after gravity has been established. Note the discontinuity in bulk stress at the soil-rock interface. This is a result of unequal K_0 values for the two materials. This may or may not be indicative of actual in-situ conditions at a soil-rock interface, because of uncertain geologic history.

The boundary condition at the top of the grid for all problems was a free surface, i.e., zero stress (atmospheric pressure was neglected). In order to simulate the effect of an infinite rock layer below the soil, a transmitting (or nonreflecting) boundary was used at the bottom of the grid after gravity had been established. A transmitting boundary allowing incident waves, which has been used by [Moriwaki et. al. (1981)] for shear waves, was adapted for compressional waves and the effect of gravity. Basically, the velocity of the boundary point is calculated based on a $\sigma = \rho cv$ relationship. Referring to Figure 3.5, Newton's Law for the boundary element may be expressed as:

$$m \ddot{x} = \Sigma F_B \quad (3.2)$$

where

$$m = \text{boundary mass} = \frac{1}{2} \rho \Delta x \quad (3.3)$$

ΣF_B , the sum of the live forces acting on the boundary element, includes $(\sigma - \sigma_G)$, the live stress in the zone above the boundary, and σ_B , the boundary stress, where

$$\sigma_B = \rho c(\dot{x} - 2\dot{X}) \quad (3.4)$$

The quantity c is the compressional wave speed of the imaginary infinite media below the boundary, and \dot{X} is the applied incident velocity at the boundary. With the timing of the calculation as shown in Figure 3.5., and using superscripts n and l to denote new and old times, respectively, the current acceleration and velocities are:

$$\ddot{x} = \frac{\dot{x}^n - \dot{x}^l}{\Delta t} \quad (3.5a)$$

$$\dot{x} = \frac{\dot{x}^n + \dot{x}^l}{2} \quad (3.5b)$$

$$\dot{x} = \frac{\dot{x}^n + \dot{x}^l}{2} \quad (3.5c)$$

Substituting in Equation (3.2) for m , \dot{x} , and ΣF_B yields

$$\left(\frac{1}{2} \rho \Delta x\right) \left(\frac{\dot{x}^n - \dot{x}^l}{\Delta t}\right) = (\sigma - \sigma_G) - \rho c \left[\left(\frac{\dot{x}^n + \dot{x}^l}{2}\right) - (\dot{x}^n + \dot{x}^l) \right] \quad (3.6a)$$

and solving for the desired boundary velocity, \dot{x}^n yields

$$(\dot{x}^n - \dot{x}^l) = \frac{2\Delta t(\sigma - \sigma_G)}{\rho \Delta x} - \frac{c\Delta t}{\Delta x}(\dot{x}^n + \dot{x}^l) - \frac{2c\Delta t}{\Delta x}(\dot{x}^n + \dot{x}^l) \quad (3.6b)$$

$$\dot{x}^n = \frac{\dot{x}^l \left(1 - \frac{c\Delta t}{\Delta x}\right) + \frac{2\Delta t(\sigma - \sigma_G)}{\rho \Delta x} - \frac{2c\Delta t}{\Delta x}(\dot{x}^n + \dot{x}^l)}{\left(1 + \frac{c\Delta t}{\Delta x}\right)} \quad (3.7)$$

Using the boundary condition defined by Equation 3.7, it is possible to propagate a pulse up into undisturbed material while simultaneously allowing reflected waves to pass down through the bottom of the grid and out of the problem. Figure 3.6 shows characteristic planes for two cases, one with a pressure boundary at the bottom and another with the transmitting boundary. It is apparent that the latter case, Figure 3.6b, with no increase in grid size, more closely models actual conditions, such as those shown in Figure 3.1. Therefore the transmitting boundary allows analysis of spall motions, unobstructed by peripheral reflections.

The velocity pulse used to generate spall in the top soil layer is shown in Figure 3.2. It consists of a linear rise with subsequent sinusoidal decay to zero. The peak velocity, V_{pk} , was varied, while maintaining the pulse duration at 20 ms.

D. Discussion of Results

After establishing suitable boundary conditions, several calculations

were performed to meet the following objectives:

- i) Examine the case of no spall, where the soil material is not allowed to separate in tension;
- ii) Examine a baseline spall problem, for which the general characteristics of spall can be examined and against which the results of parameter variations can be compared;
- iii) Assess the effect of load pulse magnitude on spall;
- iv) Assess the effect of soil tensile strength on spall;
- v) Determine the importance of numerical noise in the calculations which may produce spall motions; and
- vi) Examine a case in which spall blocks are forced back together ("forced rejoin"), in order to ascertain the basic characteristics of the resulting waveforms.

Table 3.1 is a matrix of calculations with values for the parameters which were varied, viz: tensile cutoff and peak incident velocity at the bottom of the grid. In addition, for all the calculations except No. 6, the tensile stress in a zone was required to exceed P_{MIN} for three cycles before spall was allowed to occur. All problems were started with an established gravity stress field at time = 0 and were run for 250 ms.

The results from Calculation No. 1 illustrate what the waveforms in a material with a large tensile strength would look like for the loading of interest. The material remains intact and the oscillations can be easily predicted. Figure 3.7 shows the calculated stress and velocity time histories at a depth of 0.5 m. (Note the sign conventions, which will be used throughout this section.) Below each waveform the characteristic plane for the problem is shown. As reflected energy passes through the

rock and out of the grid, the motions eventually damp out to zero.

When the tensile strength of the soil is reduced to a reasonable level, motions are dramatically altered. Figure 3.8 shows a comparison between the cases of spall ($P_{MIN} = 0.10$ MPa) and no spall ($P_{MIN} = 100$ MPa).

There are several spall-significant events in the calculation which contribute to the waveform differences seen in Figure 3.8. The following is a summary of these events in chronological order, along with a list of the more pertinent parameters controlling them:

- i) The upward propagating compressive pulse hits the boundary between soil and rock (time = 5 ms). Part of the wave reflects back into the rock as a tensile wave, and part transmits through as a compressive wave. At this point, the soil separates from the rock (see Figure 3.9).

parameters: P_{MIN} (soil and rock)

c_u (soil and rock)

- ii) The initial compressive wave travels upward, compressing the hysteretic soil material (see Figure 3.10). Note that because a net upward displacement is imposed on the bottom of the rock layer by the incident velocity pulse, the final position of a soil node is not dependent only on soil compression. When the free surface is encountered (at approximately 26 ms), the wave reflects as a tensile wave. At the depth at which

$$P_{reflected} < P_{MIN}$$

spall first occurs.

parameters: t_{s1} = time of first spall

d_{s1} = depth of first spall

iii) The tensile wave continues to propagate downward at the soil unloading wavespeed, and may or may not create more spall planes depending on the material model being used. Eventually it reaches the free surface which has been created between the rock and soil. At this time (approximately 37 ms) the entire soil block realizes it is undergoing projectile motion. The tensile pulse must reflect as a compression wave.

parameters: n = number of initial spall planes formed

$t_{s,2...n}$ = times of subsequent initial spall plane formation

$d_{s,2...n}$ = depths of above

iv) There is a period of motion with constant acceleration (projectile motion, $1g$ dwell, freefall, etc.) for the soil. Energy trapped within the discrete spall blocks moves between the free surfaces of the blocks. This causes small oscillations during the $1g$ dwell, whose frequency depends directly on spall block size (see Figure 3.8). The magnitude of these trapped waves may be high enough in some blocks to cause further spall.

parameters: t_d = duration of $1g$ dwell
(varies with depth)

v) Rejoin of spalled material begins at the rock surface. The time at which rejoin occurs for each node is roughly determinable from the initial velocity (\dot{x}_0) and displacement (x_0) at the time spall occurs. The equation of motion for constant acceleration ($\ddot{x} = g$) is:

$$x = x_0 + \dot{x}_0 t + \frac{1}{2} \ddot{x} t^2 \quad (3.8)$$

where t = time from spall. Solving for the duration of spall, t_d , yields

$$t_d = \frac{-\dot{x}_0 + \sqrt{\dot{x}_0^2 - 2\ddot{x}(x_0 - x_d)}}{\ddot{x}} \quad (3.9)$$

In Equation (3.9), x_d is the particle position at the time of rejoin, and depends on the compressibility of the soil and the incident velocity pulse. For estimating dwell time, x_d may be set to zero, i.e., the pre-spall position. Figure 3.11 illustrates the calculation of dwell time at the 5 m depth.

parameters: $t_r = t_s + t_d$ = time of rejoin

- vi) Rejoin progresses from the bottom of the soil upwards. When two spall blocks impact, a compressive signal travels both upwards and downwards. An upward pulse encounters a free surface (because the block above has not rejoined yet) and reflects. This reflection may cause further spall in the soil. The downward pulse reflects and transmits at the rock boundary. A negative pulse (due to the impedance mismatch) follows this reflection up and may also cause further spall. As a result, spallation of zones accompanies rejoin and the number of spall planes increases due to impact, creating somewhat of a "shattering" effect. Rejoin propagates slower as it approaches the surface because the upper soil zones have been lofted somewhat higher.

parameters: v_r - rejoin (or impact) velocities

- vii) Subsequent spall motion occurs and may be referred to as secondary or multiple spall. During this phase, spall planes

are simultaneously opening and closing. Figure 3.12 shows the formation of several spall planes due to the first reflection, and subsequent spall plane formation during the rejoin and secondary spall phases. As rejoin energy is transmitted through the soil/rock boundary and through the nonreflecting boundary, motions damp-out and the grid elements come to rest.

parameters: t_{ms} = times of multiple spall

t_{mr} = times of multiple spall rejoin

SECTION IV

The Pore Air Effect

A. Introduction

Spall in dynamically loaded granular soil occurs when soil masses lose contact with each other and undergo ballistic motion (free fall). An important cause of spall near the ground surface, in the presence of explosion-induced airblast pressure is the pore air effect. Although sometimes discussed as a parallel phenomenon with spall, the pore air effect is best considered as a spall mechanism [Merkle (1980:24)].

The pore air effect is a consequence of soil being both particulate and multiphase [Lambe and Whitman (1969:18-19)]. Under the action of a pore pressure gradient, soil pore fluid flows in the direction opposite to that of the pore pressure gradient. An increase in the mass of pore fluid stored in a saturated soil element occurs if the soil void volume increases, and/or the pore fluid mass density increases. In general, both can happen. If inertia is neglected, and the equations for pore fluid flow and storage are combined, the result is a diffusion equation which can be written with pore pressure as the unknown.

If the pore fluid flow equation is assumed to be linear, the pore fluid incompressible, and the soil skeleton linearly elastic, the result is Terzaghi's consolidation equation [Terzaghi (1943:265); Taylor (1948:225)].

If the pore fluid flow equation is again assumed to be linear, the pore fluid (air) to undergo isothermal compression, and the soil skeleton

to be rigid, the result is a nonlinear diffusion equation [Zernow et al (1973:13); Muskat (1937); Carman (1956)].

If the soil particles are assumed to be in a spalled condition, i.e., not in contact, and the pore air to undergo adiabatic compression, the resulting sonic velocity (which applies to a propagation, rather than a diffusion problem) is that for a heavy gas [Ullrich (1978:19); Merkle (1980:35)]. In this model the mass of the heavy gas is supplied entirely by soil particles, and the compressibility entirely by pore air. There is no viscous, diffusive flow in this model, but there is compressible flow in the sense of compressive wave particle motion.

The above pore air models and other more general models are discussed in detail below. Emphasis is on developing equations for pore air pressure prior to spall, to gain insight into how pore air pressure can cause spall.

Two pore air phenomena have been proposed as possible causes of spall:

pore air expansion, and

pore air flow.

Saying that pore air expansion causes spall can be misleading, because adiabatic pore air expansion is accompanied by a pore pressure decrease, which, by itself, would cause an increase in effective hydrostatic stress carried by the soil skeleton, resulting in compression rather than expansion of the soil skeleton. What actually happens when airblast pressure acts on a soil surface is that air flows into the soil, compressing the pore air near the loaded surface. The compressed pore air has a tendency to expand rapidly, especially when the surface airblast pressure decreases, and this rapid expansion produces a flow of

pore air toward the soil surface. The pore air flow in turn causes a seepage or drag force to act on soil particles in the flow regime, which tends to reduce the effective stresses produced by gravity and eventually may cause spall. Thus it is pore air expansion and flow, together, which can cause spall. A profitable way to view the pore air effect is to consider the pore air seepage force (the negative of the pore pressure gradient) as a body force acting on the soil skeleton, the deformation of which is governed by effective stress. The effective stress carried by the soil skeleton, and the pore air pressure are always such that the soil void volume and the pore air volume are equal.

B. Previous Investigations

1. Hampton (1964)

Hampton performed a shock tube study of dynamic pore air pressure in three dry soils subjected to surface airblast pressure. The loaded soil surface was confined by a screen (presumably to prevent lofting or spall), because interest centered on the rate of attenuation of peak pore air pressure in soil, as it affects the design of buried structures, foundations for surface and buried structures, and model experiments on soil-structure interaction. In particular, Hampton was concerned with the depth to which pore air pressure induced in soil will penetrate, the distribution of pore air pressure with depth, and the relative velocity of pore air pressure propagation and effective stress waves. The study was entirely experimental, but with a final recommendation that an analytical theory of pore-air pressure propagation in soil subjected to an air shock wave be developed. Hampton measured the physical permeability, k_0 , of the three soils tested, with the following average

results:

pea gravel: $2.42 \times 10^{-6} \text{ CM}^2$

20-30 Ottawa sand: $6.11 \times 10^{-7} \text{ CM}^2$

silty sand: $9.81 \times 10^{-10} \text{ CM}^2$

Physical permeability is used in the Darcy flow equation in the form

$$v = - \frac{k_o}{\mu} \frac{dP}{ds} \quad (4.1)$$

where

v = flow velocity, CM/SEC

k_o = physical permeability, CM^2

μ = viscosity, DYNE SEC/ CM^2

P = pressure, DYNE/ CM^2

s = distance, CM

The value of μ for air is [Vennard (1954:7)]

$$\begin{aligned} \mu_{\text{AIR}} &= 3.77 \times 10^{-7} \frac{\text{LB SEC}}{\text{FT}^2} \\ &= \frac{(3.77 \times 10^{-7})(4.448222 \times 10^5)}{(30.48)^2} = 1.81 \times 10^{-4} \frac{\text{DYNE SEC}}{\text{CM}^2} \end{aligned}$$

Equation (4.1) is often written in the form

$$v = -B_1 \frac{dP}{ds} \quad (4.2)$$

where the effective permeability coefficient, B_1 , is given by the expression

$$B_1 = \frac{k_o}{\mu} \quad (4.3)$$

For air flowing through standard 20-30 Ottawa sand, the above values yield

$$B_1 = \frac{6.11 \times 10^{-7}}{1.81 \times 10^{-4}} = 3.38 \times 10^{-3} \frac{\text{CM}^4}{\text{DYNE SEC}}$$

2. Zernow et al (1973)

Zernow et al also performed a shock tube study of Number 30 silica sand subjected to surface airblast overpressure. However, their principal objectives were to determine the amount of near-surface soil lofted (or spalled) by the airblast-induced "reverse percolation" process, and to measure the resulting soil particle motions. Their study was motivated by the possibility of dust cloud formation by a near-surface nuclear detonation, caused by a combination of lofting and airblast sweep-up. The possibility of such a phenomenon had been suggested by Brode in 1971.

A theoretical description of the lofting process was also accomplished, based on a linear form of the equation for isothermal diffusion of air through a rigid, porous medium. The relevant equations, which were not derived in the above report, are derived in Appendix A. The basic linear diffusion equation employed to calculate pore air pressure was

$$\frac{\partial P}{\partial t} = D \frac{\partial^2 P}{\partial x^2} \quad (\text{A.6})$$

where the diffusion coefficient for isothermal flow is

$$D = \frac{B_1 P}{n} \quad (\text{A.7})$$

Although the shock tube soil samples were of finite length (35 IN for the 4 IN shock tube [Zernow, Figure 9], and 71 IN for the 8 IN shock tube

[Zernow, Figure 22]), the boundary and initial conditions used to solve Equation (A.6) were those for a halfspace [Carslaw and Jaeger (1959:64)]:

$$P(0,t) = P_0 e^{-\alpha t} \quad (t>0) \quad (4.4)$$

$$P(\infty,t) = 0 \quad (t>0) \quad (4.5)$$

$$P(x,0) = 0 \quad (x>0) \quad (4.6)$$

The rationale for Equation (4.5) was that the standard soil samples were supported by a vented end plate having a porosity of about 19 percent for the 4 IN shock tube and 16 percent for the 8 IN shock tube, whereas the sample porosity was about 33 percent. This the authors argued would simulate the flow resistance of the imaginary soil beneath the finite sample [Zernow, pp. 39 and 71]. Unfortunately, two facts contradict the above argument:

- a) No attempt was made to simulate the pore air storage characteristics of the imaginary soil beneath the finite sample.
- b) With a vented end plate it is difficult to conclude that the pore air pressure at the sample bottom could have been anything but close to zero (gage).

Therefore transient solutions to Equation (A.6) have been obtained in Appendices B and C for the following boundary and initial conditions:

Appendix B (vented sample)

$$P(0,t) = P_0 e^{-\alpha t} \quad (t>0) \quad (4.4)$$

$$P(1,t) = 0 \quad (t>0) \quad (B.2)$$

$$P(x,0) = 0 \quad (0<x<1) \quad (B.3)$$

Appendix C (unvented sample)

$$P(0,t) = P_0 e^{-\alpha t} \quad (t > 0) \quad (4.4)$$

$$\frac{\partial P}{\partial x}(1,t) = 0 \quad (t > 0) \quad (C.2)$$

$$P(x,0) = 0 \quad (0 < x < 1) \quad (C.3)$$

The reason for deriving the above solutions was to give the linear diffusion theory as realistic a test as possible. If the linear theory is judged inadequate for predicting dynamic pore air pressures, it should be because the phenomenon really is not linear, rather than because inappropriate boundary conditions were used for the linear theory. The linear theory should not be hastily abandoned, because as Zernow et al point out, it serves as a source of useful physical insight in terms of parametric variations.

Figures 4.1, 4.2 and 4.3 show dynamic pore air pressure isochrones for a vented sample of finite length, subjected to a decaying exponential airblast pressure on one face. Measured peak pore air pressures and their time of occurrence are shown in Table 4.1, and the appropriate linear diffusion parameters are calculated in Table 4.2. Calculated values for comparison with the measured values shown in Table 4.1 are shown in Figures 4.4, 4.5 and 4.6 and in Table 4.3. The agreement between measured values of P_{MAX} and t_{MAX} shown in Table 4.1, and corresponding calculated values shown in Table 4.3 is not good. Because of this lack of agreement, and because Zernow's measured soil permeability values have already been questioned by [Morrison (1979a:5)], the above calculations were rerun for soil Groups I, II and III using the effective permeability for Ottawa sand calculated following Equation

(4.3) ($3.4 \times 10^{-3} \text{ CM}^4/\text{DYNE SEC}$). Since this value is one-fifth that shown in Table 4.1 for Groups I, II and III, the adjusted value for Group IV in Table 4.4 was also taken as one-fifth that shown in Table 4.1 for Group IV. The comparison between calculated values of P_{MAX} and t_{MAX} shown in Table 4.5 and corresponding values shown in Table 4.1 is much improved. The degree of agreement could be further improved by decreasing the assumed permeability even more to account for the greater fraction of fine sand and silt size particles in Zernow's material than in standard Ottawa sand. It thus appears that the early phase of the pore air effect prior to spall can be described, at least approximately, by a linear diffusion model.

Note the upward pore air flow near the surface in Figures 4.8d, e and f. This is the flow which can cause spall (lofting), and the depth of spall can be estimated as the depth to the point at which the isochrone slope is zero.

Figures 4.13 through 4.18 show the results of a linear diffusion analysis of transient pore air flow in an unvented sample, using Equation (C.29). The effect of the impervious boundary at $x = 1$ is dramatic, and the tendency toward upward air flow much greater than for a vented sample. The impervious boundary could be a water table, a rock layer, or even a clay layer.

Because Zernow et al did not obtain satisfactory agreement between measured pore air pressures and motions and those predicted using linear diffusion theory, they developed a more accurate, nonlinear diffusion theory. Their nonlinear theory considers the pore air flow to be adiabatic rather than isothermal, and recognizes the spatial variation of

pore air density. The equations are developed in Appendix D. Comparison of measured and predicted peak pore air pressure and time to peak pressure using the nonlinear theory was still not satisfactory, but halfspace boundary conditions were again used instead of those for a finite layer. Because of the unsatisfactory comparison, the authors recommended further development of the nonlinear model to eliminate the constraints of a rigid medium with constant properties.

The authors also stated that there was no information on how permeability varies with porosity. However, this subject has been fairly thoroughly studied [Taylor (1948:111); Leonards (1962:121); Lambe and Whitman (1969:283); Mitchell (1976:346)].

3. Ullrich (1978)

Ullrich examined MISER'S BLUFF single and multiple burst data to determine the limits of superposition as a means of predicting multiple burst groundshock response using single burst groundshock data. He concluded that superposition of single burst groundshock records yielded good predictions of multiple burst groundshock motions at all depths outside the multiple charge array, and for depths greater than 10 feet inside the array. At depths less than 10 feet inside the array superposition failed, and he suggested four mechanisms which caused superposition to fail:

- a) airblast pressure enhancement
- b) soil rebound
- c) soil tensile failure [spall]
- d) pore air expansion

Ullrich used the term pore air expansion to describe "the expansion,

during the negative overpressure phases, of air initially entrained in the ground", and concluded that this mechanism was the dominant cause of superposition failure in MISER'S BLUFF.

Ullrich noted that the single burst ground motion records used in the attempted prediction of a near surface multiple burst ground motion response near the center of a charge array did not show spall, but the corresponding multiple burst ground motion record did show spall. This situation points out the existence of two classes of spall prediction problems in a superposition context:

- a) how to combine component records which themselves show spall, and
- b) how to combine component records which themselves do not show spall, but which in combination will (in reality) cause spall.

Ullrich realized that the only fundamental approach to such nonlinear problems is with an accurate, nonlinear material model, and he proposed one for already spalled soil. The model is that of a heavy gas, consisting of disconnected soil particles suspended in air. His analysis used the term "piston model", but in fact the model can be used for two- or three-dimensional analyses because it is basically a volumetric model. Ullrich's equations are derived, using conventional soil mechanics nomenclature, in Appendix E. Although Ullrich's model has been called a "no flow" model, it does yield particle motion associated with a compressive wave. It is a propagation, not a diffusion model, and does not treat viscous flow of air through the soil skeleton or around the suspended soil particles. Ullrich's model can be used in a computer code when the soil volumetric strain is positive, and another diffusion model used when the soil volumetric strain is negative.

4. Morrison (1979a)

Morrison reviewed several previous studies related to the pore air effect. He questioned whether Zernow's vented shock tube sample adequately simulated a semi-infinite soil column, but did not attempt to correct Zernow's linear solution for the vented case. Instead, he presented a derivation of the nonlinear equation for three-dimensional adiabatic diffusion of air through a rigid, porous, isotropic medium, using air density as the dependent variable. The derivation is slightly simpler when pressure is used as the dependent variable, and is presented in Appendix F, including a pseudo-linear form simple enough for even hand calculation.

Morrison indicated that a finite difference code (presumably one-dimensional) had been developed, in which the porous medium behaves elastically (and presumably linearly) in compression, but allows air flow between zones when expanded. Neither equations nor numerical results were presented, but the equations of motion were ascribed to the WONDY finite difference code. Soil permeability is input initially, then altered as the soil porosity changes. The computational sequence is as follows:

- a) Using previous total stress and total density as inputs to WONDY, solve equations of motion to obtain new displacements.
- b) Calculate new strain and porosity.
- c) Calculate new effective stress.
- d) Calculate new permeability.
- e) Assuming adiabatic compression without flow, calculate intermediate pore air pressure.
- f) Allowing adiabatic flow, calculate new pore air pressure.

- g) Calculate new pore air density.
- h) Calculate new total stress.
- i) Calculate new total density.
- j) Return to (a).

5. Morrison (1979b)

In a briefing to the 1979 DNA Spall Workshop, Morrison described an experimental device designed to apply transient negative (gage) airblast pressure to the top surface of an unjacketed, vertical, cylindrical soil sample, in an attempt to isolate the negative phase portion of the pore air effect. Sixteen millimeter high speed photo movies were shown illustrating the dramatic influence of porosity and particle gradation on near-surface particle motion, as summarized below:

<u>Soil Type</u>	<u>Pore Air Flow</u>	<u>Particle Motion</u>
sand	very little	particles retain initial relative position
MISERS BLUFF	[very little]	local fluidization and extensive mixing of layers
gravel with fines	extensive	fines carried through gravel to surface; little motion of gravel

After reviewing previous data on airblast penetration from [Hampton (1964)], and near-surface soil particle lofting from [Zernow, et al (1973)], Morrison presented additional data on the effect of sub-atmospheric airblast pressure in MISERS BLUFF II-2 to show pore air expansion effects. A definite correlation was established between negative airblast pressure and both vertical extensional strain and vertical particle velocity. He then described the calculational model for

pore air expansion discussed in [Morrison (1979a)], and presented some preliminary results in which peak displacement and velocity were plotted as functions of permeability and weapon yield for a given peak (negative) airblast pressure. Morrison concluded that permeability may be an important site characterization factor.

6. Rosenblatt, Orphal and Hassig (1979)

In another presentation to the 1979 DNA Spall Workshop, Rosenblatt et al reported a fundamental approach to analysis of the pore air effect, using the DICE computer code. They first presented a concise but comprehensive summary of previous observations concerning the pore air effect:

a) The magnitude of near-surface ground response to the small secondary airblast peak (commonly called "repete") suggests the ground has been highly dilated and has a relatively low impedance (for soil).

b) The very low propagation velocity of the above secondary compression signal is consistent with the assumption of a two phase medium.

c) A secondary upward velocity appears to be associated with the arrival of the airblast negative phase, and is hypothesized to be caused by upward expansion (flow) of pore air.

d) Inclusion of Ullrich's "no flow" adiabatic expansion model significantly improves the correlation between calculated and measured near-surface soil vertical particle motion during the negative airblast phase, for dry, high-porosity soils.

e) Then current pore air expansion models made no provision for pore air flow or the associated viscous drag or seepage force on the soil skeleton. Rosenblatt et al suggested that the pore air flow mechanism is

an important part of the pore air effect.

f) The shock tube experiments by [Zernow et al (1973)] showed conclusively that, under their test conditions, gas permeation of the sand column was necessary to produce significant upward column motion.

g) The above experiments also showed that upward soil particle velocities are enhanced by: higher peak surface airblast pressure, more rapid overpressure decay, smaller particle size, and an underlying impermeable layer; and are reduced by: very high porosity and permeability, and very low permeability. [In this regard, soil susceptibility to the pore air effect is similar to soil susceptibility to frost heave.]

Several questions were also raised:

a) Is the pore air effect two-dimensional, i.e., are horizontal motions also affected?

b) Is the negative airblast phase required to produce the pore air effect, or just an upward pore air flow?

c) What is the influence of soil tensile strength?

d) How does pore air related behavior scale between HE and NE surface bursts?

Specific objectives of the reported effort, which was just beginning at the time of the presentation, were:

a) Formulate a one-dimensional mathematical model of "forward" and "reverse" air flow into the ground, and "validate" it against reverse percolation laboratory data reported by [Zernow, et al (1973)].

b) Using the above model, calculate relevant vertical ground motions for the MISERS BLUFF II experiments.

c) Calculate ground motions for a 1 MT nuclear surface burst, to assess the importance of two-phase phenomena for nuclear yields of interest and to investigate scalability.

Adaptation of the DICE code to handle soil/air interaction was outlined, but the definition of stress in the soil skeleton appeared to be different from the concept of effective stress used in conventional soil mechanics. The formulation did allow permeability to vary with soil porosity over a wide range of porosity, as well as with soil particle size. The results of this work have since been presented in more detail by [Rosenblatt, Hassig and Orphal (1982)], and are discussed below.

7. Morrison, Berglund and Kelly (1979)

Morrison, Berglund and Kelly performed a combined experimental and theoretical study of soil subjected to transient negative (gage) airblast pressure. Both their shock tube experiments and numerical computer calculations were one-dimensional. The study deliberately provided an isolated view of that portion of the pore air effect caused by the negative phase of an explosively-produced air shock. The main problem with such an approach is that in both chemical and nuclear explosions a positive airblast phase precedes the first negative phase, so the soil is not apt to have a zero internal pore air pressure distribution when the external airblast negative pressure phase begins. Thus, the positive and negative airblast phase effects cannot be isolated from each other. Of course, if the entire process were linear, the positive and negative phase effects could be considered separately and the results superposed. However, there is good reason to believe that not all aspects of the pore air phenomenon are linear, particularly the soil motions.

The study had three stated primary objectives:

- a) form a basic analytical model that describes soil motion due to pore air expansion;
- b) develop an experimental apparatus and technique that can illustrate and measure the effects of pore air expansion; and
- c) provide a comparison between data and theory so theoretical limitations and possibilities for future work can be defined.

Expansion of pore air due to pressure differentials with depth, and actual pore air flow through the soil skeleton are treated as separate soil lifting mechanisms, with emphasis on the former. However, an effective stress (or soil skeleton oriented) approach shows that the pore air pressure gradient associated with flow constitutes a distributed body force acting throughout the soil skeleton, and it is this distributed seepage force which helps cause lifting or spall. Thus pore air expansion and pore air flow are not two phenomena, but slightly different aspects of the same single phenomenon.

The computer code employed was a revision of the one described by [Morrison (1979a)], and employed the following features:

- a) a one-dimensional wave equation, using total stress and total density, and including gravity and artificial soil viscosity;
- b) a soil stress-strain relation using effective stress but no viscosity;
- c) Ullrich's adiabatic relation between pore air pressure, soil porosity and soil volumetric strain, Equation (E.9);
- d) a total mass conservation equation which assumes no pore air flow; and

e) a one-dimensional, nonlinear diffusion equation for isothermal pore air flow through a rigid, porous soil skeleton, Equation (A.5), which assumes the validity of Darcy's law, Equation (A.1).

Three different expressions are given for the viscous stress used in the one-dimensional wave equation: one in the text, one in an appendix, and one in the computer program listing. No mention is made of the pore air seepage force, or of the fact that both adiabatic and isothermal conditions are assumed in the same set of equations. Therefore, Appendix F of this report presents the derivation of a pseudo-linear diffusion equation for adiabatic pore air flow through a rigid, porous soil skeleton which is even simple enough for hand calculation.

The only mention of bottom boundary conditions imposed in the above calculations is the observation that "Dramatic differences [50 to 75 mm (2 to 3 in)] in deflections were observed when the total sample depth was varied by only 25 mm (1 in)." However, only two tests are reported in which only the sample depth was varied. Mention is made of a single calculation having been made using an airblast input with both positive and negative phases, but the results are not reported. A theoretical analysis of the linear pore pressure response in a rigid, porous solid, subjected to surface airblast loading having both a positive and a negative phase is presented in Appendix G of this report.

8. Merkle (1980)

Merkle examined current soil spall theories, including Ullrich's pore air expansion mechanism. The pore air expansion equations were derived using conventional soil mechanics nomenclature, and were shown not to be restricted to one-dimensional effects. They define the propagation

velocity of a pressure wave in a two-phase fluid, in which one phase is compressible but massless, while the other phase has mass but is incompressible.

9. Labreche (1980)

Labreche described a series of finite difference computer calculations, using the codes WONDY and WONDY/POREAIR, to study the differences, if any, between pore air effects for a 1 MT nuclear loading and a high explosive loading scaled to 1 MT, both with the same peak side-on airblast overpressure. The HE loadings selected for comparison were from MISERS BLUFF Phase I Event 2 and Phase II Event 1. The soil profiles used above were adjusted and scaled versions of the MISERS BLUFF Phase I and Phase II test site profiles. Several other calculations were made in support of vertical shock tube studies, and for comparison with results obtained by others using a no flow model. The soil total stress-strain model used in the WONDY code was the AFWL Engineering Model.

Two sets of calculations were run for the HE/NE comparison cases: one set used the code WONDY, and ignored the pore air effect; the other used the code WONDY/POREAIR and included the pore air effect. The difference between the soil particle motions predicted by WONDY/POREAIR and by WONDY alone was taken as the measure of the pore air effect. When the WONDY/POREAIR code was used the pore air diffusion equations in POREAIR were bypassed when the soil extensional strain reached a predetermined limiting value, determined by the maximum stable soil porosity. At this point the soil particles were assumed to be no longer in contact, and to undergo ballistic motion. At this point the airblast-loaded surface was effectively shifted down to the top of the

first nonspalled element. During initial compression, WONDY/POREAIR assumed soil porosity, permeability, pore air density and pore air pressure to all be constant. Numerical stability was studied by varying the WONDY propagation time step, Δt , and the necessarily smaller POREAIR diffusion time step, $\Delta t/N$.

10. Morrison, et al (1981)

Morrison, Labreche, and Lamb reported in detail the results of evacuation chamber tests and HE/NE comparison calculations which had been outlined by [Labreche (1980)]. They also gave preliminary results of vertical shock tube tests, in which the airblast load had both a positive and a negative phase. They concluded that pore air effects are sensitive to soil permeability, which in turn is affected by soil particle gradation and degree of saturation, as well as to the water phase in a partly saturated soil. Saturated soil exhibits no pore air effects, because there is no connected gaseous pore air phase.

In this report, pore air expansion of soil is defined as "expansion of the soil which results when the pore air pressure in the soil voids exceeds the confining stress of the soil matrix". A literal interpretation of the above definition implies a negative effective stress. This was not intended. The situation envisioned by the definition is that of a finite soil mass, in which the pore air pressure within some interior region exceeds the pore air pressure over some surface region, thus producing an outward pore air flow, the seepage force from which tends to cause soil particle contact loss.

Near-surface displacement-time curves from evacuation chamber tests were obtained from high speed photographs and also double integration of

accelerometer data. The integrated accelerometer records indicated much larger peak upward displacements than did the photographs, and the accelerometers came to rest nearer the surface than they had been placed. This led to the conclusion that the near-surface accelerometers did not move with the surrounding soil (perhaps at least in part because their air drag characteristics were different from those of soil particles).

11. Rosenblatt, Hassig and Orphal (1982)

Rosenblatt, Hassig and Orphal described some of the theoretical fundamentals used to modify the DICE code to treat pore air effects related to lofting, and gave results of their calculations. This is the work outlined in their 1979 DNA Spall Workshop presentation discussed above.

The conventional soil mechanics definition of effective stress is presented in the theoretical discussion, but some of the calculations (e.g. Figure 4.10(a)) appear to show a large effective stress at theunjacketed surface of a soil mass loaded only by pore air pressure. Since the effective stress at such a surface is always zero, it is not clear that the DICE code actually used the conventional soil mechanics definition of effective stress. This situation is encountered in conventional geotechnical engineering practice in connection with a change of water level in a reservoir or river. It also happens continually in tidal areas.

Results of the DICE code calculations showed reasonable agreement with some of Zernow's shock tube test results, although that was not the stated objective of the calculations. In fact, the calculations used different bottom displacement and pore pressure boundary conditions than

those appropriate for Zernow's samples; they also kept the airblast decay rate constant and varied soil permeability in obtaining results which were compared with those of tests in which the airblast decay rate varied and the soil permeability remained constant. Nevertheless, the DICE code results' qualitative agreement with Zernow's indicate that the code has the capability to model the essential features of the pore air effect.

C. Simple Discrete Models

The above pore air effect analyses employ sets of equations which are only partially coupled, in the sense that the equations describing stress wave propagation and those describing pore air diffusion are solved sequentially, rather than simultaneously for each time increment. The difficulty of formulating and solving a completely coupled set of equations for the pore air effect was recognized early in this study. Therefore, to gain insight into both the physical mechanisms and the mathematical processes involved, some simple mathematical models were constructed, the behavior of which could be analyzed in closed form.

The first model, analyzed in Appendix H, actually arose during a discussion of the response of anunjacketed soil test sample immersed in water in a closed pressure vessel, when the fluid pressure suddenly increased. This of course is the reservoir or tidal basin problem mentioned previously. The simple piston model analyzed in Appendix H is massless, so there are no inertial effects. The main thing this model shows is that when a saturated, unjacketed soil sample is subjected to a sudden increase in external fluid pressure, the sample first undergoes

undrained composite compression, in which the soil skeleton and the internal pore fluid experience the same volume decrease. Subsequent drainage allows compressed pore fluid to flow into the soil skeleton, and the soil skeleton to expand to its original volume (if elastic).

The second model, analyzed in Appendix I, is the same as the first except that both the soil skeleton and the pore air have mass. With this model, initial, instantaneous undrained deformation does not occur (see Equation (I.44)), because of the inertia of both soil skeleton and pore fluid. However, the numerical evaluation of Equation (I.62) shows that a small deformation of the soil skeleton, associated with pore air compression, does occur very rapidly. Subsequent deformation of the soil skeleton, associated with pore air flow, occurs much more slowly. The final equilibrium condition of this model is the same as that for the massless model. The internal pore fluid eventually attains the same pressure as the external fluid, and the soil skeleton returns to its initial configuration.

Since both the above models are linear, their response to any prescribed airblast input can be obtained by superposition.

D. General Equations

The advantage of the above two discrete models of soil pore air behavior is that they are relatively simple and linear, so that their response can be obtained in closed form. This permits parametric studies and physical interpretation of the results. Nevertheless what is obtained is an exact solution to an approximate problem, rather than an approximate solution to the real problem. The general equations describing the "real" one-dimensional pore air problem are developed in Appendix M. They are a

set of coupled, nonlinear, second order partial differential equations involving soil skeleton displacement and pore air pressure. The most practical approach to their solution appears to be by the method of finite differences.

SECTION V

Prediction of Negative Airblast Overpressures From Near-Surface Explosions

It will be shown in Section VI that a major portion of the shallow spall observed in experiments with near-surface explosions, detonated over granular materials with essentially zero tensile strength, results from the negative overpressure portion of the airblast loading. Thus, the negative airblast overpressure must be known in order to develop a model to predict this phenomenon. A review of the literature revealed that no method was available to accurately define the negative airblast overpressure from near-surface explosions. Accordingly, available data and calculations were reviewed, and a procedure developed for predicting the maximum negative airblast overpressure as a function of scaled range.

Figure 5.1 presents measured maximum negative airblast overpressure, ΔP^- , versus scaled range, \bar{R} , from several high explosive near-surface detonations. Note that the maximum measured value of ΔP^- is approximately 48 kPa. Lack of data at higher values of ΔP^- indicates the difficulty of developing instrumentation to make such measurements.

Figure 5.1 also presents the results of numerical calculations [Needham, 1969]] for a 500 ton high explosive surface tangent event. The calculated values for 30 kPa and below are in reasonable agreement with the measured data in Figure 5.1, but indicate a somewhat flatter decay rate with scaled range than an upper bound to the measured data. The calculations for surface tangent and slightly aboveground detonations

indicate the formation of a toe of detonation products near ground level, which significantly influences the airblast parameters. The value of $\bar{R} \approx 0.10 \text{ km}/(\text{kt})^{1/3}$, at which a jump in ΔP^- occurs, is the scaled range at which a normal shock is formed. At smaller values of \bar{R} , the results approach a maximum value of -1 atmosphere.

An analytical approximation to both the measured and calculated data, consisting of two straight lines, is also shown in Figure 5.1. The equations for this proposed approximation are:

$$\Delta P^- = 36.0[\bar{R}]^{-0.168}, \text{ kPa for } \bar{R} < 0.15 \text{ km}/(\text{kt})^{1/3} \quad (5.1)$$

and

$$\Delta P^- = 3.98[\bar{R}]^{-1.329}, \text{ kPa for } \bar{R} \geq 0.15 \text{ km}/(\text{kt})^{1/3} \quad (5.2)$$

This analytical approximation is nearly an upper bound to the measured points. The breakover point and slope of the upper portion of the analytical approximation are based on engineering judgment, and are not in exact agreement with the calculated values.

Measured airblast results from several large yield (10kt - 10mt) nuclear events conducted in the Pacific are summarized in scaled format in Table 5.1. The ΔP^- versus \bar{R} nuclear data are plotted in Figure 5.2. Again there are no data at the larger ΔP^- values, i.e., for $\Delta P^- > 28 \text{ kPa}$. Results of calculations utilizing the 1 kt nuclear standard [Needham (1975)] are also presented in Figure 5.2 for comparison. The calculated values again indicate a flatter decay rate than an upper bound to the measured data, but in this instance the calculated values are larger at most scaled ranges. The calculations indicate a breakover point at an \bar{R} of approximately $0.12 \text{ km}/(\text{kt})^{1/3}$. At smaller values of \bar{R} the results approach a maximum value of

approximately $-1/3$ atmosphere instead of the -1 atmosphere indicated for high explosives.

The high explosive approximation for the peak negative airblast overpressure was corrected by a factor of $2W$ to account for radiation loss occurring in a nuclear detonation ($1 \text{ kt nuclear} = 1/2 \text{ kt high explosive}$). This corrected line is shown in Figure 5.2. It provides an excellent fit as an upper bound to the measured nuclear data. Thus, it appears that a single straight line, corrected by $2W$, can be used to fit both the nuclear and high explosive measured data at larger scaled ranges. The nuclear breakover point is maintained at $0.15 \text{ km}/(\text{kt})^{1/3}$, and the slope of the proposed upper line in the nuclear approximation is reduced somewhat from the high explosive approximation. The proposed equations for the nuclear approximations are:

$$\Delta P^- = 27.3[\bar{R}]^{-0.132}, \text{ kPa for } \bar{R} < 0.15 \text{ km}/(\text{kt})^{1/3} \quad (5.3)$$

and

$$\Delta P^- = 2.90[\bar{R}]^{-1.313}, \text{ kPa for } \bar{R} \geq 0.15 \text{ km}/(\text{kt})^{1/3} \quad (5.4)$$

The two analytic approximations for predicting peak negative airblast overpressure versus scaled range are presented in Figure 5.3. The yield for the appropriate type of explosive is utilized without correction for this figure. The curves provide upper bounds to the available measured data. Considerable uncertainty exists at scaled ranges less than $0.15 \text{ km}/(\text{kt})^{1/3}$, and the above results should be used with caution for scaled ranges below that value.

SECTION VI

Review of Spall Data From HE and NE Detonations

Spall has been recently studied by [Stump and Reinke (1980), Merkle (1980), and Auld, et al (1981)]. For the purposes of this report, the following criteria will be utilized to identify spall in ground motion records:

1. $-1g$ (-0.5 to -2.0) vertical acceleration dwell (≥ 5 ms), which is identifiable directly on a vertical acceleration record, or as the slope of a vertical velocity record;
2. identifiable impulsive rejoin signal on both the vertical and horizontal acceleration records;
3. rejoin amplitude (≥ 0.05 m/s) observed on the vertical velocity record.

These criteria are similar to those utilized by previous investigators, but with numerical values specified.

[Auld, et al (1981)] suggested that the zone of spalled material surrounding a near-surface explosion can be considered to consist of two parts: a bowl-shaped volume of material, designated the "coupled spall region"; and a shallow extension of the basic spalled volume, designated the "negative airblast wing region". Figure 6.1 illustrates these two zones as they might occur from a typical near-surface detonation. Any of the possible spall mechanisms, or a combination of these mechanisms may be responsible for the spall observed in the coupled region, e.g., direct waves, head waves, reflected waves, or surface waves. The predominant

spall mechanism in the negative airblast wing region is the negative overpressure portion of the airblast loading. Spall can occur in this region only when the applied peak negative airblast overpressure exceeds the tensile strength of the near-surface material. Accordingly, many tests do not exhibit the negative airblast spall wing because the explosive charge was slightly buried (thereby suppressing the airblast), the surface material had a significant tensile strength in comparison to the applied peak negative airblast overpressure, or the instrumentation was placed in holes backfilled with grout instead of with negligible tensile strength material, e.g., sand. Note that "soil matching" grout can be utilized to backfill instrumentation holes in the coupled spall zone and spall can still be detected.

[Auld, et al (1981)] also suggested that a simple model can be used to estimate the depth of spall in the negative airblast wing for a material with zero tensile strength. This model equates the geostatic vertical total stress at the depth of spall to the value of the peak negative airblast overpressure at the range of interest, thereby obtaining the equation:

$$\bar{z}_s = \Delta P^- / \gamma \quad (6.1)$$

where

\bar{z}_s = depth of spall at the range of interest (see Figure 6.1);

ΔP^- = peak negative airblast overpressure;

γ = soil total unit weight.

For $\rho \cong 1900 \text{ kg/m}^3$, and ΔP^- in kPa, Equation 6.1 reduces to:

$$\bar{z}_s = \frac{1000 \Delta P^-}{(9.80665)(1900)} = 0.054 \Delta P^-, m \quad (6.2)$$

The peak negative airblast overpressure must be known to calculate \bar{z}_s from Equation 6.2. Accordingly, the technique for predicting peak negative airblast overpressure developed in Section V should be utilized.

Table 6.1 summarizes the high explosive events which were examined in detail, to develop an understanding of spall phenomena and to develop techniques for predicting the extent of spall associated with a near-surface detonation. Emphasis was placed on large yield events ($W \geq 100$ tons) and on events with sufficient instrumentation to produce a good definition of the spalled region. The events summarized in Table 6.1 were conducted on a wide range of geologic profiles, ranging from deep dry soil to layered soil over rock, with and without high water tables. In addition, the near-surface materials ranged from dry powdery silt, with essentially zero tensile strength, to highly competent granite. High explosive yields ranged from a fraction of a ton to 500 tons. Charge configurations consisted of slight height of burst (HOB), surface tangent spheres (STS), surface tangent cylinders with hemispherical caps (STC), half buried spheres (HBS), berms, and slight depth of burial (DOB). All high explosive events studied had identifiable regions of spall, except the three shots conducted on granite, i.e., MINERAL ROCK, MINE ORE, and MINE UNDER. There may have been spall associated with the granite events; however, it is reasonable to assume that high rock strength limited the spall region to the extent that violent cratering motions masked its presence.

Spall was detected on only one nuclear event, JANGLE-U. Ground

motion records were also examined for MIKE, CACTUS, KOA, PRISCILLA, JOHNNIE BOY, SMALL BOY, and JANGLE-S, without detecting motions satisfying the previously specified spall criteria. The high water table associated with events conducted in the Pacific may have precluded spall. Grouted instrumentation holes, old style instrumentation, and less sophisticated data processing techniques may have contributed to masking of spall in nuclear events conducted at the Nevada Test Site (NTS). In addition, the ground motion instrumentation was placed too deep (e.g., 1.5 m) to record much of the spall phenomena on all of the nuclear events. Figure 7.1 shows the extent to which spall in the negative airblast wing region can be overlooked by using a minimum gauge depth of this magnitude. Figure 7.1 also indicates that using a much shallower minimum gauge depth for high explosive experiments increases the probability of detecting spall. Note that high explosive events at NTS have produced significant spall regions. However, it should not be concluded on the basis of these results that nuclear events do not produce spall.

The extent of the spalled volume of material can be defined by two quantities: radius of spall, R_s , and maximum depth of spall, z_s . R_s will vary widely, depending on whether the negative airblast spall wing is present (see Figure 6.1). The depth of the negative airblast spall wing is a slowly decaying function of range, and the radius of spall for zero depth can only be crudely approximated. Accordingly, R_s is arbitrarily defined for a depth of 0.5 m in this report, and values corresponding to this definition are given in Table 6.1. The radius of spall for any other chosen depth can be estimated by using Equation 6.2,

or other techniques given below. In the coupled spall region there is essentially no difference in the radius of spall for depths of zero and 0.5 m. There have been a very limited number of close-in measurements made on near-surface detonations, and the estimates of z_s are based almost entirely on extrapolation of data using a preconceived concept of the general shape of the spalled volume. Therefore, there is a great deal of uncertainty associated with z_s .

Two general methods were utilized to estimate the values of R_s and z_s presented in Table 6.1. The first method consisted of evaluating ground motion records using the established spall criteria. Each instrumentation location was then labelled as showing spall (S), questionable spall (?S), or no spall (NS). If the instrumentation array is sufficiently large and dense, the zone of spalled material can then be estimated as shown in Figure 6.2. A second method was developed to estimate the radius of spall from the magnitude of rejoin amplitudes observed on vertical velocity records. It was noted that the radius at which the near-surface vertical velocity rejoin amplitude approached zero correlated well with the radius of spall defined by the first method. For example, vertical velocity rejoin data from two of the PRE-MINE THROW-IV (PMT-IV) events are presented in Figure 6.3, for a depth of 0.23 m. The radius of spall can easily be estimated by extrapolating the data to the range where the rejoin amplitude is zero. However, this radius of spall does not meet the above definition of R_s (i.e., $z = 0.50$ m); and since the PMT events had airblast spall wings, this slight depth difference may produce significant variations in the radius of spall. Also note that there is a dip in the rejoin amplitude data,

which extrapolates to a range of approximately 10 m. This range corresponds well to the R_s obtained from experiments where there was no negative airblast spall wing, and suggests that high quality rejoin amplitude versus range data can be used to estimate the radius of spall for both coupled and negative airblast wing regions.

Figure 6.4 shows rejoin amplitude plotted against scaled range, $\bar{R}(m/0.5 \text{ ton}^{1/3})$, for all PMT events. This figure illustrates the main difficulty in comparing spall data from different events, when the ground motion instrumentation for each event is placed at a single depth which varies from event to event.

These data suggest that the scaled value of \bar{R}_s for $z = 0.50 \text{ m}$ adequately represent all PMT events, and that apparent differences in \bar{R}_s result from the depth of the ground motion instrumentation rather than from differences in spall phenomena. The insert in Figure 6.4 illustrates a technique for crudely estimating the in-situ tensile strength of the near-surface material. Equation 6.2 was used in conjunction with measured values of ΔP^- to estimate the maximum depth of spall at various ranges, for a zero tensile strength material. The difference between the geostatic vertical total stress at spall depth and the applied value of ΔP^- was assumed to result from the tensile strength of the material at that depth. The four points obtained produce a σ_T versus depth curve that is quite plausible for that particular site.

The values of spall radius, R_s , at a depth of 0.5 m obtained by either of the general methods previously described are summarized in Figure 6.5 by plotting scaled radius of spall, $\bar{R}_s(m/100 \text{ ton}^{1/3})$,

versus depth to the second layer, which may be either the water table or competent rock. The data generally fall into two groups: those with a negative airblast spall wing, and those without. Yield cube root ($W^{1/3}$) scaling for the radius of spall appears to order the data. Neither charge configuration nor details of the deeper geologic profile greatly influences \bar{R}_S when the negative airblast spall wing is present. Of course the near-surface material must be very weak to produce a negative airblast spall wing. \bar{R}_S is influenced by the charge configuration when the negative airblast spall wing is not present, and the value of \bar{R}_S increases with increased charge coupling (HOB-STC-STC-HBS-Berm). A surface tangent cylinder appears to be essentially equivalent to a half buried sphere instead of a surface tangent sphere. The widest data scatter occurs for the STS events. Similar observations have previously been noted with regard to cratering parameters, such as the crater radius or depth. Again, there is no indication of dependence on geological features, such as the depth to the second layer.

\bar{R}_S for the JANGLE-U event is also shown in Figure 6.5. This event had a slight depth of burial (5.18 m) and should have produced results comparable to the bermed high explosive event. A comparison of these two data points will be used in Section VII to estimate a nuclear to high explosive spall efficiency factor, and thereby develop a nuclear spall prediction technique.

The range of \bar{R}_S values for the various charge configurations is summarized in Table 6.2 for both high explosive and nuclear events.

The dependence of \bar{R}_S on charge configuration for the events with no

negative airblast wing, i.e., with only a coupled spall region, suggests that there might be a correlation between unscaled radius, R_s , and crater size. However, yield cube root scaling collapsed the data better than scaling by either crater radius or crater volume.

The relation between maximum depth of spall, z_s , and depth to the second layer (either the water table or competent rock) is shown in Figure 6.6. It appears that there is no strong dependence on charge configuration, as was the case in Figure 6.5. However, a dependence on geology is indicated. The maximum depth of spall appears to be limited by the depth to the water table when there is no shallower rock layer. This limitation is indicated by the data for which the spall zone ends in soil falling on or to the left of the line for which maximum depth of spall equals depth to the second layer. However, as indicated by the two data points for which the spall zone ends in rock, when spall does penetrate into weak to intermediate strength rock (sandstone or shale), the water table may not stop it. The data are limited but suggest that the maximum depth of spall is less for the case of a water table over a rock layer than for the case of dry soil extending to the rock layer.

The relation between maximum depth of spall and yield is shown in Figure 6.7. A clear dependence on yield is indicated. In addition, the geology dependence previously seen in Figure 6.6 is again evident, and there is a suggestion that charge configuration may also be of some, but lesser importance. These data are insufficient to account for detailed differences in geology, but the following equations can be utilized to estimate z_s for a surface tangent charge configuration (either STC or STS):

$$\begin{aligned}
 z_s &= \text{depth of water table*} \\
 &\text{or } 3.2 (W, \text{tons})^{1/6}, \text{m} \\
 &\text{whichever is smaller.} \qquad (6.3)
 \end{aligned}$$

A similar equation applies to the case where the charge is half buried (HBS):

$$\begin{aligned}
 z_s &= \text{depth of water table*} \\
 &\text{or } 5.0 (W, \text{tons})^{1/6}, \text{m.} \qquad (6.4)
 \end{aligned}$$

Neither Equation (6.3) nor Equation (6.4) applies when a competent rock layer is encountered above z_s .

*If there is a rock layer at a depth of z_s or less disregard the water table.

SECTION VII

Prediction of Spall Region for Near-Surface Detonations

A. Introduction

The prediction techniques presented in this section are based on the negative airblast predictions from Section V and the measured spall data presented in Section VI. Note that spall was detected on only one nuclear event. Therefore, the extrapolation from high explosive to nuclear involves a great deal of uncertainty, and these results should be used with caution. Also, no spall was observed in very competent rock such as granite.

As previously discussed, the volume of spalled material from a near-surface detonation can be characterized by two parameters, the maximum radius of spall, R_s , and the maximum depth of spall, z_s . R_s is arbitrarily defined to be at a depth of 0.5 m, and may be associated with either the coupled spall region or the negative airblast wing, when this region is present (see Figure 6.1).

To make predictions of R_s and z_s , the following information must be known:

1. Yield (W): tons of TNT or kt of nuclear;
2. Charge configuration: surface tangent or half buried sphere (small HOB for nuclear is assumed);
3. Geology
 - a. depth to water table
 - b. depth to rock layer and type of rock
 - c. nature of the near-surface material (does it have a negligible tensile strength?, i.e., $\sigma_T \leq 10$ kPa?)

B. Spall Associated With High Explosive Detonations

When the near-surface material has a negligible tensile strength and airblast is present, a negative airblast wing region can be expected. In this instance the expected scaled maximum radius of spall can be estimated from Figure 6.5 to be

$$\bar{R}_s = \frac{150}{(100)^{1/3}} = 32 \text{ m/ton}^{1/3} \quad (7.1)$$

Additional definition of the shape of the negative airblast wing region can be obtained through the use of Figure 7.1. This figure was derived by combining the predictions of ΔP^- from Figure 5.3 with Equation 6.2. Since the tensile strength of the near-surface material is assumed to be zero, the results will be conservative. The predicted depth of spall can be easily obtained for any scaled radius from Figure 7.1, and the shape of the negative airblast wing region estimated. Note that the theoretical scaled radius of HE spall for a depth of 0.5 m shown in Figure 7.1 is $0.520 \text{ km/kt}^{1/3}$. This scales to $240 \text{ m/100 ton}^{1/3}$ as indicated on Figure 6.5, and is considerably larger than the mean measured value of $150 \text{ m/100 ton}^{1/3}$ used above in Equation (7.1).

When the near-surface material does not have a negligible tensile strength no negative airblast wing develops and there is only a coupled spall region. In this instance, the radius of spall is dependent upon the charge configuration, and the following equations, based on the data in Figure 6.5, can be utilized to make predictions:

$$\text{HOB: } \bar{R}_s = \frac{30}{(100)^{1/3}} = 6.5 \text{ m/ton}^{1/3} \quad (7.2)$$

$$\text{STS: } \bar{R}_s = \frac{60}{(100)^{1/3}} = 13 \text{ m/ton}^{1/3} \quad (7.3)$$

$$\text{STC or HBS: } \bar{R}_s = \frac{90}{(100)^{1/3}} = 19.5 \text{ m/ton}^{1/3} \quad (7.4)$$

The maximum depth of spall can be obtained from the following equations:

$$\begin{aligned} \text{STS or STC: } z_s &= \text{depth of water table* or } 3.2(W, \text{tons})^{1/6}, \text{m} \\ &\text{whichever is smaller} \end{aligned} \quad (6.3)$$

$$\begin{aligned} \text{HBS: } z_s &= \text{depth of water table* or } 5.0(W, \text{tons})^{1/6}, \text{m} \\ &\text{whichever is smaller} \end{aligned} \quad (6.4)$$

The high explosive predictions should be accurate to approximately ± 33 percent.

C. Spall Associated With Nuclear Detonations

Referring to Figure 6.5, it can be seen that \bar{R}_s is approximately $50\text{m}/(100 \text{ ton})^{1/3}$ for JANGLE-U and $140\text{m}/(100 \text{ ton})^{1/3}$ for the bermed high explosive event presented. Assuming that any difference in the spall data from these two events is attributable to the energy available to create ground shock, one obtains a nuclear to high explosive ratio of approximately 36 percent. \bar{R}_s for the coupled nuclear spall region can be estimated from Figure 6.5 to be

$$\bar{R}_s = (50)(10)^{1/3} = 108 \text{ m/kt}^{1/3} \quad (7.5)$$

In a similar manner z_s can be estimated from Equation (6.3) as

$$\begin{aligned} z_s &= \text{depth of water table*} \\ &\text{or } (3.2)(1000)^{1/6} = 10.1(W, \text{kt})^{1/6}, \text{m} \\ &\text{whichever is smaller.} \end{aligned} \quad (7.6)$$

*If there is a rock layer at a depth of z_s or less, disregard the water table.

When the near-surface material has a negligible tensile strength a negative airblast wing region can be expected. Definition of the shape of this region can again be obtained through the use of Figure 7.1. For this instance, the nuclear \bar{R}_S can be estimated as:

$$\bar{R}_S = (0.78)(150)(10)^{1/3} = 252 \text{ m/kt}^{1/3} \quad (7.7)$$

Equation (7.7) was obtained by taking the \bar{R} ratio of nuclear to high explosive from Figure 7.1 for a constant depth, which is 0.78, and applying this ratio to Equation (7.1) with appropriate changes in yield.

SECTION VIII

Summary and Conclusions

This report presents theoretical, numerical, and empirical analyses of soil and rock spall due to near-surface explosions, both chemical and nuclear.

Section VII presents an empirically based technique for predicting the maximum radius of spall, R_s , and the maximum depth of spall, z_s , for a single near-surface explosion, either chemical or nuclear. The prediction technique is based on analyses of airblast and explosive ground motion data presented in Sections V and VI.

Section III presents a one-dimensional numerical analysis of spall in a tensile weak, hysteretic material with a free surface, using the computer code STEALTH 1D. The results must be considered preliminary, but they do demonstrate the ability of STEALTH 1D to handle propagation problems involving the creation of numerous new boundaries (spall planes), as well as the influence of gravity. One problem which will arise in two-dimensional spall calculations, which does not arise in one-dimensional calculations, is how to handle rejoin grid mismatch, i.e., the fact that two grid points which coincide prior to spall probably will not coincide after rejoin. This situation also arises in numerical analyses of explosive welding [Merkle and Cannon (1977)].

Section IV presents a series of theoretical analyses of the pore air effect, a principal near-surface spall mechanism in airblast loaded dry soil. Several of these analyses yield finite difference equations

suitable for use in parametric studies. Even closed form linear analyses demonstrate the dramatic influence of both boundary conditions and soil permeability on the transient pore air pressure distribution which can cause spall.

A fundamental understanding of soil spall, especially that caused by local airblast loading, requires an effective stress approach in which both the soil skeleton stress-strain-strength relations and the transient effect of flowing pore fluid are considered explicitly. This approach underlies other numerical and empirical analyses which yield results useful to designers of hardened structures and their shock isolation systems.

APPENDICES

APPENDIX A

Isothermal Fluid Diffusion Through a Rigid Porous Medium

Darcy's law for percolation of a fluid through a porous medium can be written in the form

$$v = -B_1 \frac{\partial P}{\partial x} \quad (A.1)$$

where

v = fluid discharge velocity (flow rate divided by total area)

B_1 = effective permeability

P = fluid pressure

x = distance

Under isothermal conditions, the fluid is assumed to obey the perfect gas law

$$P = a\rho \quad (A.2)$$

where

a = constant

ρ = fluid mass density

When the porosity of the porous medium remains constant, the equation of fluid mass conservation takes the form

$$n \frac{\partial \rho}{\partial t} = - \frac{\partial}{\partial x}(\rho v) \quad (A.3)$$

where

n = porosity, defined by Equation (E.1)

Introducing Equations (A.1) and (A.2) into Equation (A.3) yields

$$\frac{n \partial P}{a \partial t} = B_1 \frac{\partial}{\partial x} \left(\frac{P \partial P}{a \partial x} \right)$$

or

$$\frac{\partial P}{\partial t} = \frac{B_1}{n} \frac{\partial}{\partial x} \left(P \frac{\partial P}{\partial x} \right) \quad (\text{A.4})$$

Equation (A.4) can be written in the nonlinear form

$$\frac{\partial P}{\partial t} = \frac{B_1}{2n} \frac{\partial^2}{\partial x^2} (P^2) \quad (\text{A.5})$$

On the other hand, if the spatial variation of ρ is ignored in Equation (A.3), substitution of Equations (A.1) and (A.2) yields

$$\frac{\partial P}{\partial t} = \frac{B_1 P}{n} \frac{\partial^2 P}{\partial x^2} = D \frac{\partial^2 P}{\partial x^2} \quad (\text{A.6})$$

where

$$D = \frac{B_1 P}{n} \quad (\text{A.7})$$

Equation (A.6) can be considered linear if the parameter D is assumed to be constant.

APPENDIX B

Transient Linear Pore Air Diffusion in a Vented Layer

It is desired to calculate the dynamic pore air pressure, $P(x,t)$, satisfying the following conditions:

$$\frac{\partial P}{\partial t} = D \frac{\partial^2 P}{\partial x^2} \quad (0 < x < 1) \quad (\text{A.6})$$

$$P(0,t) = F(t) \quad (t > 0) \quad (\text{B.1})$$

$$P(1,t) = 0 \quad (t > 0) \quad (\text{B.2})$$

$$P(x,0) = 0 \quad (0 < x < 1) \quad (\text{B.3})$$

First, consider the associated problem having homogeneous boundary conditions [Hildebrand (1962:431); Taylor (1948:229)], which is

$$\frac{\partial P}{\partial t} = a \frac{\partial^2 P}{\partial x^2} \quad (0 < x < 2H) \quad (\text{B.4})$$

$$P(0,t) = 0 \quad (t > 0) \quad (\text{B.5})$$

$$P(2H,t) = 0 \quad (t > 0) \quad (\text{B.6})$$

$$P(x,0) = P_i(x) \quad (0 < x < 2H) \quad (\text{B.7})$$

Using the method of separation of variables [Hildebrand (1962:430)], we assume that

$$P(x,t) = \phi(x)\psi(t) \quad (\text{B.8})$$

Substitution of Equation (B.8) into Equation (B.4) yields

$$\phi \dot{\psi} = a \phi'' \psi \quad (\text{B.9})$$

and, dividing both sides of Equation (B.9) by the product $a\phi\psi = aP$,

assumed not to be zero everywhere, we obtain

$$\frac{1}{a} \frac{\dot{\psi}}{\psi} = \frac{\phi''}{\phi} \quad (\text{B.10})$$

Since ϕ is a function of x only, and ψ is a function of t only, and yet Equation (B.10) must hold for all values of x and t , it must be that both sides of Equation (B.10) are equal to the same constant, i.e.,

$$\frac{1}{a} \frac{\dot{\psi}}{\psi} = \frac{\phi''}{\phi} = -\omega^2 \quad (\text{B.11})$$

Equation (B.11) yields

$$\phi'' + \omega^2 \phi = 0 \quad (\text{B.12})$$

$$\dot{\psi} + a\omega^2 \psi = 0 \quad (\text{B.13})$$

The solutions to Equations (B.12) and (B.13) are

$$\phi(x) = C_1 \cos \omega x + C_2 \sin \omega x \quad (\text{B.14})$$

and

$$\psi(t) = C_3 e^{-a\omega^2 t} \quad (\text{B.15})$$

so that Equation (B.8) yields

$$P(x, t) = \phi(x)\psi(t) = (C_4 \cos \omega x + C_5 \sin \omega x) e^{-a\omega^2 t} \quad (\text{B.16})$$

where

$$C_4 = C_1 C_3 \quad (\text{B.17})$$

and

$$C_5 = C_2 C_3 \quad (\text{B.18})$$

In order to satisfy Equation (B.5) it must be that

$$C_4 = 0 \quad (\text{B.19})$$

and in order to satisfy Equation (B.6) it must be that

$$2\omega H = n\pi \quad (n = 1, 2, 3, \dots) \quad (\text{B.20})$$

which means that

$$\omega = \frac{n\pi}{2H} \quad (n = 1, 2, 3, \dots) \quad (\text{B.21})$$

Thus an infinite number of functions of the form

$$C_5 \sin \frac{n\pi x}{2H} e^{-\frac{n^2 \pi^2 a t}{4H^2}}$$

each satisfies Equations (B.4), (B.5) and (B.6), and since Equation (B.4) is linear and Equations (B.5) and (B.6) are homogeneous, any linear combination of the above functions is also a solution. Thus we can write

$$P(x, t) = \sum_{n=1}^{\infty} B_n \sin \frac{n\pi x}{2H} e^{-\frac{n^2 \pi^2 a t}{4H^2}} \quad (\text{B.22})$$

The constants B_n ($n = 1, 2, 3, \dots$) are determined from Equation (B.7).

$$P(x, 0) = P_i(x) = \sum_{n=1}^{\infty} B_n \sin \frac{n\pi x}{2H} \quad (\text{B.23})$$

Equation (B.23) is a Fourier sine series, and since, with

$$\frac{\pi x}{2H} = \theta \quad (\text{B.24})$$

we have

$$\begin{aligned} \int_0^{2H} \sin \frac{m\pi x}{2H} \sin \frac{n\pi x}{2H} dx &= \frac{2H}{\pi} \int_0^{\pi} \sin m\theta \sin n\theta d\theta \\ &= \frac{H}{\pi} \int_0^{\pi} [\cos(m-n)\theta - \cos(m+n)\theta] d\theta \end{aligned}$$

$$= \frac{H}{\pi} \left[\frac{\sin(m-n)\theta}{m-n} - \frac{\sin(m+n)\theta}{m+n} \right]_0^{\pi} = 0 \quad (m \neq n) \quad (B.25)$$

and

$$\begin{aligned} \int_0^{2H} \sin^2 \frac{n\pi x}{2H} dx &= \frac{2H}{\pi} \int_0^{\pi} \sin^2 n\theta d\theta \\ &= \frac{H}{\pi} \int_0^{\pi} (1 - \cos 2n\theta) d\theta = H \end{aligned} \quad (B.26)$$

then if both sides of Equation (B.23) are multiplied by $\sin m\pi x/2H$, and the results integrated on x from 0 to $2H$, the result is

$$\int_0^{2H} P_i(x) \sin \frac{m\pi x}{2H} dx = B_m H$$

so that

$$B_n = \frac{1}{H} \int_0^{2H} P_i(x) \sin \frac{n\pi x}{2H} dx \quad (B.27)$$

We now consider the problem identical to that defined by Equations (A.6), (B.1), (B.2) and (B.3), except that the function $F(t)$ in Equation (B.1) is assumed to be constant, i.e.,

$$P(0,t) = F \quad (t > 0) \quad (B.28)$$

The approach to this problem is to assume that [Carslaw and Jaeger (1959:99)]

$$P = U + W \quad (B.29)$$

where

$$\frac{d^2 U}{dx^2} = 0 \quad (0 < x < 1) \quad (B.30)$$

$$U(0,t) = F \quad (t > 0) \quad (B.31)$$

$$U(1,t) = 0 \quad (t > 0) \quad (B.32)$$

and

$$\frac{\partial W}{\partial t} = D \frac{\partial^2 W}{\partial x^2} \quad (0 < x < 1) \quad (\text{B.33})$$

$$W(0, t) = 0 \quad (t > 0) \quad (\text{B.34})$$

$$W(1, t) = 0 \quad (t > 0) \quad (\text{B.35})$$

$$W(x, 0) = -U(x) \quad (0 < x < 1) \quad (\text{B.36})$$

The expression for U is easily found to be

$$U(x) = F(1 - \frac{x}{l}) \quad (\text{B.37})$$

and the expression for W is found from Equation (B.22)

$$W(x, t) = \sum_{n=1}^{\infty} B_n \sin \frac{n\pi x}{l} e^{-\frac{n^2 \pi^2 D t}{l^2}} \quad (\text{B.38})$$

where Equations (B.27), (B.36) and (B.37) yield

$$B_n = -\frac{2F}{l} \int_0^l (1 - \frac{x}{l}) \sin \frac{n\pi x}{l} dx \quad (\text{B.39})$$

The integral on the RHS of Equation (B.39) can be integrated by parts by setting

$$u = 1 - \frac{x}{l} \quad (\text{B.40})$$

$$du = -\frac{dx}{l} \quad (\text{B.41})$$

$$dv = \sin \frac{n\pi x}{l} dx \quad (\text{B.42})$$

$$v = -\frac{l}{n\pi} \cos \frac{n\pi x}{l} \quad (\text{B.43})$$

so that

$$\begin{aligned}
-\frac{1B_n}{2F} &= -\frac{1}{n\pi} \left(1 - \frac{x}{l}\right) \cos \frac{n\pi x}{l} \Big|_0^l - \frac{1}{n\pi} \int_0^l \cos \frac{n\pi x}{l} dx \\
&= \frac{1}{n\pi}
\end{aligned} \tag{B.44}$$

and therefore

$$B_n = -\frac{2F}{n\pi} \tag{B.45}$$

Thus, Equations (B.29), (B.37), (B.38) and (B.45) yield

$$P(x,t) = F \left[\left(1 - \frac{x}{l}\right) - \frac{2}{\pi} \sum_{n=0}^{\infty} \frac{1}{n} \sin \frac{n\pi x}{l} e^{-\frac{n^2 \pi^2 D t}{l^2}} \right] \tag{B.46}$$

[cf. Carslaw and Jaeger (1959:103)].

We can now return to the original problem defined by Equations (A.6), (B.1), (B.2) and (B.3), for which the boundary value in Equation (B.1) is a function of time. Because the system is linear, the solution can be written as a Duhamel integral in the form

$$P(x,t) = \int_0^t F(\lambda) h(x,t-\lambda) d\lambda \tag{B.47}$$

where

$h(x,t-\lambda)$ = solution for a unit impulse at $(0,\lambda)$.

However, what we have obtained above is not $h(x,t-\lambda)$, but its integral,

$s(x,t-\lambda)$ = solution for a unit step at $(0,\lambda)$.

In order to use the step function response, we integrate Equation (B.47) by parts, by setting

$$u = F(\lambda) \tag{B.48}$$

$$du = F'(\lambda) d\lambda \tag{B.49}$$

$$dv = h(x, t-\lambda) d\lambda \quad (B.50)$$

$$v = -s(x, t-\lambda) \quad (B.51)$$

so that

$$\begin{aligned} P(x, t) &= -F(\lambda)s(x, t-\lambda) \int_0^t + \int_0^t F'(\lambda)s(x, t-\lambda) d\lambda \\ &= -F(t)s(x, 0) + F(0)s(x, t) + \int_0^t F'(\lambda)s(x, t-\lambda) d\lambda \end{aligned} \quad (B.52)$$

where, from Equation (B.46), we have

$$s(x, t-\lambda) = \left(1 - \frac{x}{l}\right) - \frac{2}{\pi} \sum_{n=1}^{\infty} \frac{1}{n} \sin \frac{n\pi x}{l} e^{-\frac{n^2 \pi^2 D(t-\lambda)}{l^2}} \quad (B.53)$$

$$s(x, t) = \left(1 - \frac{x}{l}\right) - \frac{2}{\pi} \sum_{n=1}^{\infty} \frac{1}{n} \sin \frac{n\pi x}{l} e^{-\frac{n^2 \pi^2 D t}{l^2}} \quad (B.54)$$

Now if

$$F(\lambda) = P_0 e^{-\alpha \lambda} \quad (B.55)$$

so that

$$F(0) = P_0 \quad (B.56)$$

and

$$F'(\lambda) = -\alpha P_0 e^{-\alpha \lambda} \quad (B.57)$$

then the terms in Equation (B.52) are

$$F(0)s(x, t) = P_0 \left[\left(1 - \frac{x}{l}\right) - \frac{2}{\pi} \sum_{n=1}^{\infty} \frac{1}{n} \sin \frac{n\pi x}{l} e^{-\frac{n^2 \pi^2 D t}{l^2}} \right] \quad (B.58)$$

and

$$\begin{aligned}
\int_0^t F'(\lambda) s(x, t-\lambda) d\lambda &= -\alpha P_0 \left(1 - \frac{x}{l}\right) \int_0^t e^{-\alpha \lambda} d\lambda \\
&+ \frac{2\alpha P_0}{\pi} \sum_{n=1}^{\infty} \frac{1}{n} \sin \frac{n\pi x}{l} e^{-\frac{n^2 \pi^2 D t}{l^2}} \int_0^t e^{\left(\frac{n^2 \pi^2 D}{l^2} - \alpha\right) \lambda} d\lambda \\
&= P_0 \left(1 - \frac{x}{l}\right) \left[e^{-\alpha \lambda} \right]_0^t \\
&+ \frac{2\alpha P_0}{\pi} \sum_{n=1}^{\infty} \frac{1}{n} \sin \frac{n\pi x}{l} e^{-\frac{n^2 \pi^2 D t}{l^2}} \left[\frac{e^{\left(\frac{n^2 \pi^2 D}{l^2} - \alpha\right) \lambda}}{\frac{n^2 \pi^2 D}{l^2} - \alpha} \right]_0^t \\
&= P_0 \left(1 - \frac{x}{l}\right) (e^{-\alpha t} - 1) \\
&- \frac{2\alpha P_0}{\pi} \sum_{n=1}^{\infty} \frac{1}{n} \sin \frac{n\pi x}{l} \left(\frac{e^{-\frac{n^2 \pi^2 D t}{l^2}}}{\frac{n^2 \pi^2 D}{l^2} - \alpha} - e^{-\alpha t} \right) \quad (B.59)
\end{aligned}$$

Finally, substitution of Equations (B.58) and (B.59) into Equation (B.52) yields

$$\begin{aligned}
P(x, t) &= P_0 \left[\left(1 - \frac{x}{l}\right) e^{-\alpha t} \right. \\
&\quad \left. - \frac{2}{\pi} \sum_{n=1}^{\infty} \frac{1}{n} \sin \frac{n\pi x}{l} \left(\frac{e^{-\frac{n^2 \pi^2 D t}{l^2}}}{\frac{n^2 \pi^2 D}{l^2} - \alpha} - \alpha e^{-\alpha t} \right) \right] \quad (B.60)
\end{aligned}$$

If we set

$$\frac{Dt}{l^2} = T \quad (\text{B.61})$$

$$\frac{l^2 \alpha}{D} = \beta \quad (\text{B.62})$$

$$\frac{x}{l} = \xi \quad (\text{B.63})$$

then Equation (B.60) can be written in the form

$$P(\xi, T) = P_0 \left[(1-\xi)e^{-\beta T} - \frac{2}{\pi} \sum_{n=1}^{\infty} \frac{1}{n} \sin n\pi\xi \left(\frac{n^2 \pi^2 e^{-n^2 \pi^2 T} - \beta e^{-\beta T}}{n^2 \pi^2 - \beta} \right) \right] \quad (\text{B.64})$$

APPENDIX C

Transient Linear Pore Air Diffusion in an Unvented Layer

It is desired to calculate the dynamic pore air pressure, $P(x,t)$, satisfying the following conditions:

$$\frac{\partial P}{\partial t} = D \frac{\partial^2 P}{\partial x^2} \quad (0 < x < 1) \quad (\text{A.6})$$

$$P(0,t) = F(t) \quad (t > 0) \quad (\text{C.1})$$

$$\frac{\partial P}{\partial x}(1,t) = 0 \quad (t > 0) \quad (\text{C.2})$$

$$P(x,0) = 0 \quad (0 < x < 1) \quad (\text{C.3})$$

The above solution can be most easily obtained as the first half of the solution, symmetric about $x = 1$, for which

$$\frac{\partial P}{\partial t} = D \frac{\partial^2 P}{\partial x^2} \quad (0 < x < 21) \quad (\text{C.4})$$

$$P(0,t) = F(t) \quad (t > 0) \quad (\text{C.1})$$

$$P(21,t) = F(t) \quad (t > 0) \quad (\text{C.5})$$

$$P(x,0) = 0 \quad (0 < x < 21) \quad (\text{C.6})$$

We will again use the solution for homogeneous boundary conditions defined by Equations (B.22) and (B.27).

We now consider the problem identical to that defined by Equations (C.4), (C.1), (C.5) and (C.6), except that the function $F(t)$ in Equations (C.1) and (C.5) is assumed to be constant, i.e.,

$$P(0,t) = P(21,t) = F \quad (t > 0) \quad (\text{C.7})$$

As in Appendix B, we assume a solution of the form

$$P = U + W \quad (C.8)$$

where, in this case

$$\frac{d^2 U}{dx^2} = 0 \quad (0 < x < 2l) \quad (C.9)$$

$$U(0, t) = F \quad (t > 0) \quad (C.10)$$

$$U(2l, t) = F \quad (t > 0) \quad (C.11)$$

and

$$\frac{\partial W}{\partial t} = D \frac{\partial^2 W}{\partial x^2} \quad (0 < x < 2l) \quad (C.12)$$

$$W(0, t) = 0 \quad (t > 0) \quad (C.13)$$

$$W(2l, t) = 0 \quad (t > 0) \quad (C.14)$$

$$W(x, 0) = -U(x) \quad (0 < x < 2l) \quad (C.15)$$

The expression for U is easily found to be

$$U(x) = F \quad (C.16)$$

and the expression for W is obtained from Equation (B.22)

$$W(x, t) = \sum_{n=1}^{\infty} B_n \sin \frac{n\pi x}{2l} e^{-\frac{n^2 \pi^2 D t}{4l^2}} \quad (C.17)$$

where Equations (B.27), (C.15) and (C.16) yield

$$\begin{aligned} B_n &= -\frac{F}{l} \int_0^{2l} \sin \frac{n\pi x}{2l} dx = -\frac{2F}{n\pi} \left[-\cos \frac{n\pi x}{2l} \right]_0^{2l} \\ &= -\frac{2F}{n\pi} (1 - \cos n\pi) = -\frac{4F}{n\pi} \quad (n \text{ odd}) \\ &= 0 \quad (n \text{ even}) \end{aligned} \quad (C.18)$$

cf. [Taylor (1948:232)]. Thus Equations (C.8), (C.16), (C.17) and (C.18) yield

$$P(x,t) = F \left[1 - \frac{4}{\pi} \sum_{n=1}^{\infty} \frac{\sin \frac{(2n-1)\pi x}{2l}}{2n-1} e^{-\frac{(2n-1)^2 \pi^2 D t}{4l^2}} \right] \quad (C.19)$$

We can now return to the original problem defined by Equations (C.4), (C.1), (C.5) and (C.6), for which the boundary value in Equations (C.1) and (C.5) is a function of time. Equation (B.52) again applies, where from Equation (C.19),

$$s(x,t-\lambda) = 1 - \frac{4}{\pi} \sum_{n=1}^{\infty} \frac{\sin \frac{(2n-1)\pi x}{2l}}{2n-1} e^{-\frac{(2n-1)^2 \pi^2 D (t-\lambda)}{4l^2}} \quad (C.20)$$

$$s(x,t) = 1 - \frac{4}{\pi} \sum_{n=1}^{\infty} \frac{\sin \frac{(2n-1)\pi x}{2l}}{2n-1} e^{-\frac{(2n-1)^2 \pi^2 D t}{4l^2}} \quad (C.21)$$

Assuming the boundary value inputs are again defined by Equations (B.55), (B.56) and (B.57), the terms in Equation (B.52) are

$$F(0)s(x,t) = P_0 \left[1 - \frac{4}{\pi} \sum_{n=1}^{\infty} \frac{\sin \frac{(2n-1)\pi x}{2l}}{2n-1} e^{-\frac{(2n-1)^2 \pi^2 D t}{4l^2}} \right] \quad (C.22)$$

and

$$\begin{aligned} \int_0^t F'(\lambda) s(x,t-\lambda) d\lambda &= -\alpha P_0 \int_0^t e^{-\alpha \lambda} d\lambda \\ &+ \frac{4\alpha P_0}{\pi} \sum_{n=1}^{\infty} \frac{\sin \frac{(2n-1)\pi x}{2l}}{2n-1} e^{-\frac{(2n-1)^2 \pi^2 D t}{4l^2}} \int_0^t e^{\left[\frac{(2n-1)^2 \pi^2 D}{4l^2} - \alpha \right] \lambda} d\lambda \end{aligned}$$

$$\begin{aligned}
&= P_0 \left[e^{-\alpha \lambda} \right]_0^t \\
&+ \frac{4\alpha P_0}{\pi} \sum_{n=1}^{\infty} \frac{\sin \frac{(2n-1)\pi x}{2l}}{2n-1} e^{-\frac{(2n-1)^2 \pi^2 D t}{4l^2}} \left\{ \frac{\left[\frac{(2n-1)^2 \pi^2 D}{4l^2} - \alpha \right] \lambda}{\frac{(2n-1)^2 \pi^2 D}{4l^2} - \alpha} \right\}^t \bigg|_0 \\
&= P_0 (e^{-\alpha t} - 1) \\
&- \frac{4\alpha P_0}{\pi} \sum_{n=1}^{\infty} \frac{\sin \frac{(2n-1)\pi x}{2l}}{2n-1} \left[\frac{e^{-\frac{(2n-1)^2 \pi^2 D t}{4l^2}} - e^{-\alpha t}}{\frac{(2n-1)^2 \pi^2 D}{4l^2} - \alpha} \right] \quad (C.23)
\end{aligned}$$

Finally, substitution of Equations (C.22) and (C.23) into Equation (B.52) yields

$$\begin{aligned}
P(x,t) &= P_0 e^{-\alpha t} \\
&- \frac{4P_0}{\pi} \sum_{n=1}^{\infty} \frac{\sin \frac{(2n-1)\pi x}{2l}}{2n-1} \left[\frac{\frac{(2n-1)^2 \pi^2 D}{4l^2} e^{-\frac{(2n-1)^2 \pi^2 D t}{4l^2}} - \alpha e^{-\alpha t}}{\frac{(2n-1)^2 \pi^2 D}{4l^2} - \alpha} \right] \quad (C.24)
\end{aligned}$$

cf. [Carslaw and Jaeger (1959:105)].

If we set

$$\frac{Dt}{4l^2} = T \quad (C.25)$$

$$\frac{4l^2 \alpha}{D} = \beta \quad (C.26)$$

$$\frac{x}{2T} = \xi \quad (C.27)$$

$$2n - 1 = N \quad (C.28)$$

then Equation (C.24) can be written in the form

$$P(\xi, T) = P_0 \left[e^{-\beta T} - \frac{4}{\pi} \sum_{n=1}^{\infty} \frac{1}{N} \sin N\pi\xi \left(\frac{N^2 \pi^2 e^{-N^2 \pi^2 T} - \beta e^{-\beta T}}{N^2 \pi^2 - \beta} \right) \right] \quad (C.29)$$

APPENDIX D

Adiabatic Fluid Diffusion Through a Rigid Porous Medium

Darcy's law for percolation of a fluid through a porous medium can be written in the form

$$v = -B_1 \frac{\partial P}{\partial x} \quad (A.1)$$

where the terms in the above equation are defined in Appendix A.

Under adiabatic conditions, the fluid is assumed to obey the relation

$$P = a\rho^\gamma \quad (D.1)$$

where $\gamma = 1.4$ for air, and the remaining terms are defined in Appendix A.

When the porosity of the porous medium remains constant, the equation of fluid mass conservation takes the form

$$n \frac{\partial \rho}{\partial t} = - \frac{\partial}{\partial x} (\rho v) \quad (A.3)$$

where n is porosity, as defined by Equation (E.1). Introducing Equations (A.1) and (D.1) into Equation (A.3) yields

$$\frac{n}{\gamma} \left(\frac{P}{a} \right)^{\frac{1}{\gamma} - 1} \cdot \frac{1}{a} \frac{\partial P}{\partial t} = B_1 \frac{\partial}{\partial x} \left[\left(\frac{P}{a} \right)^{1/\gamma} \frac{\partial P}{\partial x} \right]$$

or

$$\frac{\partial P}{\partial t} = \frac{B_1 \gamma P^{1-1/\gamma}}{n} \frac{\partial}{\partial x} \left(P^{1/\gamma} \frac{\partial P}{\partial x} \right) \quad (D.2)$$

Setting $\gamma = 1$ in Equation (D.2) yields

$$\frac{\partial P}{\partial t} = \frac{B_1}{n} \frac{\partial}{\partial x} \left(P \frac{\partial P}{\partial x} \right) \quad (\text{A.4})$$

and neglecting the spatial variation of ρ (i.e., $P^{1/\gamma}$) in Equation (D.2) yields

$$\frac{\partial P}{\partial t} = \frac{B_1 \gamma P}{n} \frac{\partial^2 P}{\partial x^2} = D \frac{\partial^2 P}{\partial x^2} \quad (\text{D.3})$$

where

$$D = \frac{B_1 \gamma P}{n} \quad (\text{D.4})$$

Equation D.3) can be considered linear if the parameter D is assumed to be constant.

If no assumption is made concerning the terms in Equation (D.2), and the RHS is expanded, the result is

$$\begin{aligned} \frac{\partial P}{\partial t} &= \frac{B_1 \gamma P^{1-1/\gamma}}{n} \left[\frac{1}{\gamma} P^{1/\gamma} - 1 \left(\frac{\partial P}{\partial x} \right)^2 + P^{1/\gamma} \frac{\partial^2 P}{\partial x^2} \right] \\ &= \frac{B_1}{n} \left[\left(\frac{\partial P}{\partial x} \right)^2 + \gamma P \frac{\partial^2 P}{\partial x^2} \right] \end{aligned} \quad (\text{D.5})$$

which is the nonlinear equation used by [Zernow, et al (1973:101)]. The first term in brackets on the RHS of Equation (D.5) reflects the spatial variation of ρ ; the second term reflects the spatial variation of v .

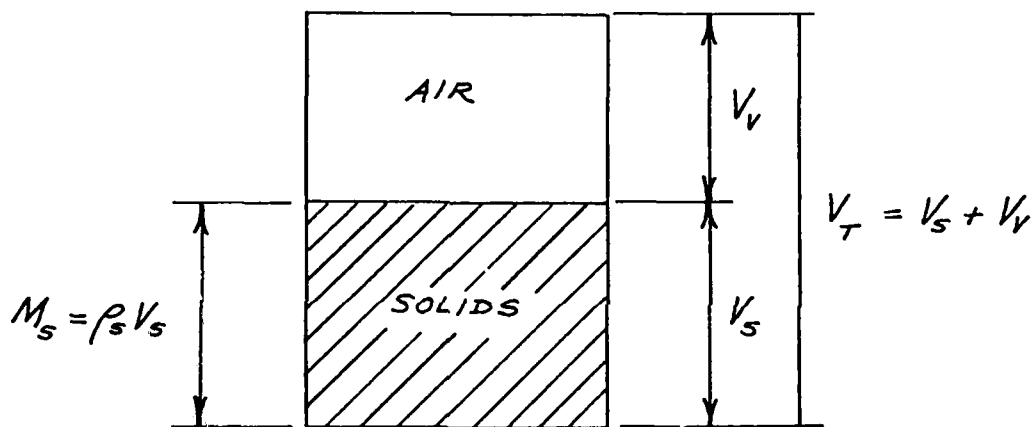
See Appendix F for a finite difference approximation to Equation (D.5).

APPENDIX E

Propagation Velocity in Spalled Soil

It is assumed that the soil skeleton is distended, and therefore occupies volume but carries no load. Thus the material can transmit hydrostatic pressure, but not shear.

The standard soil phase diagram applies,



and the following definitions apply:

$$\text{porosity: } n = \frac{V_v}{V_T} \quad (\text{E.1})$$

$$\text{total density: } \rho_T = \frac{M_S}{V_T} \quad (\text{E.2})$$

$$\text{volumetric strain: } \epsilon = \frac{V_T}{V_{T0}} - 1 \quad (\text{E.3})$$

The sound speed, c , at pressure, P , for the mixture of soil particles in air is given by the equation

$$c^2 = - \frac{1}{\rho_T} \frac{dP}{\frac{dV_T}{V_T}} \quad (\text{E.4})$$

where

$$V_T = V_{T0}(1 + \epsilon) \quad (\text{E.5})$$

$$dV_T = V_{T0} d\epsilon \quad (\text{E.6})$$

$$\rho_T = \frac{\rho_s V_s}{V_{T0}(1+\epsilon)} = \rho_s \left(\frac{1-n_0}{1+\epsilon} \right) \quad (\text{E.7})$$

Thus, Equation (E.4) can be written in the form

$$c^2 = - \frac{(1 + \epsilon)^2}{\rho_s (1-n_0)} \frac{dP}{d\epsilon} \quad (\text{E.8})$$

For rapid pressure changes, the relation between pore air pressure and pore air (void) volume is the adiabatic equation

$$P = P_0 \left(\frac{V_V}{V_{V0}} \right)^{-\gamma} = P_0 \left(\frac{n_0 + \epsilon}{n_0} \right)^{-\gamma} \quad (\text{E.9})$$

where $\gamma = 1.4$ for air. Therefore, we have

$$\frac{dP}{d\epsilon} = - \frac{\gamma P_0}{n_0} \left(\frac{n_0 + \epsilon}{n_0} \right)^{-(\gamma+1)} \quad (\text{E.10})$$

so that Equation (E.8) can be written in the form

$$c^2 = \frac{\gamma P_0}{\rho_s n_0 (1-n_0)} (1+\epsilon)^2 \left(\frac{n_0}{n_0 + \epsilon} \right)^{\gamma+1} \quad (\text{E.11})$$

and finally

$$c = \left[\frac{\gamma_p^0}{\rho_s n_0 (1-n_0)} \right]^{1/2} (1+\epsilon) \left(\frac{n_0}{n_0 + \epsilon} \right)^{\frac{\gamma+1}{2}} \quad (E.12)$$

The value of c for a typical soil has been tabulated as a function of strain by [Merkle (1980:38)].

APPENDIX F

Three-Dimensional Adiabatic Fluid Diffusion Through a Rigid, Porous, Isotropic Medium

Darcy's law for fluid diffusion through a porous, isotropic medium can be written in the form

$$\bar{v} = -B_1 \bar{\nabla} P \quad (F.1)$$

where

\bar{v} = fluid discharge velocity vector

B_1 = effective isotropic permeability

P = fluid pressure

$\bar{\nabla} = \frac{\partial}{\partial x_1} \bar{e}_1 + \frac{\partial}{\partial x_2} \bar{e}_2 + \frac{\partial}{\partial x_3} \bar{e}_3$ = gradient vector operator

x_1, x_2, x_3 = rectangular Cartesian coordinates

$\bar{e}_1, \bar{e}_2, \bar{e}_3$ = unit vectors in the three coordinate directions

Under adiabatic conditions, the fluid is assumed to obey the relation

$$P = a\rho^\gamma \quad (F.2)$$

where

a = constant

ρ = fluid mass density

γ = ratio of specific heats (= 1.4 for air)

When the porosity of the porous medium remains constant, the equation of fluid mass conservation takes the form

$$n \frac{\partial p}{\partial t} = -\bar{\nabla} \cdot (\rho \bar{\nabla}) \quad (\text{F.3})$$

where

n = porosity

Introducing Equations (F.1) and (F.2) into Equation (F.3) yields

$$\frac{n}{\gamma} \left(\frac{p}{a} \right)^{\frac{1}{\gamma} - 1} \frac{1}{a} \frac{\partial p}{\partial t} = B_1 \bar{\nabla} \cdot \left[\left(\frac{p}{a} \right)^{1/\gamma} \bar{\nabla} p \right]$$

or

$$\frac{\partial p}{\partial t} = \frac{B_1 \gamma p^{1-1/\gamma}}{n} \bar{\nabla} \cdot (p^{1/\gamma} \bar{\nabla} p) \quad (\text{F.4})$$

Setting $\gamma = 1$ in Equation (F.4) yields

$$\frac{\partial p}{\partial t} = \frac{B_1}{n} \bar{\nabla} \cdot (p \bar{\nabla} p) \quad (\text{F.5})$$

and neglecting the spatial variation of ρ (i.e., $p^{1/\gamma}$) in Equation F.4 yields

$$\frac{\partial p}{\partial t} = \frac{B_1 \gamma p}{n} \nabla^2 p = D \nabla^2 p \quad (\text{F.6})$$

where

$$D = \frac{B_1 \gamma p}{n} \quad (\text{F.7})$$

Equation [F.6] can be considered linear if the parameter D is assumed to be constant.

If no assumption is made concerning the terms in Equation (F.4), and the RHS is expanded, the result is [Hildebrand (1962:278)]

$$\frac{\partial p}{\partial t} = \frac{B_1 \gamma p^{1-1/\gamma}}{n} \left[\frac{1}{\gamma} p^{1/\gamma} - 1 \right] |\bar{\nabla} p|^2 + p^{1/\gamma} \nabla^2 p = \frac{B_1}{n} (|\bar{\nabla} p|^2 + \gamma p \nabla^2 p) \quad (F.8)$$

The first term in parentheses on the RHS of Equation (F.8) reflects the spatial variation of p ; the second term reflects the spatial variation of $\bar{\nabla}$.

If we set

$$p_{i,j,k} = \text{pressure at } (x_i, y_j, t_k)$$

then the two dimensional finite difference approximation to Equation (F.8) is [Crandall (1956:246,376)]

$$\begin{aligned} \frac{p_{i,j,k+1} - p_{i,j,k}}{\Delta t} = & \frac{B_1}{n} \left[\frac{(p_{i+1,j,k} - p_{i-1,j,k})^2 + (p_{i,j+1,k} - p_{i,j-1,k})^2}{4h^2} \right. \\ & \left. + \gamma p_{i,j,k} \left(\frac{p_{i-1,j,k} + p_{i+1,j,k} + p_{i,j-1,k} + p_{i,j+1,k} - 4p_{i,j,k}}{h^2} \right) \right] \quad (F.9) \end{aligned}$$

where

$$h = \Delta x = \Delta y \quad (F.10)$$

so that

$$\begin{aligned} p_{i,j,k+1} = & p_{i,j,k} + \frac{B_1 \Delta t}{nh^2} \left[\frac{(p_{i+1,j,k} - p_{i-1,j,k})^2 + (p_{i,j+1,k} - p_{i,j-1,k})^2}{4} \right. \\ & \left. + \gamma p_{i,j,k} (p_{i-1,j,k} + p_{i+1,j,k} + p_{i,j-1,k} + p_{i,j+1,k} - 4p_{i,j,k}) \right] \quad (F.11) \end{aligned}$$

For the one dimensional case, Equation (F.11) reduces to

$$P_{i,k+1} = P_{i,k} + \frac{B_1 \Delta t}{nh^2} \left[\left(\frac{P_{i+1,k} - P_{i-1,k}}{2} \right)^2 + \gamma P_{i,k} (P_{i+1,k} - 2P_{i,k} + P_{i-1,k}) \right]^2 \quad (F.12)$$

An alternate formulation of the above equations results in a pseudo-linear partial differential equation without any approximation. Substituting Equation (F.1) into Equation (F.3) yields

$$n \frac{\partial \rho}{\partial t} = -\bar{\nabla} \cdot (-\rho B_1 \bar{\nabla} P) = B_1 \bar{\nabla} \cdot (\rho \bar{\nabla} P) \quad (F.13)$$

Now Equation (F.2) can be written in the form

$$\rho = \left(\frac{P}{a} \right)^{1/\gamma} \quad (F.14)$$

so that substituting Equation (F.14) into Equation (F.13) yields

$$n \frac{\partial}{\partial t} \left[\left(\frac{P}{a} \right)^{1/\gamma} \right] = B_1 \bar{\nabla} \cdot \left[\left(\frac{P}{a} \right)^{1/\gamma} \bar{\nabla} P \right]$$

or

$$\frac{\partial}{\partial t} (P^{1/\gamma}) = \frac{B_1}{n} \bar{\nabla} \cdot (P^{1/\gamma} \bar{\nabla} P) \quad (F.15)$$

Now on the RHS of Equation (F.15) we have

$$P^{1/\gamma} \bar{\nabla} P = \frac{1}{1/\gamma + 1} \bar{\nabla} (P^{1/\gamma+1}) \quad (F.16)$$

so that Equation (F.15) can be written in the pseudo-linear form

$$\frac{\partial}{\partial t} (P^{1/\gamma}) = \frac{B_1}{n(1/\gamma + 1)} \nabla^2 (P^{1/\gamma+1}) \quad (F.17)$$

The one-dimensional form of Equation (F.17) is

$$\frac{\partial}{\partial t}(p^{1/\gamma}) = \frac{B_1}{n(1/\gamma + 1)} \frac{\partial^2}{\partial x^2}(p^{1/\gamma+1}) \quad (F.18)$$

For the isothermal case, setting $\gamma = 1$ reduces Equation (F.18) to Equation (A.5). The finite difference approximation to Equation (F.18) is

$$\frac{p_{i,k+1}^{1/\gamma} - p_{i,k}^{1/\gamma}}{\Delta t} = \frac{B_1}{n(1/\gamma + 1)} \left[\frac{p_{i-1,k}^{\frac{1}{\gamma} + 1} - 2p_{i,k}^{\frac{1}{\gamma} + 1} + p_{i+1,k}^{\frac{1}{\gamma} + 1}}{(\Delta x)^2} \right] \quad (F.19)$$

so that

$$p_{i,k+1}^{1/\gamma} = p_{i,k}^{1/\gamma} + \frac{B_1(\Delta t)}{n(1/\gamma + 1)(\Delta x)^2} (p_{i-1,k}^{\frac{1}{\gamma} + 1} - 2p_{i,k}^{\frac{1}{\gamma} + 1} + p_{i+1,k}^{\frac{1}{\gamma} + 1}) \quad (F.20)$$

where

$$p_{i,k+1}^{1/\gamma+1} = (p_{i,k+1}^{1/\gamma})^{1+\gamma} \quad (F.21)$$

and

$$p_{i,k+1} = (p_{i,k+1}^{1/\gamma})^\gamma \quad (F.22)$$

A similar pseudo-linear formulation can be constructed with ρ as the dependent variable. Substituting Equation (F.2) into Equation (F.18) yields

$$\frac{\partial}{\partial t}(a^{1/\gamma} \rho) = \frac{B_1}{n(1/\gamma + 1)} \nabla^2 [(a \rho^\gamma)^{\frac{1}{\gamma} + 1}]$$

or

$$\frac{\partial \rho}{\partial t} = \frac{B_1 a}{n(1/\gamma + 1)} \nabla^2 (\rho^{1+\gamma}) \quad (F.23)$$

The one-dimensional form of Equation (F.23) is

$$\frac{\partial \rho}{\partial t} = \frac{B_1 a}{n(1/\gamma + 1)} \frac{\partial^2}{\partial x^2} (\rho^{1+\gamma}) \quad (F.24)$$

The finite difference approximation to Equation (F.24) is straightforward, but not quite as convenient for computation as Equations (F.20), (F.21) and (F.22), since pressure boundary conditions must be converted to density. Equations (F.20), (F.21) and (F.22) are even convenient for hand computation.

APPENDIX G

Transient Linear Pore Air Diffusion in a Vented Layer Subjected to Surface Airblast Loading Having a Negative Phase

All the equations of Appendix B apply, up to and including Equation (B.54). In place of Equation (B.55) we assume that

$$F(\lambda) = P e^{-\alpha\lambda} \left(1 - \frac{\lambda}{\lambda_0}\right) \quad (G.1)$$

so that

$$F(0) = P_0 \quad (G.2)$$

$$\begin{aligned} F'(\lambda) &= -\alpha P_0 e^{-\alpha\lambda} \left(1 - \frac{\lambda}{\lambda_0}\right) - \frac{P_0}{\lambda_0} e^{-\alpha\lambda} \\ &= -\alpha \left(1 + \frac{1}{\alpha\lambda_0}\right) P_0 e^{-\alpha\lambda} - \frac{\alpha}{\lambda_0} P_0 \lambda e^{-\alpha\lambda} \end{aligned} \quad (G.3)$$

If we set

$$F'_1(\lambda) = -\alpha \left(1 + \frac{1}{\alpha\lambda_0}\right) P_0 e^{-\alpha\lambda} \quad (G.4)$$

$$F'_2(\lambda) = \frac{\alpha}{\lambda_0} P_0 \lambda e^{-\alpha\lambda} \quad (G.5)$$

then Equation (G.3) can be written in the form

$$F'(\lambda) = F'_1(\lambda) + F'_2(\lambda) \quad (G.6)$$

The terms in Equation (B.52) then are

$$F(0)s(x,t) = P_0 \left[\left(1 - \frac{x}{l}\right) - \frac{2}{\pi} \sum_{n=1}^{\infty} \frac{1}{n} \sin \frac{n\pi x}{l} e^{-\frac{n^2 \pi^2 D t}{l^2}} \right] \quad (G.7)$$

and

$$\begin{aligned} \int_0^t F_1'(\lambda) s(x, t-\lambda) d\lambda &= P_0 \left(1 + \frac{1}{\alpha \lambda_0}\right) \left(1 - \frac{x}{l}\right) (e^{-\alpha t} - 1) \\ &\quad - \frac{2\left(\alpha + \frac{1}{\lambda_0}\right) P_0}{\pi} \sum_{n=1}^{\infty} \frac{1}{n} \sin \frac{n\pi x}{l} \left(\frac{e^{-\frac{n^2 \pi^2 D t}{l^2}} - e^{-\alpha t}}{\frac{n^2 \pi^2 D}{l^2} - \alpha} \right) \end{aligned} \quad (G.8)$$

and finally

$$\begin{aligned} \int_0^t F_2'(\lambda) s(x, t-\lambda) d\lambda &= P_0 \frac{\alpha}{\lambda_0} \left(1 - \frac{x}{l}\right) \int_0^t \lambda e^{-\alpha \lambda} d\lambda \\ &\quad - \frac{2\alpha P_0}{\pi \lambda_0} \sum_{n=1}^{\infty} \frac{1}{n} \sin \frac{n\pi x}{l} e^{-\frac{n^2 \pi^2 D t}{l^2}} \int_0^t \lambda e^{\left(\frac{n^2 \pi^2 D}{l^2} - \alpha\right) \lambda} d\lambda \end{aligned} \quad (G.9)$$

Both integrals in Equation (G.9) are of the form

$$I = \int_0^t \lambda e^{r\lambda} d\lambda \quad (G.10)$$

which can be integrated by parts by setting

$$U = \lambda \quad (G.11)$$

$$dU = d\lambda \quad (G.12)$$

$$dV = e^{r\lambda} d\lambda \quad (G.13)$$

$$V = \frac{1}{r} e^{r\lambda} \quad (G.14)$$

AD-A125 592

EFFECT OF SPALL ON THE CHARACTERISTICS OF EXPLOSIVE
GROUND MOTION(U) APPLIED RESEARCH ASSOCIATES INC
ALBUQUERQUE NM D H MERKLE ET AL 10 SEP 82

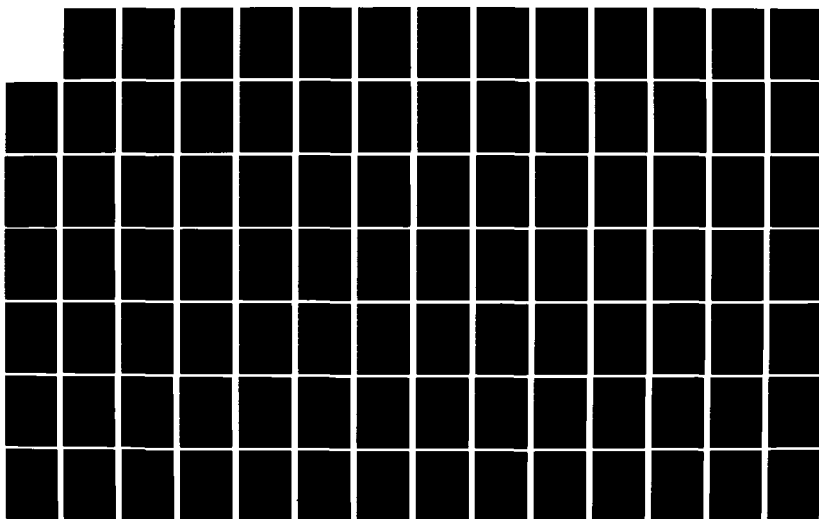
2/3

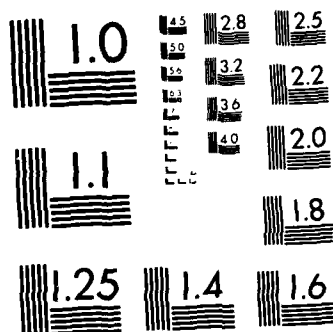
UNCLASSIFIED

AFOSR-TR-83-0060 F49620-81-C-0066

F/G 18/3

NL





MICROCOPY RESOLUTION TEST CHART
NATIONAL BUREAU OF STANDARDS 1963 A

so that

$$I = \frac{\lambda}{r} e^{r\lambda} \Big|_0^t - \frac{1}{r} \int_0^t e^{r\lambda} d\lambda$$

$$= \left[\left(\frac{\lambda}{r} - \frac{1}{r^2} \right) e^{r\lambda} \right]_0^t = \left(\frac{t}{r} - \frac{1}{r^2} \right) e^{rt} + \frac{1}{r^2} \quad (G.15)$$

Thus, Equation (G.9) yields

$$\int_0^t F_2'(\lambda) s(x, t-\lambda) d\lambda = P_0 \frac{\alpha}{\lambda_0} \left(1 - \frac{x}{l} \right) \left[\frac{1}{\alpha^2} - \left(\frac{t}{\alpha} + \frac{1}{\alpha^2} \right) e^{-\alpha t} \right]$$

$$- \frac{2\alpha P_0}{\pi \lambda_0} \sum_{n=1}^{\infty} \frac{1}{n} \sin \frac{n\pi x}{l} \left\{ \frac{e^{-\frac{n^2 \pi^2 D t}{l^2}}}{\left(\frac{n^2 \pi^2 D}{l^2} - \alpha \right)^2} + \left[\frac{t}{\frac{n^2 \pi^2 D}{l^2} - \alpha} - \frac{1}{\left(\frac{n^2 \pi^2 D}{l^2} - \alpha \right)^2} \right] e^{-\alpha t} \right\} \quad (G.16)$$

When Equations (G.7), (G.8) and (G.16) are substituted into Equation (B.52), the coefficients of key functions are

$$P_0 \left(1 - \frac{x}{l} \right): 1 + e^{-\alpha t} - 1 + \frac{e^{-\alpha t}}{\alpha \lambda_0} - \frac{1}{\alpha \lambda_0} + \frac{1}{\alpha \lambda_0}$$

$$- \left(\frac{t}{\lambda_0} + \frac{1}{\alpha \lambda_0} \right) e^{-\alpha t} = \left(1 - \frac{t}{\lambda_0} \right) e^{-\alpha t} \quad (G.17)$$

and with

$$\frac{n^2 \pi^2 D}{l^2} = \Gamma_n \quad (G.18)$$

$$- \frac{2P_0}{\pi} \frac{1}{n} \sin \frac{n\pi x}{l} e^{-\Gamma_n t}: 1 + \frac{\alpha + \frac{1}{\lambda_0}}{\Gamma_n - \alpha} + \frac{\alpha}{\lambda_0 (\Gamma_n - \alpha)^2}$$

$$= \frac{\Gamma_n}{\Gamma_n - \alpha} + \frac{\Gamma_n}{\lambda_0(\Gamma_n - \alpha)^2} \quad (G.19)$$

$$- \frac{2P_0}{\pi} \frac{1}{n} \sin \frac{n\pi x}{l} e^{-\alpha t} : - \frac{\alpha + \frac{1}{\lambda_0}}{\Gamma_n - \alpha} - \frac{\alpha}{\lambda_0(\Gamma_n - \alpha)^2} + \frac{\alpha t}{\lambda_0(\Gamma_n - \alpha)}$$

$$= - \frac{\alpha}{\Gamma_n - \alpha} - \frac{\Gamma_n}{\lambda_0(\Gamma_n - \alpha)^2} + \frac{\alpha t}{\lambda_0(\Gamma_n - \alpha)} \quad (G.20)$$

Thus, if we set

$$\frac{\alpha}{\Gamma_n - \alpha} + \frac{n}{\lambda_0(\Gamma_n - \alpha)^2} = \theta_n \quad (G.21)$$

then Equation (B.52) takes the form

$$P(x, t) = P_0 \left[\left(1 - \frac{x}{l}\right) \left(1 - \frac{t}{\lambda_0}\right) e^{-\alpha t} \right. \\ \left. - \frac{2}{\pi} \sum_{n=1}^{\infty} \frac{1}{n} \sin \frac{n\pi x}{l} \left\{ (1 + \theta_n) e^{-\Gamma_n t} - \left[\theta_n - \frac{\alpha t}{\lambda_0(\Gamma_n - \alpha)} \right] e^{-\alpha t} \right\} \right] \quad (G.22)$$

If we set

$$\frac{Dt}{l^2} = \tau \quad (B.61)$$

$$\frac{l^2 \alpha}{D} = \beta \quad (B.62)$$

$$\frac{l^2}{\lambda_0 D} = \phi \quad (G.23)$$

$$\frac{x}{l} = \xi \quad (B.63)$$

then

$$\begin{aligned}\theta_n &= \frac{\alpha}{\frac{n^2 \pi^2 D}{l^2} - \alpha} + \frac{\frac{n^2 \pi^2 D}{l^2}}{\lambda_0 \left(\frac{n^2 \pi^2 D}{l^2} - \alpha \right)^2} \\ &= \frac{\beta}{n^2 \pi^2 - \beta} + \frac{n^2 \pi^2 \phi}{(n^2 \pi^2 - \beta)^2}\end{aligned}\quad (G.24)$$

and

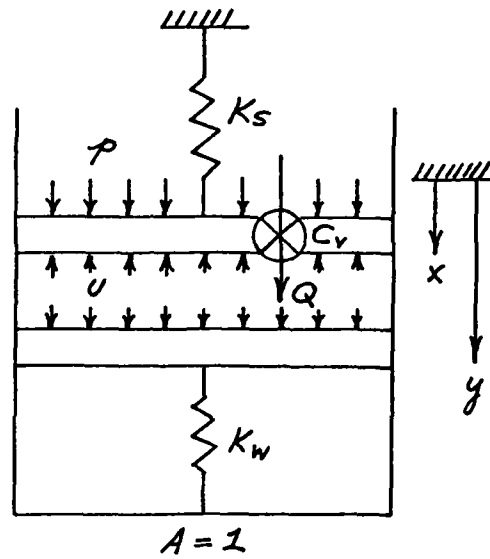
$$\frac{\alpha t}{\lambda_0 \left(\frac{n^2 \pi^2 D}{l^2} - \alpha \right)} = \frac{\beta \phi T}{n^2 \pi^2 - \beta} \quad (G.25)$$

so that Equation (G.22) can be written in the form

$$\begin{aligned}P(\xi, T) &= P_0 \left\{ (1 - \xi)(1 - \phi T)e^{-\beta T} \right. \\ &\quad \left. - \frac{2}{\pi} \sum_{n=1}^{\infty} \frac{1}{n} \sin n\pi\xi \left[(1 + \theta_n)e^{-n^2 \pi^2 T} - \left(\theta_n - \frac{\beta \phi T}{n^2 \pi^2 - \beta} \right) e^{-\beta T} \right] \right\}\end{aligned}\quad (G.26)$$

APPENDIX H

A Simple Piston Model for the Pore Air Effect



The volume change of the soil skeleton depends on effective stress.

$$p - u = k_s x \quad (H.1)$$

The volume change of the initial volume of pore fluid depends on the pore pressure.

$$u = k_w y \quad (H.2)$$

The rate at which new pore fluid flows into the soil void space depends on the pore pressure difference.

$$\frac{d}{dt} (y - x) = \frac{1}{C_v} (p - u) \quad (H.3)$$

Written together, Equations (H.1), H.2) and (H.3) take the form

$$\left. \begin{array}{rcl} k_s x & + u & = p \\ & k_w y & - u = 0 \\ -C_v \dot{x} + C_v \dot{y} & + u & = p \end{array} \right\} \quad (H.4)$$

Eliminating the pore pressure, u , we obtain

$$\left. \begin{array}{rcl} C_v \dot{x} - C_v \dot{y} + k_s x & & = 0 \\ -C_v \dot{x} + C_v \dot{y} & + k_w y & = p \end{array} \right\} \quad (H.5)$$

or, in matrix form

$$C_v \begin{bmatrix} 1 & -1 \\ -1 & 1 \end{bmatrix} \begin{Bmatrix} x \\ y \end{Bmatrix} + \begin{bmatrix} k_s & 0 \\ 0 & k_w \end{bmatrix} \begin{Bmatrix} x \\ y \end{Bmatrix} = \begin{Bmatrix} 0 \\ p \end{Bmatrix} \quad (H.6)$$

In operator notation, Equations (H.5) take the form

$$\begin{aligned} (C_v D + k_s)x - C_v D y &= 0 \\ -C_v D x + (C_v D + k_w)y &= p \end{aligned} \quad (H.7)$$

We eliminate y as follows:

$$\begin{aligned} (C_v D + k_s)(C_v D + k_w)x - C_v D(C_v D + k_w)y &= 0 \\ (+) \quad - (C_v D)^2 x + C_v D(C_v D + k_w)y &= C_v D p \\ \hline [C_v(k_s + k_w)D + k_s k_w]x &= C_v D p \end{aligned} \quad (H.8)$$

When Equation (H.8) has been solved for x , the first of Equations (H.4) yields the solution for u :

$$u = p - k_s x \quad (H.9)$$

and the second of Equations (H.4) yields the solution for y :

$$y = \frac{u}{k_w} \quad (H.10)$$

Equation (H.8) can be written in the form

$$\left[D + \frac{k_s k_w}{C_v(k_s + k_w)} \right] x = \left(\frac{1}{k_s + k_w} \right) D p \quad (H.11)$$

or

$$(D + a)x = bDp \quad (H.12)$$

where

$$a = \frac{k_s k_w}{C_v (k_s + k_w)} \quad (H.13)$$

$$b = \frac{1}{k_s + k_w} \quad (H.14)$$

The complete solution to Equation (H.12) for which $x(0) = 0$ is [Cheng (1959:15)]

$$x(t) = b \int_0^t \frac{dp}{d\lambda} e^{-a(t-\lambda)} d\lambda \quad (t > 0) \quad (H.15)$$

The integral on the RHS of Equation (H.15) can be integrated by parts by setting

$$U = e^{-a(t-\lambda)} \quad (H.16)$$

$$dU = ae^{-a(t-\lambda)} d\lambda \quad (H.17)$$

$$dV = \frac{dp}{d\lambda} d\lambda \quad (H.18)$$

$$V = p(\lambda) \quad (H.19)$$

so that

$$\begin{aligned} x(t) &= bp(\lambda)e^{-a(t-\lambda)} \Big|_0^t - ab \int_0^t p(\lambda)e^{-a(t-\lambda)} d\lambda \\ &= bp(t) - bp(0)e^{-at} - ab \int_0^t p(\lambda)e^{-a(t-\lambda)} d\lambda \end{aligned} \quad (H.20)$$

When

$$p(0) = 0 \quad (H.21)$$

Equation (H.20) reduces to

$$x(t) = b \left[p(t) - a \int_0^t p(\lambda) e^{-a(t-\lambda)} d\lambda \right] \quad (t > 0) \quad (\text{H.22})$$

When $p(t)$ is a step pulse, i.e., when

$$\begin{aligned} p(t) &\approx 0 & (t \leq 0) \\ &= P & (t > 0) \end{aligned} \quad (\text{H.23})$$

$$\frac{dp}{dt} = P\delta(t)$$

then Equation (H.15) yields

$$\begin{aligned} x(t) &= bP \int_0^t \delta(\lambda) e^{-a(t-\lambda)} d\lambda \\ &= bPe^{-at} = \frac{P}{k_s + k_w} e^{-at} \quad (t > 0) \end{aligned} \quad (\text{H.24})$$

Equation (H.9) then yields

$$u(t) = P \left[1 - \left(\frac{k_s}{k_s + k_w} \right) e^{-at} \right] \quad (t > 0) \quad (\text{H.25})$$

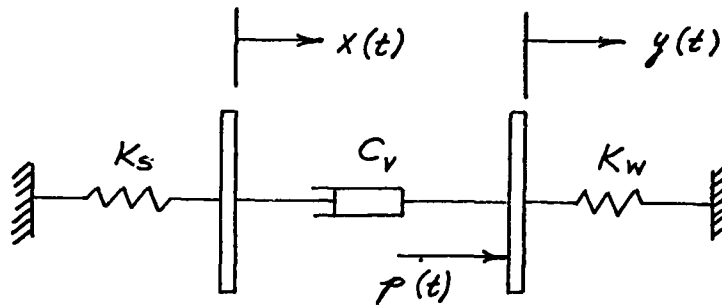
and Equation (H.10) yields

$$y(t) = \frac{P}{k_w} \left[1 - \left(\frac{k_s}{k_s + k_w} \right) e^{-at} \right] \quad (t > 0) \quad (\text{H.26})$$

Note that Equations (H.24) and (H.26) yield

$$x(0^+) = y(0^+) = \frac{P}{k_s + k_w} \quad (\text{H.27})$$

The reasonableness of the above solution can be examined by constructing the model associated with Equations (H.5) or (H.6), which is shown below.



Initial application of the step pulse P produces equal instantaneous displacements $x(0+)$ and $y(0+)$, so that no dashpot force acts. The springs k_s and k_w resist the load in parallel. At $t = \infty$ the spring k_w resists the entire load, and the soil piston has returned to its original position.

The response is composite compression followed by recovery. Initial undrained loading produces a sharing of internal stress between the soil skeleton and the pore fluid, in such a manner that the initial volume changes of soil skeleton and pore fluid are equal. Subsequently, drainage occurs in response to the difference between the back pressure and the pore pressure, as a result of which the pore pressure eventually becomes equal to the back pressure. At this point the change in effective stress in the soil skeleton is zero, and its initial undrained volume change has been recovered.

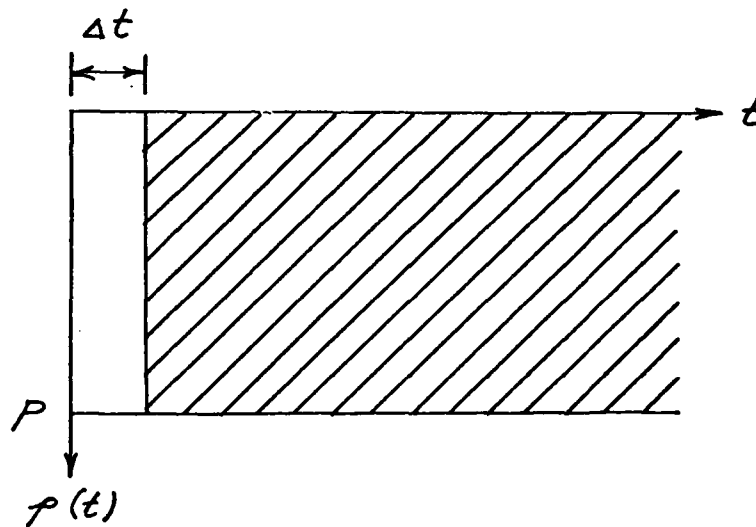
When $p(t)$ is an impulse, i.e.,

$$p(t) = \delta(t) \quad (H.28)$$

then Equation (H.22) yields

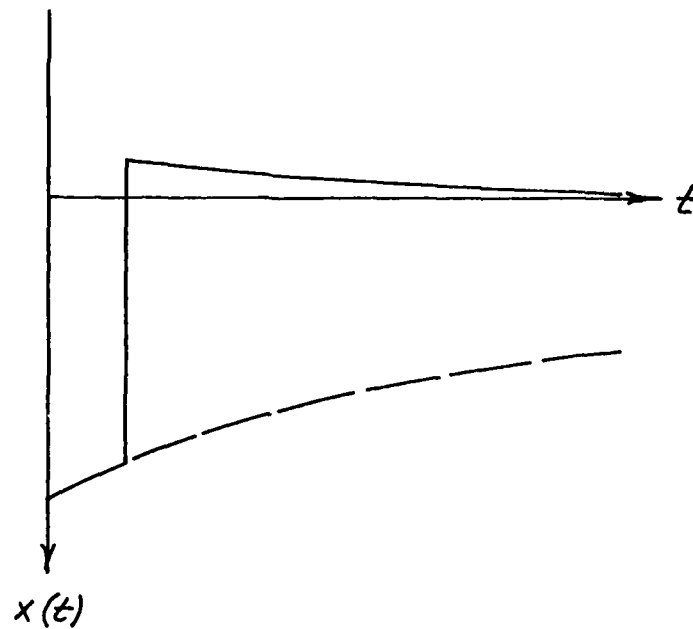
$$h(t) = -abe^{-at} \quad (H.29)$$

The fact that an upward displacement results from a downward impulse can be explained by the fact that a downward impulse can be viewed as the successive application of two step pulses, the first downward and the second upward.



Equation (H.24) therefore yields

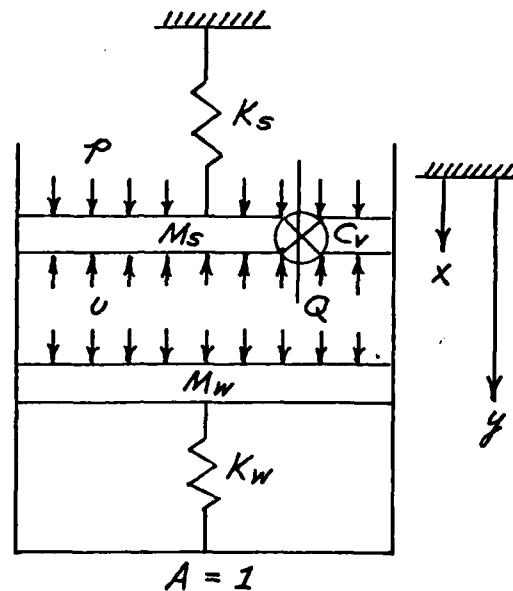
$$\begin{aligned} h(t) &= bP[e^{-at} - e^{-a(t-\Delta t)}] \\ &= bP\left[\frac{d}{dt}(e^{-at})\Delta t\right] \\ &= -abe^{-at}(P\Delta t) = -abe^{-at} \end{aligned} \quad (H.30)$$



The net upward displacement following a downward impulse is due to the fact that displacement recovery begins immediately following the application of a step pulse. This is caused by flow of pore fluid into the soil skeleton in response to the difference between the backpressure and the pore pressure.

APPENDIX I

A Simple Dynamic Piston Model for the Pore Air Effect



The equation of motion for the soil skeleton is

$$(p - u) - K_s x = M_s \ddot{x} \quad (I.1)$$

The equation of motion for the pore fluid is

$$u - K_w y = M_w \ddot{y} \quad (I.2)$$

The rate at which new pore fluid flows into the soil void space depends on the pore pressure difference

$$\frac{d}{dt} (y - x) = \frac{1}{C_v} (p - u) \quad (I.3)$$

Written together, Equations (I.1), (I.2) and (I.3) take the form

$$\left. \begin{aligned} M_S \ddot{x} + K_S x + u &= p \\ M_W \ddot{y} + K_W y - u &= 0 \\ -C_V \dot{x} + C_V \dot{y} + u &= p \end{aligned} \right\} \quad (I.4)$$

Eliminating the pore pressure, u , we obtain

$$\left. \begin{aligned} M_S \ddot{x} + C_V \dot{x} - C_V \dot{y} + K_S x &= 0 \\ M_W \ddot{y} - C_V \dot{x} + C_V \dot{y} + K_W y &= p \end{aligned} \right\} \quad (I.5)$$

or, in matrix form

$$\begin{bmatrix} M_S & 0 \\ 0 & M_W \end{bmatrix} \begin{Bmatrix} \ddot{x} \\ \ddot{y} \end{Bmatrix} + C_V \begin{bmatrix} 1 & -1 \\ -1 & 1 \end{bmatrix} \begin{Bmatrix} \dot{x} \\ \dot{y} \end{Bmatrix} + \begin{bmatrix} K_S & 0 \\ 0 & K_W \end{bmatrix} \begin{Bmatrix} x \\ y \end{Bmatrix} = \begin{Bmatrix} 0 \\ p \end{Bmatrix} \quad (I.6)$$

In operator notation, Equations (I.5) take the form

$$\begin{aligned} L_1 x - L_2 y &= 0 \\ -L_2 x + L_3 y &= p \end{aligned} \quad (I.7)$$

where

$$L_1 = M_S D^2 + C_V D + K_S \quad (I.8)$$

$$L_2 = C_V D \quad (I.9)$$

$$L_3 = M_W D^2 + C_V D + K_W \quad (I.10)$$

To eliminate y from Equations (I.7), we proceed as follows:

$$\begin{aligned} L_1 L_3 x - L_2 L_3 y &= 0 \\ (+) \quad -L_2^2 x + L_2 L_3 y &= L_2 p \\ \hline (L_1 L_3 - L_2^2) x &= L_2 p \end{aligned} \quad (I.11)$$

Expanding Equation (I.11), we obtain

$$[M_S D^2 + C_V D + K_S](M_W D^2 + C_V D + K_W) - C_V^2 D^2]x = C_V Dp$$

or

$$\begin{aligned} &([M_S M_W D^4 + C_V(M_S + M_W)D^3 + (M_S K_W + M_W K_S)D^2 \\ &+ C_V(K_S + K_W)D + K_S K_W]x = C_V Dp \end{aligned} \quad (I.12)$$

When Equation (I.12) has been solved for x , the first of Equations (I.4) yields the solution for u :

$$u = p - (M_S D^2 + K_S)x \quad (I.13)$$

and the third of Equations (I.4) yields the solution for y :

$$y(t) = x(t) + \frac{1}{C_V} \int_0^t [p(\lambda) - u(\lambda)] d\lambda \quad (I.14)$$

Equation (I.12) can be written in the form

$$\begin{aligned} &\left\{ D^4 + \left[\frac{C_V(M_S + M_W)}{M_S M_W} \right] D^3 + \left(\frac{M_S K_W + M_W K_S}{M_S M_W} \right) D^2 \right. \\ &\quad \left. + \left[\frac{C_V(K_S + K_W)}{M_S M_W} \right] D + \left(\frac{K_S K_W}{M_S M_W} \right) \right\} x = \left(\frac{C_V}{M_S M_W} \right) Dp \end{aligned} \quad (I.15)$$

or

$$(D^4 + bD^3 + cD^2 + dD + f)x = gDp \quad (I.16)$$

where

$$b = \frac{C_V(M_S + M_W)}{M_S M_W} \quad (I.17)$$

$$c = \frac{M_s K_w + M_w K_s}{M_s M_w} \quad (I.18)$$

$$d = \frac{C_v (K_s + K_w)}{M_s M_w} \quad (I.19)$$

$$f = \frac{K_s K_w}{M_s M_w} \quad (I.20)$$

$$g = \frac{C_v}{M_s M_w} \quad (I.21)$$

Consider first the homogeneous form of Equation (I.16), which is

$$(D^4 + bD^3 + cD^2 + dD + f)x = 0 \quad (I.22)$$

If we assume a solution of the form

$$x_H(t) = Ce^{\alpha t} \quad (I.23)$$

then substitution of Equation (I.23) into Equation (I.22) yields

$$(\alpha^4 + b\alpha^3 + c\alpha^2 + d\alpha + f)Ce^{\alpha t} = 0 \quad (I.24)$$

Assuming that $Ce^{\alpha t} \neq 0$, Equation (I.24) yields

$$\alpha^4 + b\alpha^3 + c\alpha^2 + d\alpha + f = 0 \quad (I.25)$$

The solution of Equation (I.25) is obtained in Appendix J.

Having solved Equation (I.25), we write Equation (I.23) in the form

$$x_H(t) = \sum_{j=1}^4 C_j e^{\alpha_j t} \quad (I.26)$$

We now return to Equation (I.16), which can be written in factored form

$$[(D-\alpha_1)(D-\alpha_2)(D-\alpha_3)(D-\alpha_4)]x = gDp \quad (I.27)$$

The particular solution to Equation (I.27) is developed in Appendix K.

The complete solution to Equation (I.16) is the sum of the homogeneous solution, given by Equation (I.26) and the particular solution, given by

Equation (K.16):

$$\begin{aligned} x(t) &= x_H(t) + x_p(t) \\ &= \sum_{j=1}^4 \left\{ C_j e^{\alpha_j t} + \frac{g}{\pi_j} \int_0^t \frac{dp}{d\lambda} e^{\alpha_j(t-\lambda)} d\lambda \right\} \quad (t>0) \end{aligned} \quad (I.28)$$

Thus

$$\begin{aligned} \dot{x}(t) &= \sum_{j=1}^4 \left\{ \alpha_j C_j e^{\alpha_j t} + \frac{g}{\pi_j} \left[\dot{p}(t) \right. \right. \\ &\quad \left. \left. + \alpha_j \int_0^t \frac{dp}{d\lambda} e^{\alpha_j(t-\lambda)} d\lambda \right] \right\} \quad (t>0) \end{aligned} \quad (I.29)$$

$$\begin{aligned} \ddot{x}(t) &= \sum_{j=1}^4 \left\{ \alpha_j^2 C_j e^{\alpha_j t} + \frac{g}{\pi_j} \left[\ddot{p}(t) + \alpha_j \dot{p}(t) \right. \right. \\ &\quad \left. \left. + \alpha_j^2 \int_0^t \frac{dp}{d\lambda} e^{\alpha_j(t-\lambda)} d\lambda \right] \right\} \quad (t>0) \end{aligned} \quad (I.30)$$

$$\begin{aligned} \ddot{\ddot{x}}(t) &= \sum_{j=1}^4 \left\{ \alpha_j^3 C_j e^{\alpha_j t} + \frac{g}{\pi_j} \left[\ddot{\ddot{p}}(t) + \alpha_j \ddot{\ddot{p}}(t) + \alpha_j^2 \dot{\ddot{p}}(t) \right. \right. \\ &\quad \left. \left. + \alpha_j^3 \int_0^t \frac{dp}{d\lambda} e^{\alpha_j(t-\lambda)} d\lambda \right] \right\} \quad (t>0) \end{aligned} \quad (I.31)$$

The initial values are:

$$x(0) = \sum_{j=1}^4 C_j \quad (I.32)$$

$$\dot{x}(0) = \sum_{j=1}^4 \left\{ \alpha_j C_j + \frac{g}{\pi_j} \left[\dot{p}(0) \right] \right\} \quad (I.33)$$

$$\ddot{x}(0) = \sum_{j=1}^4 \left\{ \alpha_j^2 C_j + \frac{g}{\pi_j} \left[\ddot{p}(0) + \alpha_j \dot{p}(0) \right] \right\} \quad (I.34)$$

$$\ddot{x}(0) = \sum_{j=1}^4 \left\{ \alpha_j^3 c_j + \frac{g}{\pi_j} \left[\ddot{p}(0) + \alpha_j \dot{\ddot{p}}(0) + \alpha_j^2 \ddot{p}(0) \right] \right\} \quad (I.35)$$

When $p(t)$ is a step pulse, i.e., when

$$\begin{aligned} p(t) &= 0 & (t \leq 0) \\ &= P & (t > 0) \end{aligned} \quad (I.36)$$

$$\frac{dp}{dt} = P\delta(t)$$

then

$$p(0) = \dot{p}(0) = \ddot{p}(0) = \ddot{\ddot{p}}(0) = 0 \quad (I.37)$$

so that for a system initially at rest, Equations (I.32), (I.33), (I.34) and (I.35) reduce to

$$\begin{bmatrix} 1 & 1 & 1 & 1 \\ \alpha_1 & \alpha_2 & \alpha_3 & \alpha_4 \\ \alpha_1^2 & \alpha_2^2 & \alpha_3^2 & \alpha_4^2 \\ \alpha_1^3 & \alpha_2^3 & \alpha_3^3 & \alpha_4^3 \end{bmatrix} \begin{Bmatrix} c_1 \\ c_2 \\ c_3 \\ c_4 \end{Bmatrix} = \begin{Bmatrix} 0 \\ 0 \\ 0 \\ 0 \end{Bmatrix} \quad (I.38)$$

The coefficient matrix in Equation (I.38) is nonsingular, provided

$$\alpha_i \neq \alpha_j \quad (i \neq j) \quad (I.39)$$

because its determinant is a Vandermonde determinant [Bellman (1960:186)], and therefore it must be that

$$c_1 = c_2 = c_3 = c_4 = 0 \quad (I.40)$$

In this case no homogeneous solution is required to satisfy the initial conditions, and therefore the particular solution is the complete solution. Equation (I.28) yields

$$x_s(t) = x_{ps}(t) = gP \sum_{j=1}^4 \frac{1}{\pi_j} e^{\alpha_j t} \quad (t > 0) \quad (I.41)$$

so that

$$\dot{x}_s(t) = g^p \sum_{j=1}^4 \frac{\alpha_j}{\pi_j} e^{\alpha_j t} \quad (t>0) \quad (I.42)$$

$$\ddot{x}_s(t) = g^p \sum_{j=1}^4 \frac{\alpha_j^2}{\pi_j} e^{\alpha_j t} \quad (t>0) \quad (I.43)$$

From Equations (I.41), (I.42) and (I.43) we obtain

$$\begin{aligned} x_s(0+) &= \sum_{j=1}^4 \frac{1}{\pi_j} \\ &= \frac{1}{(\alpha_1 - \alpha_2)(\alpha_1 - \alpha_3)(\alpha_1 - \alpha_4)} + \frac{1}{(\alpha_2 - \alpha_1)(\alpha_2 - \alpha_3)(\alpha_2 - \alpha_4)} \\ &\quad + \frac{1}{(\alpha_3 - \alpha_1)(\alpha_3 - \alpha_2)(\alpha_3 - \alpha_4)} + \frac{1}{(\alpha_4 - \alpha_1)(\alpha_4 - \alpha_2)(\alpha_4 - \alpha_3)} \\ &= \frac{1}{(\alpha_1 - \alpha_2)} \frac{[\alpha_2^2 - (\alpha_3 + \alpha_4)\alpha_2 + \alpha_3\alpha_4] - [\alpha_1^2 - (\alpha_3 + \alpha_4)\alpha_1 + \alpha_3\alpha_4]}{(\alpha_1 - \alpha_3)(\alpha_1 - \alpha_4)(\alpha_2 - \alpha_3)(\alpha_2 - \alpha_4)} \\ &\quad + \frac{1}{(\alpha_3 - \alpha_4)} \frac{[\alpha_4^2 - (\alpha_1 + \alpha_2)\alpha_4 + \alpha_1\alpha_2] - [\alpha_3^2 - (\alpha_1 + \alpha_2)\alpha_3 + \alpha_1\alpha_2]}{(\alpha_3 - \alpha_1)(\alpha_3 - \alpha_2)(\alpha_4 - \alpha_1)(\alpha_4 - \alpha_2)} \\ &= \frac{(\alpha_3 + \alpha_4)(\alpha_1 - \alpha_2) - (\alpha_1 + \alpha_2)(\alpha_1 - \alpha_2)}{(\alpha_1 - \alpha_2)(\alpha_1 - \alpha_3)(\alpha_1 - \alpha_4)(\alpha_2 - \alpha_3)(\alpha_2 - \alpha_4)} \\ &\quad + \frac{(\alpha_1 + \alpha_2)(\alpha_3 - \alpha_4) - (\alpha_3 + \alpha_4)(\alpha_3 - \alpha_4)}{(\alpha_3 - \alpha_4)(\alpha_3 - \alpha_1)(\alpha_4 - \alpha_1)(\alpha_3 - \alpha_2)(\alpha_4 - \alpha_2)} \\ &= 0 \end{aligned} \quad (I.44)$$

$$\begin{aligned}
\dot{x}_s(0+) &= \sum_{j=1}^4 \frac{\alpha_j}{\pi_j} \\
&= \frac{\alpha_1}{(\alpha_1-\alpha_2)(\alpha_1-\alpha_3)(\alpha_1-\alpha_4)} + \frac{\alpha_2}{(\alpha_2-\alpha_1)(\alpha_2-\alpha_3)(\alpha_2-\alpha_4)} \\
&\quad + \frac{\alpha_3}{(\alpha_3-\alpha_1)(\alpha_3-\alpha_2)(\alpha_3-\alpha_4)} + \frac{\alpha_4}{(\alpha_4-\alpha_1)(\alpha_4-\alpha_2)(\alpha_4-\alpha_3)} \\
&= \frac{1}{(\alpha_1-\alpha_2)} \frac{\alpha_1[\alpha_2^2 - (\alpha_3+\alpha_4)\alpha_2 + \alpha_3\alpha_4] - \alpha_2[\alpha_1^2 - (\alpha_3+\alpha_4)\alpha_1 + \alpha_3\alpha_4]}{(\alpha_1-\alpha_3)(\alpha_1-\alpha_4)(\alpha_2-\alpha_3)(\alpha_2-\alpha_4)} \\
&\quad + \frac{1}{(\alpha_3-\alpha_4)} \frac{\alpha_3[\alpha_4^2 - (\alpha_1+\alpha_2)\alpha_4 + \alpha_1\alpha_2] - \alpha_4[\alpha_3^2 - (\alpha_1+\alpha_2)\alpha_3 + \alpha_1\alpha_2]}{(\alpha_3-\alpha_1)(\alpha_3-\alpha_2)(\alpha_4-\alpha_1)(\alpha_4-\alpha_2)} \\
&= \frac{(\alpha_1-\alpha_2)\alpha_3\alpha_4 - (\alpha_1-\alpha_2)\alpha_1\alpha_2}{(\alpha_1-\alpha_2)(\alpha_1-\alpha_3)(\alpha_1-\alpha_4)(\alpha_2-\alpha_3)(\alpha_2-\alpha_4)} \\
&\quad + \frac{(\alpha_3-\alpha_4)\alpha_1\alpha_2 - (\alpha_3-\alpha_4)\alpha_3\alpha_4}{(\alpha_3-\alpha_4)(\alpha_3-\alpha_1)(\alpha_3-\alpha_2)(\alpha_4-\alpha_1)(\alpha_4-\alpha_2)} \\
&= 0
\end{aligned}$$

(I.45)

and

$$\begin{aligned}
\ddot{x}_s(0+) &= \sum_{j=1}^4 \frac{\alpha_j^2}{\pi_j} \\
&= \frac{\alpha_1^2}{(\alpha_1-\alpha_2)(\alpha_1-\alpha_3)(\alpha_1-\alpha_4)} + \frac{\alpha_2^2}{(\alpha_2-\alpha_1)(\alpha_2-\alpha_3)(\alpha_2-\alpha_4)} \\
&\quad + \frac{\alpha_3^2}{(\alpha_3-\alpha_1)(\alpha_3-\alpha_2)(\alpha_3-\alpha_4)} + \frac{\alpha_4^2}{(\alpha_4-\alpha_1)(\alpha_4-\alpha_2)(\alpha_4-\alpha_3)}
\end{aligned}$$

$$\begin{aligned}
&= \frac{1}{(\alpha_1 - \alpha_2)} \frac{\alpha_1^2 [\alpha_2^2 - (\alpha_3 + \alpha_4)\alpha_2 + \alpha_3\alpha_4] - \alpha_2^2 [\alpha_1^2 - (\alpha_3 + \alpha_4)\alpha_1 + \alpha_3\alpha_4]}{(\alpha_1 - \alpha_3)(\alpha_1 - \alpha_4)(\alpha_2 - \alpha_3)(\alpha_2 - \alpha_4)} \\
&+ \frac{1}{(\alpha_3 - \alpha_4)} \frac{\alpha_3^2 [\alpha_4^2 - (\alpha_1 + \alpha_2)\alpha_4 + \alpha_1\alpha_2] - \alpha_4^2 [\alpha_3^2 - (\alpha_1 + \alpha_2)\alpha_3 + \alpha_1\alpha_2]}{(\alpha_3 - \alpha_1)(\alpha_3 - \alpha_2)(\alpha_4 - \alpha_1)(\alpha_4 - \alpha_2)} \\
&= \frac{(\alpha_1 + \alpha_2)(\alpha_1 - \alpha_2)\alpha_3\alpha_4 - (\alpha_3 + \alpha_4)(\alpha_1 - \alpha_2)\alpha_1\alpha_2}{(\alpha_1 - \alpha_2)(\alpha_1 - \alpha_3)(\alpha_1 - \alpha_4)(\alpha_2 - \alpha_3)(\alpha_2 - \alpha_4)} \\
&+ \frac{(\alpha_3 + \alpha_4)(\alpha_3 - \alpha_4)\alpha_1\alpha_2 - (\alpha_1 + \alpha_2)(\alpha_3 - \alpha_4)\alpha_3\alpha_4}{(\alpha_3 - \alpha_4)(\alpha_3 - \alpha_1)(\alpha_3 - \alpha_2)(\alpha_4 - \alpha_1)(\alpha_4 - \alpha_2)} \\
&= 0
\end{aligned} \tag{I.46}$$

A numerical example shows that two roots of Equation (I.25) are real and the remaining two are a complex conjugate pair: All real quantities are negative.

$$\alpha_1 = -m \tag{I.47}$$

$$\alpha_2 = -n \tag{I.48}$$

$$\alpha_3 = -q + is \tag{I.49}$$

$$\alpha_4 = -q - is \tag{I.50}$$

Equation (I.41) can therefore be written in the form

$$x_s(t) = g^p \left[\frac{1}{\pi_1} e^{-mt} + \frac{1}{\pi_2} e^{-nt} + \frac{1}{\pi_3} e^{-qt+ist} + \frac{1}{\pi_4} e^{-qt-ist} \right] \tag{I.51}$$

Now

$$e^{ist} = \cos st + i \sin st \tag{I.52}$$

$$e^{-ist} = \cos st - i \sin st \tag{I.53}$$

so that Equation (I.51) can be written in the form

$$x_s(t) = gP \left[\frac{1}{\pi_1} e^{-mt} + \frac{1}{\pi_2} e^{-nt} + \left(\frac{1}{\pi_3} + \frac{1}{\pi_4} \right) e^{-qt} \cos st + i \left(\frac{1}{\pi_3} - \frac{1}{\pi_4} \right) e^{-qt} \sin st \right] \quad (I.54)$$

or

$$x_s(t) = gP(Ae^{-mt} + Be^{-nt} - D_1 e^{-qt} \cos st + D_2 e^{-qt} \sin st) \quad (I.55)$$

where

$$A = \frac{1}{\pi_1} = \frac{1}{(\alpha_1 - \alpha_2)(\alpha_1 - \alpha_3)(\alpha_1 - \alpha_4)} = \frac{1}{(n-m)[(q-m)^2 + s^2]} \quad (I.56)$$

$$B = \frac{1}{\pi_2} = \frac{1}{(\alpha_2 - \alpha_1)(\alpha_2 - \alpha_3)(\alpha_2 - \alpha_4)} = \frac{1}{(n-m)[(q-n)^2 + s^2]} \quad (I.57)$$

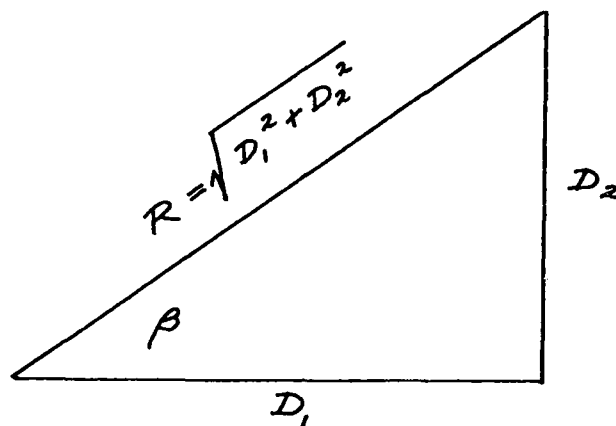
$$D_1 = - \frac{1}{\pi_3} + \frac{1}{\pi_4} \quad [\text{See last two terms of Equation (I.44).}]$$

$$\begin{aligned} &= - \frac{(\alpha_1 + \alpha_2) - (\alpha_3 + \alpha_4)}{(\alpha_3 - \alpha_1)(\alpha_4 - \alpha_1)(\alpha_3 - \alpha_2)(\alpha_4 - \alpha_2)} \\ &= \frac{m + n - 2q}{[(m-q)^2 + s^2][(n-q)^2 + s^2]} \quad (I.58) \end{aligned}$$

$$\begin{aligned} D_2 &= i \left[\frac{1}{\pi_3} - \frac{1}{\pi_4} \right] = i \left[\frac{1}{(\alpha_3 - \alpha_1)(\alpha_3 - \alpha_2)(\alpha_3 - \alpha_4)} - \frac{1}{(\alpha_4 - \alpha_1)(\alpha_4 - \alpha_2)(\alpha_4 - \alpha_3)} \right] \\ &= \frac{i}{\alpha_3 - \alpha_4} \frac{[\alpha_4^2 - (\alpha_1 + \alpha_2)\alpha_4 + \alpha_1\alpha_2] + [\alpha_3^2 - (\alpha_1 + \alpha_2)\alpha_3 + \alpha_1\alpha_2]}{(\alpha_3 - \alpha_1)(\alpha_3 - \alpha_2)(\alpha_4 - \alpha_1)(\alpha_4 - \alpha_2)} \\ &= \frac{i}{\alpha_3 - \alpha_4} \frac{[(\alpha_3^2 + \alpha_4^2) - (\alpha_1 + \alpha_2)(\alpha_3 + \alpha_4) + 2\alpha_1\alpha_2]}{(\alpha_3 - \alpha_1)(\alpha_4 - \alpha_1)(\alpha_3 - \alpha_2)(\alpha_4 - \alpha_2)} \\ &= \frac{i}{2is} \frac{[2q^2 - 2s^2 - (m+n)(2q) + 2mn]}{[(m-q)^2 + s^2][(n-q)^2 + s^2]} \end{aligned}$$

$$= \frac{mn - (m+n)q + q^2 - s^2}{s[(m-q)^2 + s^2][(n-q)^2 + s^2]} \quad (I.59)$$

Equation (I.55) can be simplified by a trigonometric substitution.



If we set

$$R = \sqrt{D_1^2 + D_2^2} \quad (I.60)$$

$$\beta = \tan^{-1} \frac{D_2}{D_1} \quad (I.61)$$

then Equation (I.55) can be written in the form

$$x_s(t) = gP[Ae^{-mt} + Be^{-nt} - Re^{-qt} \cos(st+\beta)] \quad (I.62)$$

For the case at hand, Appendix L gives

$$m = 0.115726598 \times 10^{-4} \text{ MSEC}^{-1}$$

$$n = 0.538700000 \times 10^7 \text{ MSEC}^{-1}$$

$$q = 0.462842340 \times 10^{-6} \text{ MSEC}^{-1}$$

$$s = 0.425932181 \times 10^0 \text{ MSEC}^{-1}$$

$$g = 1.508 \times 10^0 \frac{\text{FT}}{\text{LB}(\text{MSEC})^3}$$

so that

$$(m-q)^2 + s^2 = 0.1814182229 \text{ MSEC}^{-2}$$

$$(n-q)^2 + s^2 = 2.9019769 \times 10^{13} \text{ MSEC}^{-2}$$

and therefore

$$A = \frac{1}{(n-m)[(q-m)^2 + s^2]} = 1.023227294 \times 10^{-6} (\text{MSEC})^3$$

$$B = \frac{1}{(m-n)[(q-n)^2 + s^2]} = -6.396745516 \times 10^{-21} (\text{MSEC})^3$$

$$D_1 = \frac{m+n-2q}{[(m-q)^2 + s^2][(n-q)^2 + s^2]} = 1.023227293 \times 10^{-6} (\text{MSEC})^3$$

$$D_2 = \frac{mn - (m+n)q + q^2 - s^2}{s[(m-q)^2 + s^2][(n-q)^2 + s^2]} = 2.660848297 \times 10^{-11} (\text{MSEC})^3$$

$$R = \sqrt{D_1^2 + D_2^2} = 1.023227293 \times 10^{-6} (\text{MSEC})^3$$

$$\beta = \tan^{-1} \frac{D_2}{D_1} = 1.489942369 \times 10^{-3} \text{ DEG}$$

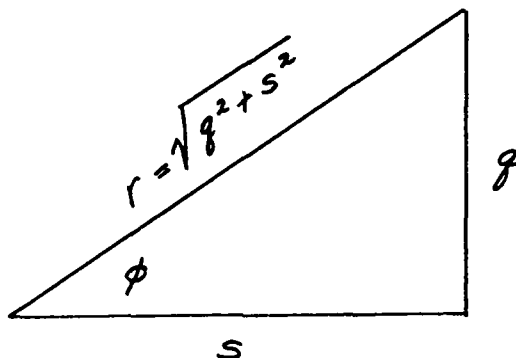
so that Equation (I.62) gives

$$\begin{aligned} \frac{x_s(t)}{p} = & 1.543026759 \times 10^{-6} e^{-0.115726598 \times 10^{-4}t} \\ & - 9.646292238 \times 10^{-21} e^{-0.538700000 \times 10^7t} \\ & - 1.543026758 \times 10^{-6} e^{-0.462842340 \times 10^{-6}t} \\ & \cdot [\cos(0.425932181t + 2.600440001 \times 10^{-5})] \text{ FT/LB} \end{aligned}$$

Differentiation of Equation (I.62) yields

$$\dot{x}_s(t) = gP[-mAe^{-mt} - nBe^{-nt} + qRe^{-qt} \cos(st+\beta) + sRe^{-qt} \sin(st+\beta)] \quad (I.63)$$

Equation (I.63) can be simplified by another trigonometric substitution.



If we set

$$r = \sqrt{q^2 + s^2} = 0.425932181 \text{ MSEC}^{-1} \quad (I.64)$$

$$\phi = \tan^{-1} q/s = 6.225759401 \times 10^{-5} \text{ DEG} \quad (I.65)$$

then Equation (I.63) can be written in the form

$$\dot{x}_s(t) = gP[-mAe^{-mt} - nBe^{-nt} + rRe^{-qt} \sin(st+\beta+\phi)] \quad (I.66)$$

where

$$\beta + \phi = 1.552199963 \times 10^{-3} \text{ DEG}$$

so that Equation (I.66) gives

$$\begin{aligned} \frac{\dot{x}_s(t)}{P} = & -1.785692374 \times 10^{-11} e^{-0.115726598 \times 10^{-4} t} \\ & + 5.196457629 \times 10^{-14} e^{-0.538700000 \times 10^{-7} t} \end{aligned}$$

$$\begin{aligned}
& + 6.572247524 \times 10^{-7} e^{-0.462842340 \times 10^{-6} t} \\
& \cdot [\sin(0.425932181t + 2.709100001 \times 10^{-5})] \quad (I.67) \\
& \text{FT/(LB MSEC)}
\end{aligned}$$

Differentiation of Equation (I.66) yields

$$\begin{aligned}
\ddot{x}_s(t) &= gP[m^2 A e^{-mt} + n^2 B e^{-nt} - qrRe^{-qt} \sin(st+\beta+\phi) \\
& + srRe^{-qt} \cos(st+\beta+\phi)] \\
& = gP[m^2 A e^{-mt} + n^2 B e^{-nt} + r^2 Re^{-qt} \cos(st+\beta+2\phi)] \quad (I.68)
\end{aligned}$$

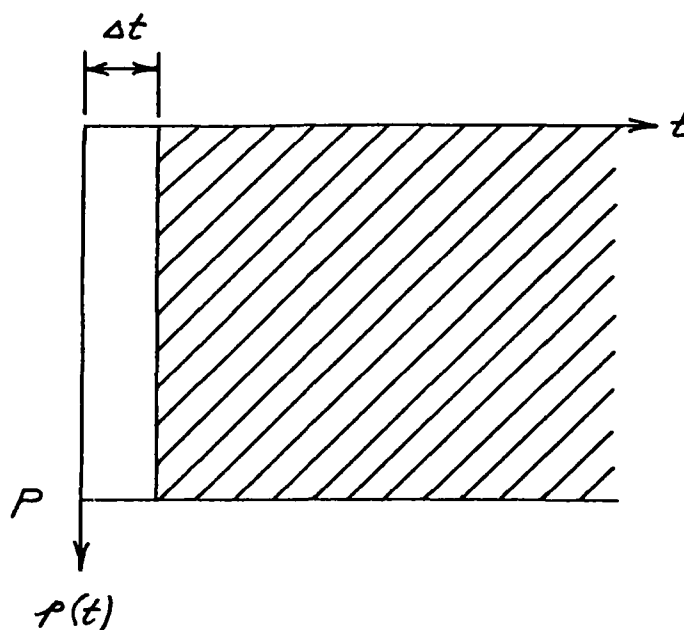
where

$$\beta + 2\phi = 1.614457557 \times 10^{-3} \text{ DEG}$$

so that Equation (I.68) gives

$$\begin{aligned}
\frac{\ddot{x}_s(t)}{P} &= 2.066521035 \times 10^{-16} e^{-0.115726598 \times 10^{-4} t} \\
& - 2.799331725 \times 10^{-7} e^{-0.538700000 \times 10^7 t} \\
& + 2.799331722 \times 10^{-7} e^{-0.462842340 \times 10^{-6} t} \\
& \cdot [\cos(0.425932181t + 2.817760001 \times 10^{-5})] \quad (I.69) \\
& \text{FT/LB(MSEC)}^2
\end{aligned}$$

The impulse response function can be obtained from Equation (I.62), or from the fact that an impulse is the successive application of two step pulses.



$$h(t) = \frac{x_s(t) - x_s(t-\Delta t)}{P\Delta t} = \frac{\frac{d}{dt} [x_s(t)]\Delta t}{P\Delta t}$$

$$= \frac{\dot{x}_s(t)}{P} = g[-mAe^{-mt} - nBe^{-nt} + rRe^{-qt} \sin(st+\beta+\phi)] \quad (I.70)$$

$$= -1.785692374 \times 10^{-11} e^{-0.115726598 \times 10^{-4}t}$$

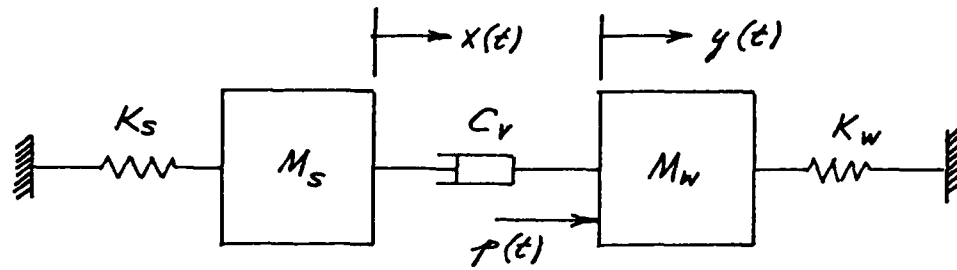
$$+ 5.196457629 \times 10^{-14} e^{-0.538700000 \times 10^7t}$$

$$+ 6.572247524 \times 10^{-7} e^{-0.462842340 \times 10^{-6}t}$$

$$\cdot [\sin(0.425932181t + 2.709100001 \times 10^{-5})] \quad (I.71)$$

FT/(LB MSEC)

The model associated with Equations (I.5) or (I.6) is identical to that associated with Equations (H.5) or (H.6), shown following Equation (H.27), except that the pistons have mass.



A suddenly applied force $p(0^+)$ will produce no initial acceleration of mass M_s because there will be no initial relative velocity $\dot{y}(0^+) - \dot{x}(0^+)$, and therefore no initial dashpot force to cause such an acceleration. For awhile the mass M_w will drag the mass M_s along with it, but when the system comes to rest the mass M_s will return to its initial position and the spring K_w will carry the entire final load.

APPENDIX J

Solution of a Fourth Order Algebraic Equation

Consider the fourth order algebraic equation with constant coefficients

$$\alpha^4 + b\alpha^3 + c\alpha^2 + d\alpha + f = 0 \quad (\text{I.25})$$

The solution of Equation (I.25) is classic, but although involved, the resulting equations need not be as useless as is commonly believed [Sokolnikoff and Sokolnikoff (1941:91)].

To eliminate the cubic term, let

$$\alpha = z - \frac{b}{4} \quad (\text{J.1})$$

so that

$$\alpha^4 = z^4 - z^3b + \frac{3}{8} z^2b^2 - \frac{1}{16} zb^3 + \frac{1}{256} b^4 \quad (\text{J.2})$$

$$\alpha^3 = z^3 - \frac{3}{4} z^2b + \frac{3}{16} zb^2 - \frac{1}{64} b^3 \quad (\text{J.3})$$

$$\alpha^2 = z^2 - \frac{1}{2} zb + \frac{1}{16} b^2 \quad (\text{J.4})$$

Substituting Equations (J.1), (J.2), (J.3) and (J.4) into Equation (I.25) yields

$$\begin{aligned} & z^4 - z^3b + \frac{3}{8} z^2b^2 - \frac{1}{16} zb^3 + \frac{1}{256} b^4 \\ & + b(z^3 - \frac{3}{4} z^2b + \frac{3}{16} zb^2 - \frac{1}{64} b^3) \\ & + c(z^2 - \frac{1}{2} zb + \frac{1}{16} b^2) \\ & + d(z - \frac{1}{4} b) + f \end{aligned}$$

$$\begin{aligned}
&= z^4 + \left(-\frac{3}{8} b^2 + c\right) z^2 + \left(\frac{1}{8} b^3 - \frac{1}{2} bc + d\right) z \\
&\quad + \left(-\frac{3}{256} b^4 + \frac{1}{16} b^2 c - \frac{1}{4} bd + f\right) = 0
\end{aligned} \tag{J.5}$$

or

$$z^4 + qz^2 + rz + s = 0 \tag{J.6}$$

where

$$q = -\frac{3}{8} b^2 + c \tag{J.7}$$

$$r = \frac{1}{8} b^3 - \frac{1}{2} bc + d \tag{J.8}$$

$$s = -\frac{3}{256} b^4 + \frac{1}{16} b^2 c - \frac{1}{4} bd + f \tag{J.9}$$

Equation (J.6) can be expressed as the product of two second order polynomials, having their linear terms equal in magnitude and opposite in sign, of the form

$$\begin{aligned}
&[(z-1)^2 - (m+n)^2][(z+1)^2 - (m-n)^2] \\
&= (z-1)^2(z+1)^2 - (z-1)^2(m-n)^2 - (z+1)^2(m+n)^2 \\
&\quad + (m+n)^2(m-n)^2 \\
&= (z^2-1)^2 - (z^2-2z+1)(m^2-2mn+n^2) \\
&\quad - (z^2+2z+1)(m^2+2mn+n^2) + (m^2-n^2)^2 \\
&= (z^4-2z^2+1) - (m^2-2mn+n^2)z^2 \\
&\quad + (2zm^2-4zmn+2zn^2) - (m^2+2mn+n^2)z^2 \\
&\quad - (2zm^2+4zmn+2zn^2) + (m^4-2m^2n^2+n^4) \\
&= z^4 - 2(m^2+n^2)z^2 - 8mnz \\
&\quad + [(1^4+m^4+n^4) - 2(1^2m^2+m^2n^2+n^21^2)] = 0
\end{aligned} \tag{J.10}$$

Comparison of Equations (J.6) and (J.10) shows that

$$-2(l^2 + m^2 + n^2) = q \quad (J.11)$$

$$-8lmn = r \quad (J.12)$$

$$(l^4 + m^4 + n^4) - 2(l^2m^2 + m^2n^2 + n^2l^2) = s \quad (J.13)$$

so that

$$l^2 + m^2 + n^2 = -\frac{q}{2} \quad (J.14)$$

$$l^2m^2 + m^2n^2 + n^2l^2 = \frac{\left(\frac{q}{2}\right)^2 - s}{4} = \frac{q^2 - 4s}{16} \quad (J.15)$$

$$l^2m^2n^2 = \frac{r^2}{64} \quad (J.16)$$

Equations (J.14), (J.15) and (J.16) define the coefficients of a cubic equation, of which l^2 , m^2 and n^2 are the roots.

$$k^3 + \frac{q}{2}k^2 + \left(\frac{q^2 - 4s}{16}\right)k - \frac{r^2}{64} = 0 \quad (J.17)$$

When l , m and n have been found by solving Equation (J.17), being careful to ensure that

$$lmn = -\frac{r}{8} \quad (J.18)$$

then the initial form of Equation (J.10) can be written in the form

$$(z-l-m-n)(z-l+m+n)(z+l-m+n)(z+l+m-n) = 0 \quad (J.19)$$

and therefore the four roots are

$$z_1 = l + m + n \quad (J.20)$$

$$z_2 = l - m - n \quad (J.21)$$

$$z_3 = -l + m - n \quad (J.22)$$

$$z_4 = -l - m + n \quad (J.23)$$

Equation (J.17) can be written in the form

$$k^3 + \beta k^2 + \gamma k^2 + \delta = 0 \quad (\text{J.24})$$

where

$$\beta = \frac{q}{2} \quad (\text{J.25})$$

$$\gamma = \frac{q^2 - 4s}{16} \quad (\text{J.26})$$

$$\delta = -\frac{r^2}{64} \quad (\text{J.27})$$

In order to eliminate the second order term in Equation (J.24), we set

$$k = w - \frac{\beta}{3} \quad (\text{J.28})$$

so that

$$k^3 = w^3 - \beta w^2 + \frac{1}{3} \beta^2 w - \frac{1}{27} \beta^3 \quad (\text{J.29})$$

$$k^2 = w^2 - \frac{2}{3} \beta w + \frac{1}{9} \beta^2 \quad (\text{J.30})$$

Substituting Equations (J.28), (J.29) and (J.30) into Equation (J.24) yields

$$(w^3 - \beta w^2 + \frac{1}{3} \beta^2 w - \frac{1}{27} \beta^3) + \beta(w^2 - \frac{2}{3} \beta w + \frac{1}{9} \beta^2) + \gamma(w - \frac{\beta}{3}) + \delta = 0$$

or

$$w^3 - (\frac{\beta}{3} - \gamma)w - (\frac{\beta\gamma}{3} - \frac{2\beta^3}{27} - \delta) = 0 \quad (\text{J.31})$$

or

$$w^3 - Pw - Q = 0 \quad (\text{J.32})$$

where

$$P = \frac{B^2}{3} - \gamma \quad (J.33)$$

$$Q = \frac{B\gamma}{3} - \frac{2B^3}{27} - \delta \quad (J.34)$$

To obtain a solution of Equation (J.32), we assume that

$$w = A + B \quad (J.35)$$

so that

$$\begin{aligned} w^3 &= A^3 + 3A^2B + 3AB^2 + B^3 \\ &= A^3 + B^3 + 3AB(A + B) \\ &= A^3 + B^3 + 3ABw \end{aligned} \quad (J.36)$$

Equation (J.36) can be written in the form

$$w^3 - 3ABw - (A^3 + B^3) = 0 \quad (J.37)$$

Comparison of Equations (J.32) and (J.37) shows that

$$3AB = P \quad (J.38)$$

$$A^3 + B^3 = Q \quad (J.39)$$

Equation (J.38) yields

$$A^3B^3 = \left(\frac{P}{3}\right)^3 \quad (J.40)$$

Thus the sum and product of A^3 and B^3 are specified, which means that they are the roots of the quadratic equation

$$\xi^2 - (A^3 + B^3)\xi + (A^3B^3) = 0$$

or

$$\xi^2 - Q\xi + \left(\frac{P}{3}\right)^3 = 0 \quad (J.41)$$

Thus

$$\xi_1 = A^3 = \frac{Q}{2} + \sqrt{\left(\frac{Q}{2}\right)^2 - \left(\frac{P}{3}\right)^3} \quad (J.42)$$

$$\epsilon_2 = B^3 = \frac{Q}{2} - \sqrt{\left(\frac{Q}{2}\right)^2 - \left(\frac{P}{3}\right)^3} \quad (\text{J.43})$$

If we set

$$R = \left(\frac{Q}{2}\right)^2 - \left(\frac{P}{3}\right)^3 \quad (\text{J.44})$$

then Equations (J.42) and (J.43) can be written in the form

$$A^3 = \frac{Q}{2} + \sqrt{R} \quad (\text{J.45})$$

$$B^3 = \frac{Q}{2} - \sqrt{R} \quad (\text{J.46})$$

When $R \leq 0$, i.e., when

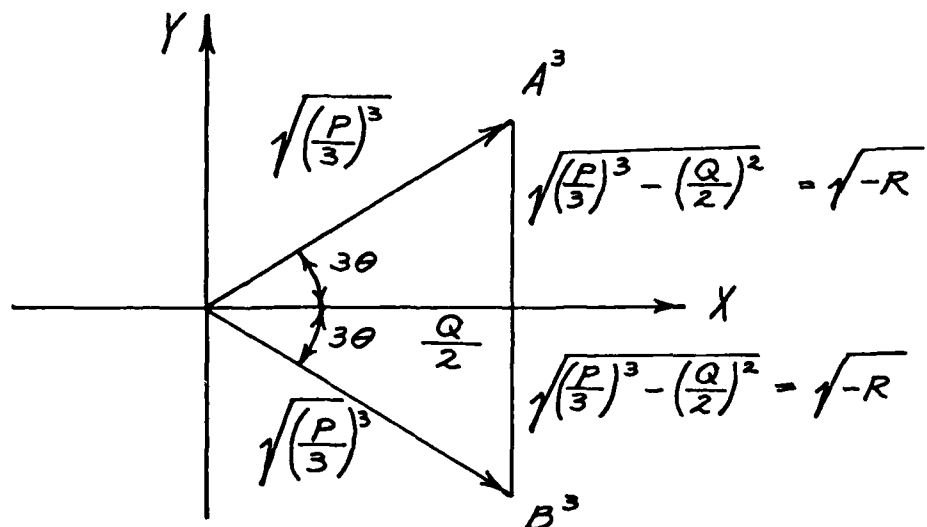
$$\left(\frac{P}{3}\right)^3 \geq \left(\frac{Q}{2}\right)^2 \quad (\text{J.47})$$

then Equations (J.45) and (J.46) take the form

$$A^3 = \frac{Q}{2} + i \sqrt{\left(\frac{P}{3}\right)^3 - \left(\frac{Q}{2}\right)^2} \quad (\text{J.48})$$

$$B^3 = \frac{Q}{2} - i \sqrt{\left(\frac{P}{3}\right)^3 - \left(\frac{Q}{2}\right)^2} \quad (\text{J.49})$$

In this case, A^3 and B^3 can be represented in the complex plane as shown below.



Thus we can write

$$A^3 = \sqrt{\left(\frac{P}{3}\right)^3} e^{i3\theta} \quad (J.50)$$

$$B^3 = \sqrt{\left(\frac{P}{3}\right)^3} e^{-i3\theta} \quad (J.51)$$

where

$$3\theta = \cos^{-1} \frac{\frac{Q}{2}}{\sqrt{\left(\frac{P}{3}\right)^3}} \quad (J.52)$$

so that

$$A_j = \sqrt{\frac{P}{3}} e^{i\phi_j} \quad (j = 1, 2, 3) \quad (J.53)$$

$$B_k = \sqrt{\frac{P}{3}} e^{-i\phi_k} \quad (k = 1, 2, 3) \quad (J.54)$$

where

$$\phi_1 = \theta = \frac{1}{3} \cos^{-1} \frac{\frac{Q}{2}}{\sqrt{\left(\frac{P}{3}\right)^3}} \quad (J.55)$$

$$\phi_2 = \theta + \frac{2\pi}{3} \quad (J.56)$$

$$\phi_3 = \theta - \frac{2\pi}{3} \quad (J.57)$$

Now Equation (J.38) requires that

$$AB = \frac{P}{3} \quad (J.58)$$

so that the choice of A_j and B_k in the relation

$$w_j = A_j + B_k \quad (J.59)$$

must be such that A_j and B_k are complex conjugates. Therefore it must be that $k = j$, so that

$$\begin{aligned} w_j &= \sqrt{\frac{P}{3}} (e^{i\phi_j} + e^{-i\phi_j}) \\ &= 2\sqrt{\frac{P}{3}} \cos \phi_j \quad (j = 1, 2, 3) \end{aligned} \quad (J.60)$$

The above three roots are all real.

When $R > 0$, i.e., when

$$\left(\frac{Q}{2}\right)^2 > \left(\frac{P}{3}\right)^3 \quad (J.61)$$

then both A^3 and B^3 , as defined by Equations (J.45) and (J.46) are real.

If we set

$$\sigma_1 = \frac{Q}{2} + \sqrt{R} \quad (J.62)$$

$$\sigma_2 = \frac{Q}{2} - \sqrt{R} \quad (J.63)$$

and

$$A_0 = |\sigma_1|^{1/3} \operatorname{sgn} \sigma_1 \quad (J.64)$$

$$B_0 = |\sigma_2|^{1/3} \operatorname{sgn} \sigma_2 \quad (J.65)$$

then

$$A_j = A_0 e^{i\phi_j} \quad (J.66)$$

$$B_k = B_0 e^{i\phi_k} \quad (J.67)$$

where

$$\phi_1 = 0 \quad (\text{J.68})$$

$$\phi_2 = \frac{2\pi}{3} \quad (\text{J.69})$$

$$\phi_3 = -\frac{2\pi}{3} \quad (\text{J.70})$$

Now

$$A_0 B_0 = \sqrt[3]{\left(\frac{Q}{2}\right)^2 - \left(\frac{Q}{2}\right)^2 + \left(\frac{P}{3}\right)^3} = \frac{P}{3} \quad (\text{J.71})$$

which means that the choices of A_j and B_k in the relation

$$w_j = A_j + B_k \quad (\text{J.59})$$

must be such that A_j and B_k are, again, complex conjugates, and therefore

$$w_1 = A_1 + B_1 = A_0 + B_0 \quad (\text{J.72})$$

$$\begin{aligned} w_2 = A_2 + B_3 &= A_0 e^{i \frac{2\pi}{3}} + B_0 e^{-i \frac{2\pi}{3}} \\ &= -\frac{1}{2} (A_0 + B_0) + i \frac{\sqrt{3}}{2} (A_0 - B_0) \end{aligned} \quad (\text{J.73})$$

$$\begin{aligned} w_3 = A_3 + B_2 &= A_0 e^{-i \frac{2\pi}{3}} + B_0 e^{i \frac{2\pi}{3}} \\ &= -\frac{1}{2} (A_0 + B_0) - i \frac{\sqrt{3}}{2} (A_0 - B_0) \end{aligned} \quad (\text{J.74})$$

In summary, to solve Equation (I.25) we do the following:

$$b = \frac{C_v (M_s + M_w)}{M_s M_w} \quad (\text{I.17})$$

$$c = \frac{M_s K_w + M_w K_s}{M_s M_w} \quad (\text{I.18})$$

$$d = \frac{C_v (K_s + K_w)}{M_s M_w} \quad (\text{I.19})$$

$$f = \frac{K_s K_w}{M_s M_w} \quad (\text{I.20})$$

$$g = \frac{C_v}{M_s M_w} \quad (\text{I.21})$$

then

$$q = -\frac{3}{8} b^2 + c \quad (\text{J.7})$$

$$r = \frac{1}{8} b^3 - \frac{1}{2} bc + d \quad (\text{J.8})$$

$$s = -\frac{3}{256} b^4 + \frac{1}{16} b^2 c - \frac{1}{4} bd + f \quad (\text{J.9})$$

then

$$\beta = \frac{q}{2} \quad (\text{J.25})$$

$$\gamma = \frac{q^2 - 4s}{16} \quad (\text{J.26})$$

$$\delta = -\frac{r^2}{64} \quad (\text{J.27})$$

then

$$P = \frac{\beta^2}{3} - \gamma \quad (\text{J.33})$$

$$Q = \frac{\beta\gamma}{3} - \frac{2\beta^3}{27} - \delta \quad (\text{J.34})$$

then

$$R = \left(\frac{Q}{2}\right)^2 - \left(\frac{P}{3}\right)^3 \quad (J.44)$$

If $R \leq 0$:

$$\theta = \frac{1}{3} \cos^{-1} \left\{ \frac{\frac{Q}{2}}{\sqrt{\left(\frac{P}{3}\right)^3}} \right\} \quad (J.55)$$

$$k_1 = 2\sqrt{\frac{P}{3}} \cos \theta - \frac{\beta}{3} \quad (J.75)$$

$$k_2 = 2\sqrt{\frac{P}{3}} \cos\left(\theta + \frac{2\pi}{3}\right) - \frac{\beta}{3} \quad (J.76)$$

$$k_3 = 2\sqrt{\frac{P}{3}} \cos\left(\theta - \frac{2\pi}{3}\right) - \frac{\beta}{3} \quad (J.77)$$

$$k_I = \text{MAX}(k_1, k_2, k_3) \quad (J.78)$$

$$\theta_p = \cos^{-1} \left(\frac{3k_I + \beta}{6 \frac{P}{3}} \right) \quad (J.79)$$

$$k_{II} = 2\sqrt{\frac{P}{3}} \cos\left(\theta_p + \frac{2\pi}{3}\right) - \frac{\beta}{3} \quad (J.80)$$

$$k_{III} = 2\sqrt{\frac{P}{3}} \cos\left(\theta_p - \frac{2\pi}{3}\right) - \frac{\beta}{3} \quad (J.81)$$

$$\Omega = \frac{1}{2} \cos^{-1}(\text{sgn } k_{II}) \quad (J.82)^+$$

$$1 = - \frac{r \cos 2\Omega}{8|k_{II}|^{1/2} |k_{III}|^{1/2}} \quad (J.83)$$

$$m = |k_{II}|^{1/2} (\cos \Omega + i \sin \Omega) \quad (J.84)$$

$+\Omega = 0 \text{ or } \pi/2$

$$n = |k_{III}|^{1/2} (\cos \Omega + i \sin \Omega) \quad (J.85)$$

The rationale for Equations (J.83), (J.84) and (J.85) is explained following Equation (J.94).

If $R > 0$:

$$\sigma_1 = \frac{Q}{2} + \sqrt{R} \quad (J.62)$$

$$\sigma_2 = \frac{Q}{2} - \sqrt{R} \quad (J.63)$$

$$A_0 = |\sigma_1|^{1/3} \operatorname{sgn} \sigma_1 \quad (J.64)$$

$$B_0 = |\sigma_2|^{1/3} \operatorname{sgn} \sigma_2 \quad (J.65)$$

$$\rho = \left\{ \left[\frac{1}{2}(A_0 + B_0) + \frac{B}{3} \right]^2 + \frac{3}{4}(A_0 - B_0)^2 \right\}^{1/4} \quad (J.86)$$

$$\Omega = \frac{1}{2} \cos^{-1} \left\{ - \frac{\frac{1}{2}(A_0 + B_0) + \frac{B}{3}}{\rho^2} \right\} \quad (J.87)$$

$$l = - \frac{r}{8\rho^2} \quad (J.88)$$

$$m = \rho(\cos \Omega + i \sin \Omega) \quad (J.89)$$

$$n = \rho(\cos \Omega - i \sin \Omega) \quad (J.90)$$

The rationale for Equation (J.88) is explained following Equation (J.94).

Equations (J.72), (J.73), (J.74), (J.86) and (J.87) can be represented graphically as shown below.

If the three roots, l^2 , m^2 and n^2 , are all real, then either one is nonnegative and the other two are negative, or all three are nonnegative. In either case, m^2 and n^2 have the same sign, which is assured by Equations (J.84) and (J.85).

If one root is real and the other two are complex, then the complex roots must be complex conjugates. Since the product of the complex conjugate roots is nonnegative, the real root must also be nonnegative.

Thus, we can always assume that

$$l^2 \geq 0 \quad (\text{J.95})$$

and therefore that l is real.

The coefficients (invariants) of a fourth order polynomial equation will be real if and only if complex roots occur only as complex conjugate pairs.

$$I_1 = \alpha_1 + \alpha_2 + \alpha_3 + \alpha_4 = (\alpha_1 + \alpha_2) + (\alpha_3 + \alpha_4) \quad (\text{J.96})$$

$$\begin{aligned} I_2 &= \alpha_1\alpha_2 + \alpha_1\alpha_3 + \alpha_1\alpha_4 + \alpha_2\alpha_3 + \alpha_2\alpha_4 + \alpha_3\alpha_4 \\ &= \alpha_1\alpha_2 + (\alpha_1 + \alpha_2)(\alpha_3 + \alpha_4) + \alpha_3\alpha_4 \end{aligned} \quad (\text{J.97})$$

$$\begin{aligned} I_3 &= \alpha_2\alpha_3\alpha_4 + \alpha_1\alpha_3\alpha_4 + \alpha_1\alpha_2\alpha_4 + \alpha_1\alpha_2\alpha_3 \\ &= \alpha_3\alpha_4(\alpha_1 + \alpha_2) + \alpha_1\alpha_2(\alpha_3 + \alpha_4) \end{aligned} \quad (\text{J.98})$$

$$I_4 = \alpha_1\alpha_2\alpha_3\alpha_4 = (\alpha_1\alpha_2)(\alpha_3\alpha_4) \quad (\text{J.99})$$

APPENDIX K

Solution of a Fourth Order Linear Ordinary Differential Equation With Constant Coefficients

Consider the fourth order, linear ordinary differential equation with constant coefficients

$$(D^4 + bD^3 + cD^2 + dD + f)x = gDp \quad (I.16)$$

which can be written in the factored form

$$[(D-\alpha_1)(D-\alpha_2)(D-\alpha_3)(D-\alpha_4)]x = gDp \quad (I.27)$$

where $\alpha_1, \alpha_2, \alpha_3$, and α_4 are the roots of the equation

$$\alpha^4 + b\alpha^3 + c\alpha^2 + d\alpha + f = 0 \quad (I.25)$$

The particular solution to Equation (I.27) can be written in the form

$$x_p(t) = \frac{1}{(D-\alpha_1)(D-\alpha_2)(D-\alpha_3)(D-\alpha_4)} gDp \quad (K.1)$$

Now if we set

$$\frac{1}{(D-\alpha_1)(D-\alpha_2)} = \frac{A}{D-\alpha_1} + \frac{B}{D-\alpha_2} \quad (K.2)$$

then it must be that

$$AD - A\alpha_2 + BD - B\alpha_1 = 1 \quad (K.3)$$

and therefore that

$$B = -A \quad (K.4)$$

so that

$$A(\alpha_1 - \alpha_2) = 1 \quad (K.5)$$

and therefore

$$A = \frac{1}{\alpha_1 - \alpha_2} \quad (K.6)$$

and

$$B = \frac{1}{\alpha_2 - \alpha_1} \quad (K.7)$$

Thus, we have

$$\frac{1}{(D-\alpha_1)(D-\alpha_2)} = \frac{1}{(\alpha_1-\alpha_2)(D-\alpha_1)} + \frac{1}{(\alpha_2-\alpha_1)(D-\alpha_2)} \quad (K.8)$$

If we set

$$\alpha_i - \alpha_j = R_{ij} \quad (i \neq j) \quad (K.9)$$

$$D - \alpha_i = D_i \quad (K.10)$$

then for distinct roots,

$$\frac{1}{D_i D_j} = \frac{1}{R_{ij} D_i} + \frac{1}{R_{ji} D_j} \quad (K.11)$$

We then have

$$\begin{aligned} \frac{1}{D_1 D_2 D_3} &= \left(\frac{1}{R_{12} D_1} + \frac{1}{R_{21} D_2} \right) \left(\frac{1}{D_3} \right) \\ &= \frac{1}{R_{12}} \left(\frac{1}{R_{13} D_1} + \frac{1}{R_{31} D_3} \right) + \frac{1}{R_{21}} \left(\frac{1}{R_{23} D_2} + \frac{1}{R_{32} D_3} \right) \\ &= \frac{1}{R_{12} R_{13} D_1} + \frac{1}{R_{21} R_{23} D_2} + \frac{1}{R_{12}} \left(\frac{1}{R_{31}} - \frac{1}{R_{32}} \right) \frac{1}{D_3} \\ &= \frac{1}{R_{12} R_{13} D_1} + \frac{1}{R_{21} R_{23} D_2} + \frac{R_{32} - R_{31}}{R_{12} R_{31} R_{32} D_3} \\ &= \frac{1}{R_{12} R_{13} D_1} + \frac{1}{R_{21} R_{23} D_2} + \frac{1}{R_{31} R_{32} D_3} \end{aligned} \quad (K.12)$$

and, in general,

$$\frac{1}{D_1 D_2 D_3 \cdots D_N} = \sum_{j=1}^N \frac{1}{R_j D_j} \quad (K.13)$$

where

$$\pi_j = R_{j1} R_{j2} R_{j3} \cdots R_{j,j-1} R_{j,j+1} \cdots R_{jN} \quad (K.14)$$

Now the particular solution for D_j^{-1} is, from Equation (H.15),

$$\frac{1}{D_j} \left[g \frac{dp}{dt} \right] = g \int_0^t \frac{dp}{d\lambda} e^{\alpha_j(t-\lambda)} d\lambda \quad (t>0) \quad (K.15)$$

Equation (K.13) therefore yields

$$x_p(t) = \frac{1}{D_1 D_2 D_3 D_4} \left[g \frac{dp}{dt} \right] = g \sum_{j=1}^4 \frac{1}{\pi_j} \int_0^t \frac{dp}{d\lambda} e^{\alpha_j(t-\lambda)} d\lambda \quad (t>0) \quad (K.16)$$

APPENDIX L

Numerical Solution of the Characteristic Equation

Equation (I.25) will be solved for one cubic foot of dry sand, constrained to undergo one dimensional compression and loaded by a 100 PSI airblast.

From [Terzaghi and Peck (1967:28)] we obtain

$$W_s = 115 \text{ LBS}$$

$$M_s = \frac{115}{32.2} = 3.5714 \frac{\text{LB SEC}^2}{\text{FT}}$$

$$n = 0.30$$

$$V_A = V_v = 0.30 \text{ FT}^3$$

and since [McGuire (1968:181)]

$$\gamma_A = 0.07651 \frac{\text{LBS}}{\text{FT}^3}$$

we have

$$W_A = (0.07651)(0.30) = 0.022953 \text{ LBS}$$

$$M_w = \frac{0.022953}{32.2} = 7.128 \times 10^{-4} \frac{\text{LB SEC}^2}{\text{FT}}$$

From [Bowles (1977:269)] we have

$$K_s = 600,000 \frac{\text{LBS}}{\text{FT}}$$

and if we assume isothermal compression, we obtain

$$\frac{dp}{p} = - \frac{dV}{V} \quad (L.1)$$

so that

$$dp = - \frac{p}{V} dV \quad (L.2)$$

and

$$A dp = \frac{pA}{V} \cdot A dy \quad (L.3)$$

$$K_w = \frac{pA^2}{V} = \frac{(100)(144)(1)^2}{0.30} = 48,000 \frac{LBS}{FT}$$

Assuming an effective permeability, as given by Equation (4.3), of

$$\begin{aligned} B_1 &= 5.054 \times 10^{-10} \frac{M^4}{N SEC} \\ &= \frac{(5.054 \times 10^{-10})(4.448222)}{(0.3048)^4} = 2.605 \times 10^{-7} \frac{FT^4}{LB SEC} \end{aligned}$$

we have

$$C_v = \frac{1}{B_1}(1 FT^3) = 3,839,249 \frac{LB SEC}{FT}$$

Thus, we obtain

$$\begin{aligned} b &= \frac{C_v(M_s + M_w)}{M_s M_w} = \frac{(3.839 \times 10^6)(3.5714 + 0.0007)}{(3.571)(0.0007128)} \\ &= 5.387 \times 10^9 SEC^{-1} \end{aligned}$$

$$\begin{aligned} c &= \frac{M_s K_w + M_w K_s}{M_s M_w} = \frac{(3.571)(48,000) + (0.0007128)(600,000)}{(3.571)(0.0007128)} \\ &= 6.751 \times 10^7 SEC^{-2} \end{aligned}$$

$$d = \frac{C_v(K_s + K_w)}{M_s M_w} = \frac{(3.839 \times 10^6)(600,000 + 48,000)}{(3.571)(0.0007128)}$$

$$= 9.773 \times 10^{14} \text{ SEC}^{-3}$$

$$f = \frac{K_s K_w}{M_s M_w} = \frac{(600,000)(48,000)}{(3.571)(0.0007128)} = 1.31 \times 10^{13} \text{ SEC}^{-4}$$

$$g = \frac{C_v}{M_s M_w} = \frac{3.839 \times 10^6}{(3.571)(0.0007128)} = 1.508 \times 10^9 \frac{\text{FT}}{\text{LB SEC}^3}$$

Changing from SEC to MSEC, we obtain

$$b = 5.387 \times 10^6 \text{ MSEC}^{-1}$$

$$c = 6.751 \times 10^1 \text{ MSEC}^{-2}$$

$$d = 9.773 \times 10^5 \text{ MSEC}^{-3}$$

$$f = 1.131 \times 10^1 \text{ MSEC}^{-4}$$

$$g = 1.508 \times 10^0 \frac{\text{FT}}{\text{LB MSEC}^3}$$

The following double precision FORTRAN computer program was used to calculate the roots of Equation I.25. The only differences between the program instructions and the equations given in Appendix J are due to lack of double precision functions for the inverse sine and cosine.

```

PROGRAM AIR(INPUT,OUTPUT)
DOUBLE PRECISION B,C,D,F,Q,R,S,B1,C1,D1,PP,QQ,RR,TH
1 COS1,COS2,COS3,THP,Y,SQL,SQM,SQN,RM,RN,XL,SM,YM,
2 XN,YN,S1,S2,EX,AO,BO,RHO,
3 OMEGA,XR1,YR1,XR2,YR2,XR3,YR3,XR4,YR4
B = 0.5387D+07
C = 0.6751D+02
D = 0.9773D+06
F = 0.1131D+02
PI=4.0*DATAN(1.0D0)
Q=-0.375*B**2+C
R=0.125*B**3-0.5*B*C+D
S=-(3.0*B**4)/256.+(C*B**2)/16.0-0.25*B*D+F
B1=Q/2.0

```

```

C1=(Q**2-4.0*S)/16.0
D1=-R**2/64.
PP=(B1**2)/3.0-C1
QQ=(B1*C1)/3.0-(2.0*B1**3)/27.0-D1
RR=(QQ/2.0)**2-(PP/3.0)**3
IF(RR.GT.0.0)GO TO 10
TH=QQ/(2.0*DSQRT(-RR))
TH=DATAN(TH)
TH=(PI/2.0-TH)/3.0
COS1=DCOS(TH)
COS2=DCOS(TH+(2.*PI)/3.0)
COS3=DCOS(TH-2.0*PI)/3.0)
COS1=DMAX1(COS1,COS2,COS3)
THP=DSQRT(1.0-COS1**2)/COS1
THP=DATAN(THP)
COS2=DCOS(THP+(2.0*PI)/3.0)
COS3=DCOS(THP-(2.0*PI)/3.0)
Y=2.0*DSQRT(PP/3.0)
SQL=Y*COS1-B1/3.0
SQM=Y*COS2-B1/3.0
SQN=Y*COS3-B1/3.0
RM=DSQRT(DABS(SQM))
RN=DSQRT(DABS(SQN))
OMEGA=0.5*(PI/2.0-2.0*DATAN(DSIGN(1.0D0,SQM+SQN)))
XL=DSQRT(SQL)
XM=RM*DCOS(OMEGA)
YM=RM*DSIN(OMEGA)
XN=RN*DCOS(OMEGA)
YN=RN*DSIN(OMEGA)
GO TO 20
10 S1=QQ/2.0+DSQRT(RR)
S2=QQ/2.0-DSQRT(RR)
EX=1./3.
AO=((DABS(S1))*EX)*DSIGN(1.0D0,S1)
BO=((DABS(S2))*EX)*DSIGN(1.0D0,S2)
RHO=((0.5*(AO+BO)+B1/3.0)**2+0.75*(AO-BO)**2)**.25
OMEGA=(AO+BO+2.0*B1/3.0)/(DSQRT(3.0D0)*(AO-BO))
OMEGA=DATAN(OMEGA)
OMEGA=0.5*(PI/2.0+OMEGA)
XL=-R/(8.0*RHO**2)
XM=RHO*DCOS(OMEGA)
YM=RHO*DSIN(OMEGA)
XN=XM
YN=-YM
20 XR1=XL+XM+XN-B/4.0
YR1=YM+YN
XR2=XL-XM-XN-B/4.0
YR2=-YM-YN
XR3=-XL+XM-XN-B/4.0
YR3=YM-YN
XR4=-XL-XM+XN-B/4.0
YR4=-YM+YN

```

```

100 PRINT 100,B,C,D,F,XR1,YR1,XR2,YR2,XR3,YR3,XR4,YR4
    FORMAT(10X,2D16.9)
    STOP
    END

```

The roots are

$$\alpha_1 = -0.115726598 \times 10^{-4} \text{ MSEC}^{-1}$$

$$\alpha_2 = -0.538700000 \times 10^7 \text{ MSEC}^{-1}$$

$$\alpha_3 = -0.462842340 \times 10^{-6} + 0.425932181i \text{ MSEC}^{-1}$$

$$\alpha_4 = -0.462842340 \times 10^{-6} - 0.425932181i \text{ MSEC}^{-1}$$

The invariants are

$$I_1 = \alpha_1 + \alpha_2 + \alpha_3 + \alpha_4 = -5,387,000$$

$$I_2 = \alpha_1\alpha_2 + (\alpha_1 + \alpha_2)(\alpha_3 + \alpha_4) + \alpha_3\alpha_4 = 67.51$$

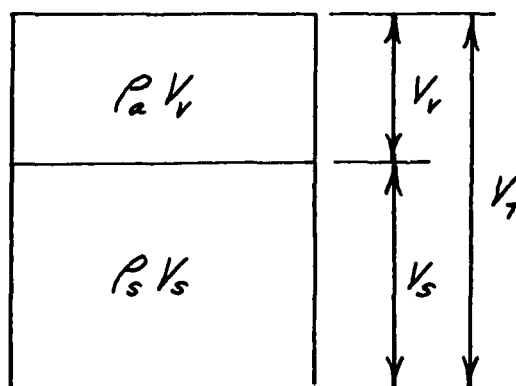
$$I_3 = (\alpha_1 + \alpha_2)\alpha_3\alpha_4 + \alpha_1\alpha_2(\alpha_3 + \alpha_4) = -977,300$$

$$I_4 = \alpha_1\alpha_2\alpha_3\alpha_4 = 11.31$$

APPENDIX M

General Equations for the Pore Air Effect

The soil phase relationships are well known. Consider the element of dry soil shown below.



The void ratio, e , is the ratio of void volume to solid volume,

$$e = \frac{V_v}{V_s} \quad (M.1)$$

whereas the porosity is the ratio of void volume to total volume.

$$n = \frac{V_v}{V_T} \quad (M.2)$$

Since total volume equals solid volume plus void volume,

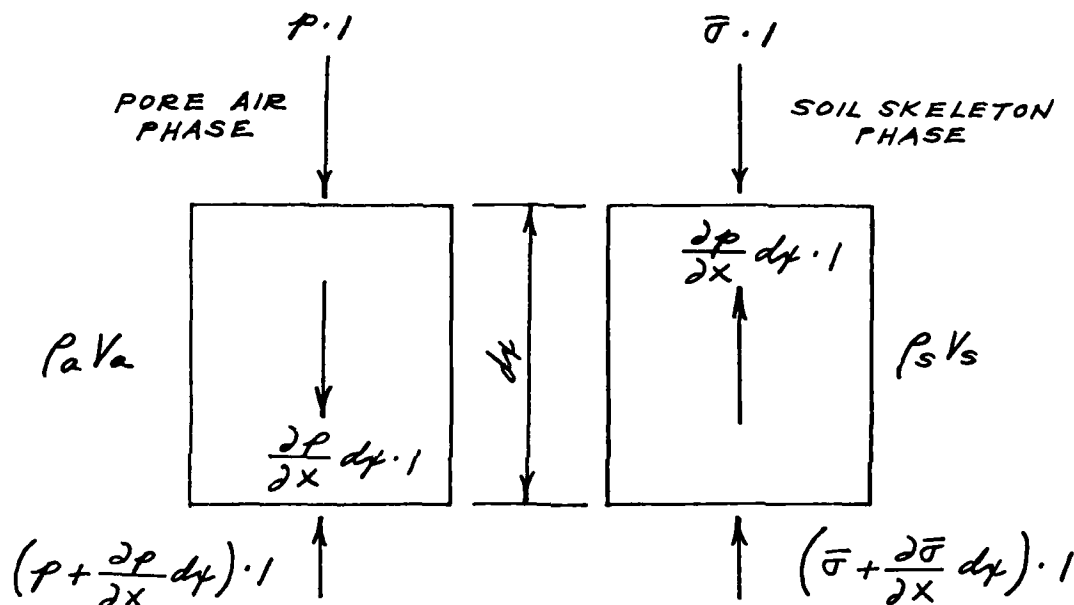
$$V_T = V_s + V_v \quad (M.3)$$

Equations (M.1) and (M.2) can be written in the forms

$$e = \frac{V_v}{V_s} = \frac{V_v}{V_T - V_v} = \frac{nV_T}{V_T - nV_T} = \frac{n}{1 - n} \quad (M.4)$$

$$n = \frac{V_v}{V_T} = \frac{V_v}{V_s + V_v} = \frac{eV_s}{V_s + eV_s} = \frac{e}{1 + e} \quad (M.5)$$

For one dimensional wave propagation and pore air diffusion, we have the following situation:



The volume of solids in a given soil element remains constant, so that [Taylor (1948:227)]

$$V_{T0} = dx \cdot 1 = V_s + V_{v0} = V_s + e_0 V_s = V_s (1 + e_0) \quad (M.6)$$

and therefore,

$$V_s = \frac{V_{T0}}{1 + e_0} = \frac{dx \cdot 1}{1 + e_0} \quad (M.7)$$

The equation of motion for the soil skeleton is

$$-\frac{\partial \bar{\sigma}}{\partial x} dx \cdot 1 - \frac{\partial p}{\partial x} dx \cdot 1 = \rho_s V_s \frac{\partial^2 u}{\partial t^2}$$

or

$$\frac{\partial \sigma}{\partial x} = - \frac{\rho_s}{1 + e_0} \frac{\partial^2 u}{\partial t^2} \quad (\text{M.8})$$

where, by definition

$$\sigma = \bar{\sigma} + p \quad (\text{M.9})$$

Effective stress is a function of strain,

$$\bar{\sigma} = \bar{\sigma}(\epsilon) \quad (\text{M.10})$$

strain is related to void ratio,

$$\epsilon = - \frac{\partial u}{\partial x} \quad (\text{M.11})$$

$$= \frac{V_{T0} - V_T}{V_{T0}} = \frac{(1 + e_0)V_s - (1 + e)V_s}{(1 + e_0)V_s} = \frac{e_0 - e}{1 + e_0} \quad (\text{M.12})$$

and void ratio is therefore related to strain.

$$e = e_0 + (1 + e_0) \frac{\partial u}{\partial x} \quad (\text{M.13})$$

For adiabatic flow,

$$p = \rho_a^\gamma \quad (\text{M.14})$$

The equation of pore air flow is

$$v - \frac{\partial u}{\partial t} = - \frac{B_1}{n} \frac{\partial p}{\partial x} \quad (\text{M.15})$$

and the equation of conservation of air mass is

$$\frac{\partial}{\partial x} [\rho_a n (v - \frac{\partial u}{\partial t})] dx \cdot 1 = - \frac{\partial}{\partial t} (\rho_a V_v) = - \frac{\partial}{\partial t} (\rho_a e V_s)$$

or

$$\frac{\partial}{\partial x} [\rho_a n(v - \frac{\partial u}{\partial t})] = - \frac{1}{1 + e_0} \frac{\partial}{\partial t} (\rho_a e) \quad (M.16)$$

Inserting Equation (M.9) in Equation (M.8) yields

$$\frac{\partial^2 u}{\partial t^2} = - \frac{1 + e_0}{\rho_s} (\frac{\partial \bar{\sigma}}{\partial x} + \frac{\partial p}{\partial x}) \quad (M.17)$$

and from Equations (M.10) and (M.11) we obtain

$$\frac{\partial \bar{\sigma}}{\partial x} = \frac{\partial \bar{\sigma}}{\partial \epsilon} \frac{\partial \epsilon}{\partial x} = -E_T \frac{\partial^2 u}{\partial x^2} \quad (M.18)$$

where

$$E_T = \frac{\partial \bar{\sigma}}{\partial \epsilon} \quad (M.19)$$

Thus, Equation (M.17) can be written in the form

$$\frac{\partial^2 u}{\partial t^2} = \frac{1 + e_0}{\rho_s} [E_T \frac{\partial^2 u}{\partial x^2} - \frac{\partial p}{\partial x}] \quad (M.20)$$

Inserting Equation (M.15) into Equation (M.16) yields

$$\frac{1}{1 + e_0} \frac{\partial}{\partial t} (\rho_a e) = B_1 \frac{\partial}{\partial x} (\rho_a \frac{\partial p}{\partial x}) \quad (M.21)$$

Inserting Equation (M.14) into Equation (M.21) yields

$$\frac{1}{1 + e_0} \frac{\partial}{\partial t} [(\frac{p}{a})^{1/\gamma} e] = B_1 \frac{\partial}{\partial x} [(\frac{p}{a})^{1/\gamma} \frac{\partial p}{\partial x}]$$

or

$$\frac{1}{1 + e_0} \left[e \frac{\partial}{\partial t} (p^{1/\gamma}) + p^{1/\gamma} \frac{\partial e}{\partial t} \right] = \frac{B_1}{\frac{1}{\gamma} + 1} \frac{\partial^2}{\partial x^2} (p^{\frac{1}{\gamma} + 1})$$

or

$$(n_0 + \frac{\partial u}{\partial x}) \left[\frac{\partial}{\partial t} (p^{1/\gamma}) \right] + p^{1/\gamma} \frac{\partial^2 u}{\partial x \partial t} = \frac{B_1}{\frac{1}{\gamma} + 1} \frac{\partial^2}{\partial x^2} (p^{\frac{1}{\gamma} + 1})$$

or

$$\frac{\partial}{\partial t} (p^{1/\gamma}) = \frac{1}{(n_0 + \frac{\partial u}{\partial x})} \left[\frac{B_1}{(\frac{1}{\gamma} + 1)} \frac{\partial^2}{\partial x^2} (p^{\frac{1}{\gamma} + 1}) - p^{1/\gamma} \frac{\partial^2 u}{\partial x \partial t} \right] \quad (M.22)$$

An alternate form of Equation (M.22) is

$$\begin{aligned} \frac{1}{\gamma} p^{\frac{1}{\gamma} - 1} \frac{\partial p}{\partial t} &= \frac{1}{(n_0 + \frac{\partial u}{\partial x})} \left[B_1 \frac{\partial}{\partial x} (p^{1/\gamma} \frac{\partial p}{\partial x}) - p^{1/\gamma} \frac{\partial^2 u}{\partial x \partial t} \right] \\ &= \frac{1}{n_0 + \frac{\partial u}{\partial x}} \left\{ B_1 \left[\frac{1}{\gamma} p^{\frac{1}{\gamma} - 1} \left(\frac{\partial p}{\partial x} \right)^2 + p^{1/\gamma} \left(\frac{\partial^2 p}{\partial x^2} \right) \right] - p^{1/\gamma} \frac{\partial^2 u}{\partial x \partial t} \right\} \end{aligned}$$

or

$$\frac{\partial p}{\partial t} = \frac{1}{n_0 + \frac{\partial u}{\partial x}} \left\{ B_1 \left[\left(\frac{\partial p}{\partial x} \right)^2 + \gamma p \left(\frac{\partial^2 p}{\partial x^2} \right) \right] - \gamma p \frac{\partial^2 u}{\partial x \partial t} \right\} \quad (M.23)$$

Equations (M.20) and (M.22) are coupled, nonlinear, second order partial differential equations for the soil skeleton displacement, u , and the pore air pressure, p . Gravitational acceleration does not appear explicitly in Equation (M.20), because the stresses involved are assumed to be "live" stresses, i.e., stresses in excess of those existing under geostatic conditions. It is the live stresses which cause motion. Note,

however, that when live stresses are used, they must be expressed in terms of live strains. This means that if the stress-strain relation, Equation (M.10), is nonlinear the geostatic stress-strain condition must be determined, because it must be used as the point of departure for the live stress-live strain relation.

The effective permeability, B_1 , has been assumed constant in Equations (M.15), (M.21), (M.22) and (M.23), although B_1 is known to vary with strain. This assumption appears reasonable prior to spall, because the strain required to cause particle separation is small, and because the exact relation between effective permeability and strain is often not precise.

REFERENCES

REFERENCES

- Auld, H.E., D.M. Bradley, R. Brown, S.E. Blouin, and B.W. Stump, "Data Analysis of the PRE-HYBRID GUST (PHG) Test Series", Applied Research Associates report to the Defense Nuclear Agency (submitted 16 August 1981; in review).
- Bellman, R., Introduction to Matrix Analysis, McGraw-Hill (1960).
- Bowles, J.E., Foundation Analysis and Design, Second Edition, McGraw-Hill (1977).
- Carman, P.C., Flow of Gases Through Porous Media, Butterworths (1956).
- Carslaw, H.S. and J.C. Jaeger, Conduction of Heat in Solids, 2nd Edition, Oxford University Press (1959).
- Cheng, D.K., Analysis of Linear Systems, Addison-Wesley (1959).
- Crandall, S.H., Engineering Analysis, McGraw-Hill (1956).
- Hampton, D., "A Study of Pore Air Pressures Generated in Soil Subjected to Air Shock", University of New Mexico Civil Engineering Research Facility report to the Air Force Weapons Laboratory, WL-TDR-64-3 (October 1964), 82 pp.
- Hildebrand, F.B., Advanced Calculus for Applications, Prentice-Hall (1962).
- Hofmann, R., "STEALTH, A Lagrange Explicit Finite-Difference Code for Solids, Structural and Thermo-hydraulic Analysis", EPRI NP-176-1, Electric Power Research Institute (Palo Alto, CA, 1978).
- Labreche, D., "Negative Pore-Air Pressure Study", University of New Mexico Engineering Research Institute in-house report (November 1980), 46 pp.
- Lambe, T.W. and R.V. Whitman, Soil Mechanics, Wiley (1969).
- Leonards, G.A., Foundation Engineering, McGraw-Hill (1962).
- McGuire, W., Steel Structures, Prentice-Hall (1968).
- Merkle, D.H., "Basic Mechanisms of Spall From Near-Surface Explosions", Applied Research Associates report to the Air Force Office of Scientific Research (30 November 1980), 88 pp.
- Merkle, D.H. and G.E. Cannon, Jr., "Explosive Impulse Welding", USAF Academy Department of Civil Engineering, Engineering Mechanics and Materials (DFCEM) report, published as Frank J. Seiler Research Laboratory Report SRL-TR-77-0012 (2 volumes), (USAF Academy, Colorado, July 1977), Vol. I, 429 pp.; Vol. II, 104 pp.

Mitchell, J.K., Fundamentals of Soil Behavior, Wiley (1976).

Moriwaki, Y., et.al., "Specification of Input Motions for Seismic Analysis of Soil-Structure Systems Within a Nonlinear Analysis Framework", EPRI NP-2097, Electric Power Research Institute (Palo Alto, CA, October 1981).

Morrison, D., "Pore Air Expansion Effects", University of New Mexico Civil Engineering Research Facility report (23 August 1979a), 16 pp.

Morrison, D., briefing presented at the DNA Spall Workshop, held at Marina del Rey, California (September 1979b); published by DASIAC DOD Nuclear Information and Analysis Center (February 1981).

Morrison, D., J. Berglund, and M. Kelly, "Effects of Pore Air Expansion on Near-Surface Soil Motion", University of New Mexico Civil Engineering Research Facility report to the Air Force Weapons Laboratory, AFWL TR 79-78 (December 1979), 70 pp.

Morrison, D., D. Labreche, and J. Lamb, "Pore Air Pressure Effects (Expansion and Flow) on Near-Surface Soil Motions", University of New Mexico Civil Engineering Research Facility draft report to the Air Force Weapons Laboratory, AFWL TR 81-70 (April 1981), 75 pp; published in February 1982 with L. Lenke added to the authors' list.

Muskat, M. and R.D. Wyckoff, The Flow of Homogeneous Fluids Through Porous Media, J.W. Edwards (Ann Arbor, Michigan, 1946).

Needham, C.E., "PRAIRIE FLAT Air Blast Calculations", Air Force Weapons Laboratory technical report AFWL TR 69-4 (February 1969).

Needham, C.E., M.L. Havens, and C.S. Knauth, "Nuclear Blast Standard (1 KT)", Air Force Weapons Laboratory technical report AFWL TR 73-55 (April 1973).

Rosenblatt, M., P. Hassig, and D. Orphal, "Soil-Air Interactions During Airblast-Induced Ground Motions", California Research and Technology draft report to the Defense Nuclear Agency, CRT 3470F (January 1982), 152 pp.

Rosenblatt, M, D. Orphal and P. Hassig, "Effects of Multiphase Flow Phenomena on Near Surface Explosion Ground Motion", paper presented at the DNA Spall Workshop, held at Marina del Rey, California (September 1979); published by DASIAC DOD Nuclear Information and Analysis Center (February 1981).

Sokolnikoff, I.S. and E.S. Sokolnikoff, Higher Mathematics for Engineers and Physicists, Second Edition, McGraw-Hill (1941).

Stump, B.W. and R.E. Reinke, "Geophysical Studies at McCormick Ranch, New Mexico and the Importance of Spall Waveforms in High Explosive Testing", AFWL/NTE draft report (August 1980).

Taylor, D.W., Fundamentals of Soil Mechanics, Wiley (1948).

Terzaghi, K., Theoretical Soil Mechanics, Wiley (1943).

Terzaghi, K. and R. Peck, Soil Mechanics in Engineering Practice, Second Edition, Wiley (1967).

Ullrich, G.W., "Airblast/Ground Motion Effects From Simultaneous Detonations of High Explosive Charges", (draft) AFWL TR-78-110 (1978); 21 pp; also Nuclear Technology Digest, Vol. I, AFWL (1978).

Vennard, J.K., Elementary Fluid Mechanics, 3rd Edition, Wiley (1954).

Zernow, L., N. Louie, W.H. Anderson, and P.J. Blatz, "An Experimental Study of the 'Reverse Percolation' Lofting Process in a Sand Medium", Whittaker Shock Hydrodynamics report to the Defense Nuclear Agency, DNA 3210F (16 November 1973), 112 pp.

TABLES

Table 3.1. One-Dimensional Calculations

Calc. No.	Description	Tensile Cutoff P_{min} , MPa	Peak Incident Velocity, m/s	Comments
1	no spall allowed	100.	1.0	3 cycles to spall
2	baseline spall calculation	0.10	1.0	3 cycles to spall
3	load variation	0.10	2.0	3 cycles to spall
4	no tensile strength	0.00	1.0	3 cycles to spall
5	higher tensile strength	0.30	1.0	3 cycles to spall
6	immediate spall	0.10	1.0	1 cycle to spall
7	forced rejoin	0.10	2.0	1.0 MPa O.P. with expon. decay at 300 ms

TABLE 4.1

SUMMARY OF PEAK PORE AIR PRESSURE BELOW THE SURFACE OF SAND
DURING EXPOSURE TO A 100 PSI SHOCK IN AN 8-INCH SHOCK TUBE
[Zernow, et al (1973:74)]

GROUP	DESCRIPTION	POROSITY n^*	PERM B_1^{**}	AIRBLAST α^{***}	DEPTH x	PRESSURE P_{MAX}	TIME t_{MAX}
		---	CM ⁴ /DYNE SEC	SEC ⁻¹	FT	PSI	SEC
Ia	standard sand	1/3	1.7×10^{-2}	5.0	2.75	19.6	0.23
Ib	standard sand	1/3	1.7×10^{-2}	5.0	2.75	25.1	0.22
II	standard sand	1/3	1.7×10^{-2}	5.0	4.80	9.0	0.32
III	standard sand	1/3	1.7×10^{-2}	6.9	5.00	5.0	0.30
IVa	coarse sand	0.85/2.4	3.0×10^{-2}	5.0	2.75	14.9	0.20
IVb	coarse sand	0.85/2.4	3.0×10^{-2}	5.0	4.80	11.7	0.28

$$*n = 1 - \frac{\gamma_T}{\gamma_S}$$

**Values of B_1 reported by Zernow et al appear to have been B_1/n .

***Calculated from measured e-fold decay time, displayed in Zernow, Figure 23.

TABLE 4.2
CALCULATED LINEAR DIFFUSION PARAMETERS
FOR ZERNOW'S 8-INCH SHOCK TUBE VENTED SAMPLES*

GROUPS	B_1	n	D	T_D	α	β
	CM ⁴ /DYNE SEC		CM ² /SEC		SEC ⁻¹	
I,II	1.7×10^{-2}	1/3	3.51×10^5	10.79	5.0	0.463
III	1.7×10^{-2}	1/3	3.51×10^5	10.79	6.9	0.639
IV	3.0×10^{-2}	0.85/2.4	5.84×10^5	17.94	5.0	0.279

*Note:

$$D = \frac{B_1 P}{n} = \frac{6.89 \times 10^6 B_1}{n}$$

$$T_D = \frac{Dt_D}{l^2} = \frac{D(1.0)}{(180.34)^2}$$

$$\beta = \frac{l^2 \alpha}{D} = \frac{(180.34)^2 \alpha}{D}$$

TABLE 4.3

CALCULATED PEAK PORE AIR PRESSURE AND TIME
OF OCCURRENCE FOR ZEROW'S 8-INCH VENTED SAMPLES*

GROUP	D	β	x	ξ	P _{MAX}	T _{MAX}	t _{MAX}
	CM ² /SEC		IN		PSI		SEC
I	3.51X10 ⁵	0.463	33.0	0.465	46.1	0.35	0.032
II	3.51X10 ⁵	0.463	57.6	0.811	16.2	0.40	0.037
III	3.51X10 ⁵	0.639	60.0	0.845	12.3	0.37	0.034
IVa	5.84X10 ⁵	0.279	33.0	0.465	48.1	0.39	0.022
IVb	5.84X10 ⁵	0.279	57.6	0.811	16.9	0.43	0.024

*Note:

$$\xi = \frac{x}{l} = \frac{x}{71}$$

$$t_{MAX} = \frac{l^2 T_{MAX}}{D} = \frac{(180.34)^2 T_{MAX}}{D}$$

TABLE 4.4

ADJUSTED LINEAR DIFFUSION PARAMETERS FOR
ZERNOW'S 8-INCH SHOCK TUBE VENTED SAMPLES*

GROUPS	B_1	n	D	τ_D	α	β
	CM ⁴ /DYNE SEC		CM ² /SEC		SEC ⁻¹	
I, II	3.4×10^{-3}	1/3	7.03×10^4	2.16	5.0	2.31
III	3.4×10^{-3}	1/3	7.03×10^4	2.16	6.9	3.19
IV	6.0×10^{-3}	0.85/2.4	1.17×10^5	3.59	5.0	1.39

*Note:

$$D = \frac{B_1 P}{n} = \frac{6.89 \times 10^6 B_1}{n}$$

$$\tau_D = \frac{Dt_D}{l^2} = \frac{D(1.0)}{(180.34)^2}$$

$$\beta = \frac{l^2 \alpha}{D} = \frac{(180.34)^2 \alpha}{D}$$

TABLE 4.5

CALCULATED PEAK PORE AIR PRESSURE AND TIME
OF OCCURRENCE FOR ZERNOW'S 8-INCH VENTED SAMPLES,
USING ADJUSTED LINEAR DIFFUSION PARAMETERS*

GROUP	D	β	x	ξ	P _{MAX}	T _{MAX}	t _{MAX}
	CM ² /SEC		IN		PSI		SEC
I	7.03X10 ⁴	2.31	33.0	0.465	34.4	0.21	0.097
II	7.03X10 ⁴	2.31	57.6	0.811	12.0	0.26	0.120
III	7.03X10 ⁴	3.19	60.0	0.845	8.9	0.24	0.111
IVa	1.17X10 ⁵	1.39	33.0	0.465	38.9	0.25	0.069
IVb	1.17X10 ⁵	1.39	57.6	0.811	13.6	0.30	0.083

*Note:

$$\xi = \frac{x}{l} = \frac{x}{71}$$

$$t_{MAX} = \frac{l^2 T_{MAX}}{D} = \frac{(180.34)^2 T_{MAX}}{D}$$

TABLE 4.6
ADJUSTED LINEAR DIFFUSION PARAMETERS FOR
8-INCH SHOCK TUBE UNVENTED SAMPLES*

GROUPS	B ₁	n	D	T _D	α	β
	CM ⁴ /DYNE SEC		CM ² /SEC		SEC ⁻¹	
I,II	3.4X10 ⁻³	1/3	7.03X10 ⁴	0.540	5.0	9.25
III	3.4X10 ⁻³	1/3	7.03X10 ⁴	0.540	6.9	12.77
IV	6.0X10 ⁻³	0.85/2.4	1.17X10 ⁵	0.897	5.0	5.56

*Note:

$$D = \frac{B_1 P}{n} = \frac{6.89 \times 10^6 B_1}{n}$$

$$T_D = \frac{Dt_D}{4l^2} = \frac{D(1.0)}{(360.68)^2}$$

$$\beta = \frac{4l^2 \alpha}{D} = \frac{(360.68)^2 \alpha}{D}$$

TABLE 4.7

CALCULATED PEAK PORE AIR PRESSURE AND TIME
OF OCCURRENCE FOR 8-INCH UNVENTED SAMPLES,
USING ADJUSTED LINEAR DIFFUSION PARAMETERS*

GROUP	D	β	x	ξ	P _{MAX}	T _{MAX}	t _{MAX}
	CM ² /SEC		IN		PSI		SEC
I	7.03X10 ⁴	9.25	33.0	0.232	70.9	0.010	0.019
II	7.03X10 ⁴	9.25	57.6	0.406	44.2	0.050	0.093
III	7.03X10 ⁴	12.77	60.0	0.423	38.8	0.045	0.083
IVa	1.17X10 ⁵	5.56	33.0	0.232	73.4	0.010	0.011
IVb	1.17X10 ⁵	5.56	57.6	0.406	51.5	0.085	0.095

*Note:

$$\xi = \frac{x}{2T} = \frac{x}{142}$$

$$t_{MAX} = \frac{41^2 T_{MAX}}{D} = \frac{(360.68)^2 T_{MAX}}{D}$$

TABLE 5.1

Scaled Airblast Parameters, Large Yield
Pacific Nuclear Data (10kt - 10mt)

Scaled Range \bar{R} , km/(kt) ^{1/3}	Peak Positive Overpressure ΔP^+ , kPa	Peak Negative Overpressure ΔP^- , kPa
0.134	345	27.6
0.151	297	15.2
0.194	159	13.8
0.244	94.5	12.4
0.933	10.0	1.86
0.956	10.1	0.90
0.977	10.3	2.74
2.948	2.21	0.66
2.996	1.65	0.56
4.060	1.17	0.44
0.048	1131	101?
0.207	175	21.9
0.244	130	13.8
0.394	48.3	9.03
0.580	24.4	4.34
2.063	2.62	0.90
2.063	3.10	1.17
0.205	121	14.4
0.281	77.2	11.6
0.381	60.8	9.10
0.221	128	14.8
0.298	85.2	8.62
0.662	18.7	4.00
1.042	9.30	2.17
1.590	3.83	0.97

TABLE 6.1

EXPERIMENTAL SPALL DATA FROM NEAR-SURFACE DETONATIONS

Event	Charge* Configuration	Yield (tons)	Charge	Test Medium	D _{wt} (m)	D _{br} (m)	R _s (m)	z _s (m)
DISTANT PLAIN 6	STS	100	TNT	silty clay and sand layers	7.6	>60	>49	>5
PRAIRIE FLAT	STS	500	TNT	silty clay and sand layers	7.6	>60	>43	>5
DIAL PACK	STS	500	TNT	silty clay and sand layers	7.6	>60	>130	>6
FLAT TOP II	HBS	20	TNT	desert playa - layers of dry silt, clay and sand	>150	>150	>20 [38]*	>0.5
FLAT TOP III	HBS	20	TNT	desert playa - layers of dry silt, clay and sand	>150	>150	>20 [35]	>5
MIXED COMPANY III	STS	500	TNT	sandy-clayey silt over sandstone	>150	2.5	125 [121]	>9 [12]
PRE-MINE THROW IV-1	STS	0.52	Nitro- methane	desert playa - layers of dry silt, clay and sand	>150	>150	[25]	only shallow data
PRE-MINE THROW IV-2	STS	0.50	TNT	desert playa - layers of dry silt, clay and sand	>150	>150	[25]	
PRE-MINE THROW IV-3	STS	7.25	NM	desert playa - layers of dry silt, clay and sand	>150	>150	[61]	
PRE-MINE THROW IV-4	STS	0.52	NM	desert playa - layers of dry silt, clay and sand	>150	>150	[25]	
PRE-MINE THROW IV-5	HBS	0.50	TNT	desert playa - layers of dry silt, clay and sand	>150	>150	[25]	
PRE-MINE THROW IV-6	STS	102.4	NM	desert playa - layers of dry silt, clay and sand	>150	>150	[147]	only shallow data
PRE-MINE THROW IV-7	HBS	0.13	TNT	desert playa - layers of dry silt, clay and sand	>150	>150	[16]	
PRE-DICE THROW II-1	STS	100	TNT	clayey silt and sand	2.1	>150	40	2
PRE-DICE THROW II-2	STC	120	ANFO	clayey silt and sand	2.1	>150	95	2
MIDDLE GUST 1	HBS	20	TNT	wet clay over shale	1.2	3.0	61	>6.1

TABLE 6.1
(Continued)

EXPERIMENTAL SPALL DATA FROM NEAR-SURFACE DETONATIONS

Event	Charge Configuration	Yield (tons)	Charge	Test Medium	D _{wt} (m)	D _{br} (m)	R _s (m)	z _s (m)
MIDDLE GUST 2	4.8m HOB sphere	100	TNT	wet clay over shale	1.2	3.0	37	>6.1
MIDDLE GUST 3	STS	100	TNT	wet clay over shale	1.2	3.0	61	>6.1
MIDDLE GUST 4	STS	100	TNT	dry clay over shale	>150	8.5	7	?
MIDDLE GUST 5	HBS	20	TNT	dry clay over shale	>150	8.5	52	12.2
PHG I-06	Berm	0.042	C-4	layers of dry silt, sand and caliche	90	>150	10.5	2.3
PHG I-07	STS	0.128	TNT	layers of dry silt, sand and caliche	90	>150	18	2.8
PHG I-09	STS	0.128	TNT	layers of dry silt, sand and caliche	90	>150	15	2.4
MISERS BLUFF II-1	STC	120	ANFO	fine silt overlying gravelly sand	10.7	30.5	>200	4.0
PRE-MULTIPLE BURST 1	HBS	0.13	TNT	layers of dry silt, sand and caliche	90	>150	16	>.23
PRE-MULTIPLE BURST 2	STS	0.13	TNT	layers of dry silt, sand and caliche	90	>150	22	>1
PRE-MULTIPLE BURST 5	HOB sphere	0.13	TNT	layers of dry silt, sand and caliche	90	>150	18	>.23
MINERAL ROCK	STS	100	TNT	granite	>150	0	NS	NS
MINE ORE	STS	100	TNT	granite	>150	0	NS	NS
MINE UNDER	HOB	100	TNT	granite	>150	0	NS	NS
JANGLE U	DDB (5.18 m)	1200	Nuclear	fine sand mixed with gravel	>150	>150	110	>6.1

*STS = surface tangent sphere
HBS = half buried sphere
STC = surface tangent cylinder with hemispherical cap
HOB = height of burst
DDB = depth of burst

**D_{wt} = depth to water table
***D_{br} = depth to bedrock
****R_s at z = 0.5 m
[] was estimated from spall impact velocity data

TABLE 6.2

Maximum Scaled Radius of Spall, \bar{R}_s ,
for Various Explosive Charge Configurations

Charge	Configuration	\bar{R}_s (m/100 ton ^{1/3}) with Negative Airblast Wing	\bar{R}_s (m/100 ton ^{1/3}) without Negative Airblast Wing
TNT	HOB	No Data	32
TNT	STS	125-200	40- 80
TNT	STC or HBS	140-200	90-105
TNT	Berm	N/A	140
Nuclear	DOB	N/A	48

FIGURES

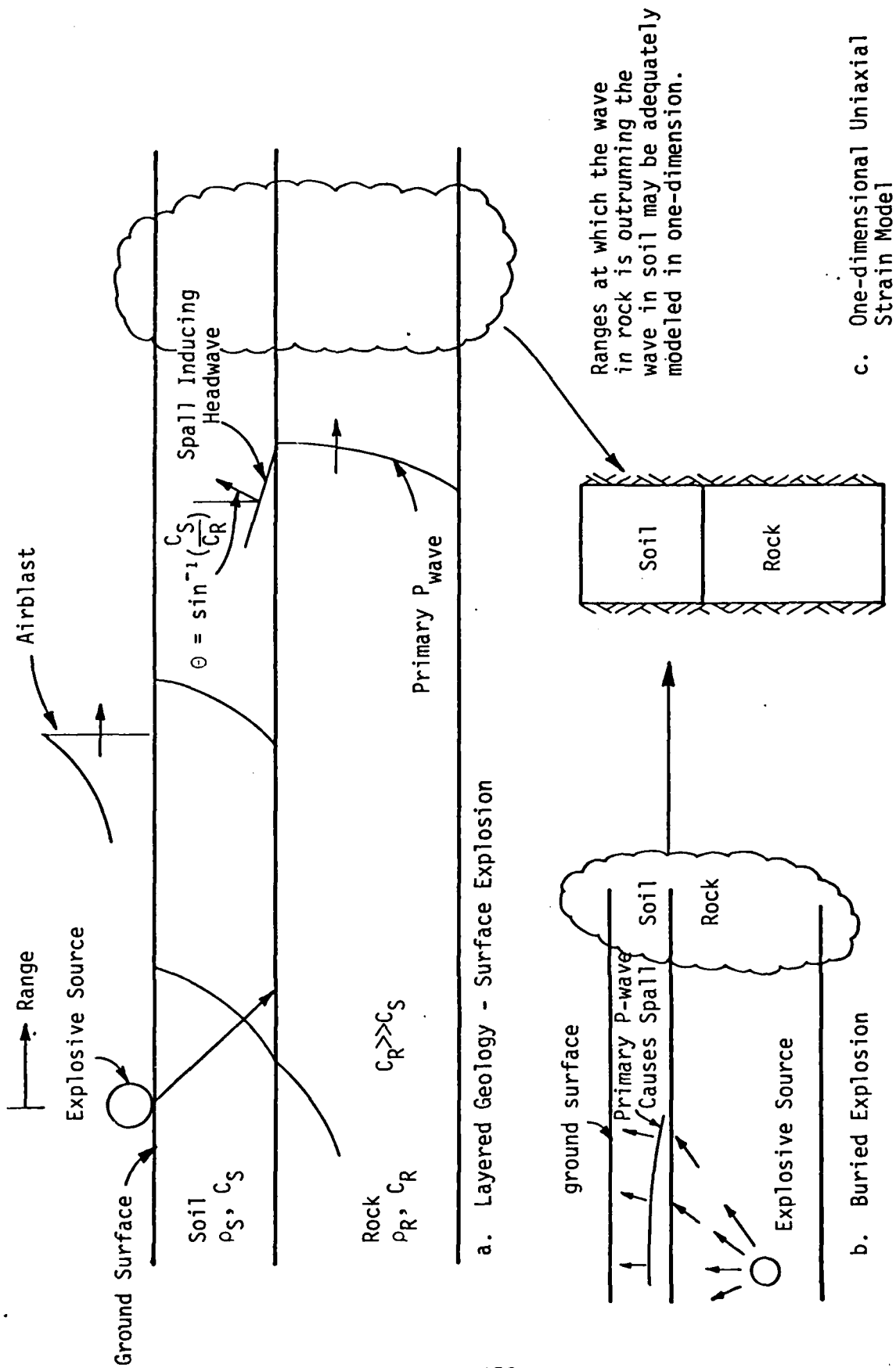


Fig. 3.1. One-Dimensional Analysis of Explosive Spall Problems

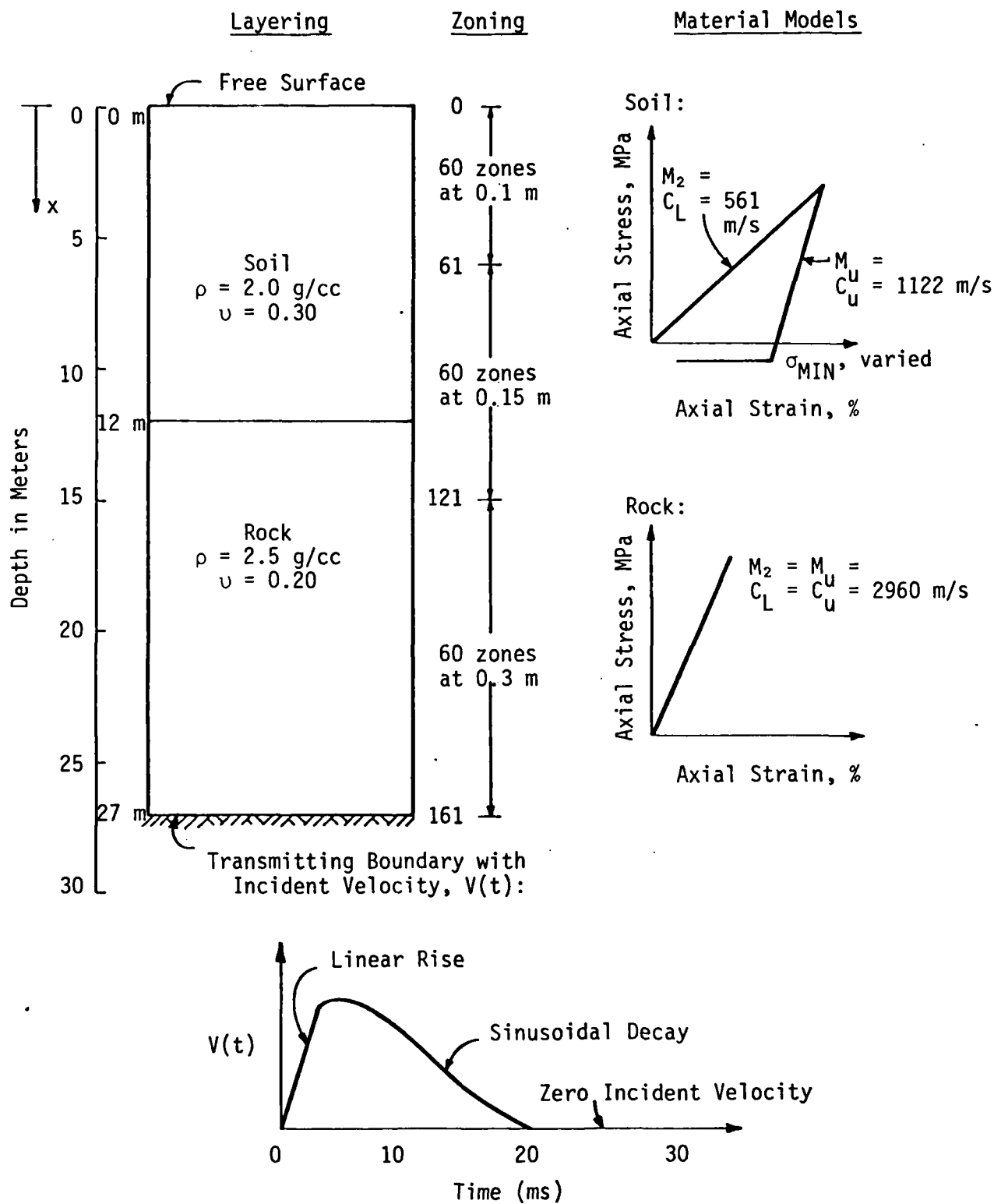


Fig. 3.2. One Dimensional (Uniaxial Strain) Spall Calculations

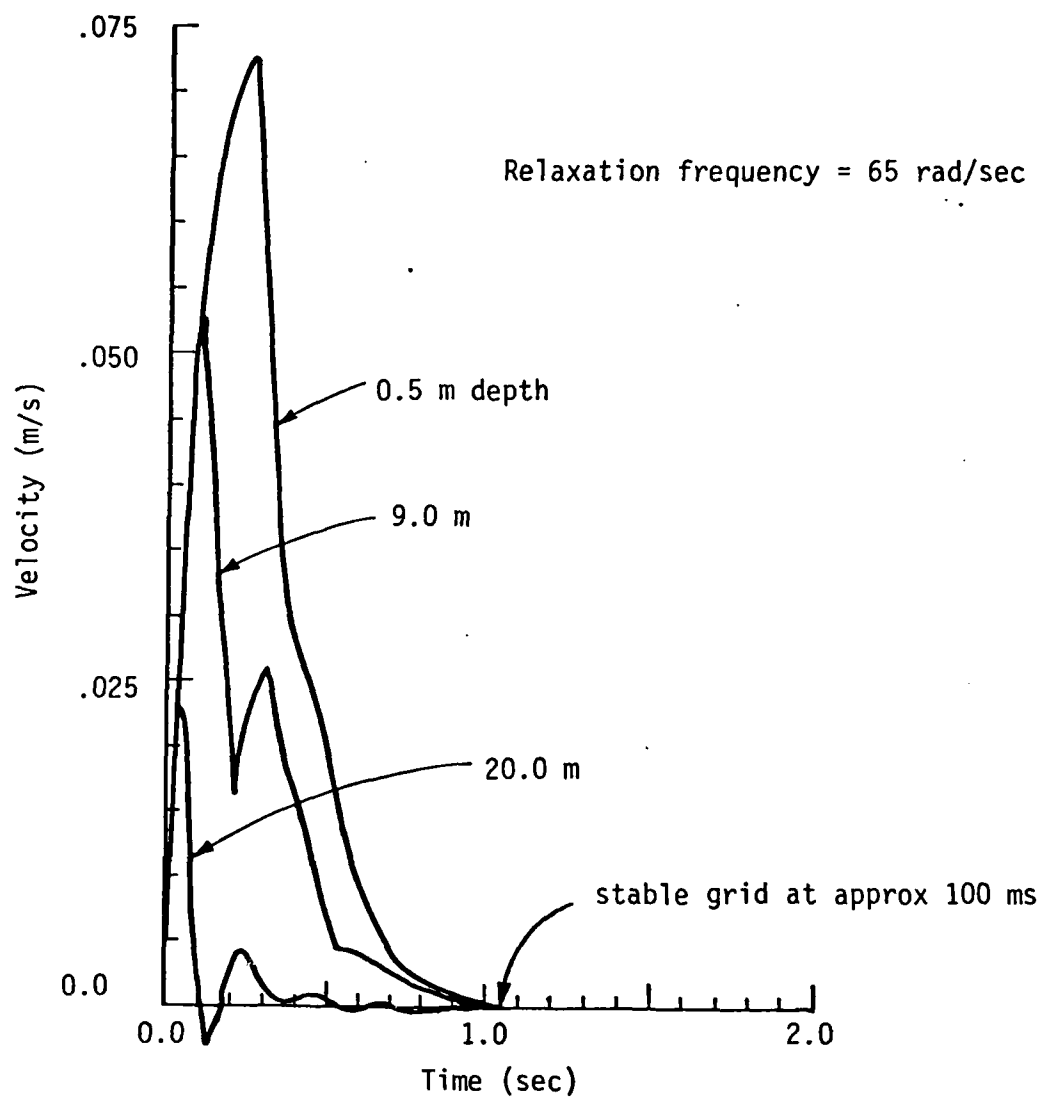


Fig. 3.3. Application of Gravity to Grid with Dynamic Relaxation

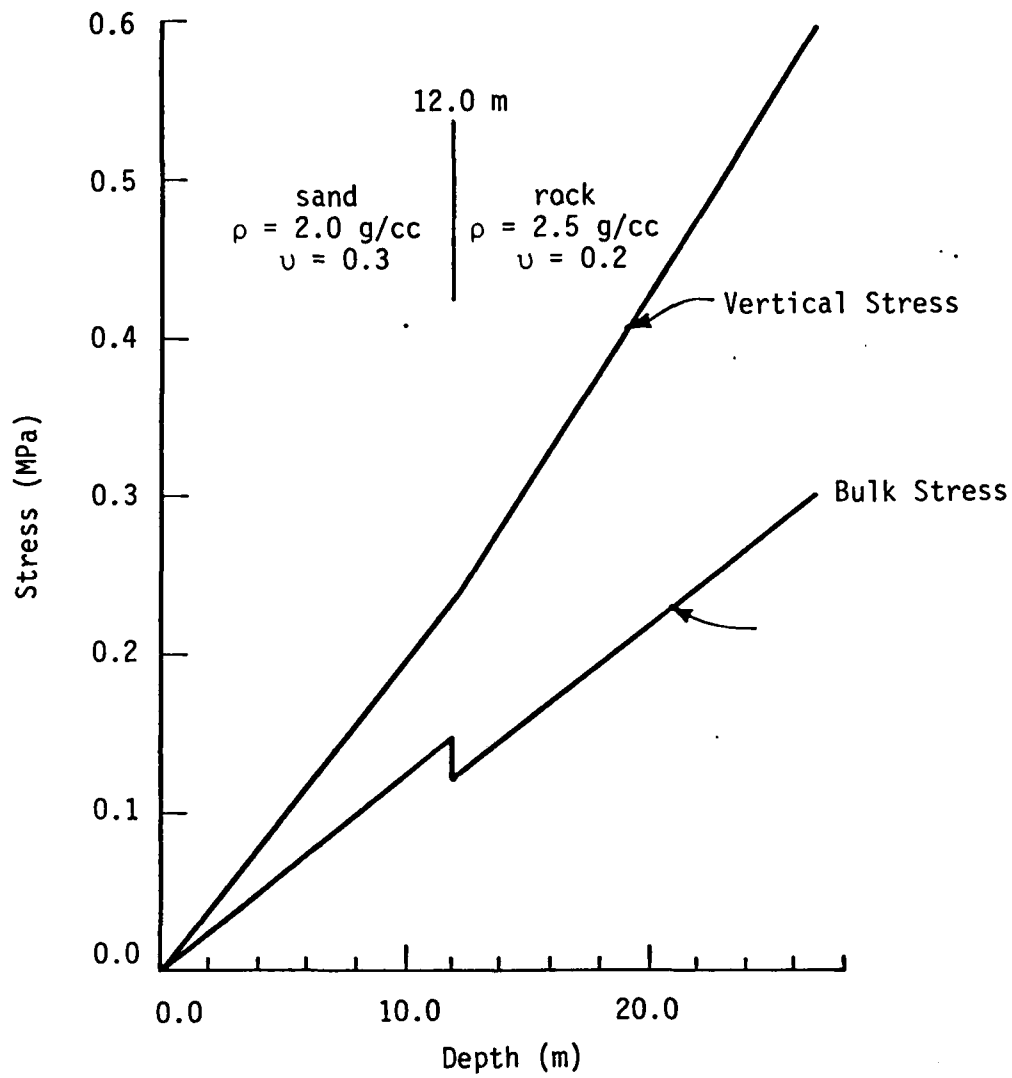
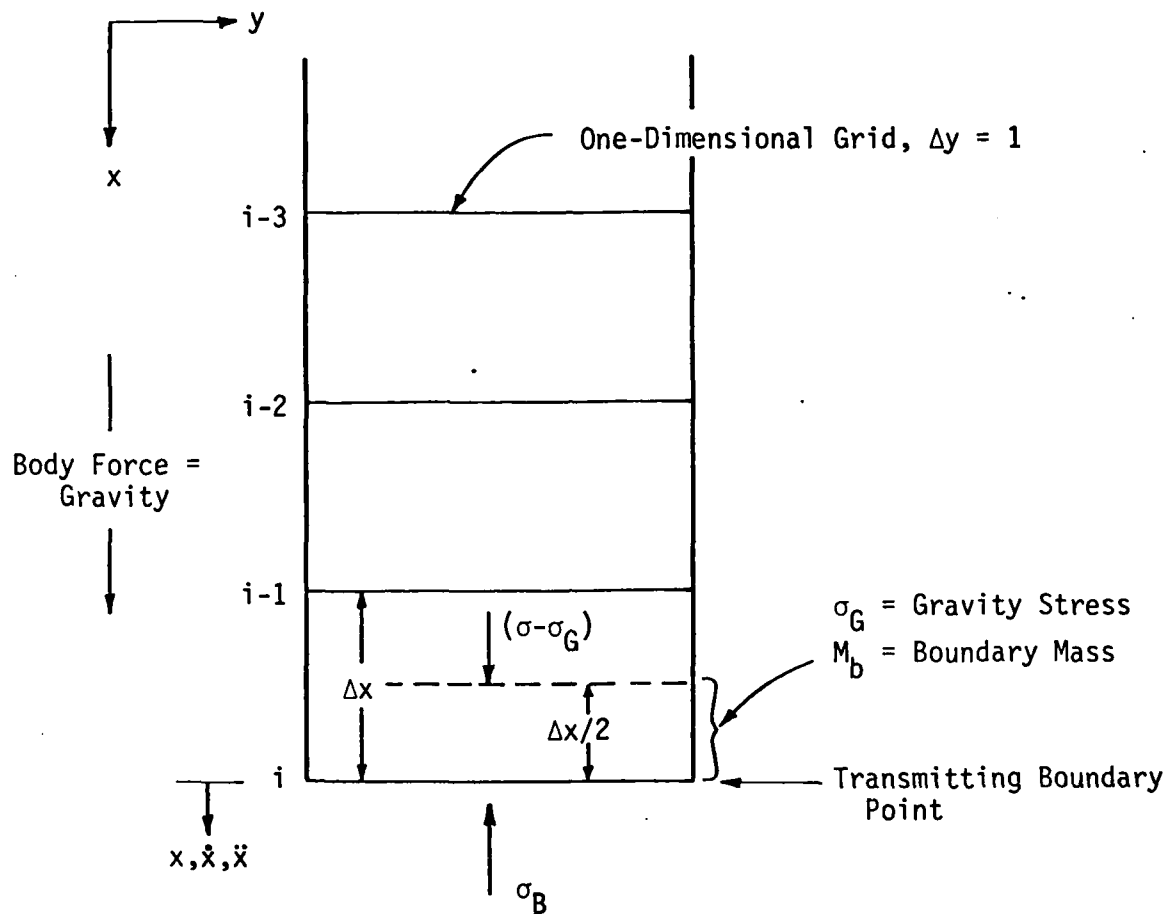


Fig. 3.4. In Situ (Gravity) Stress and Pressure Distribution



New Time = t^n
 Old Time = t^1
 Current Time = $(t^n + t^1)/2$
 Timestep = $\Delta t = t^n - t^1$

Note: Assuming small strains

Fig. 3.5. Transmitting Boundary with Incident Velocity

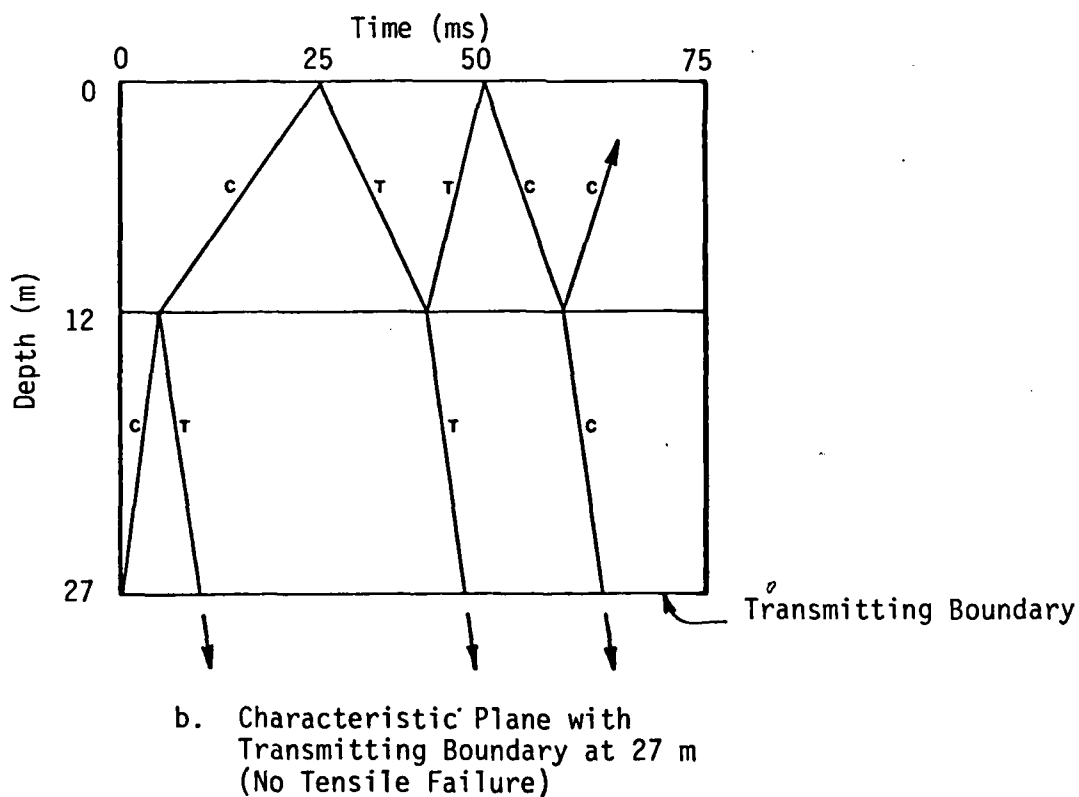
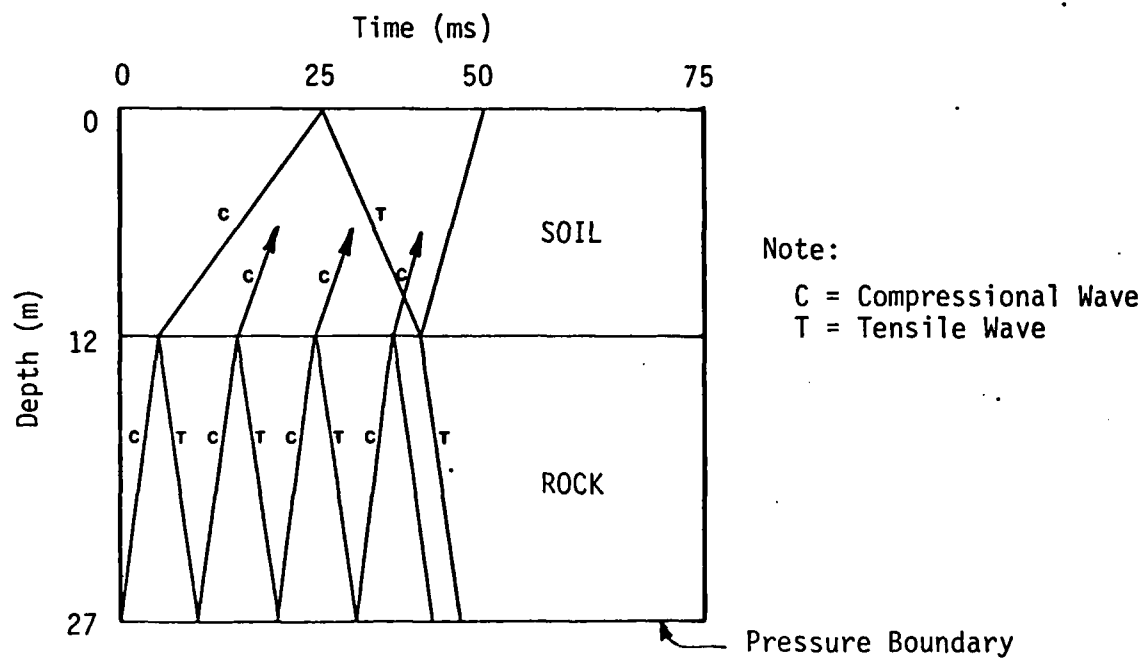
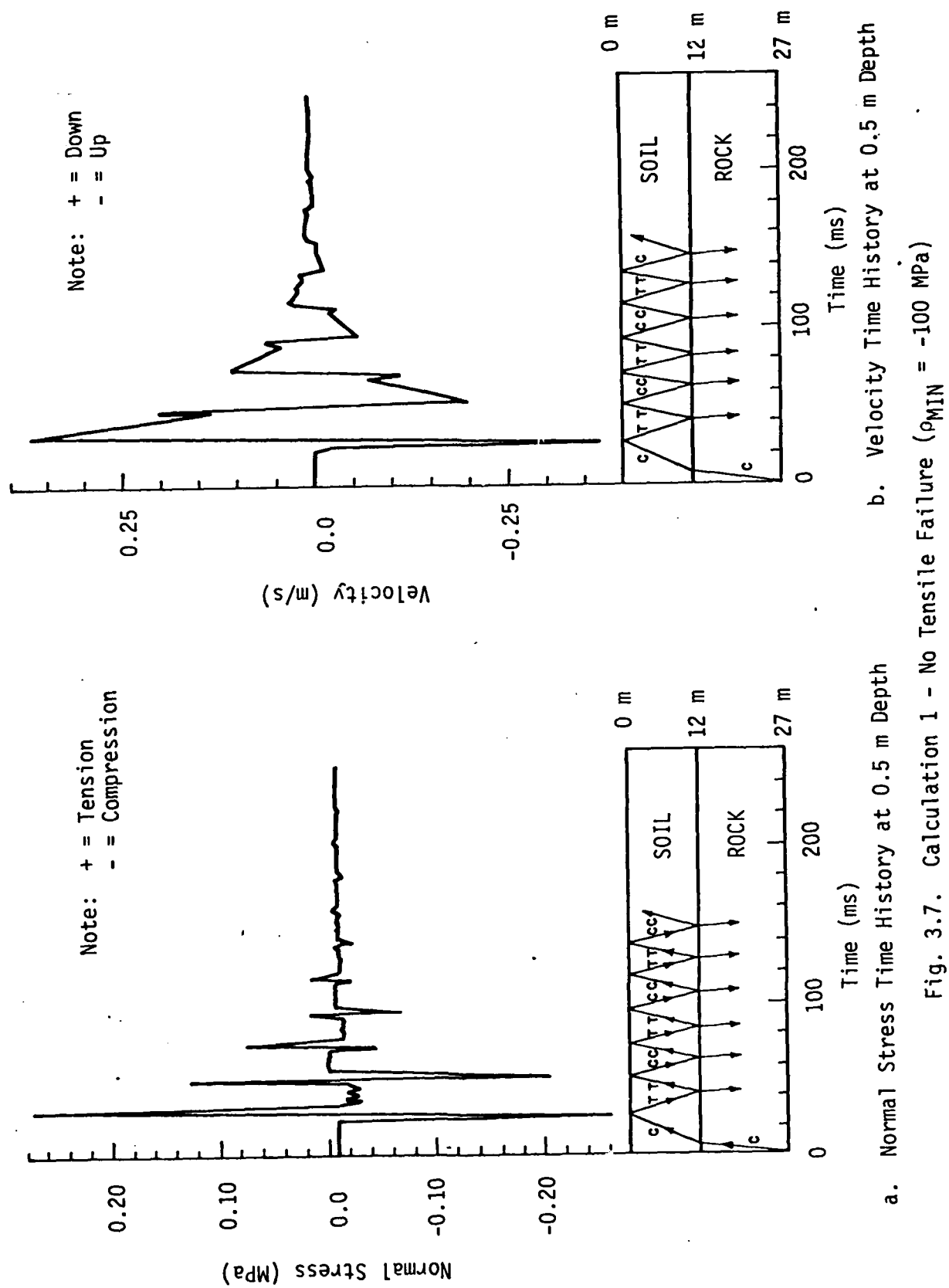
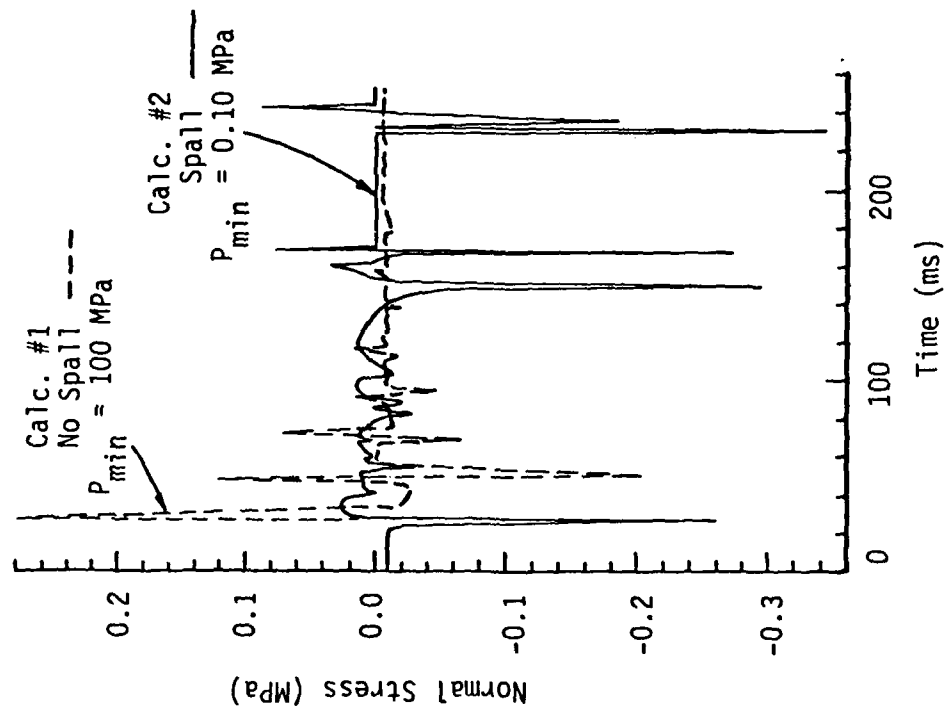


Fig. 3.6. Characteristic Planes for Two Boundary Conditions





a. Normal Stress

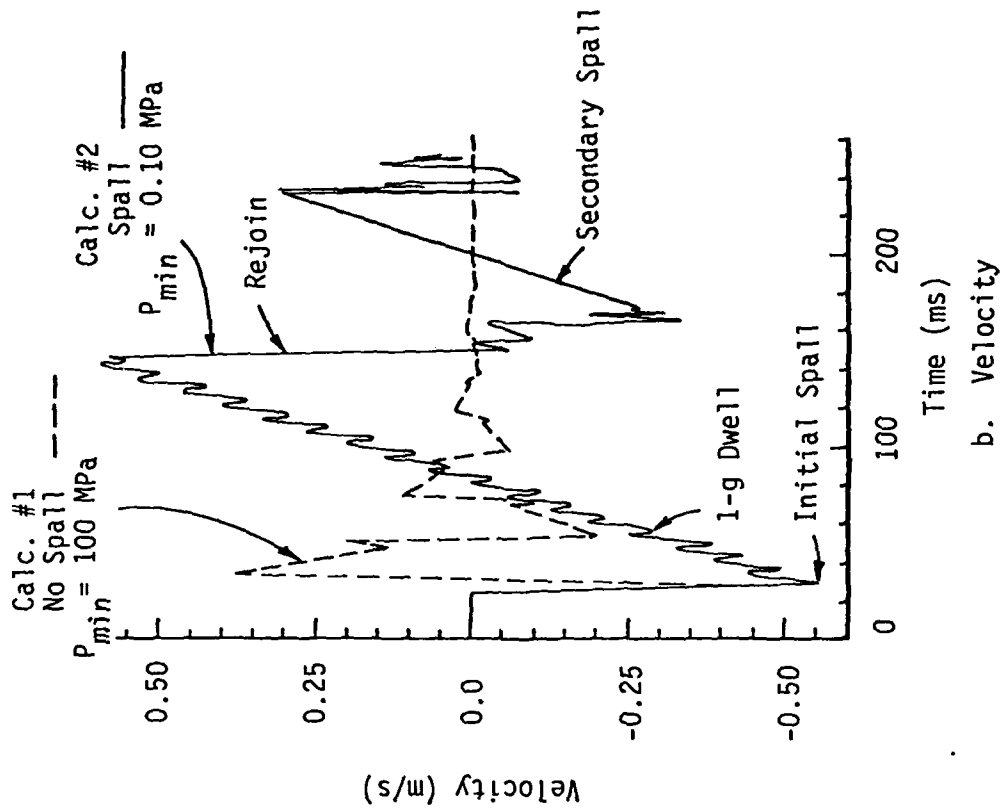


Fig. 3.8. Spall and No Spall Time History Comparisons at Depth = 0.5 m

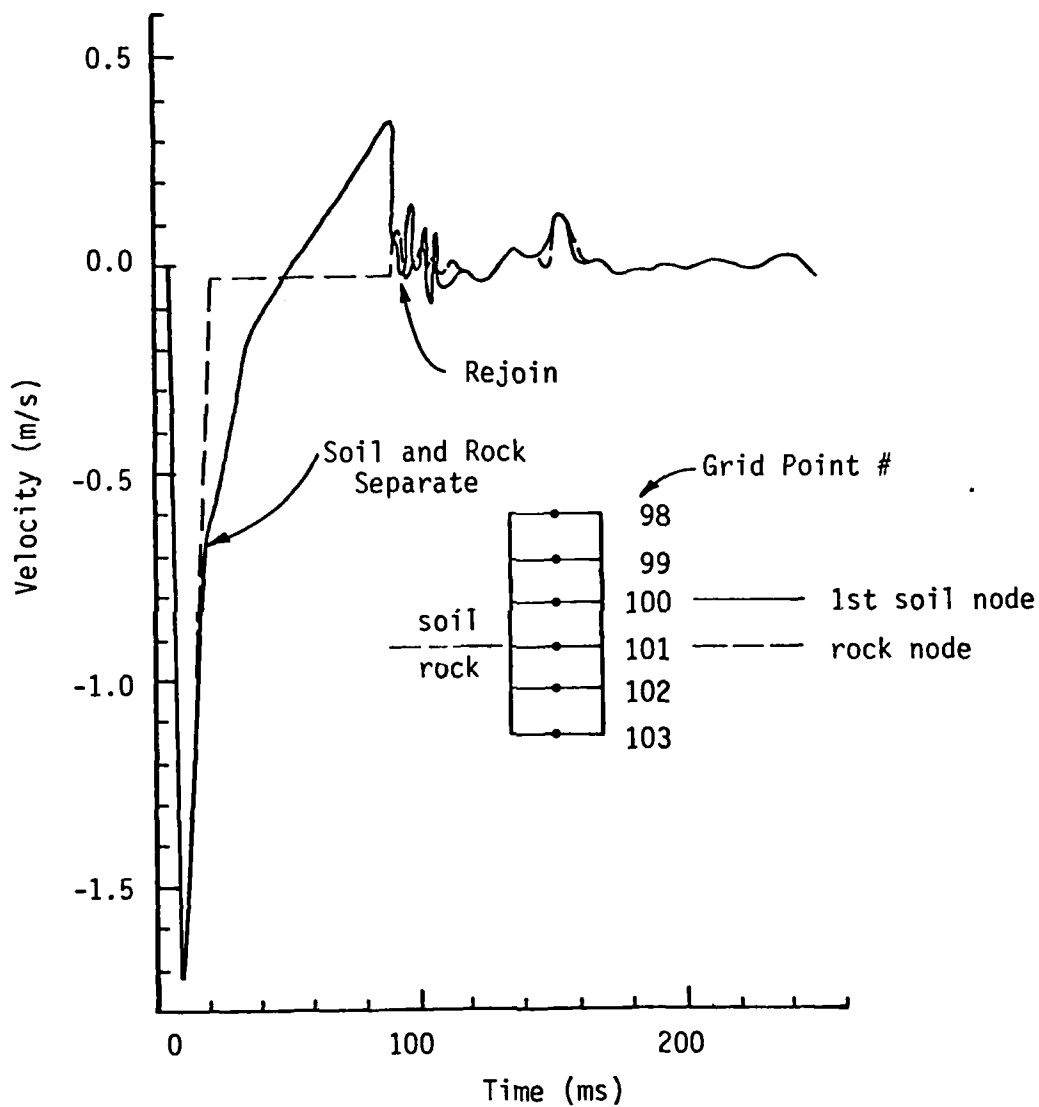


Fig. 3.9. Soil-Rock Boundary Behavior

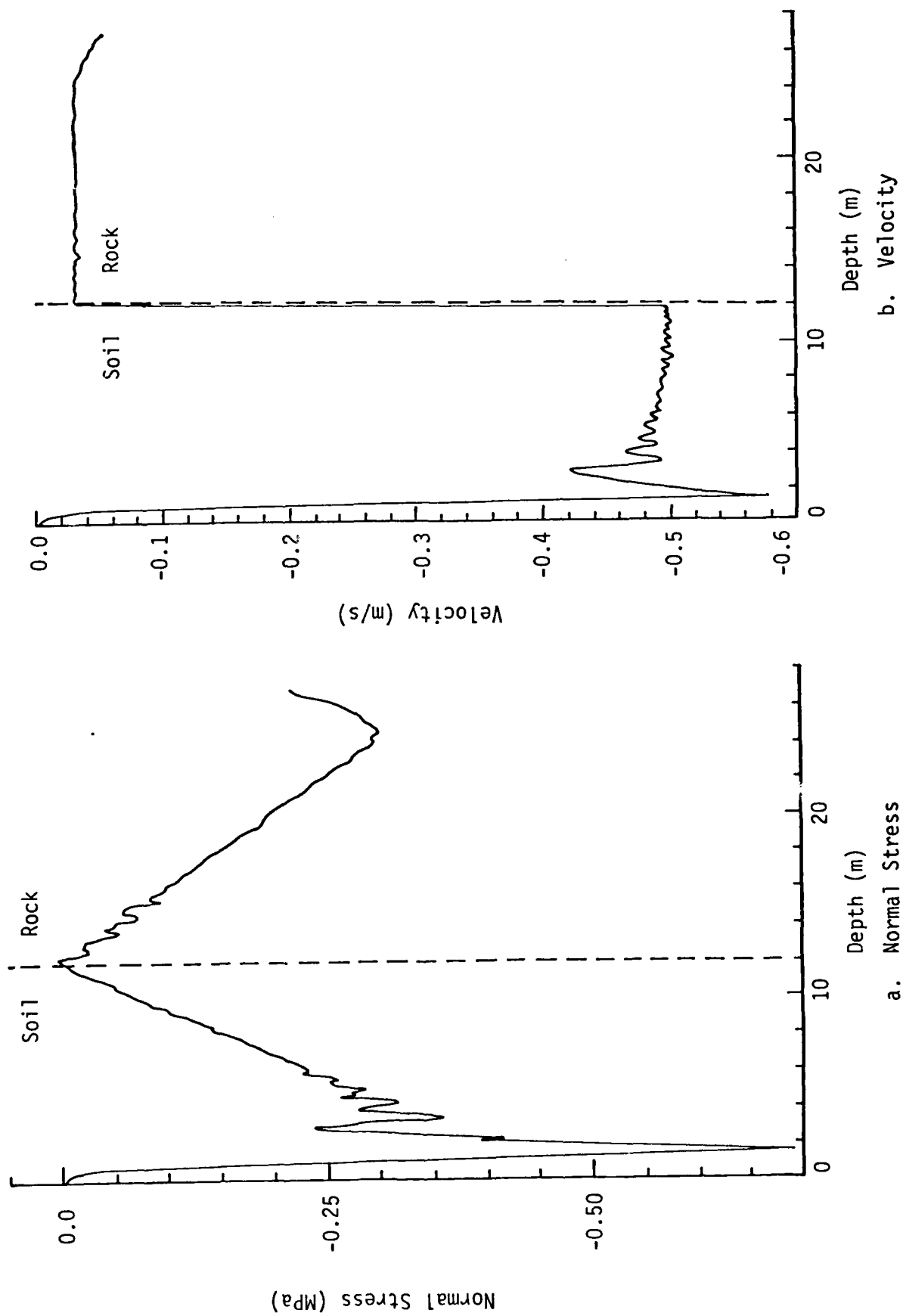
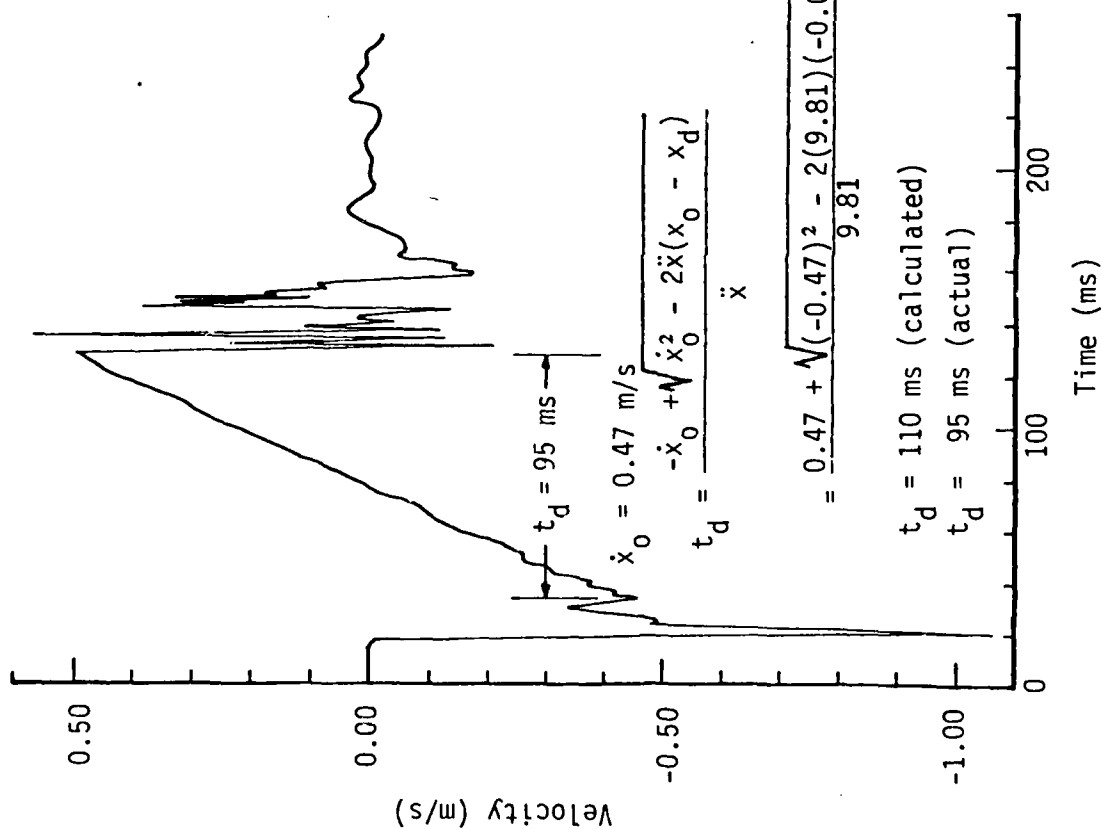
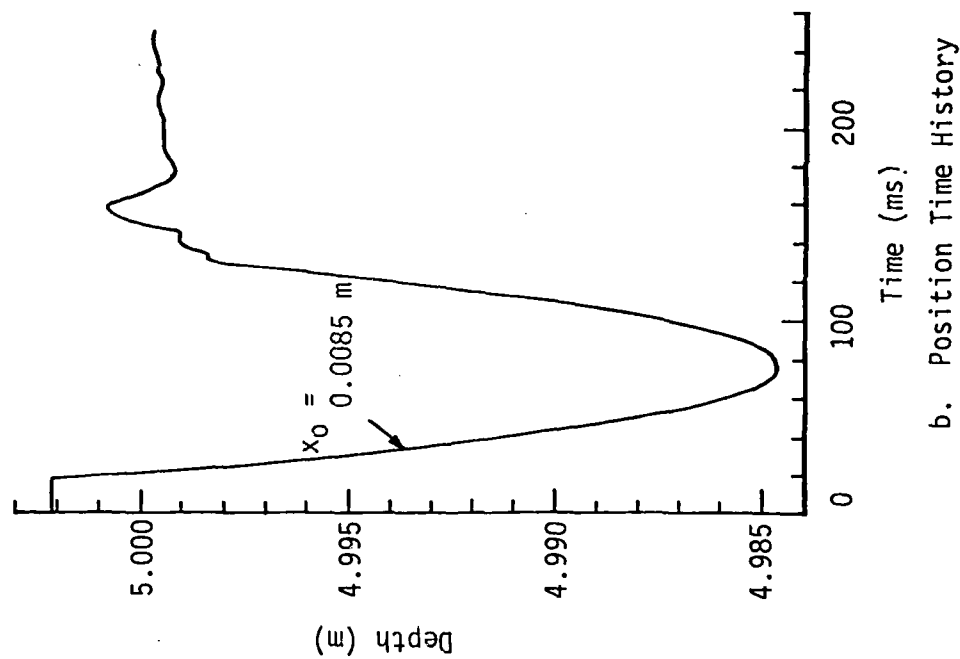


Fig. 3.10. Grid Snapshots of Incident Compressional Pulse at Time = 25 ms

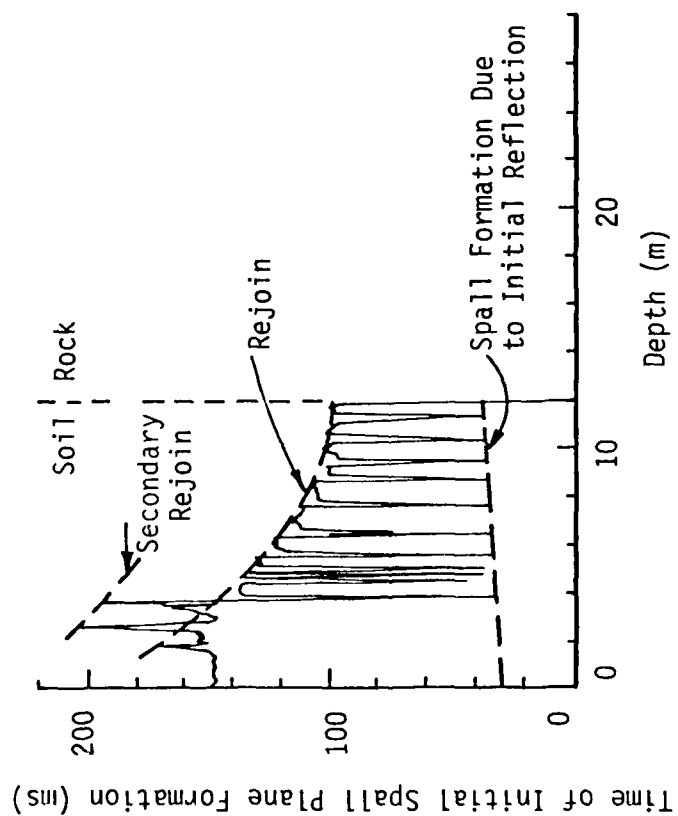


a. Velocity Time History

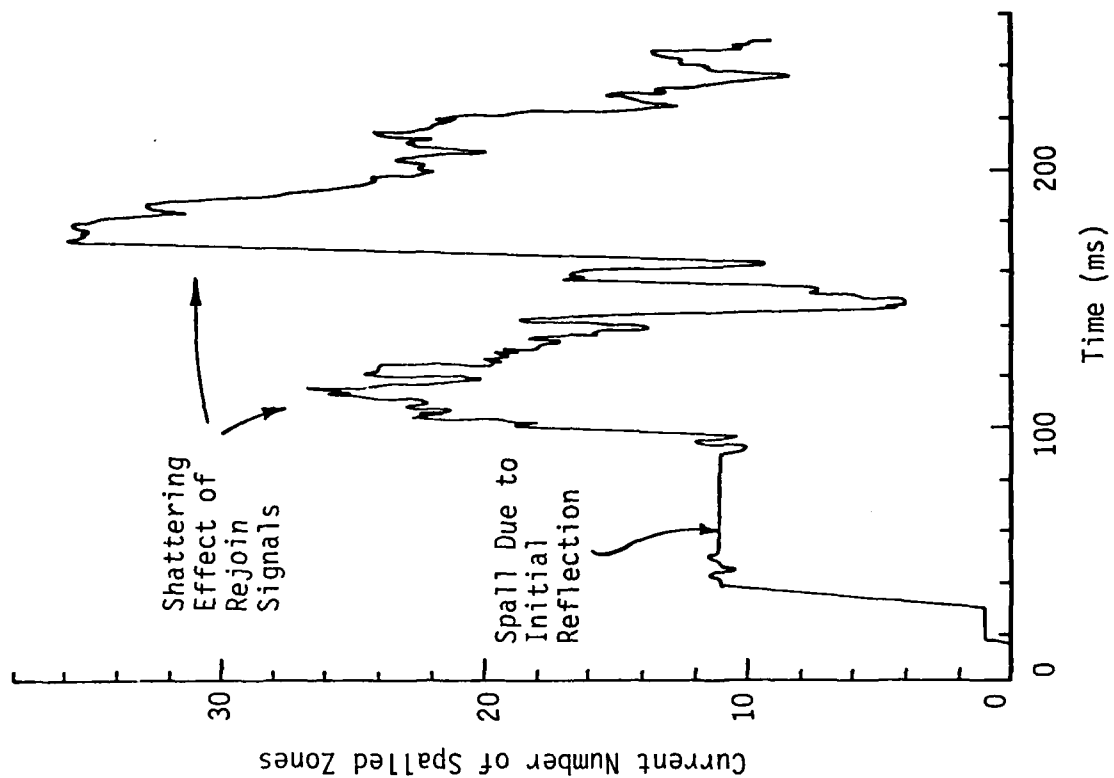


b. Position Time History

Fig. 3.11. Calculated Dwell Time for Depth = 5 m



a. Time At Which Spall First Occurs at a Particular Depth



b. Number of Spalled Zones at Any Given Time

Fig. 3.12. Spall Plane Formation

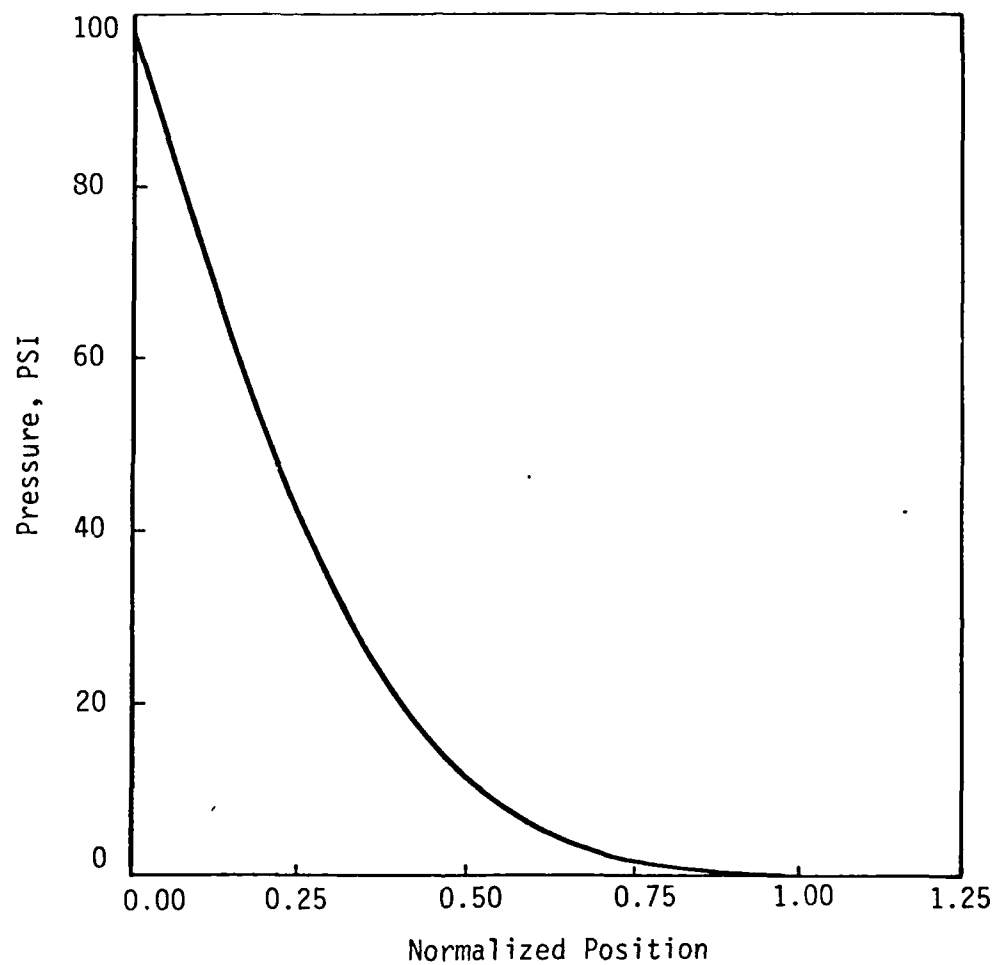


FIGURE 4.1a
Dynamic Pore Pressure Isochrone for a
Vented Sample; $\beta = 0.463$, $T = 0.05$

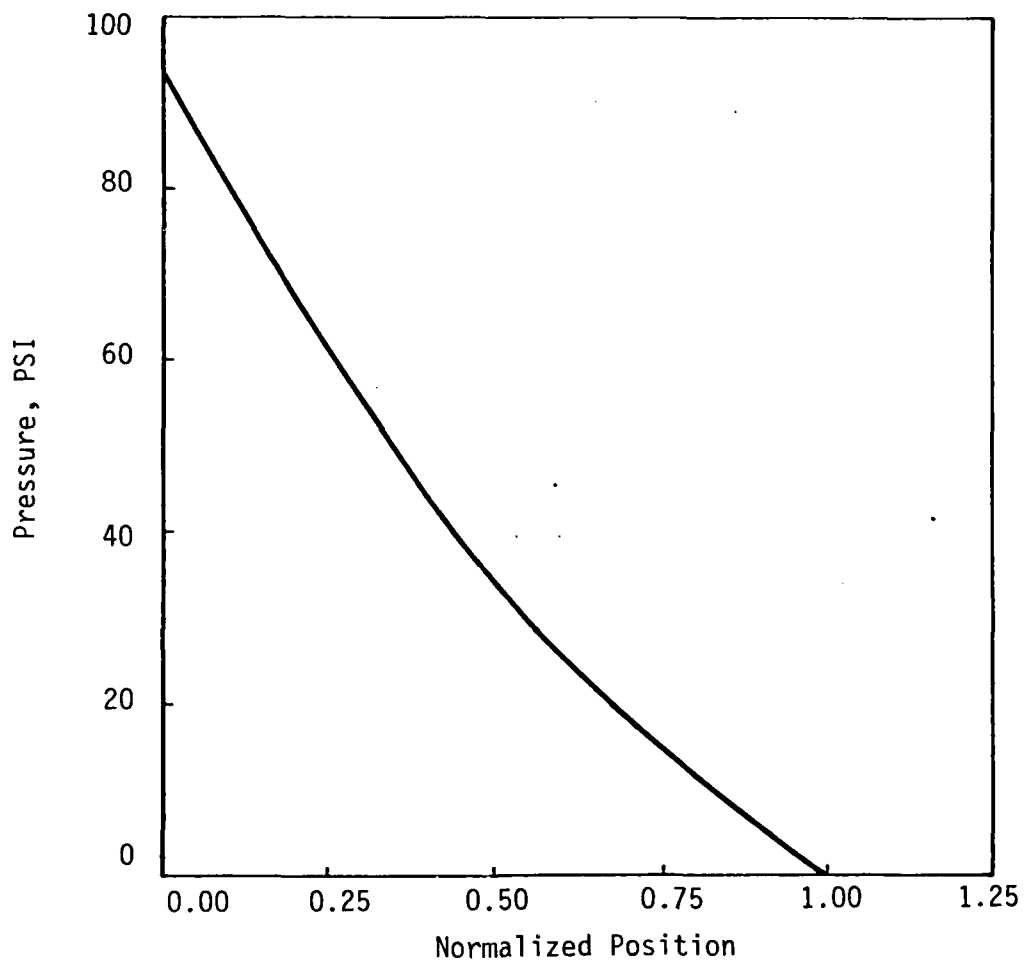


FIGURE 4.1b
Dynamic Pore Pressure Isochrone for a
Vented Sample; $\beta = 0.463$, $T = 0.15$

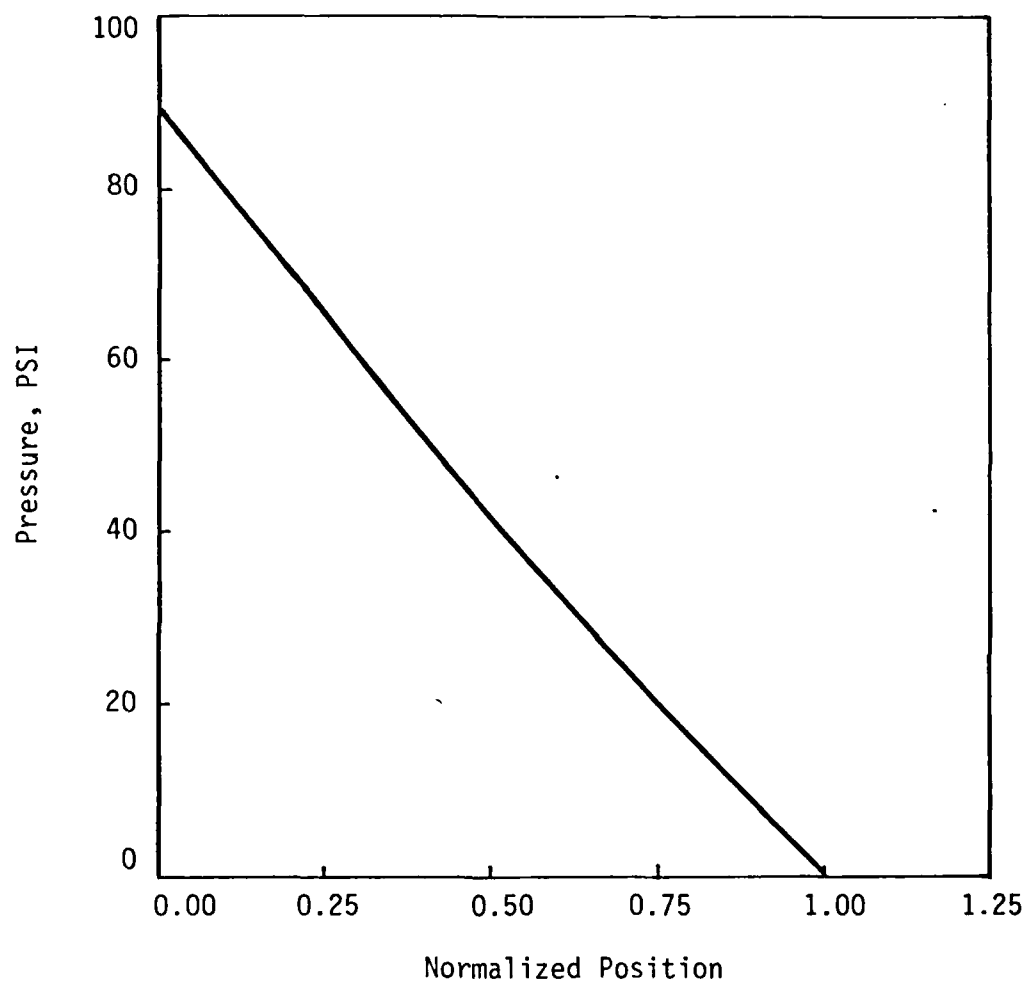


FIGURE 4.1c
Dynamic Pore Pressure Isochrone for a
Vented Sample; $\beta = 0.463$, $T = 0.25$

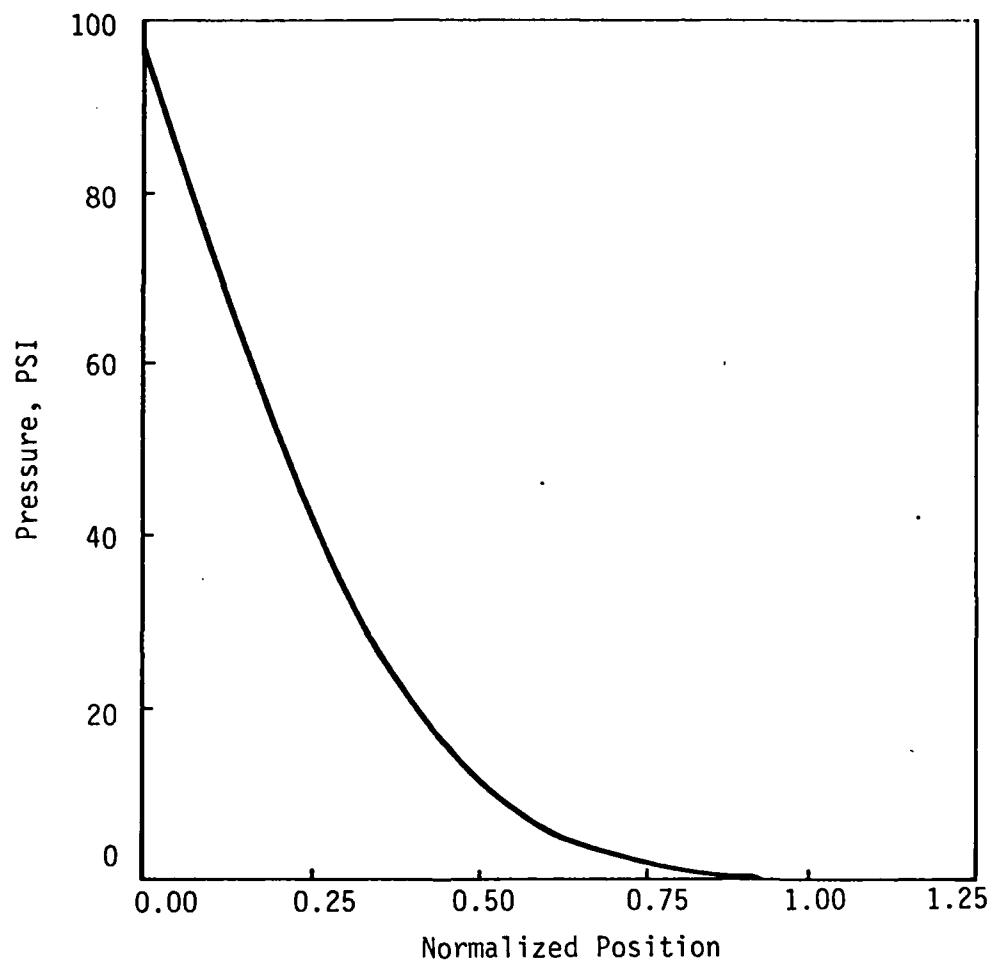


FIGURE 4.2a
Dynamic Pore Pressure Isochrone for a
Vented Sample; $\beta = 0.639$, $T = 0.05$

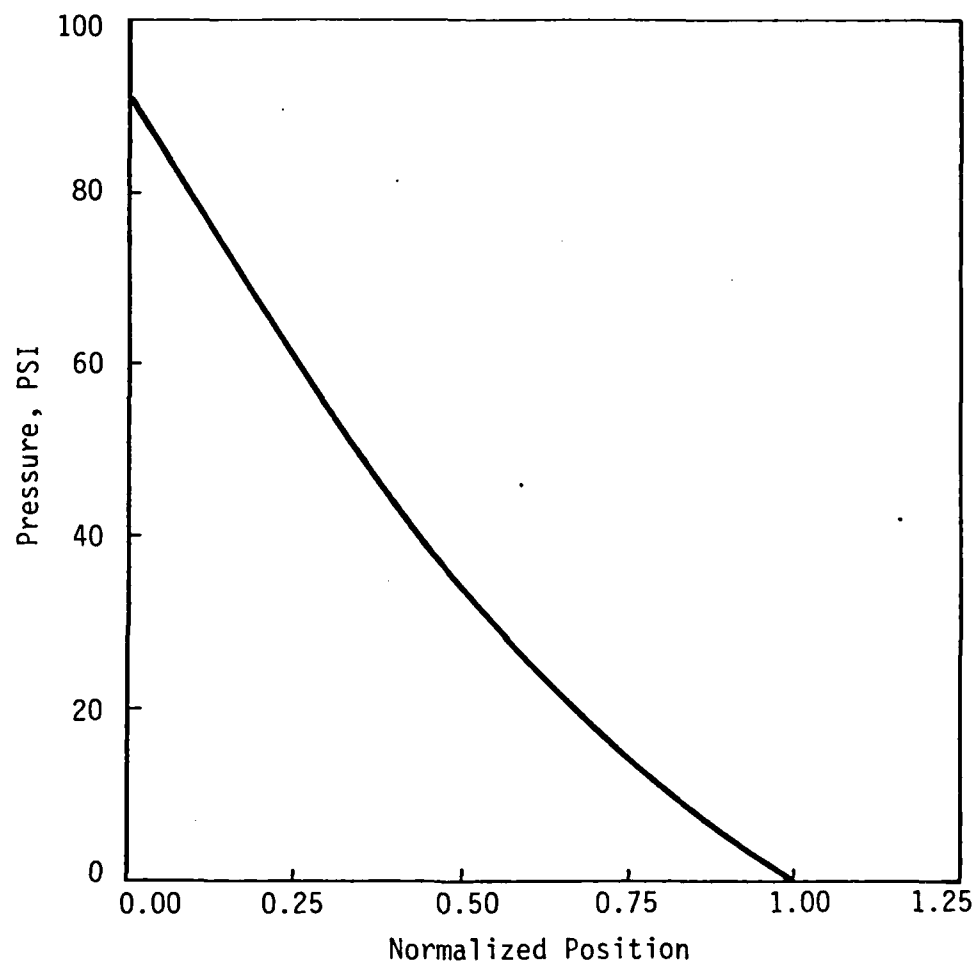


FIGURE 4.2b
Dynamic Pore Pressure Isochrone for a
Vented Sample; $\beta = 0.639$, $T = 0.15$

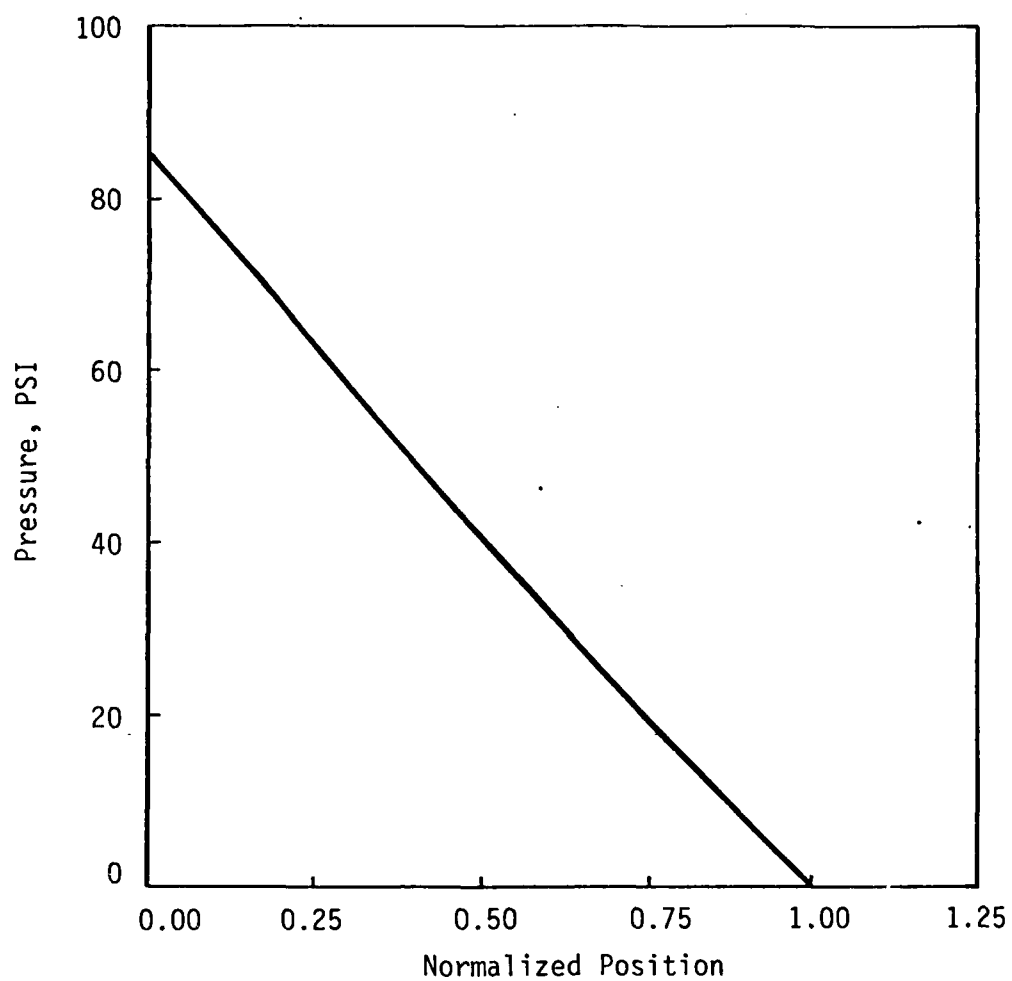


FIGURE 4.2c
Dynamic Pore Pressure Isochrone for a
Vented Sample; $\beta = 0.639$, $T = 0.25$

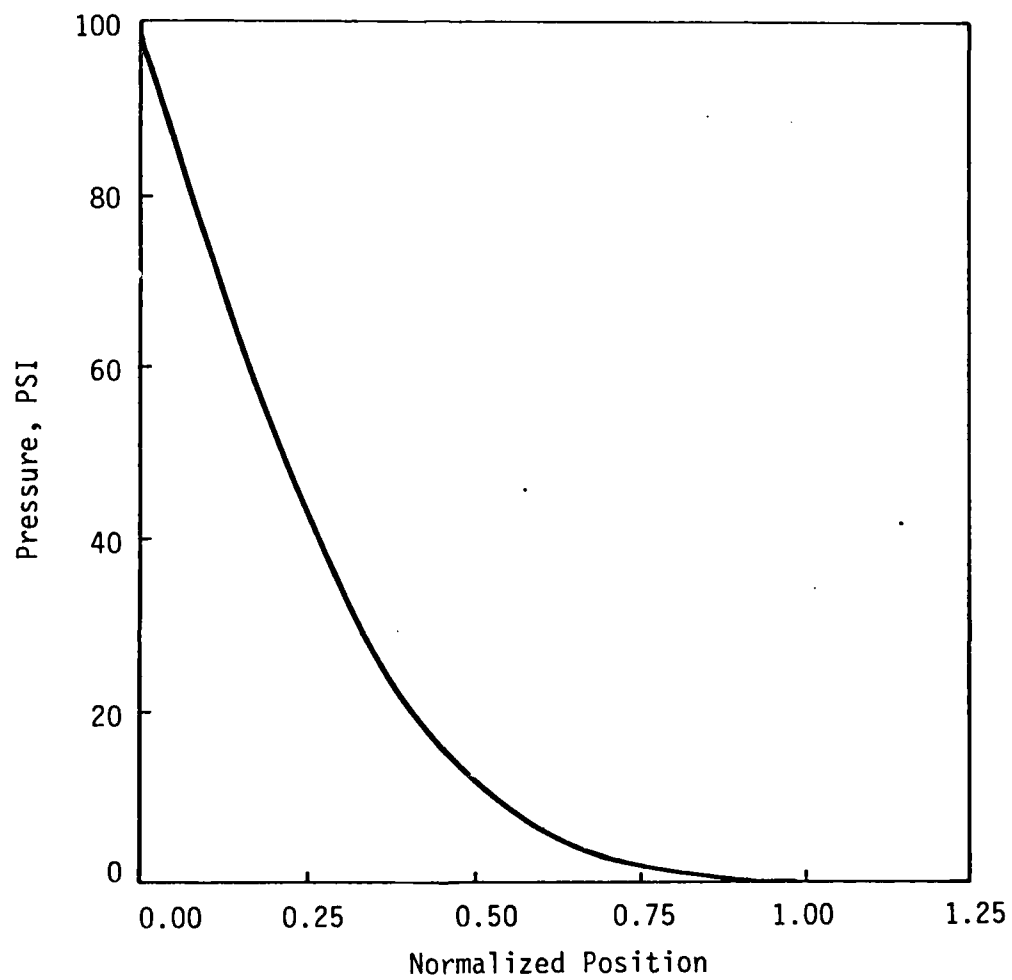


FIGURE 4.3a
Dynamic Pore Pressure Isochrone for a
Vented Sample; $\beta = 0.279$, $T = 0.05$

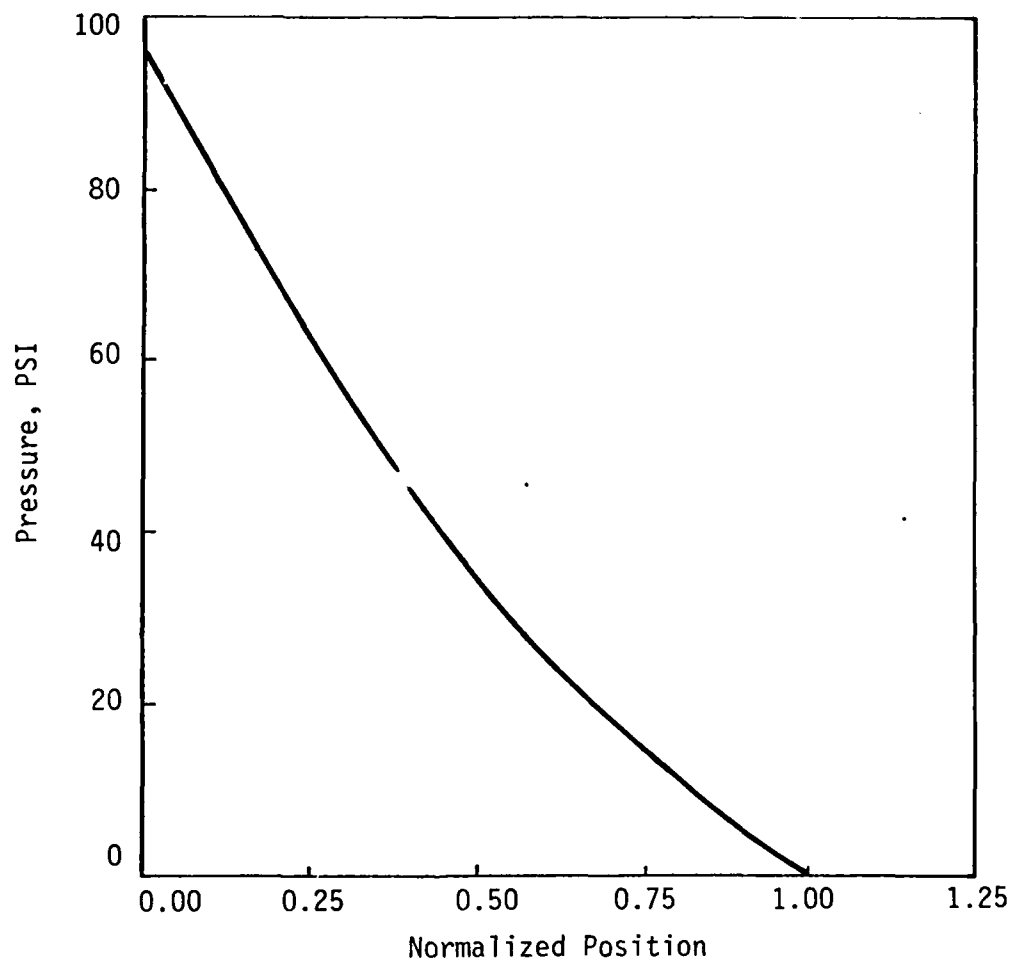


FIGURE 4.3b
Dynamic Pore Pressure Isochrone for a
Vented Sample; $\beta = 0.279$, $T = 0.15$

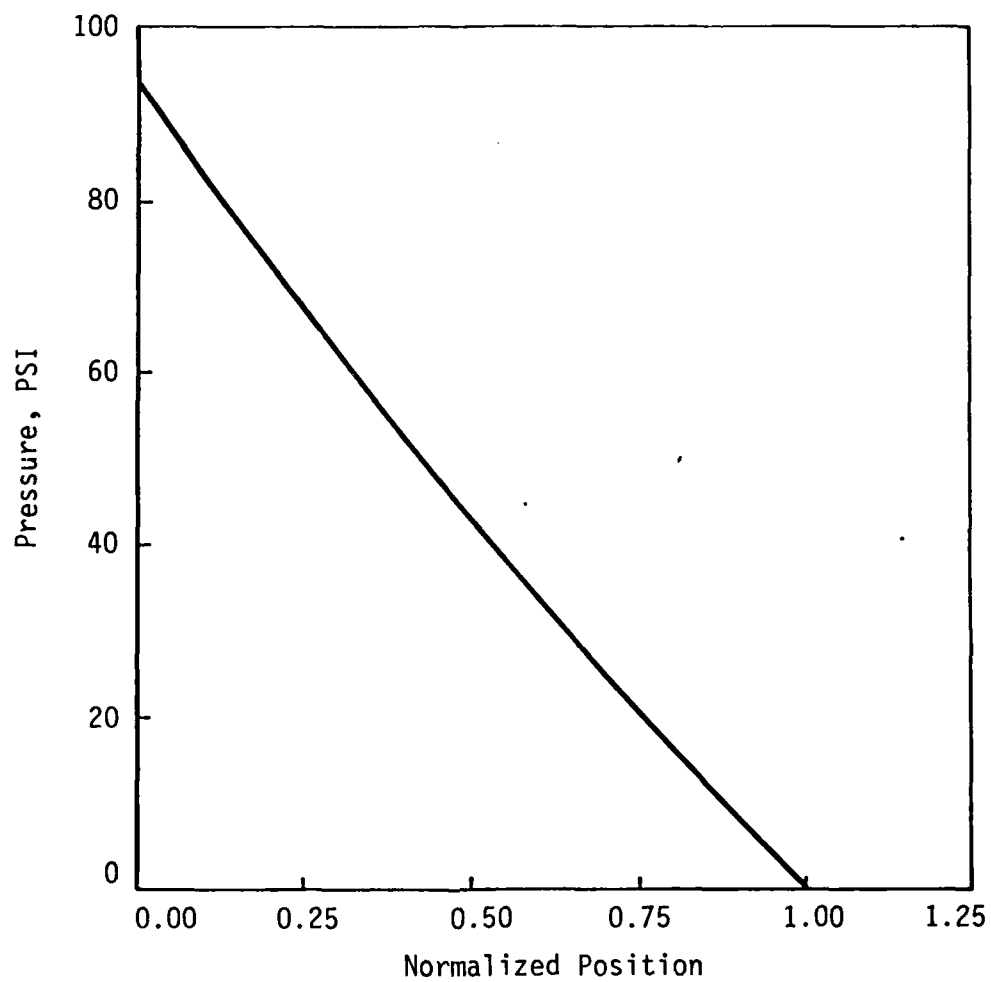


FIGURE 4.3c
Dynamic Pore Pressure Isochrone for a
Vented Sample; $\beta = 0.279$, $T = 0.25$

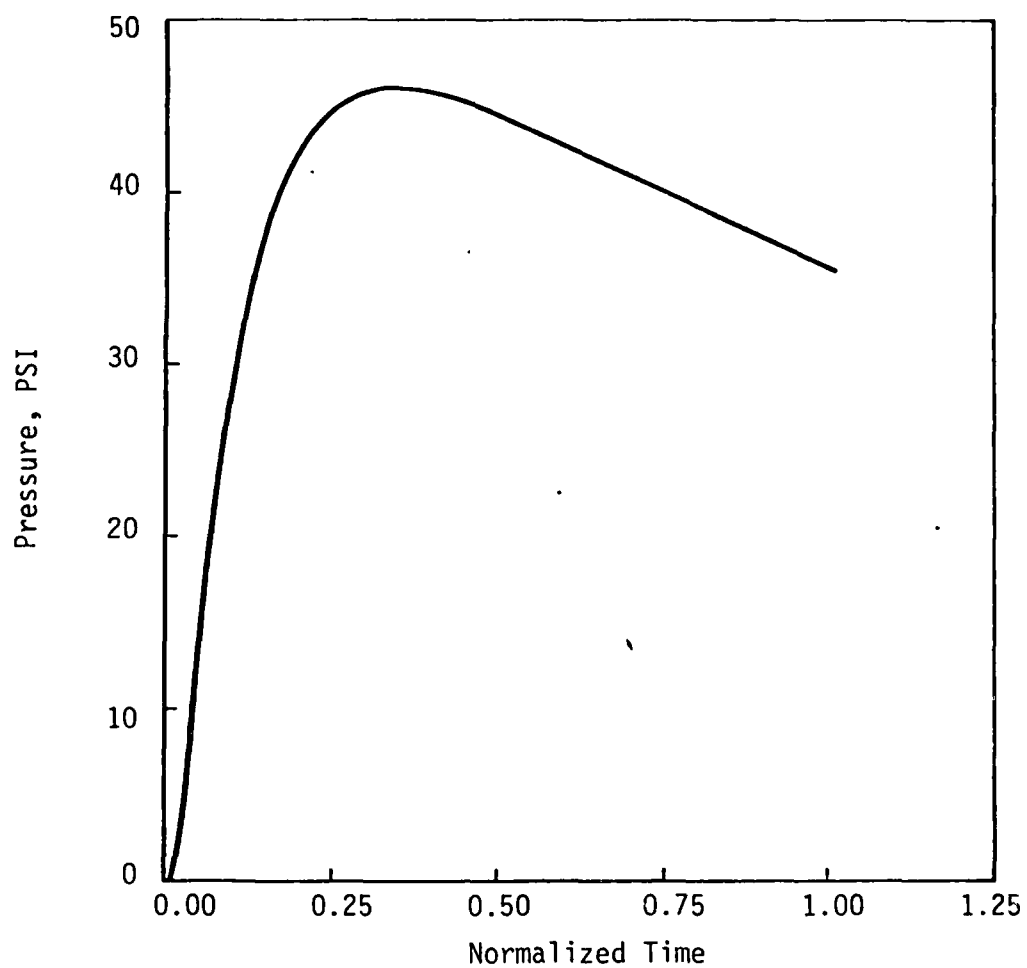


FIGURE 4.4a
Dynamic Pore Pressure Response in a
Vented Sample; $\beta = 0.463$, $\xi = 0.465$

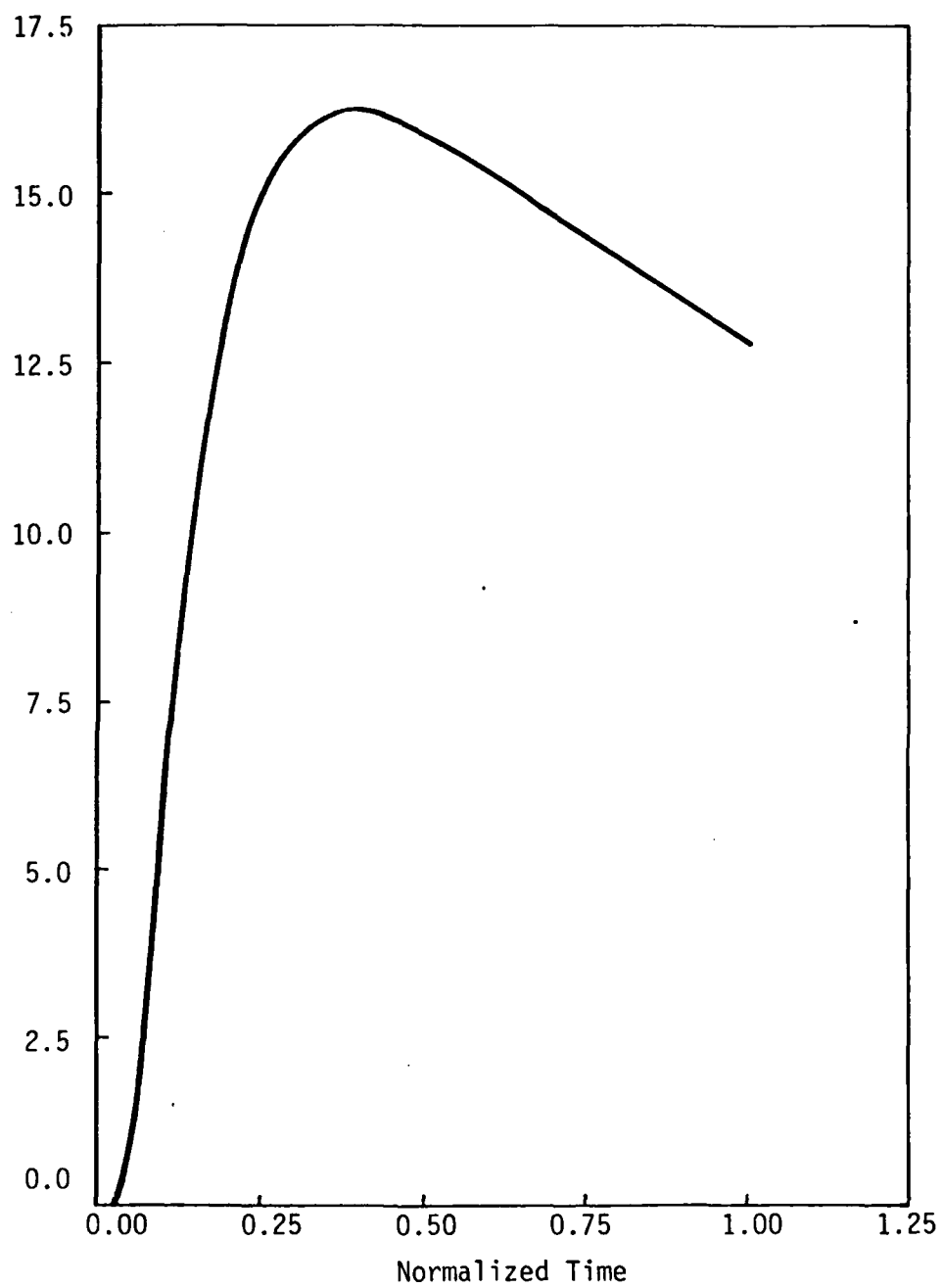


FIGURE 4.4b
Dynamic Pore Pressure Response in a
Vented Sample; $\beta = 0.463$, $\xi = 0.811$

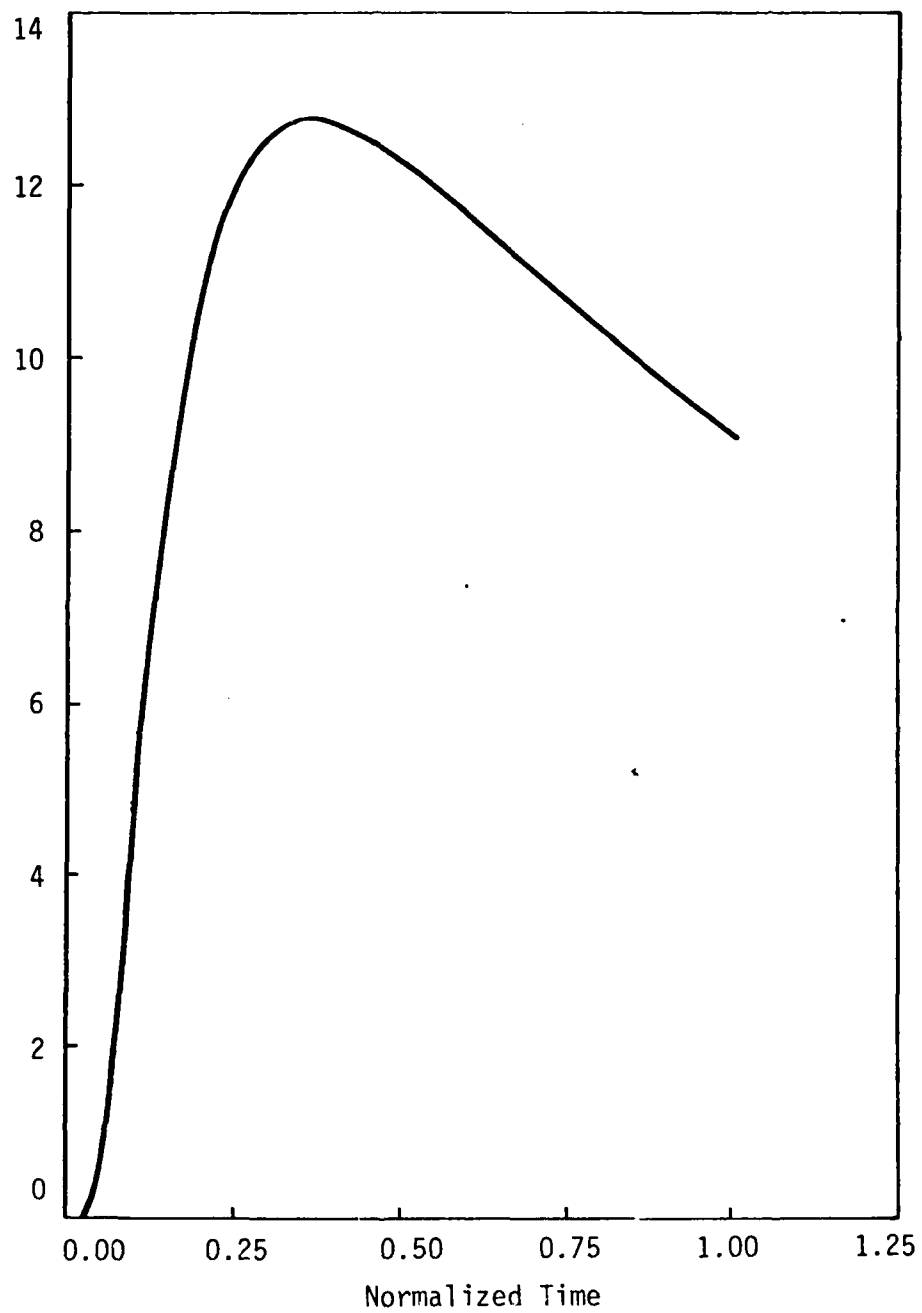


FIGURE 4.5
Dynamic Pore Pressure Response in a
Vented Sample; $\beta = 0.639$, $\xi = 0.845$

AD-A125 592

EFFECT OF SPALL ON THE CHARACTERISTICS OF EXPLOSIVE
GROUND MOTION(U) APPLIED RESEARCH ASSOCIATES INC
ALBUQUERQUE NM D H MERKLE ET AL 10 SEP 82

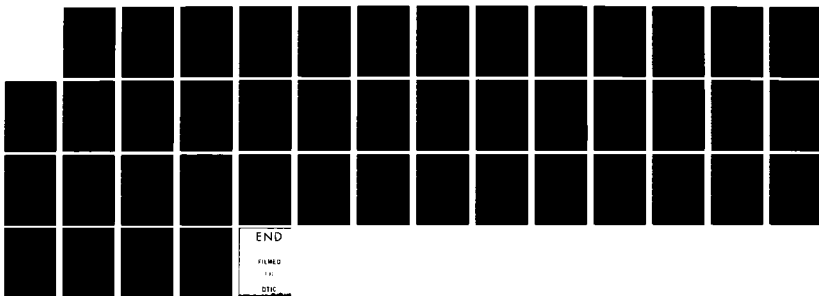
3/3

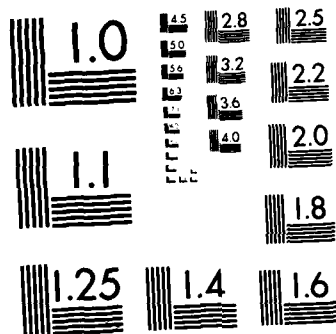
UNCLASSIFIED

AFOSR-TR-83-0060 F49620-81-C-0066

F/G 18/3

NL





MICROCOPY RESOLUTION TEST CHART
NATIONAL BUREAU OF STANDARDS-1963-A

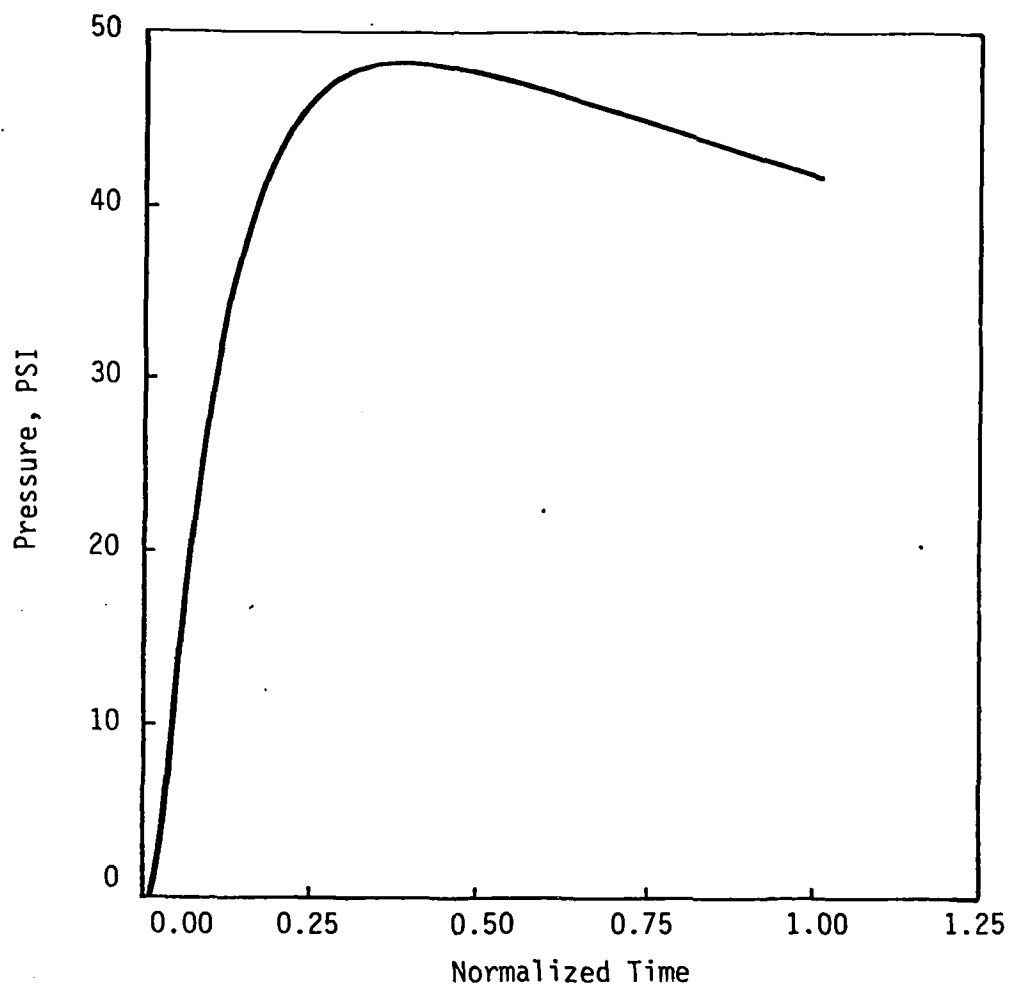


FIGURE 4.6a
Dynamic Pore Pressure Response in a
Vented Sample; $\beta = 0.279$, $\xi = 0.465$

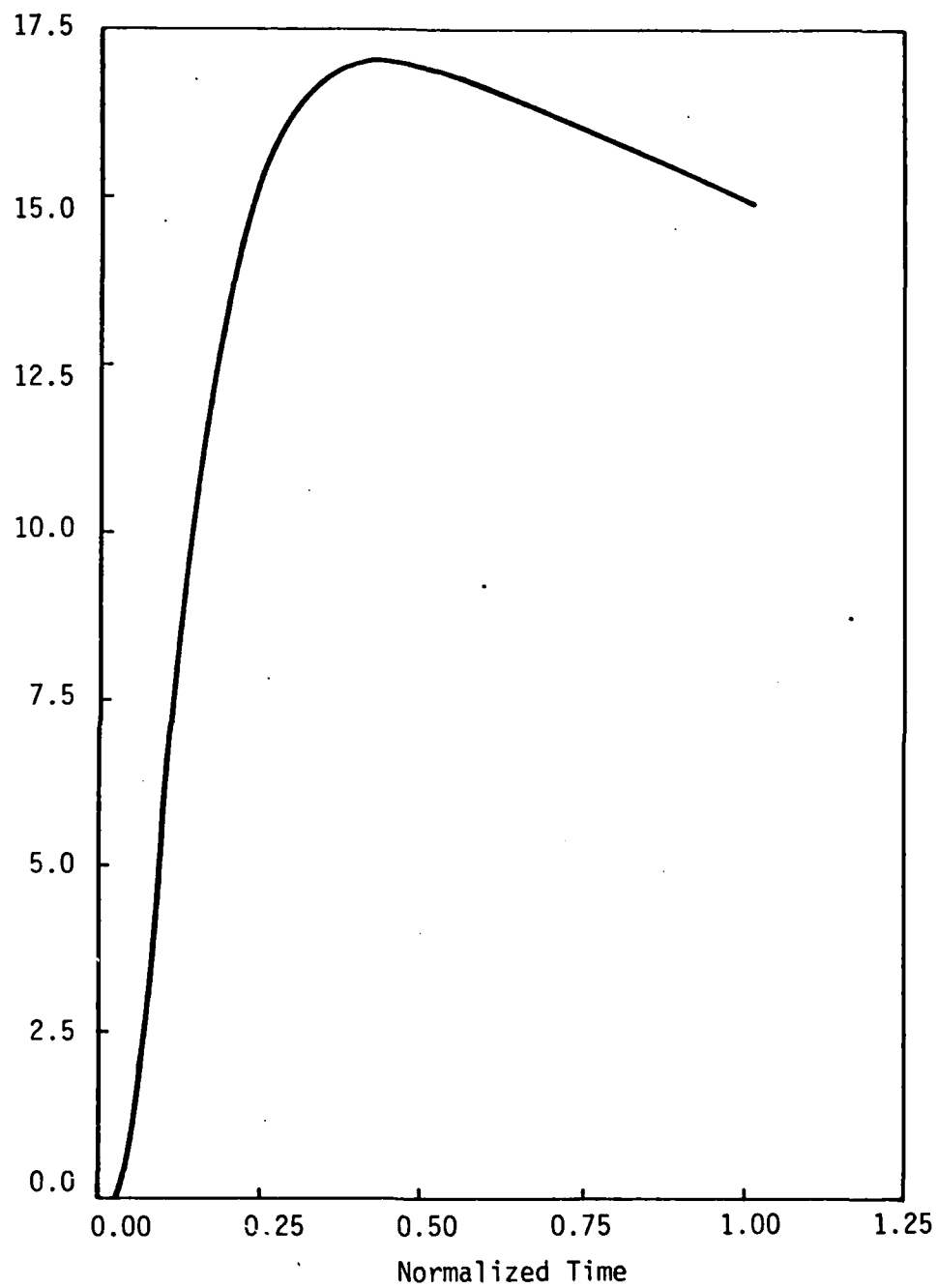


FIGURE 4.6b
Dynamic Pore Pressure Response in a
Vented Sample; $\beta = 0.279$, $\xi = 0.811$

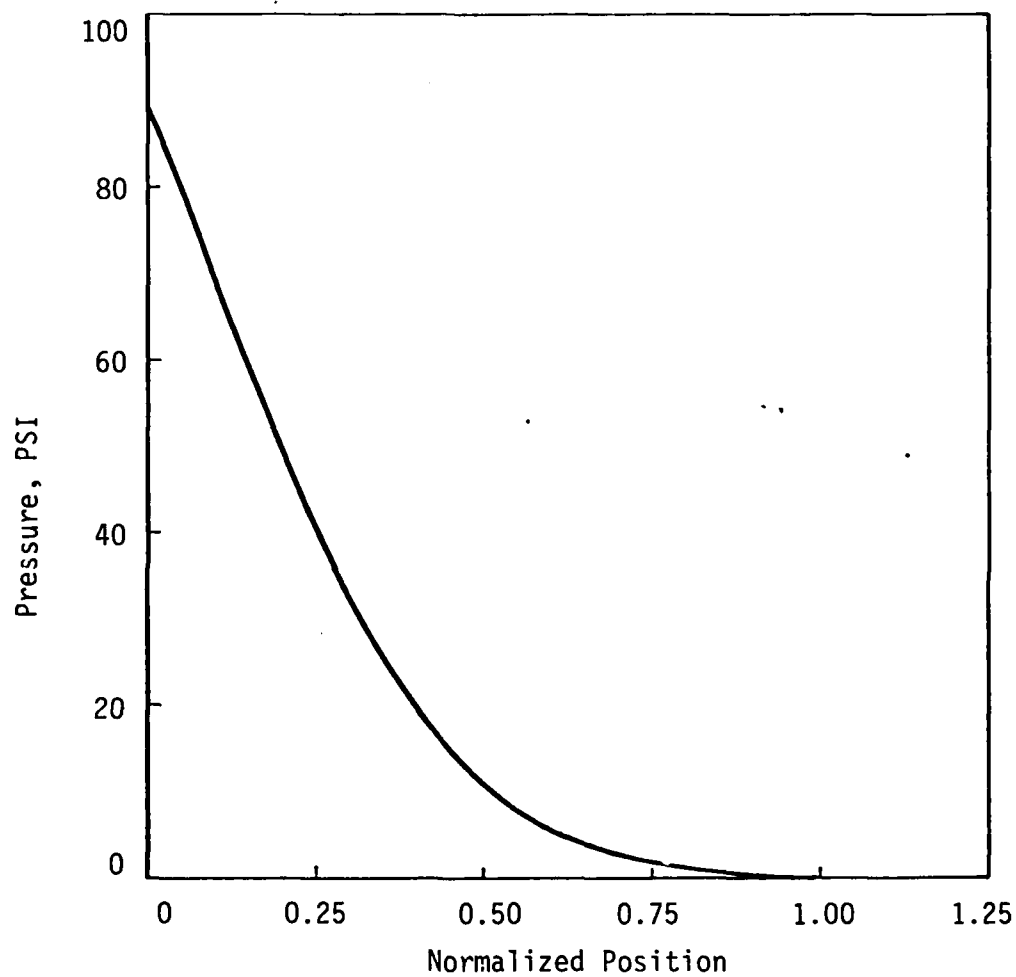


FIGURE 4.7a
Dynamic Pore Pressure Isochrone for a
Vented Sample; $\beta = 2.31$, $T = 0.05$

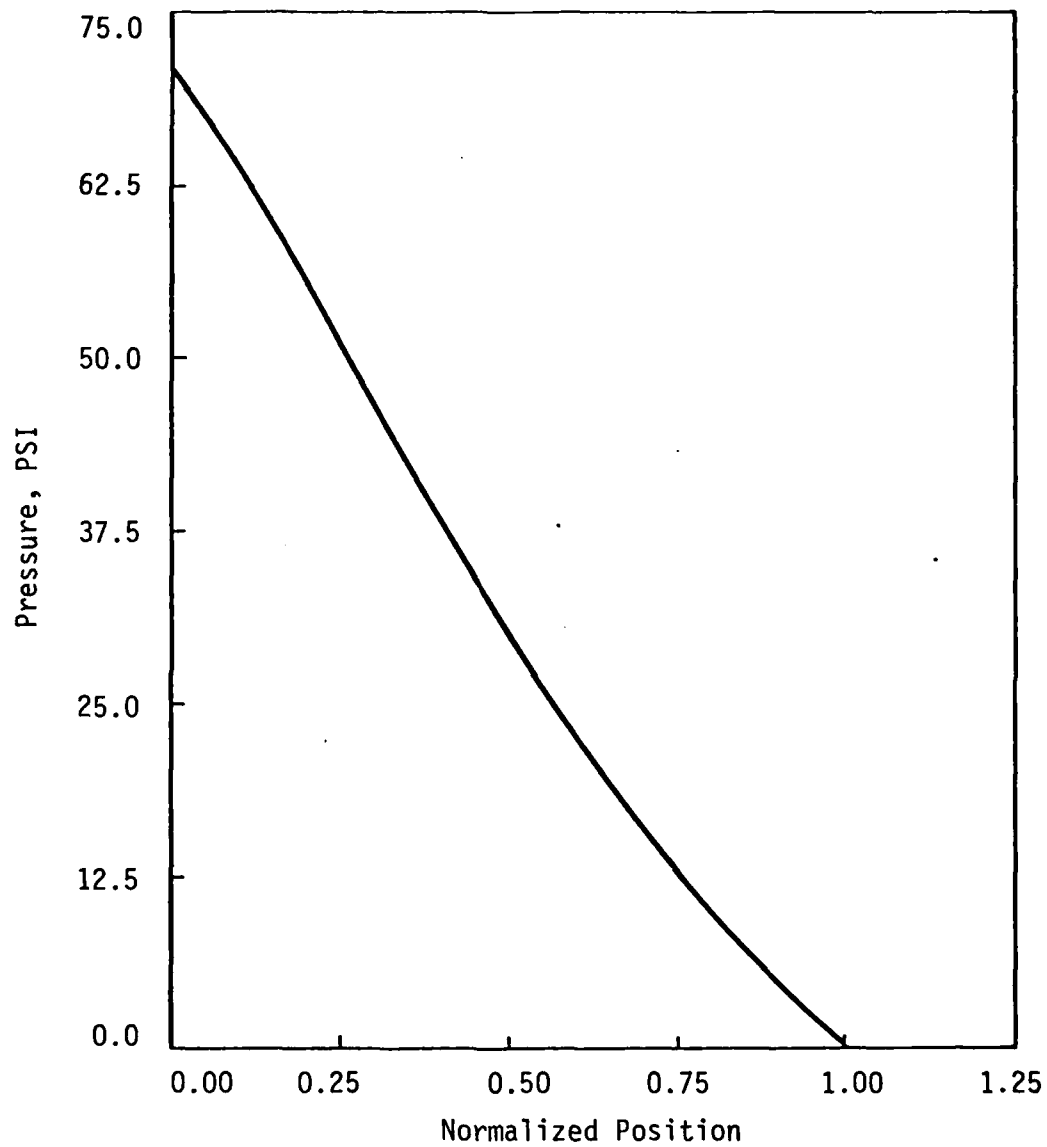


FIGURE 4.7b
Dynamic Pore Pressure Isochrone for a
Vented Sample; $\beta = 2.31$; $T = 0.15$

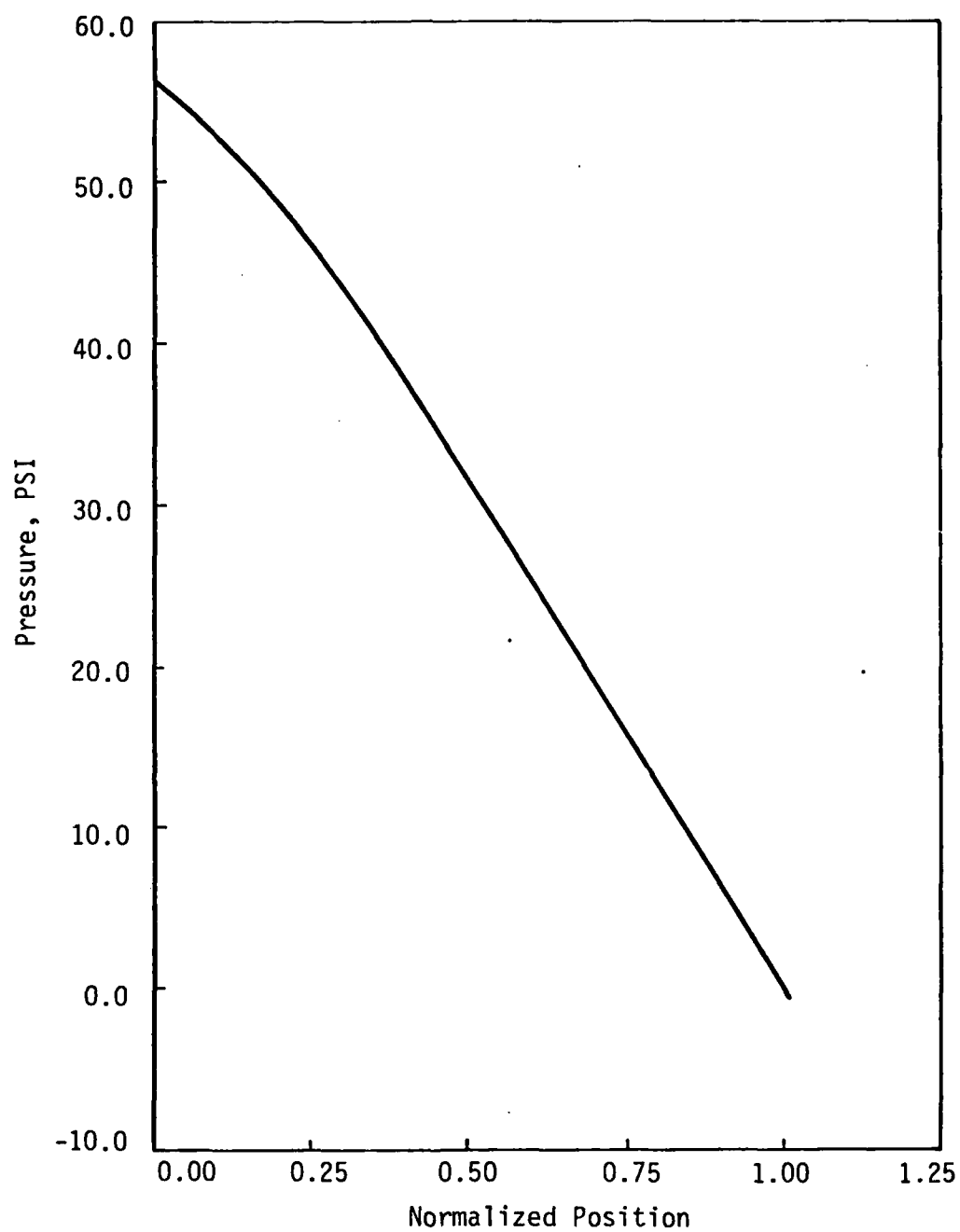


FIGURE 4.7c
Dynamic Pore Pressure Isochrone for a
Vented Sample; $\beta = 2.31$; $T = 0.25$

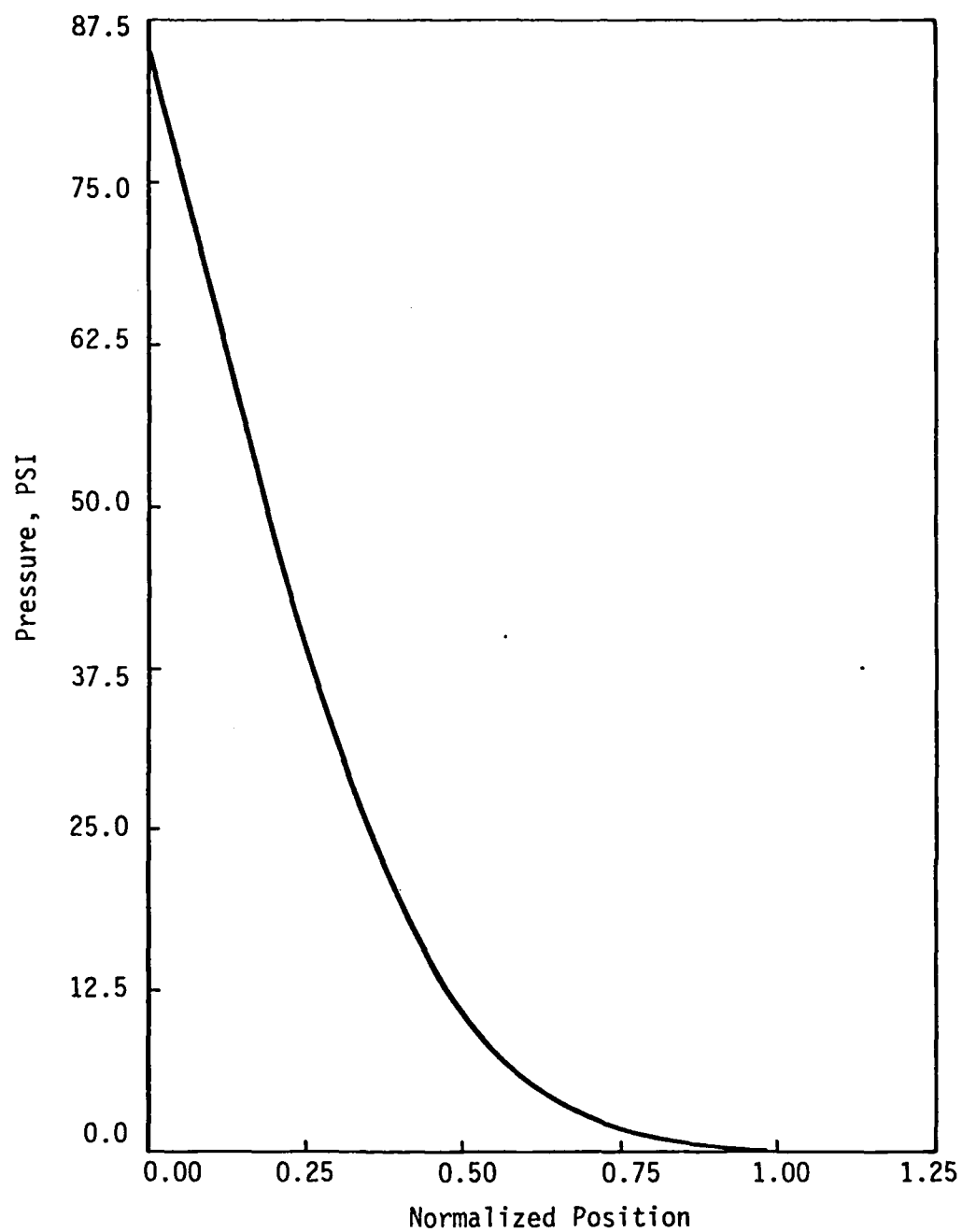


FIGURE 4.8a
Dynamic Pore Pressure Isochrone for a
Vented Sample; $\beta = 3.19$; $T = 0.05$

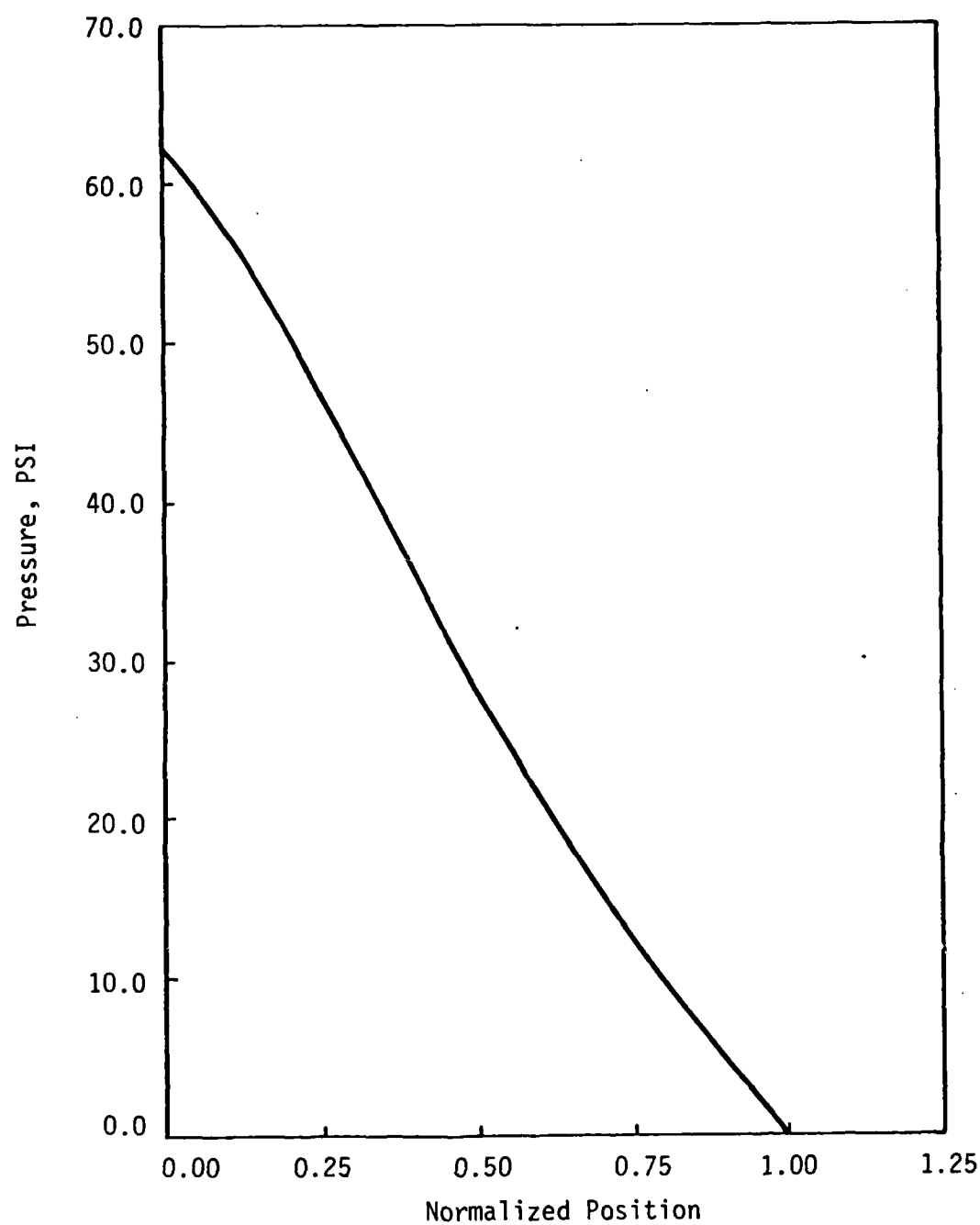


FIGURE 4.8b
Dynamic Pore Pressure Isochrone for a
Vented Sample; $\beta = 3.19$; $T = 0.15$

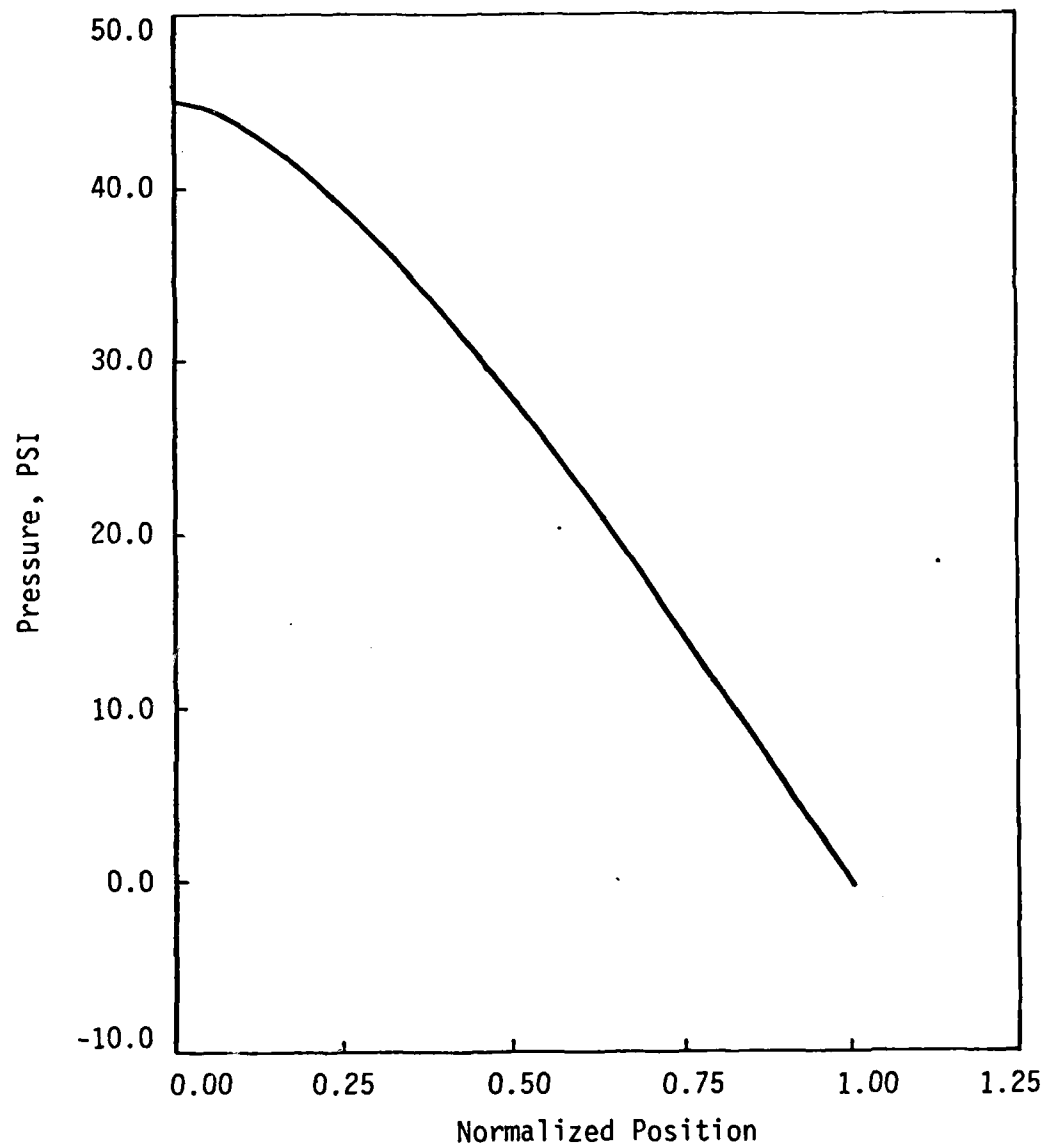


FIGURE 4.8c
Dynamic Pore Pressure Isochrone for a
Vented Sample; $\beta = 3.19$; $T = 0.25$

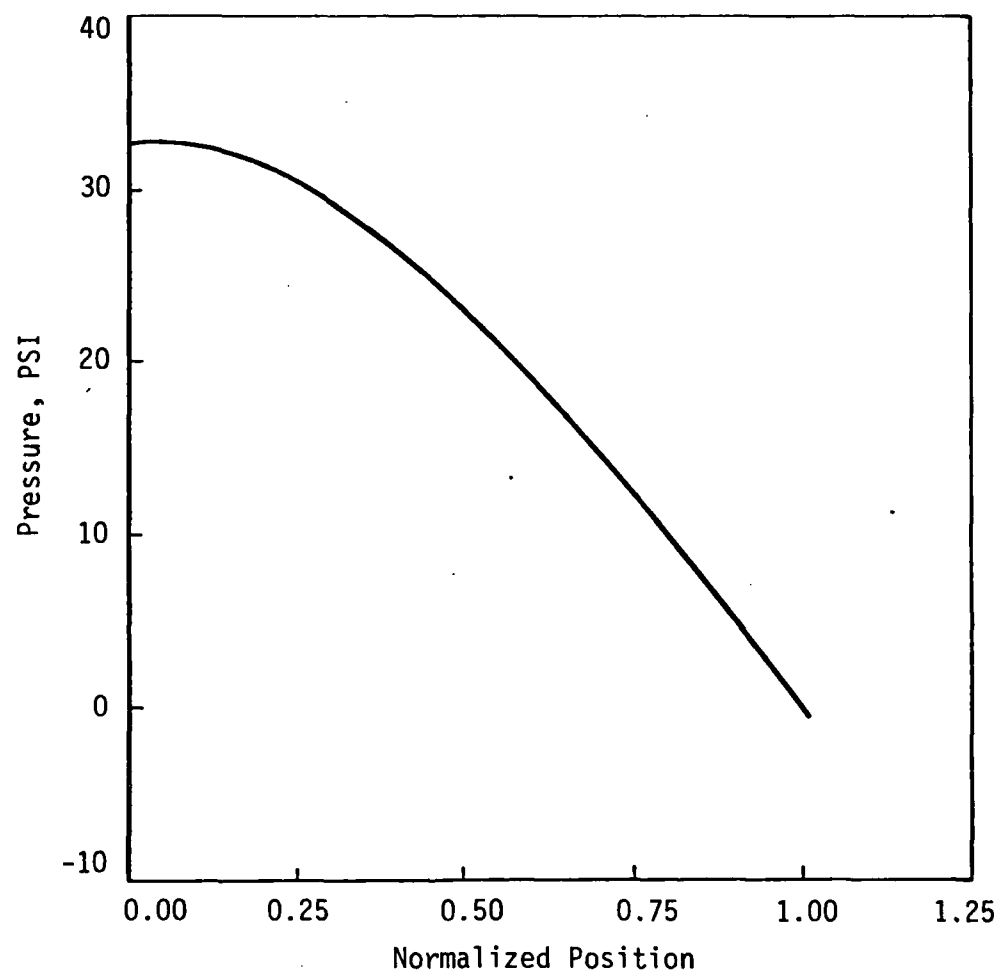


FIGURE 4.8d
Dynamic Pore Pressure Isochrone for a
Vented Sample; $\beta = 3.19$; $T = 0.35$

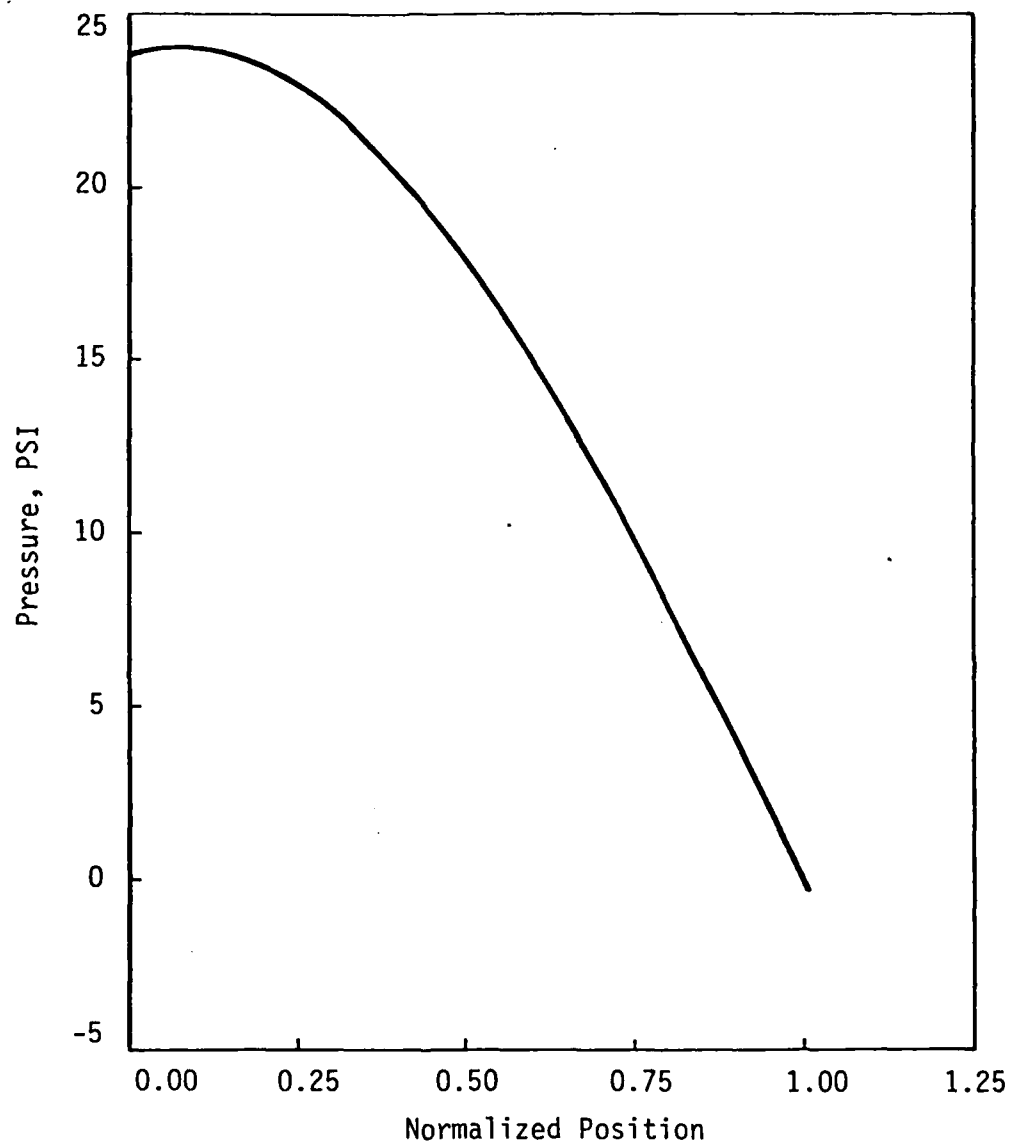


FIGURE 4.8e
Dynamic Pore Pressure Isochrone for a
Vented Sample; $\beta = 3.19$; $T = 0.45$

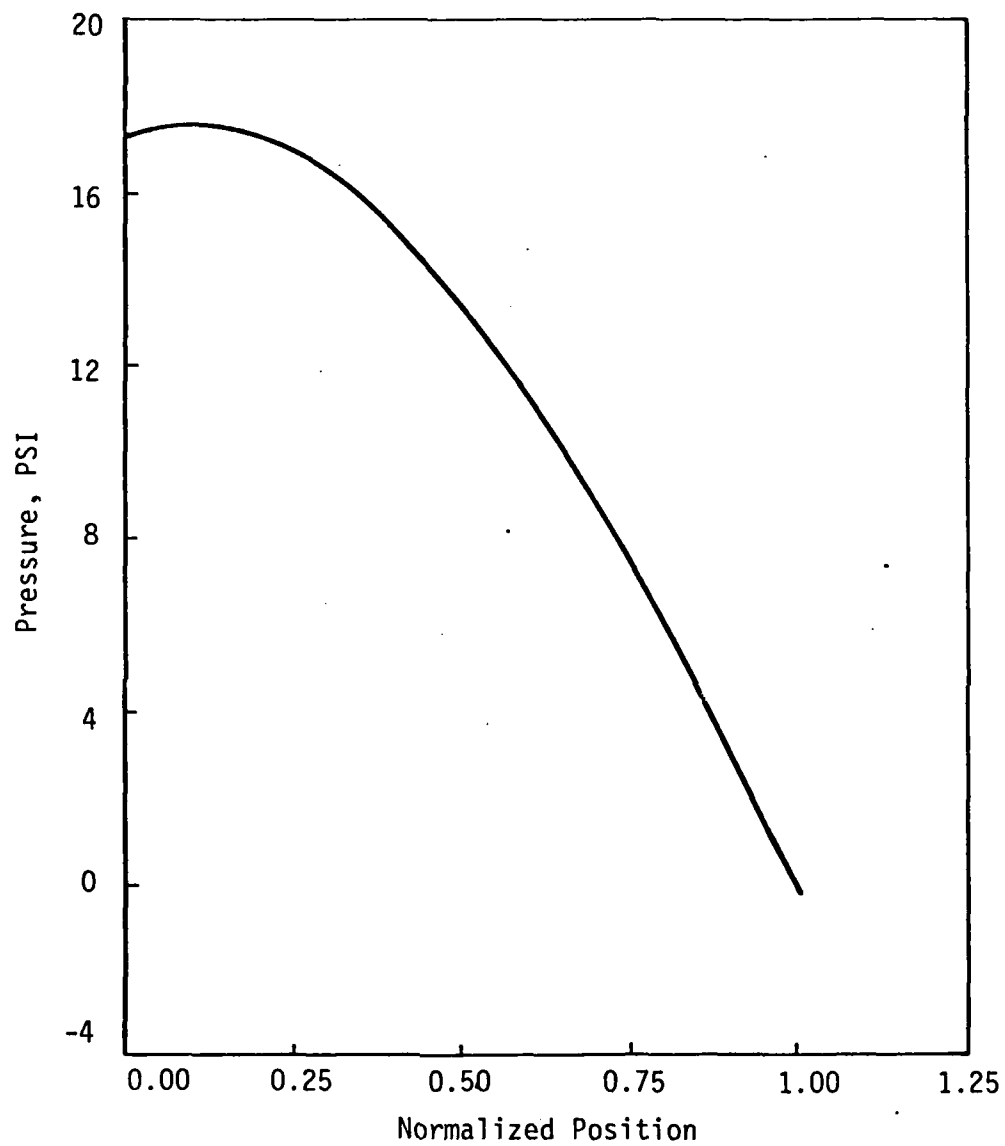


FIGURE 4.8f
Dynamic Pore Pressure Isochrone for a
Vented Sample; $\beta = 3.19$; $T = 0.55$

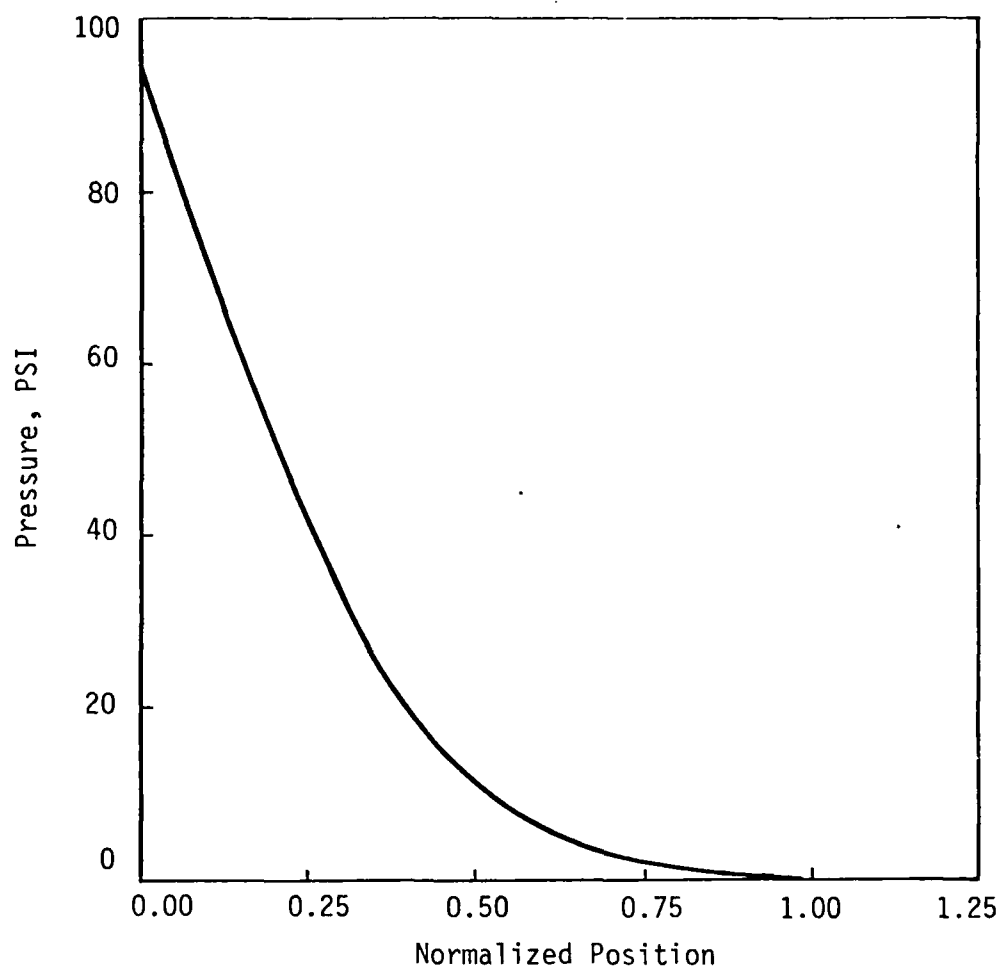


FIGURE 4.9a
Dynamic Pore Pressure Isochrone for a
Vented Sample; $\beta = 1.39$; $T = 0.05$

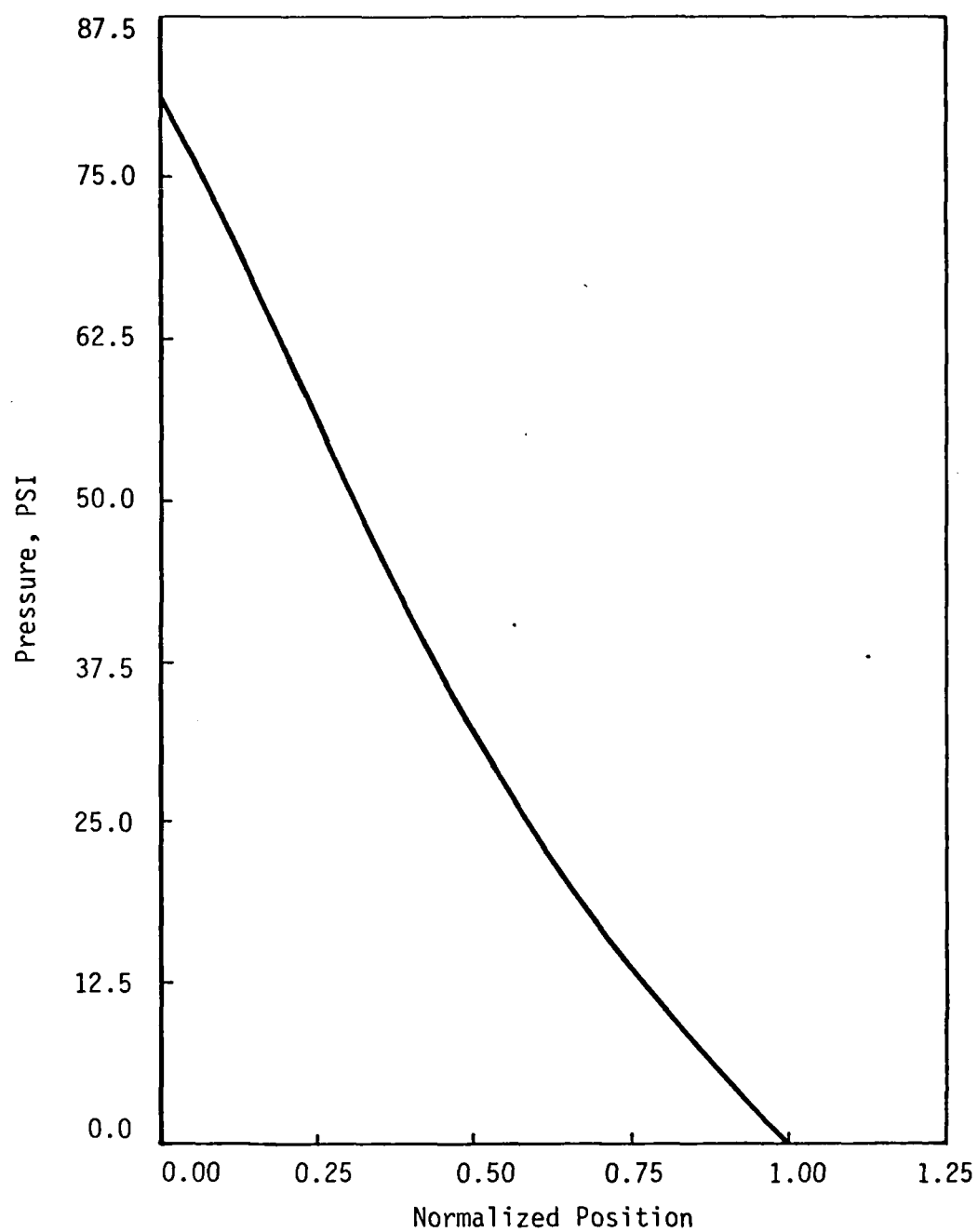


FIGURE 4.9b
Dynamic Pore Pressure Isochrone for a
Vented Sample; $\beta = 1.39$; $T = 0.15$

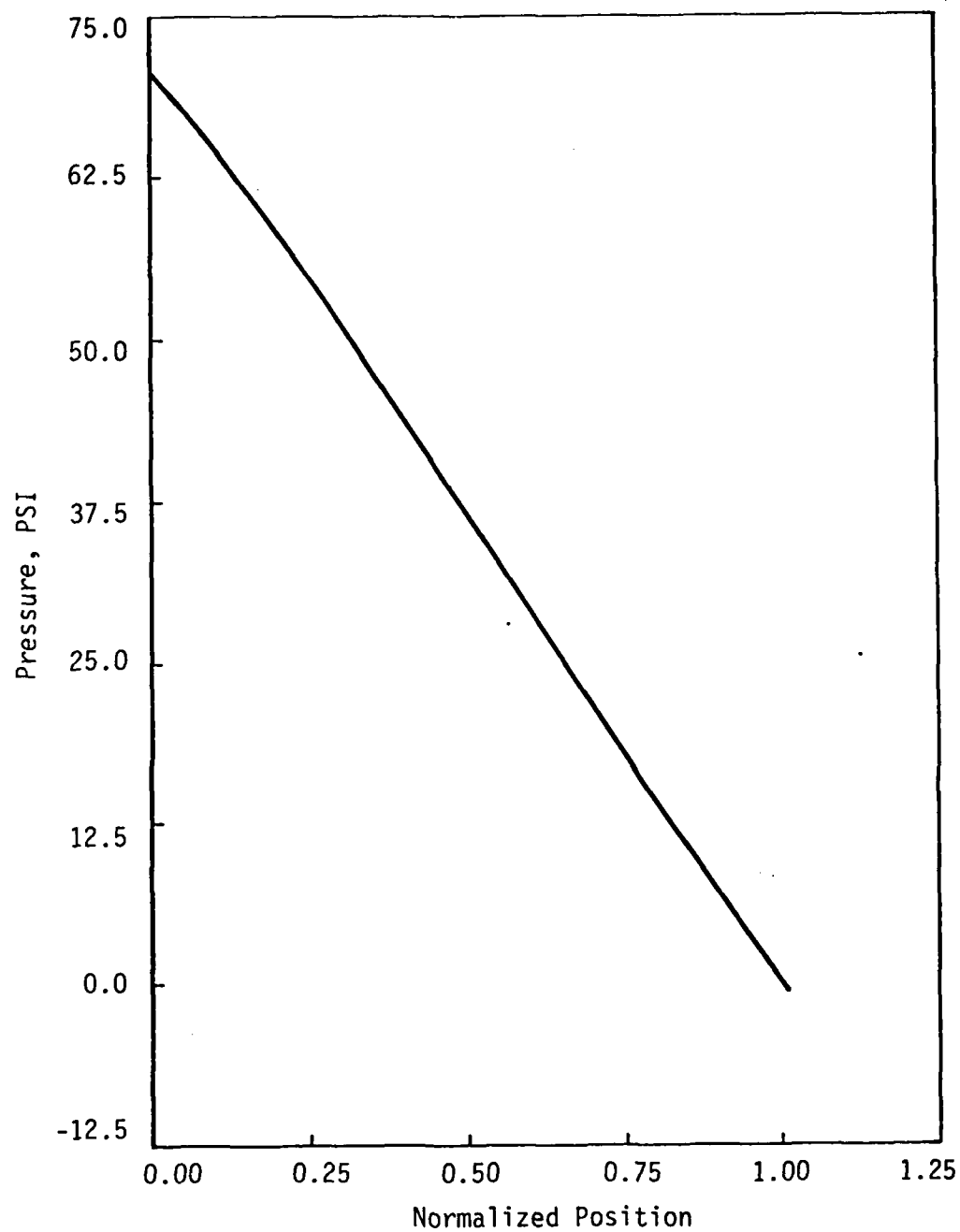


FIGURE 4.9c
Dynamic Pore Pressure Isochrone for a
Vented Sample; $\beta = 1.39$; $T = 0.25$

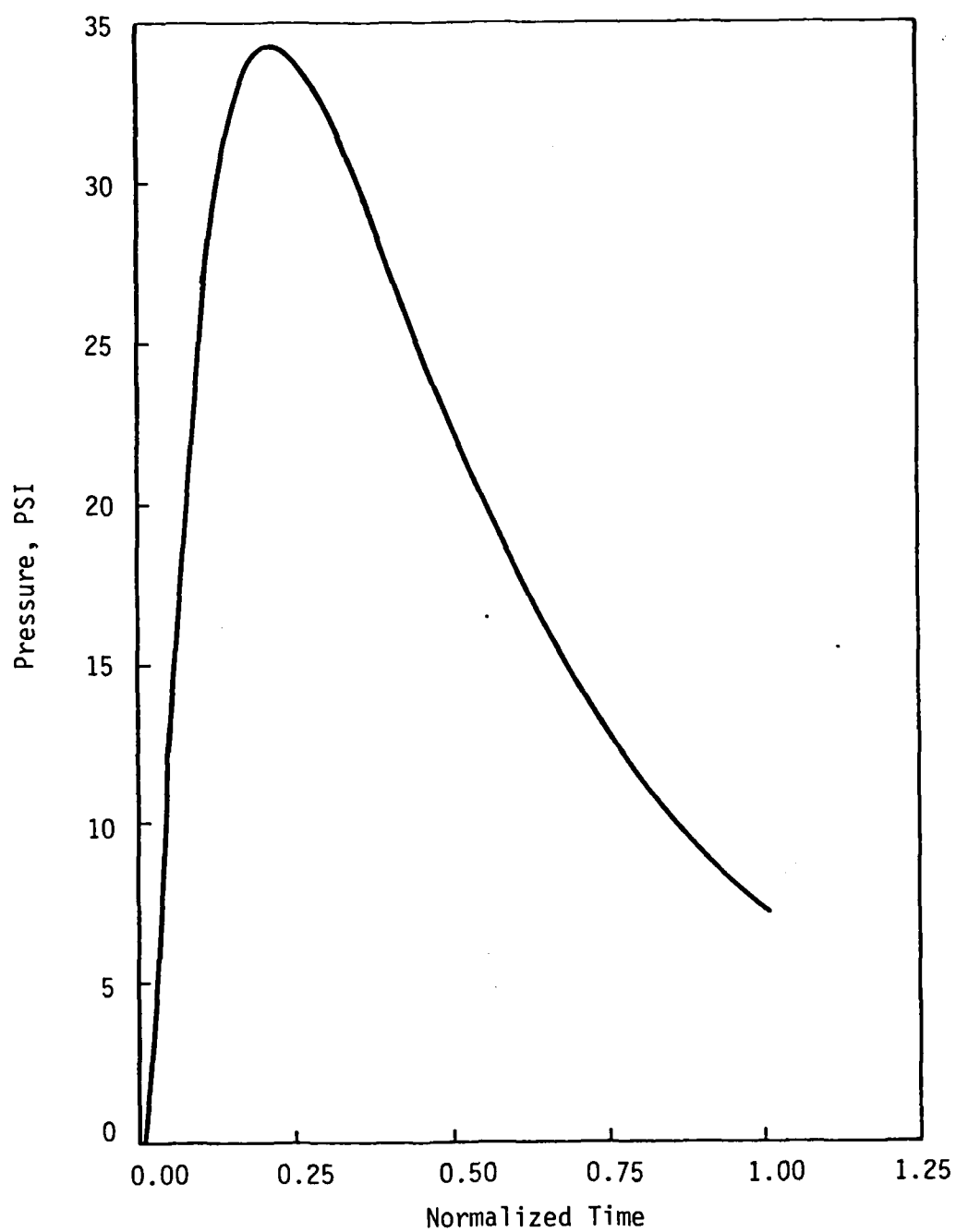


FIGURE 4.10a
Dynamic Pore Pressure Response in a
Vented Sample; $\beta = 2.31$; $\xi = 0.465$

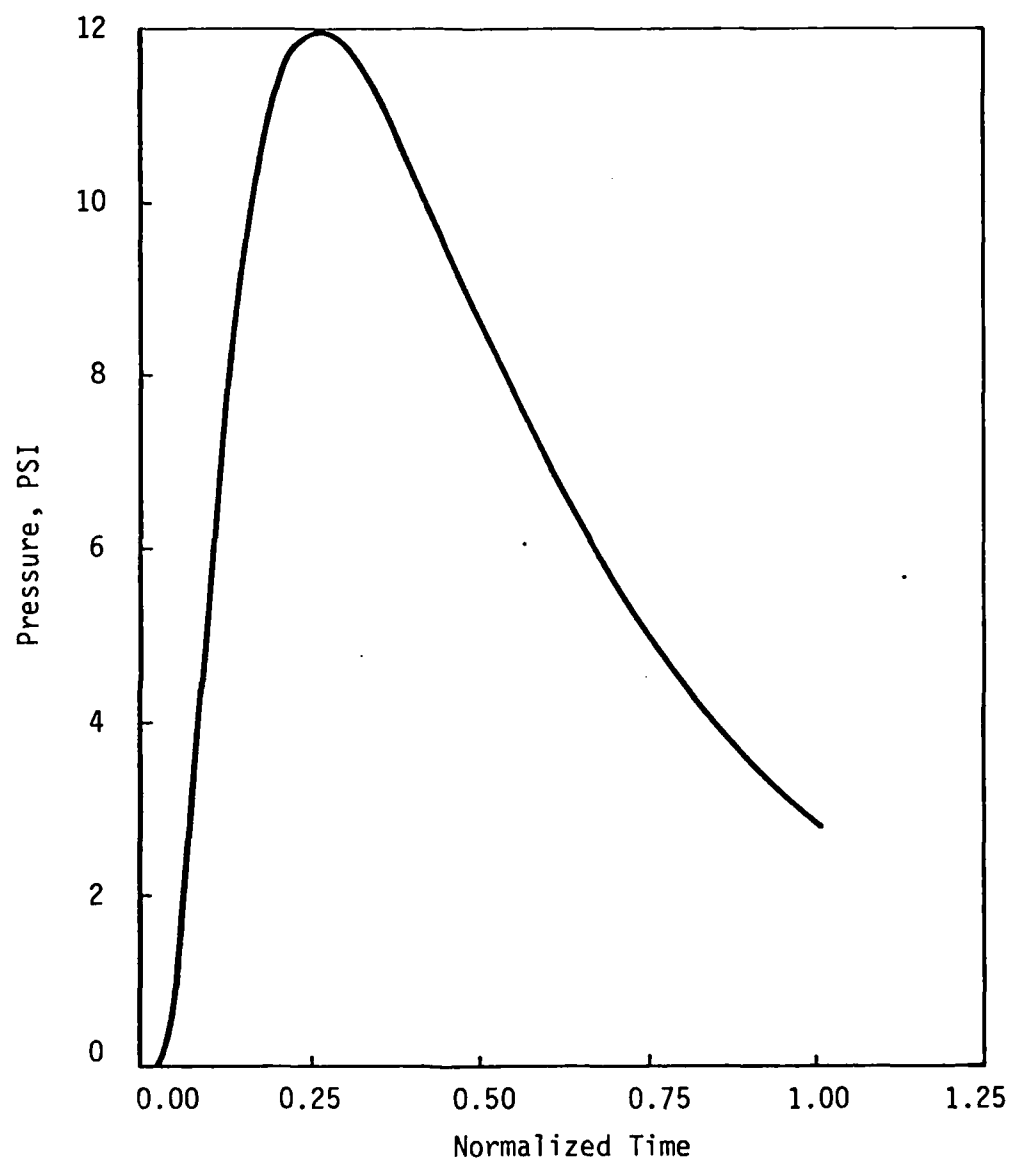


FIGURE 4.10b
Dynamic Pore Pressure Response in a
Vented Sample; $\beta = 2.31$; $\xi = 0.811$

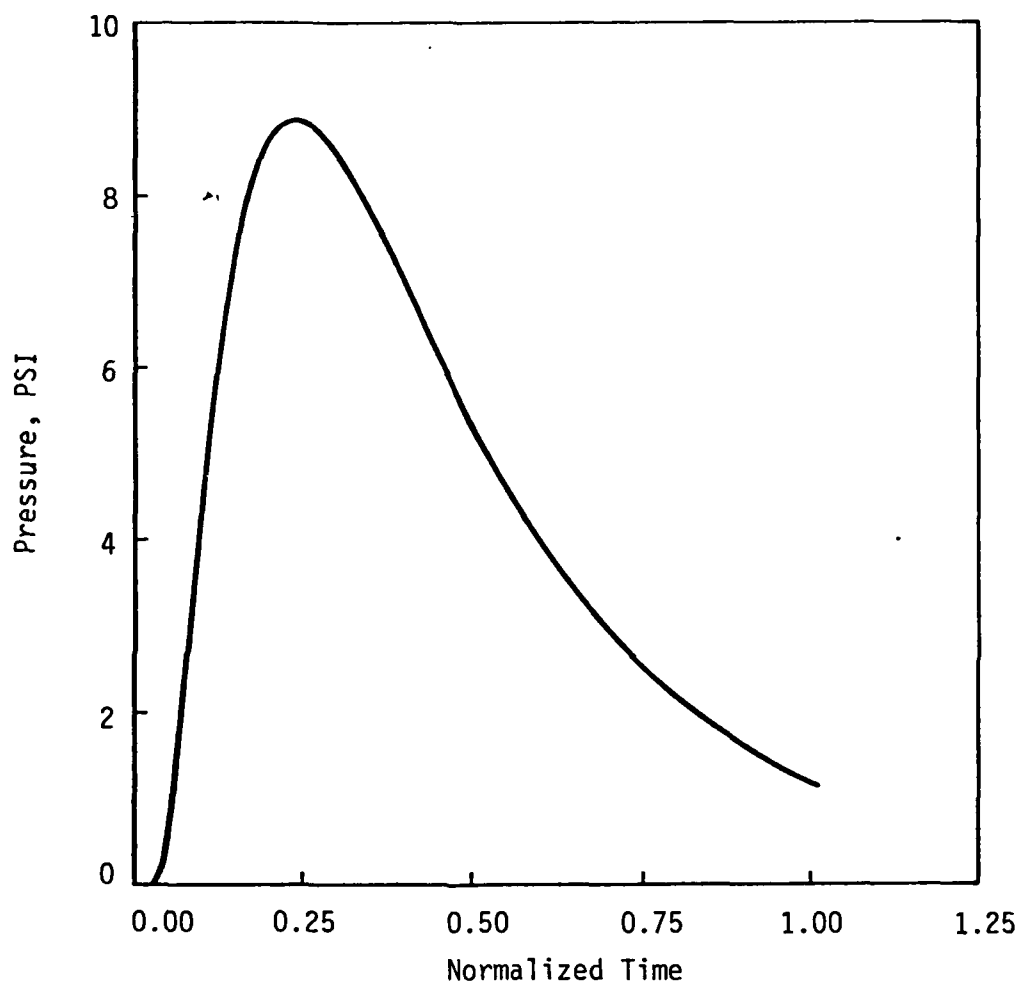


FIGURE 4.11
Dynamic Pore Pressure Response in a
Vented Sample; $\beta = 3.19$, $\xi = 0.845$

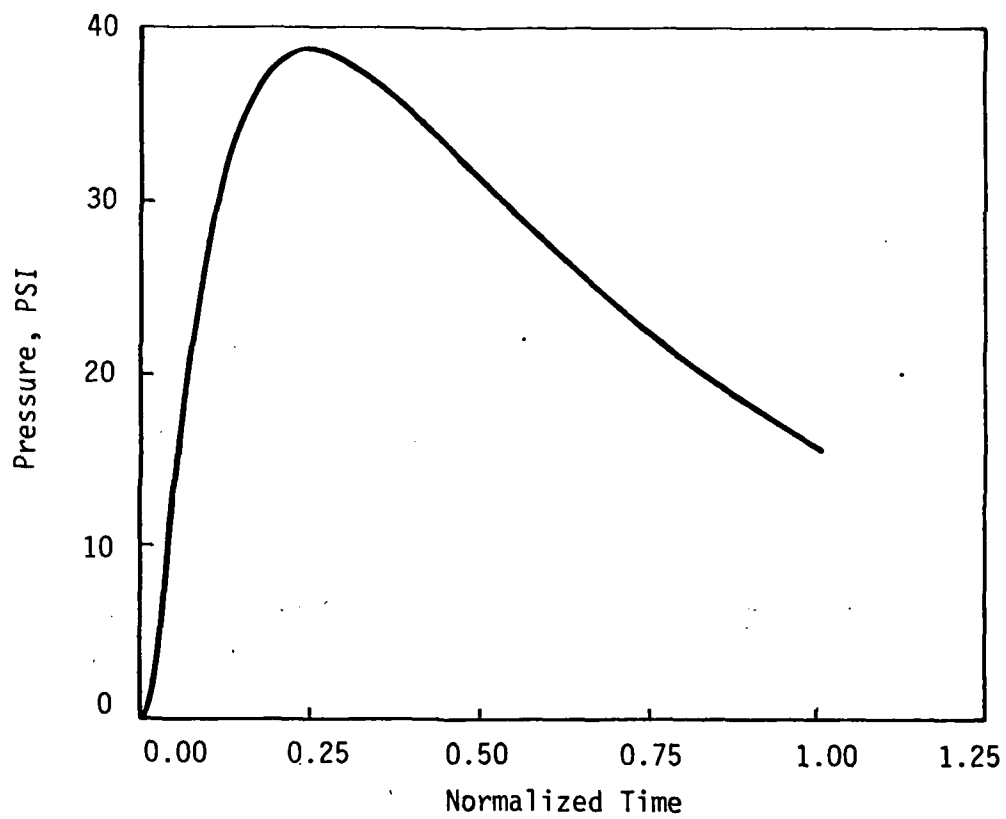


FIGURE 4.12a
Dynamic Pore Pressure Response in a
Vented Sample; $\beta = 1.39$; $\xi = 0.465$

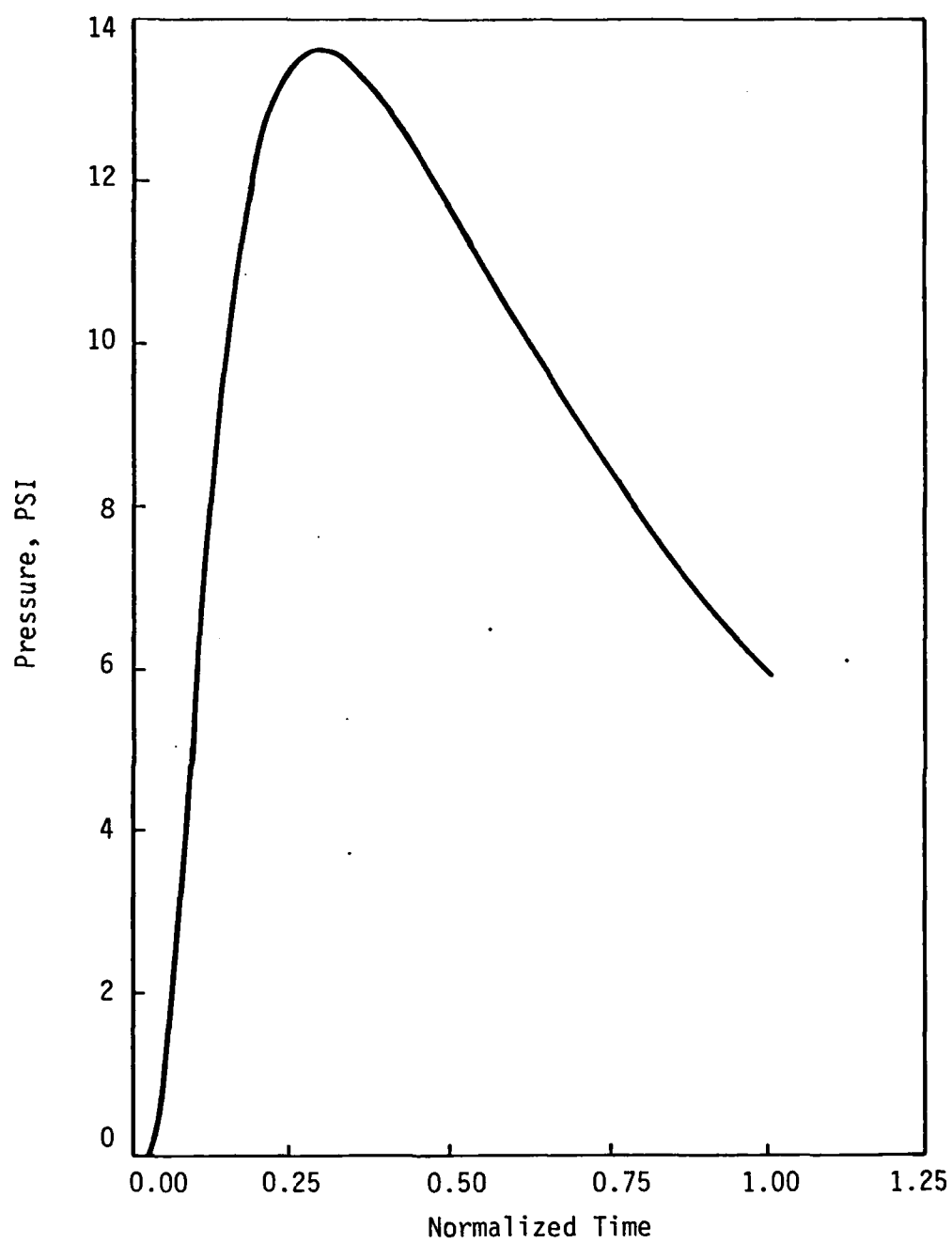


FIGURE 4.12b
Dynamic Pore Pressure Response in a
Vented Sample; $\beta = 1.39$; $\xi = 0.811$

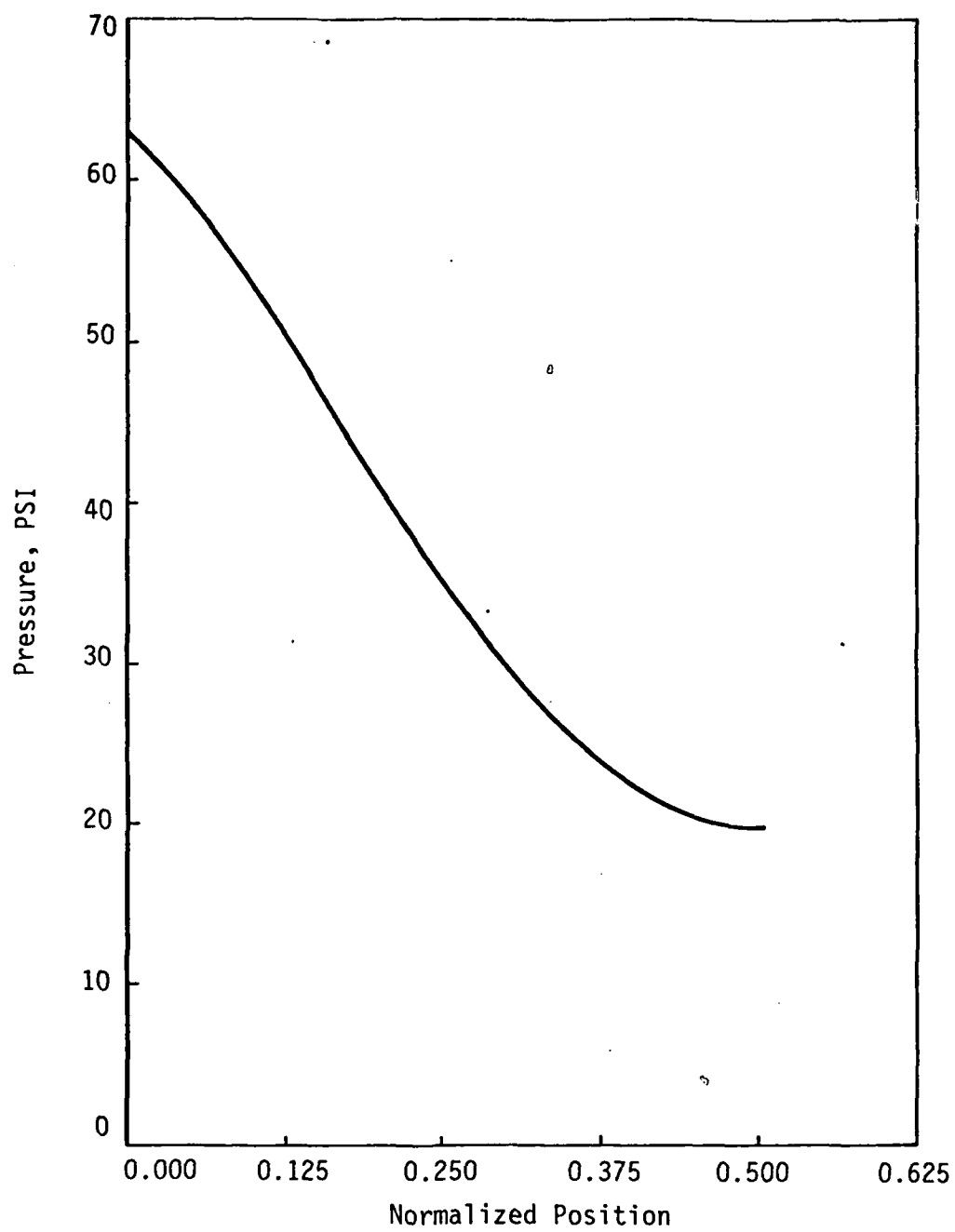


FIGURE 4.13a
Dynamic Pore Pressure Isochrone for an
Unvented Sample; $\beta = 9.25$, $T = 0.05$

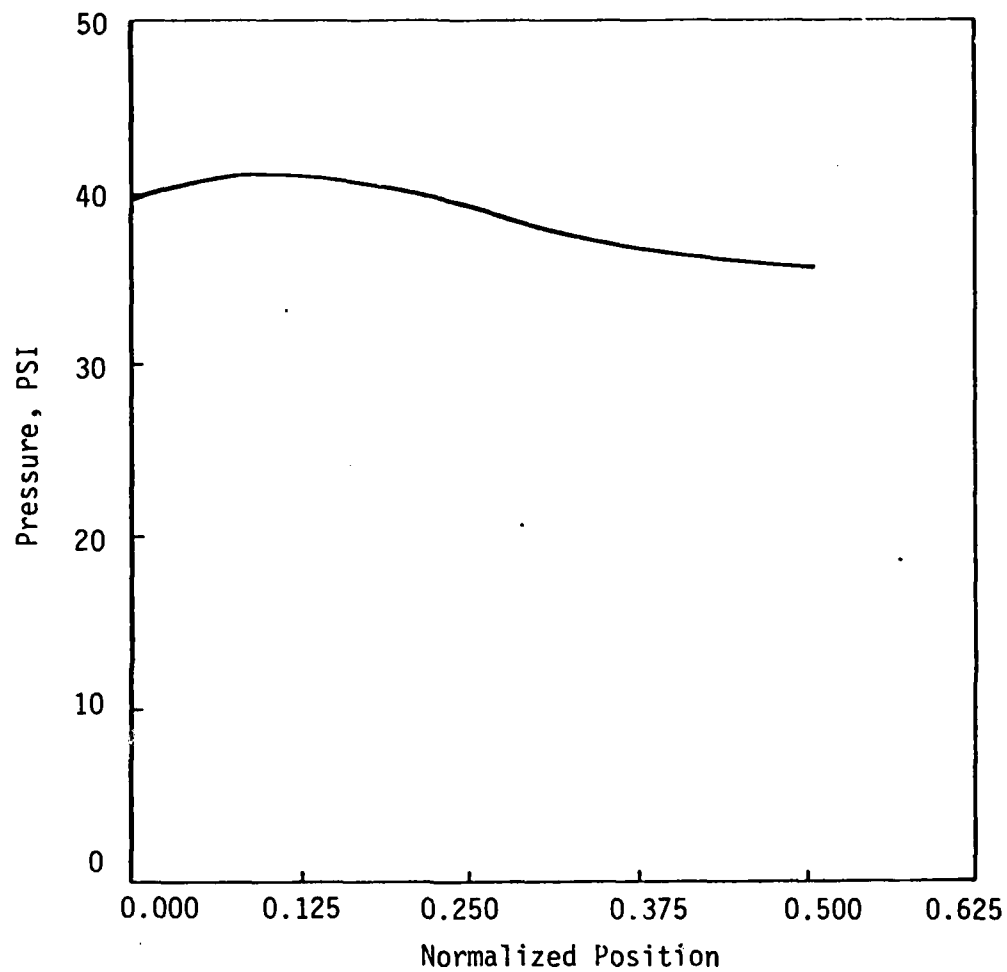


FIGURE 4.13b
Dynamic Pore Pressure Isochrone for an
Unvented Sample; $\beta = 9.25$, $\tau = 0.10$

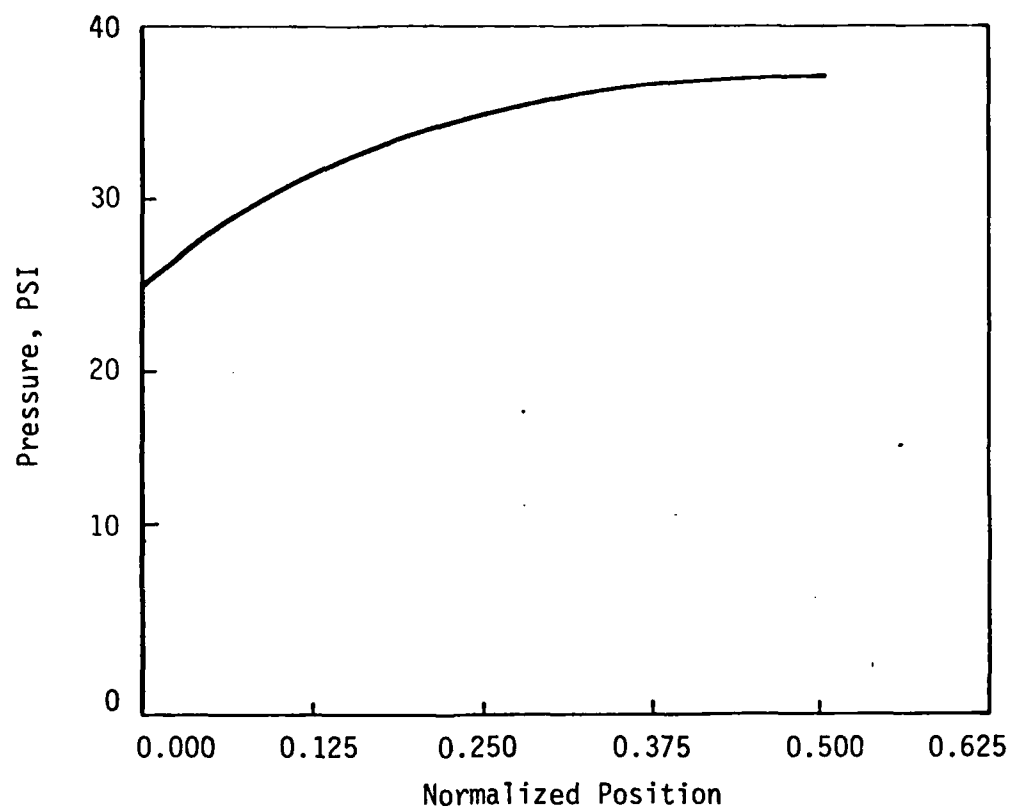


FIGURE 4.13c
Dynamic Pore Pressure Isochrone for an
Unvented Sample; $\beta = 9.25$, $T = 0.15$

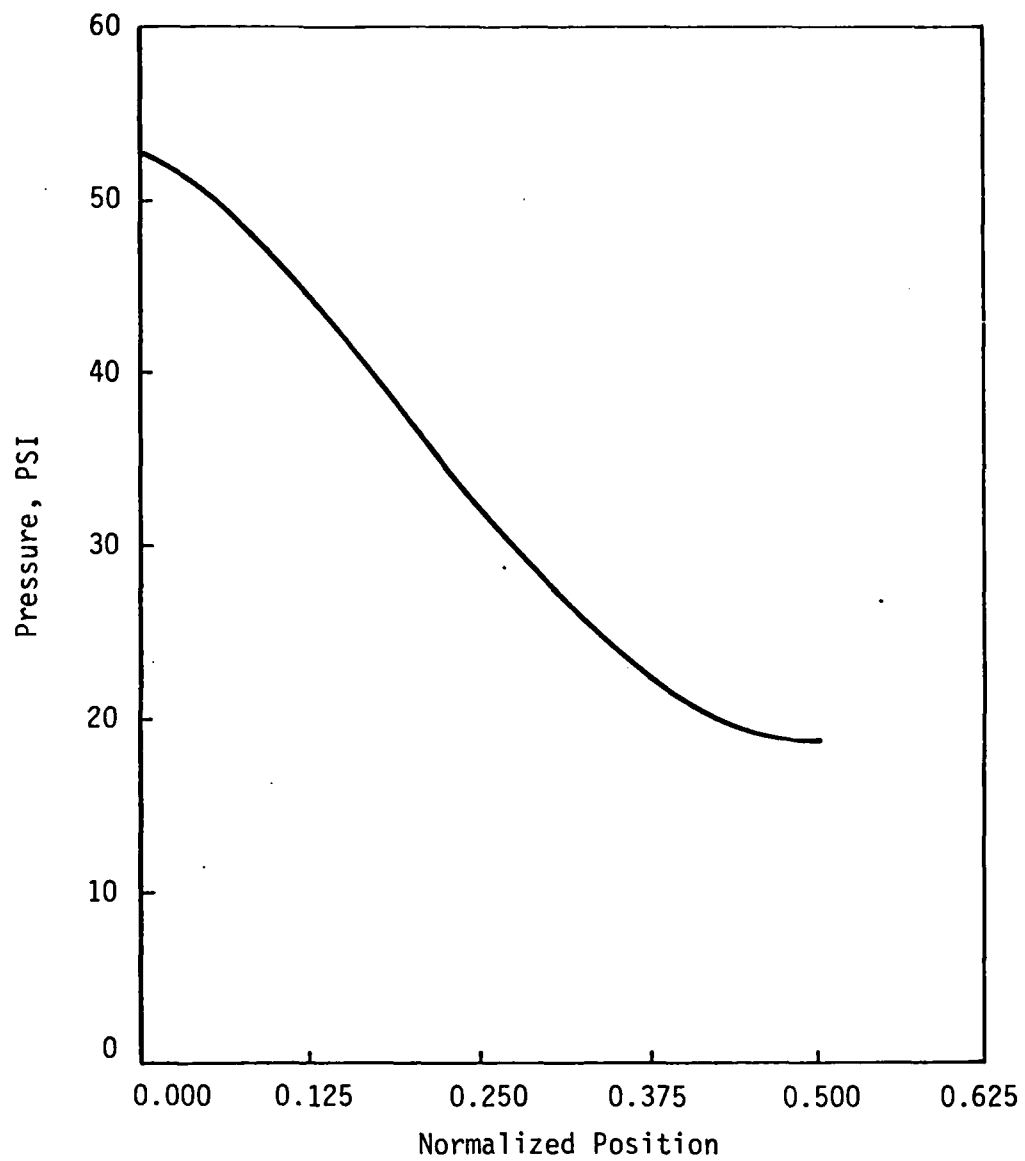


FIGURE 4.14a
Dynamic Pore Pressure Isochrone for an
Unvented Sample; $\beta = 12.77$, $T = 0.05$

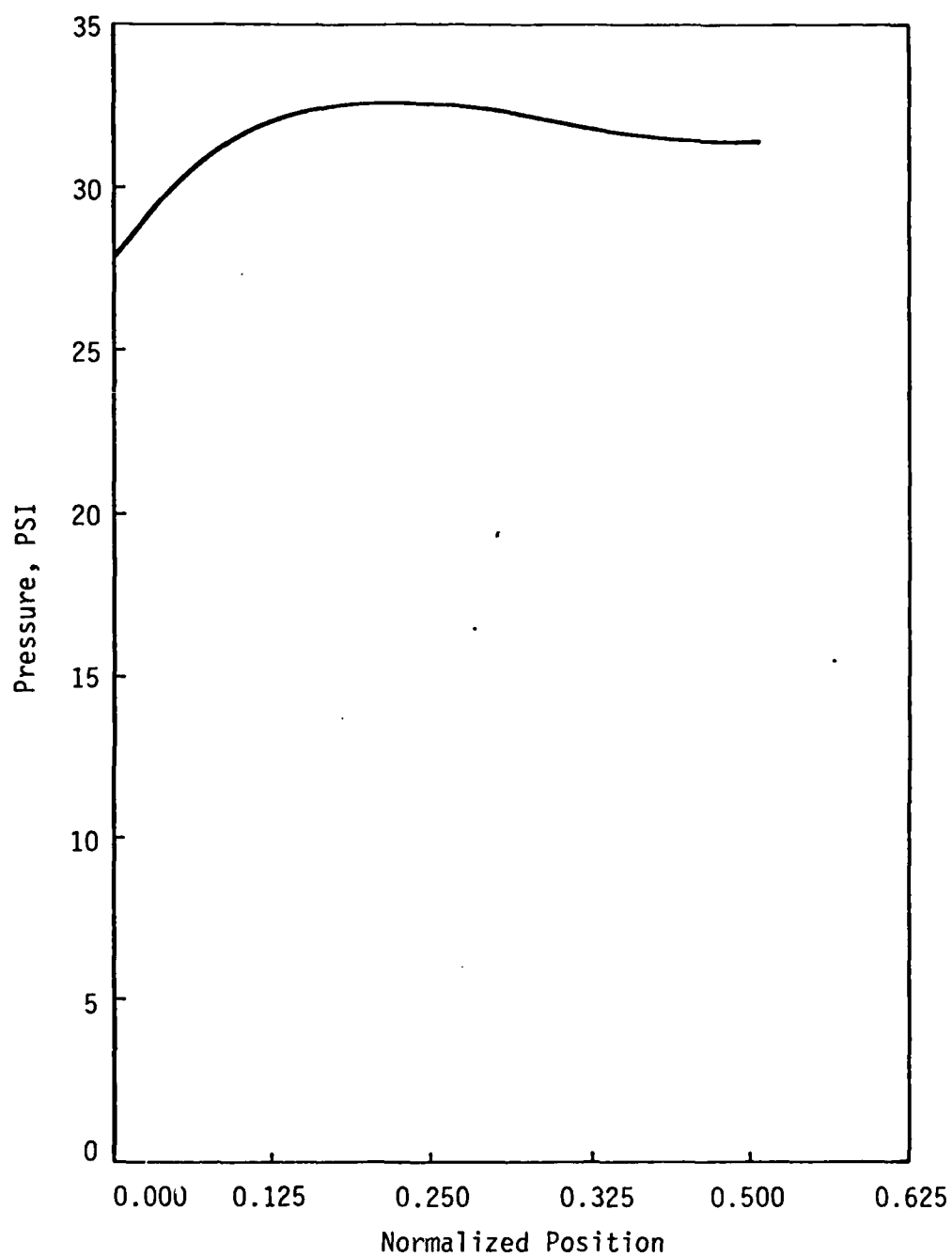


FIGURE 4.14b
Dynamic Pore Pressure Isochrone for an
Unvented Sample; $\beta = 12.77$, $T = 0.10$

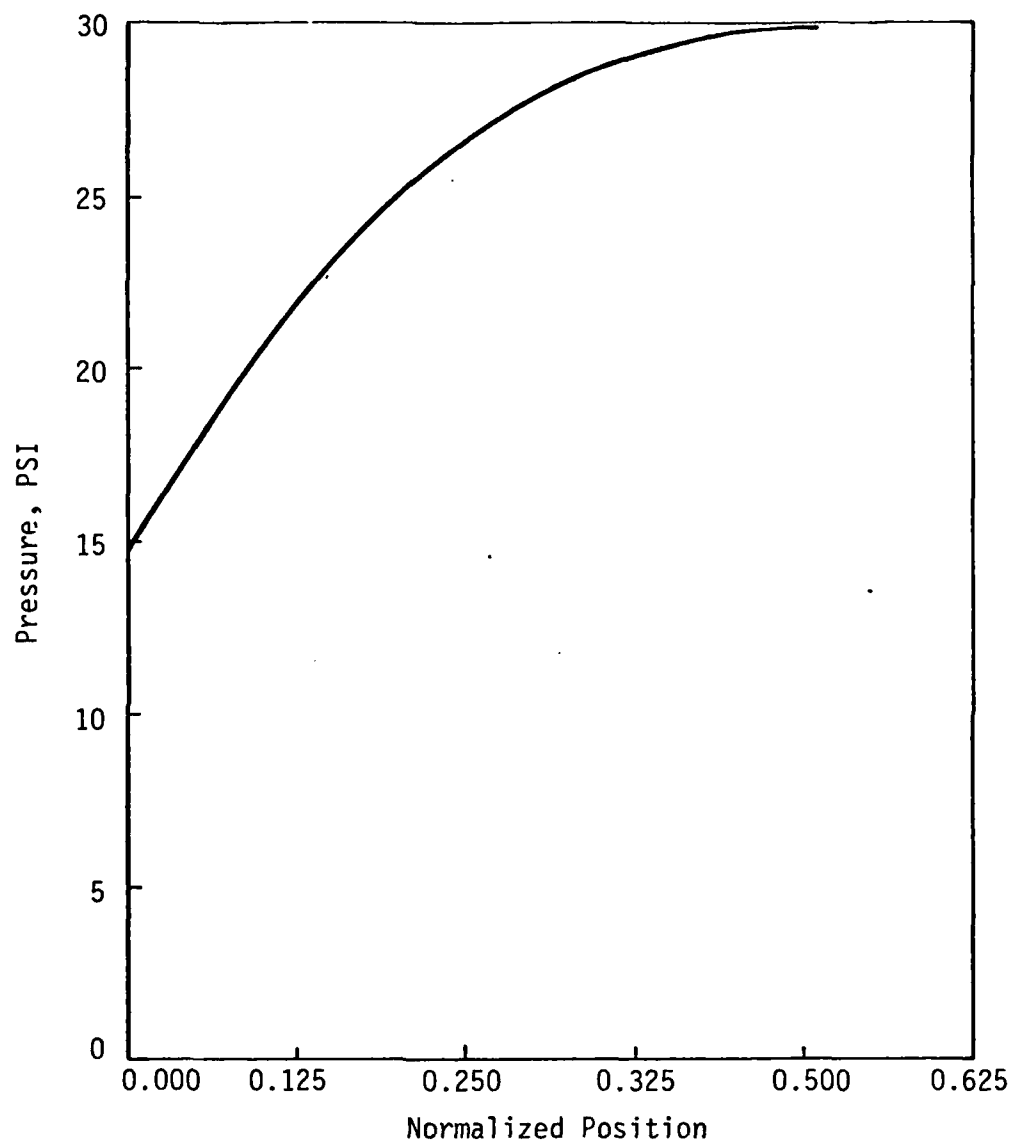


FIGURE 4.14c
Dynamic Pore Pressure Isochrone for an
Unvented Sample; $\beta = 12.77$, $T = 0.15$

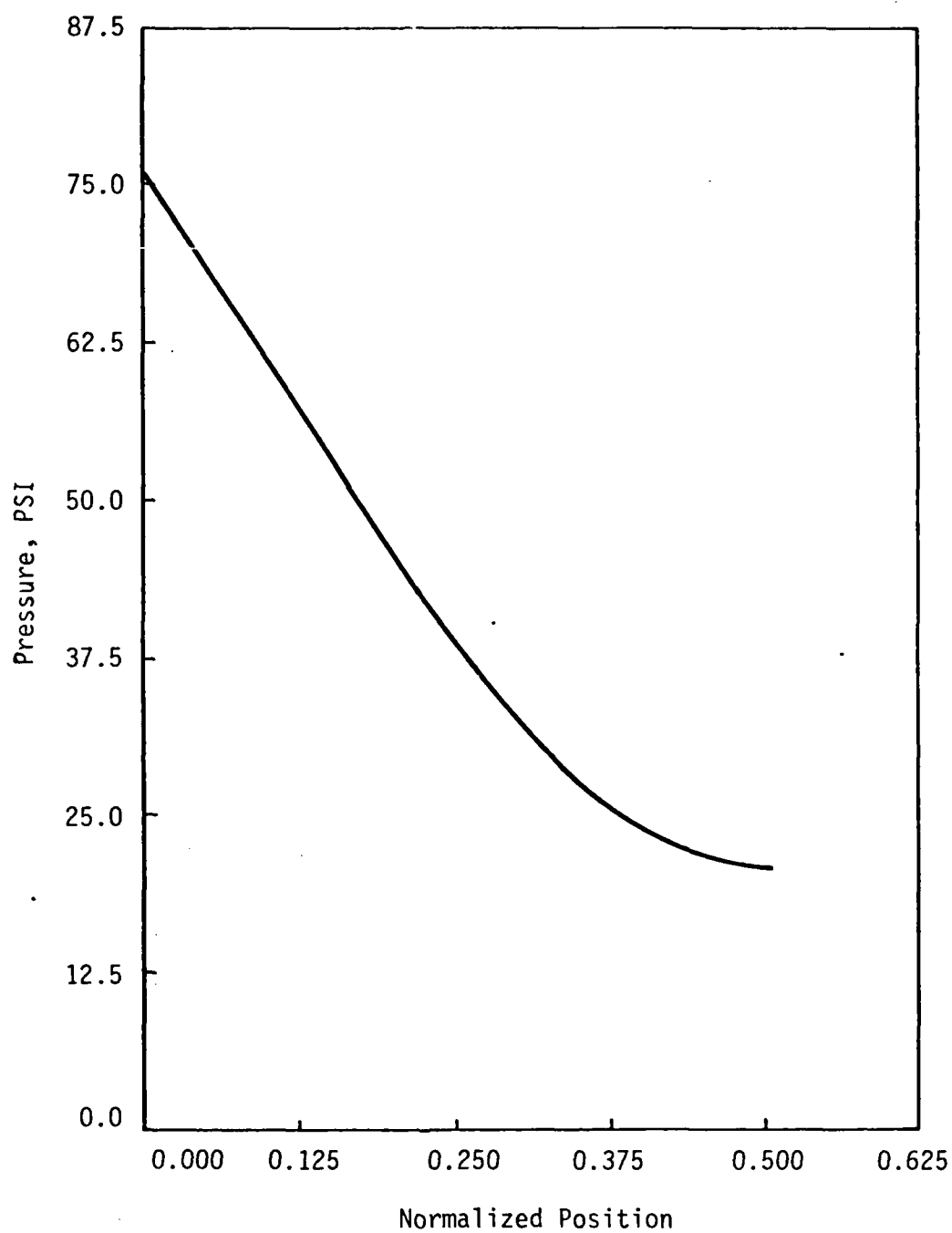


FIGURE 4.15a
Dynamic Pore Pressure Isochrone for an
Unvented Sample; $\beta = 5.56$, $T = 0.05$

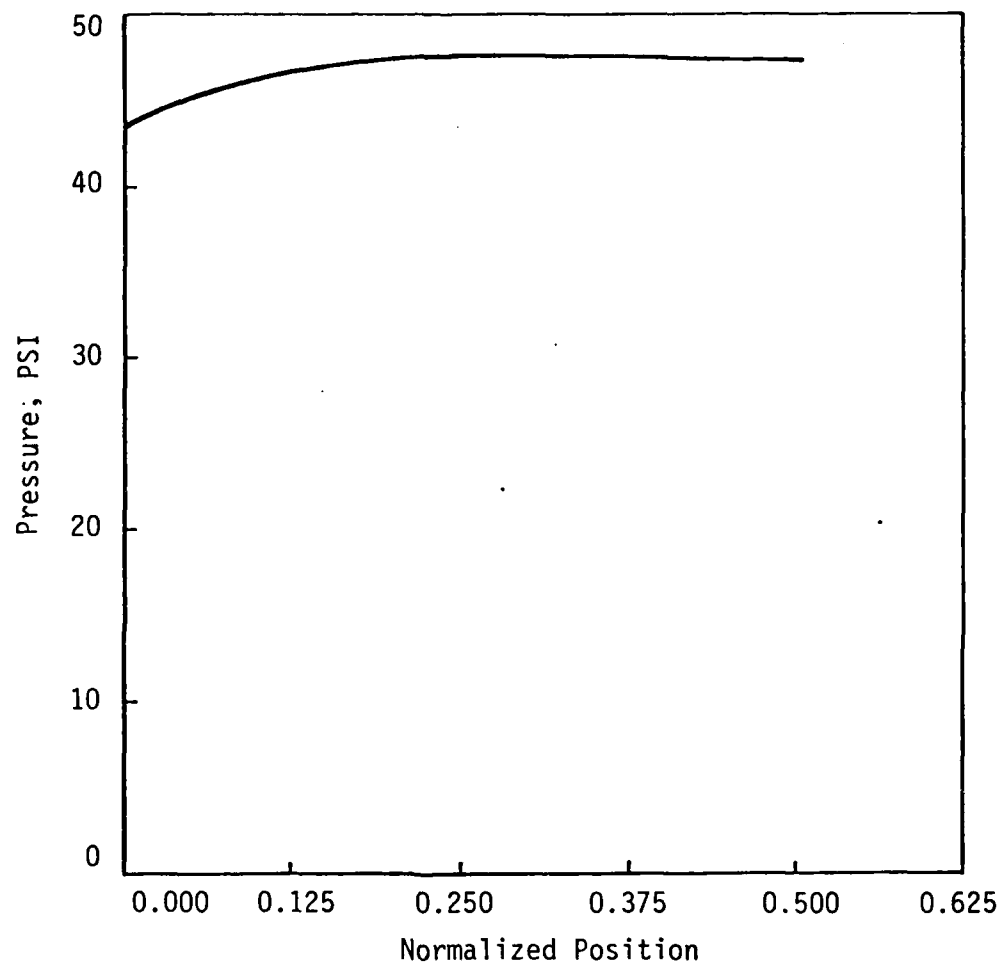


FIGURE 4.15b
Dynamic Pore Pressure Isochrone for an
Unvented Sample; $\beta = 5.56$, $T = 0.15$

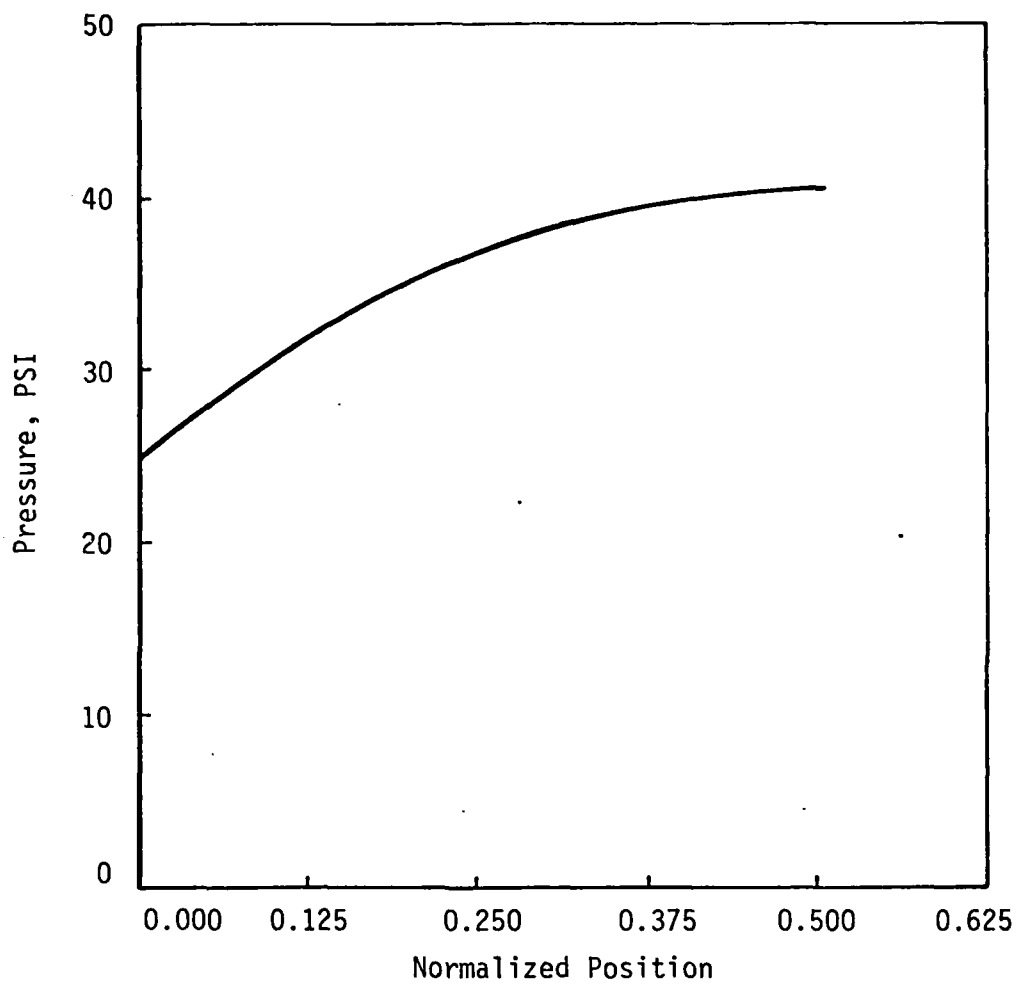


FIGURE 4.15c
Dynamic Pore Pressure Isochrone for an
Unvented Sample; $\beta = 5.56$, $T = 0.25$

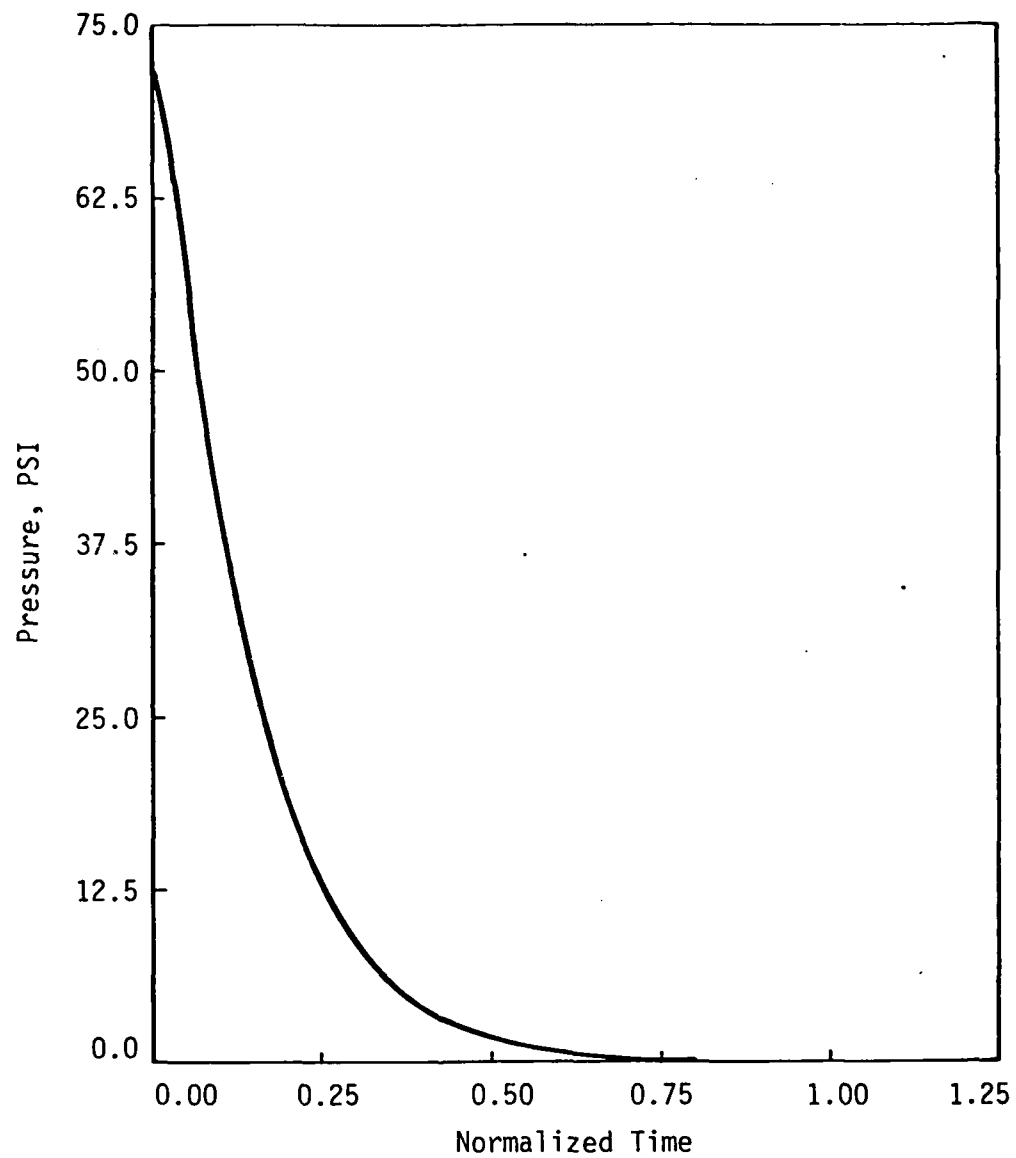


Figure 4.16a
Dynamic Pore Pressure Response in an
Unvented Sample; $\beta = 9.25$, $\xi = 0.232$

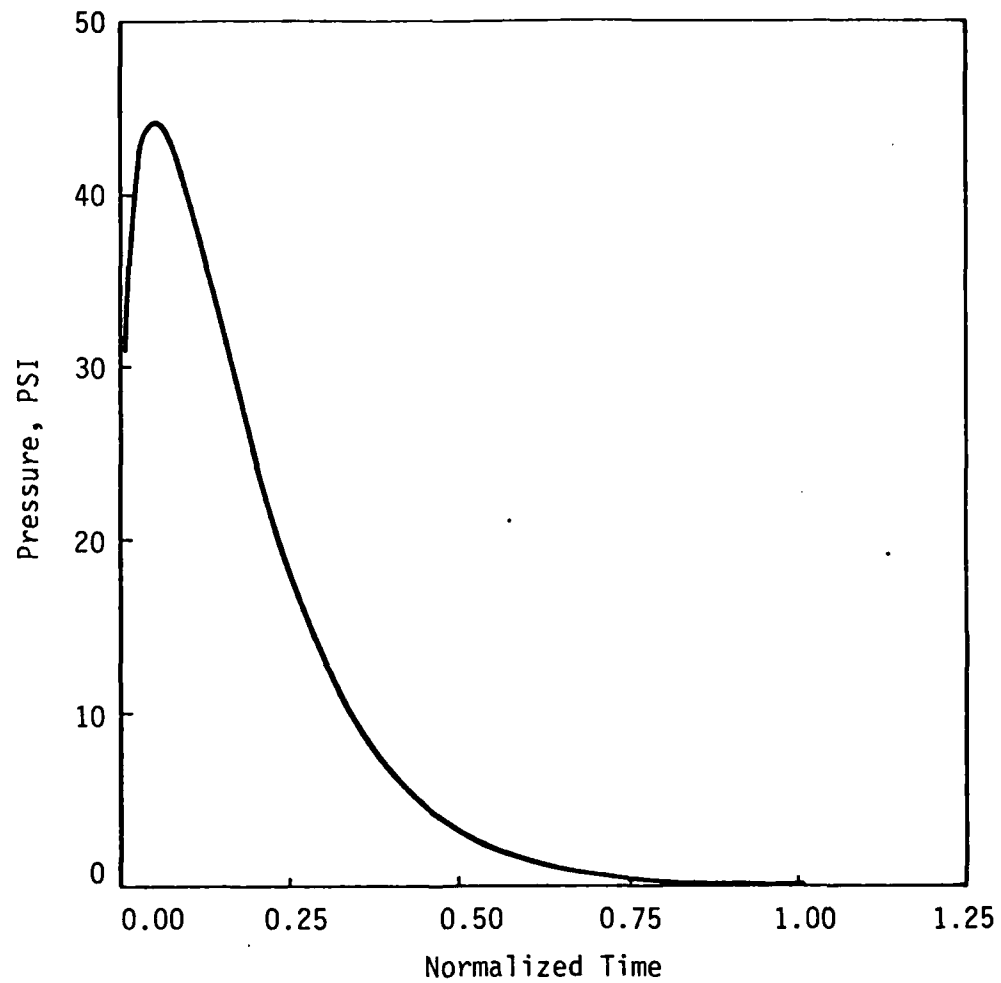


FIGURE 4.16b
Dynamic Pore Pressure Response in an
Unvented Sample; $\beta = 9.25$, $\xi = 0.406$

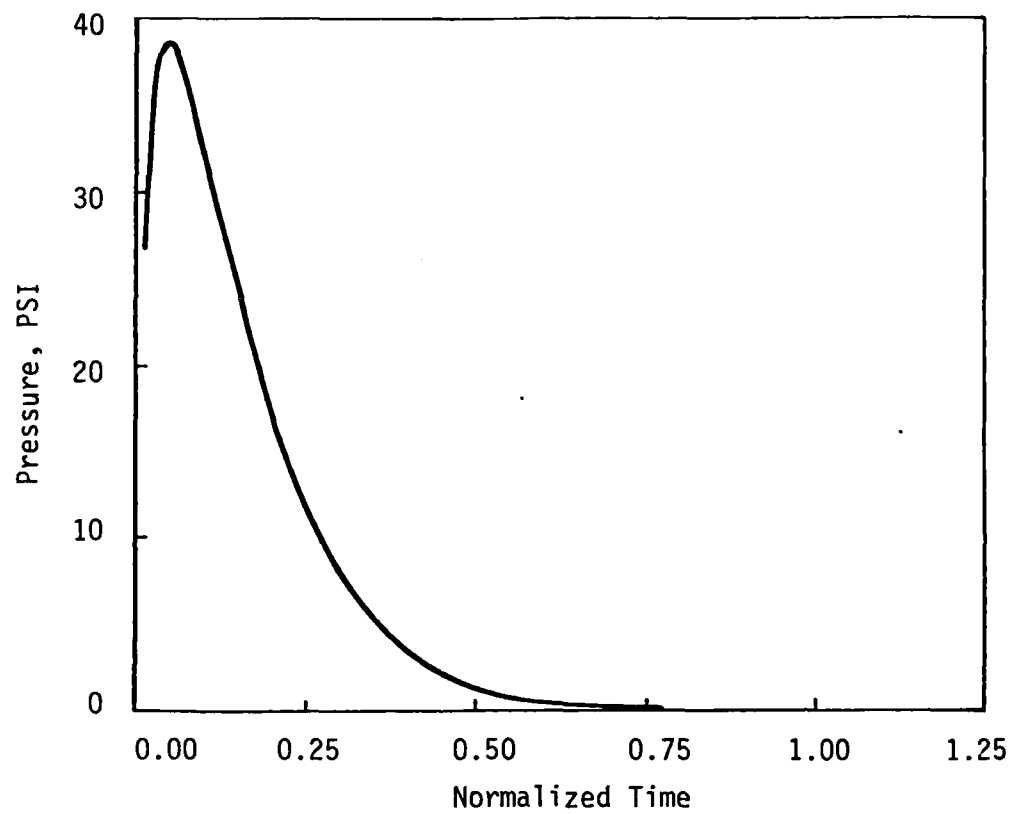


FIGURE 4.17
Dynamic Pore Pressure Response in an
Unvented Sample; $\beta = 12.77$, $\xi = 0.423$

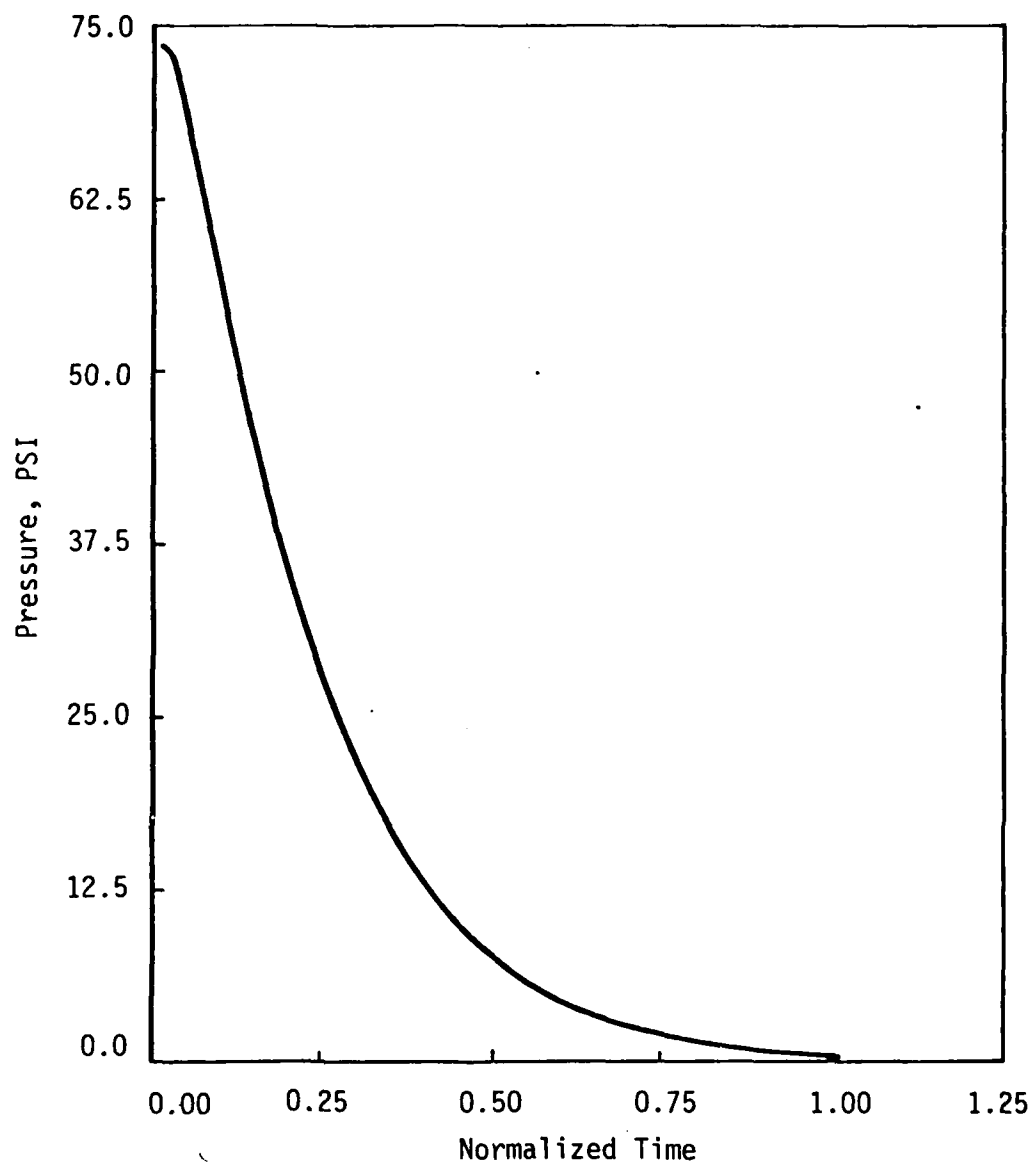


FIGURE 4.18a
Dynamic Pore Pressure Response in an
Unvented Sample; $\beta = 5.56$, $\xi = 0.232$

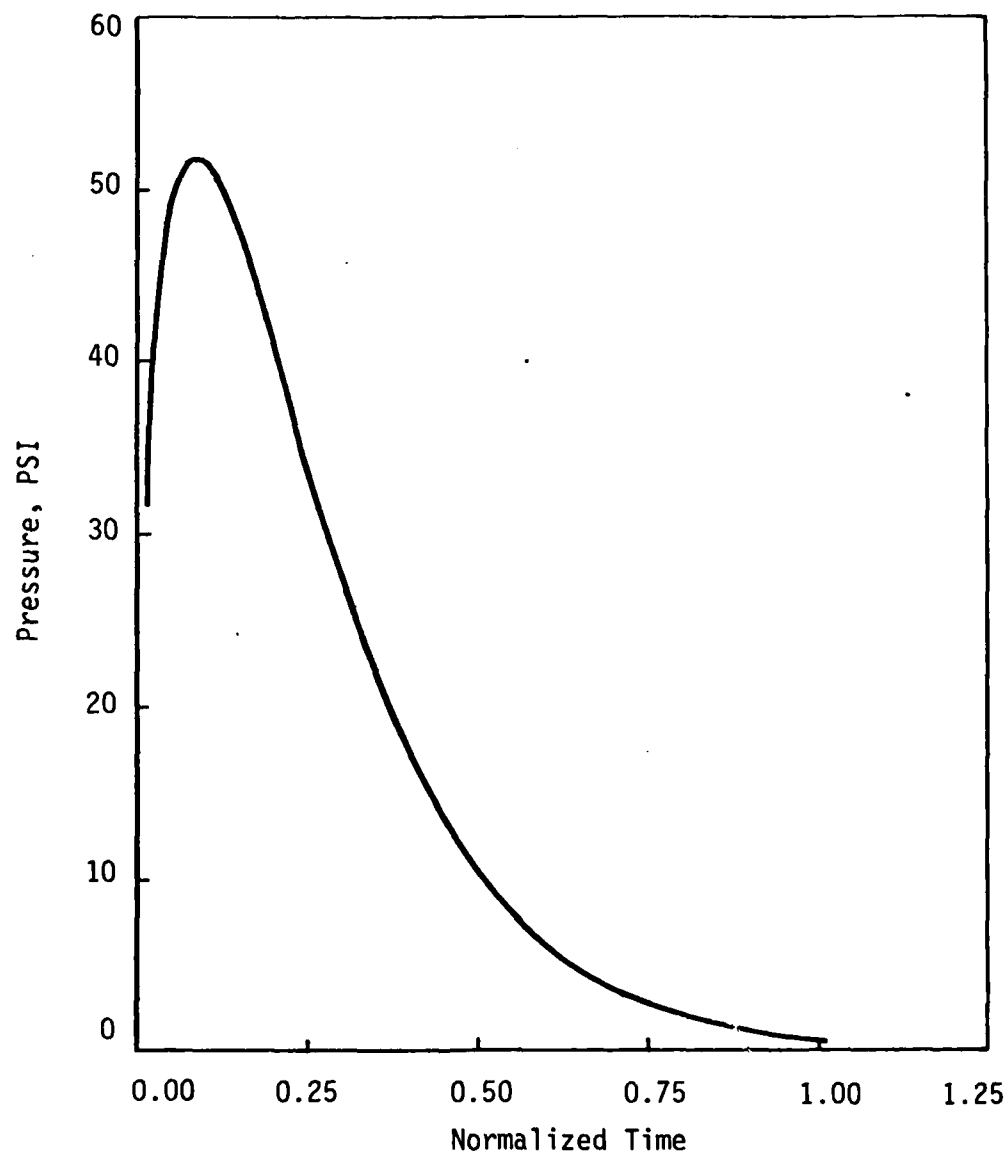


FIGURE 4.18b
Dynamic Pore Pressure Response in an
Unvented Sample; $\beta = 5.56$, $\xi = 0.406$

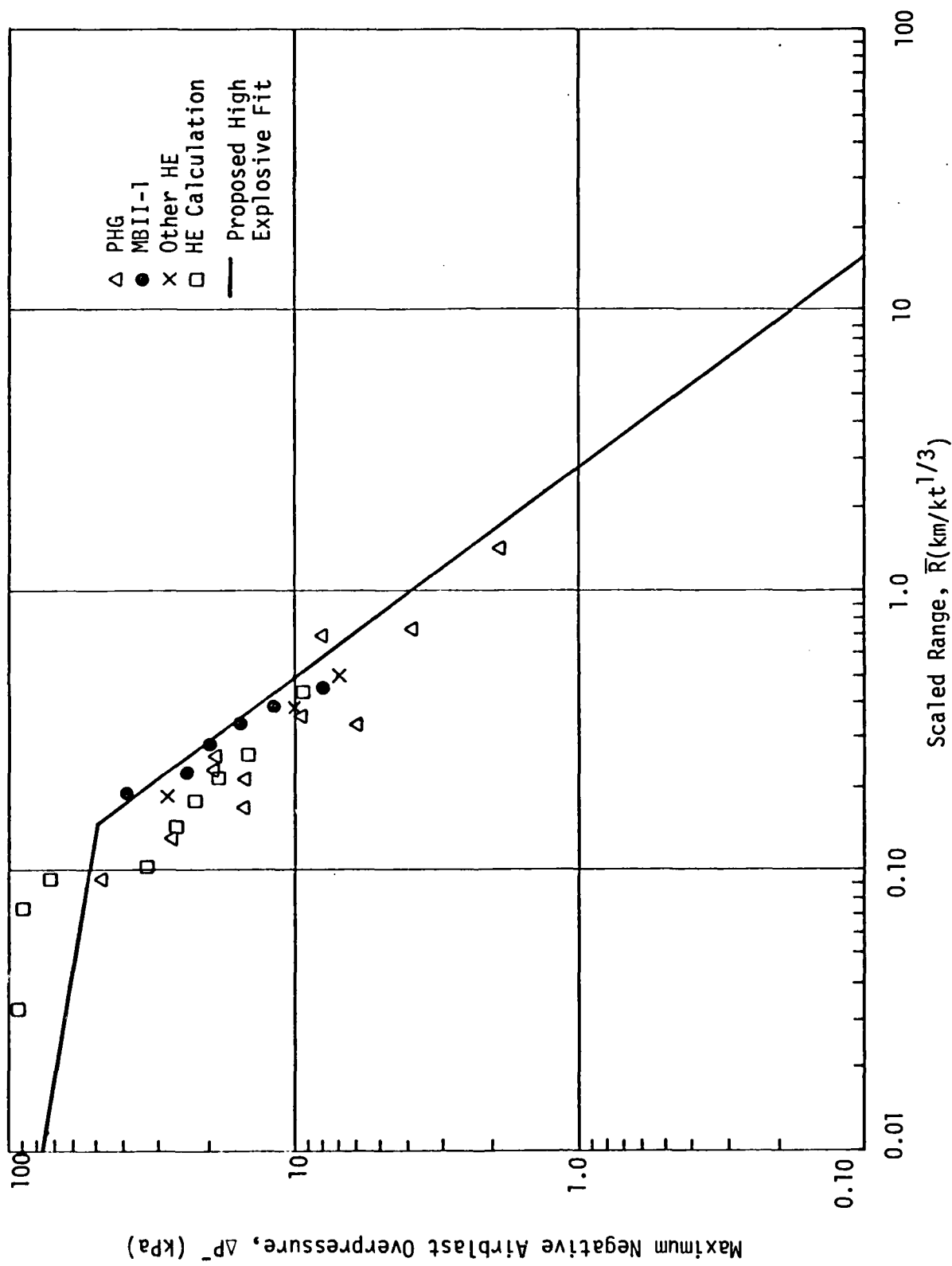


FIGURE 5.1

Peak Negative Airblast Overpressure Versus Scaled Range, High Explosive

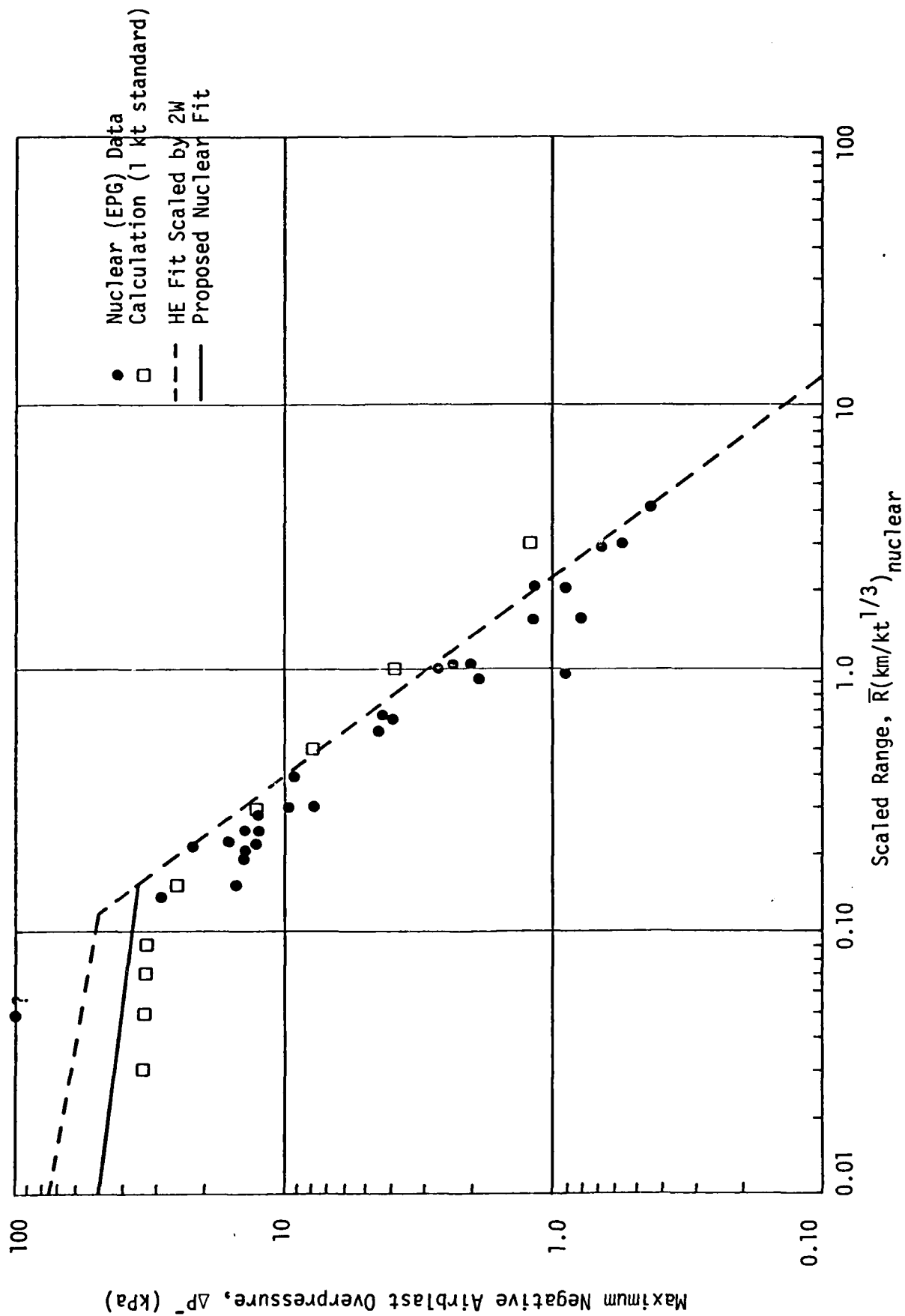


FIGURE 5.2

Peak Negative Airblast Overpressure Versus Scaled Range, Nuclear

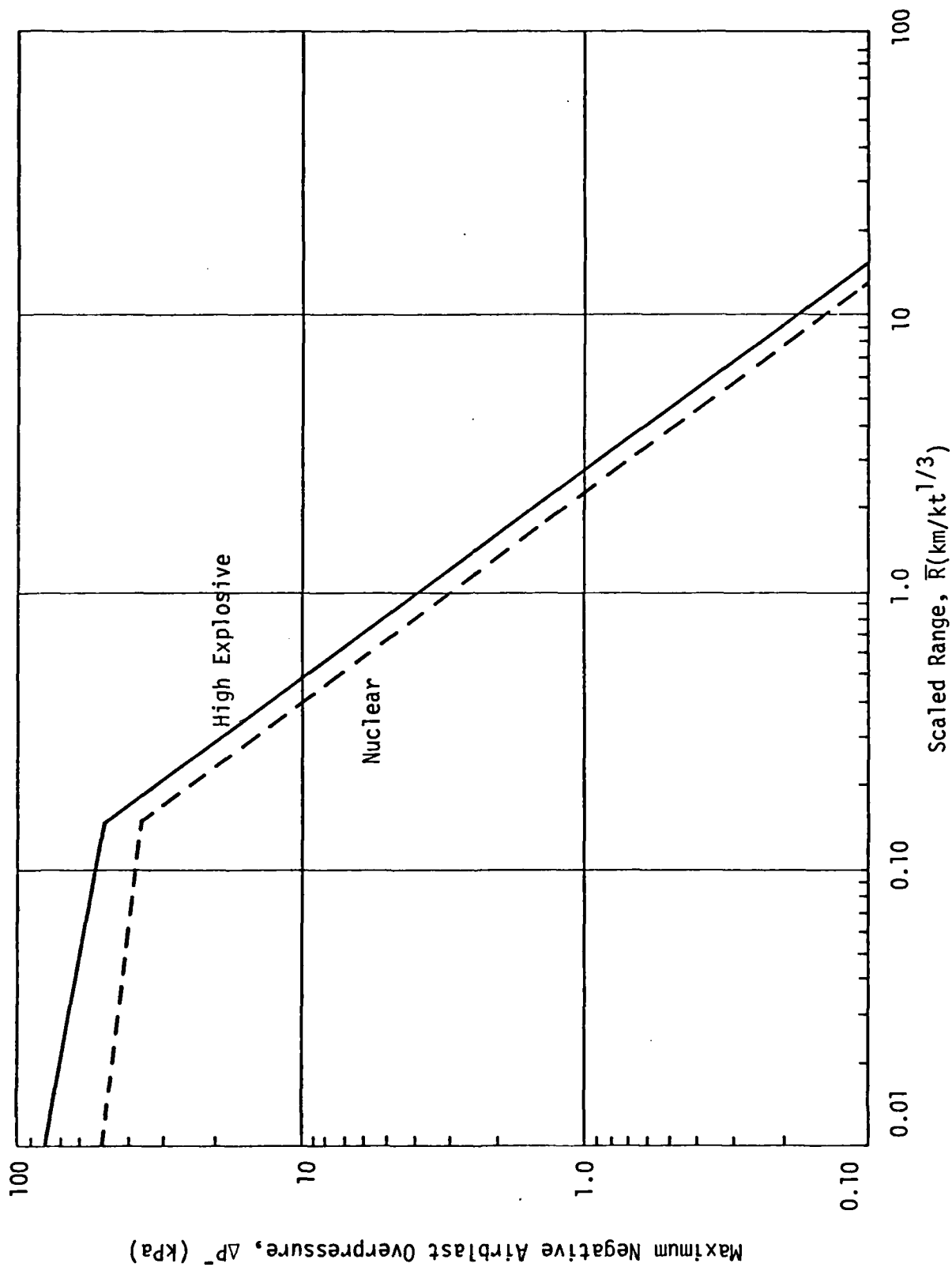


FIGURE 5.3

Peak Negative Airblast Overpressure Versus Scaled Range, High Explosive and Nuclear

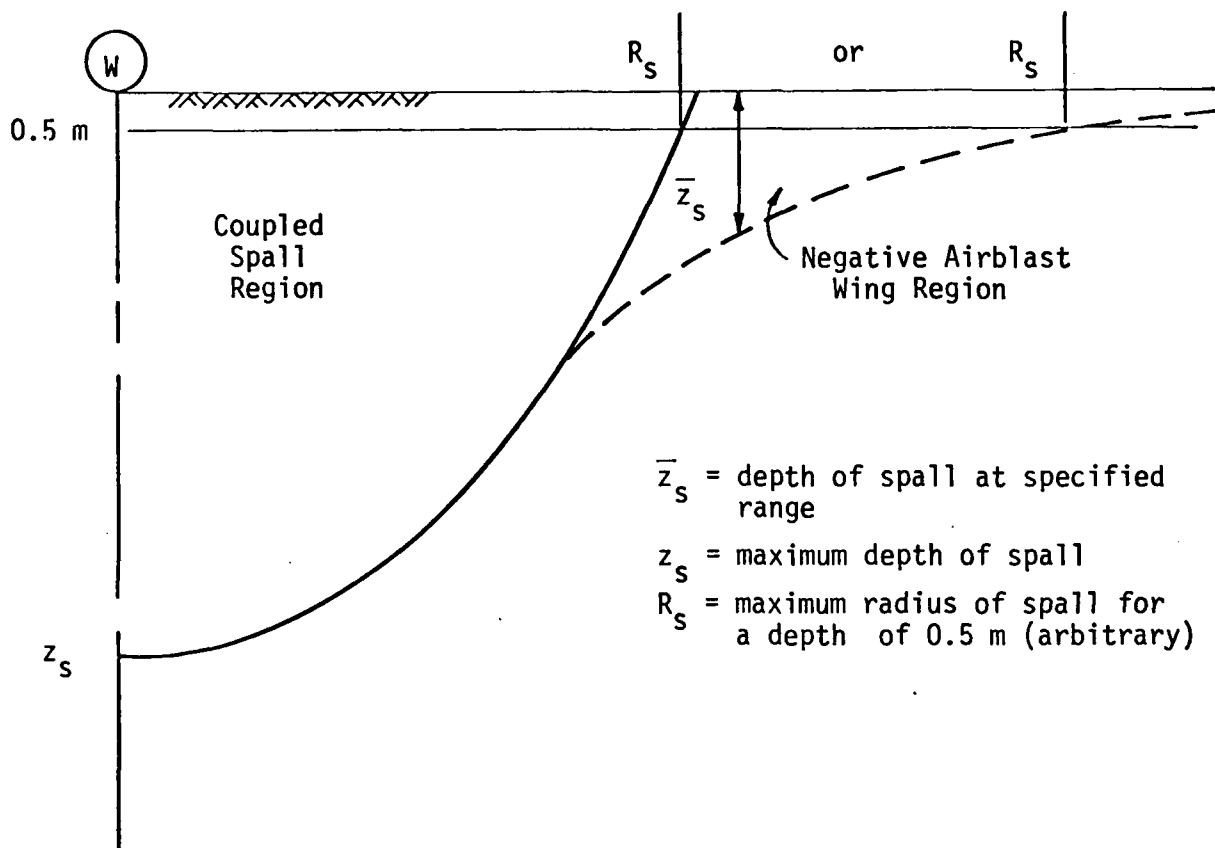


FIGURE 6.1
 Sketch of Typical Spall Regions
 and Nomenclature

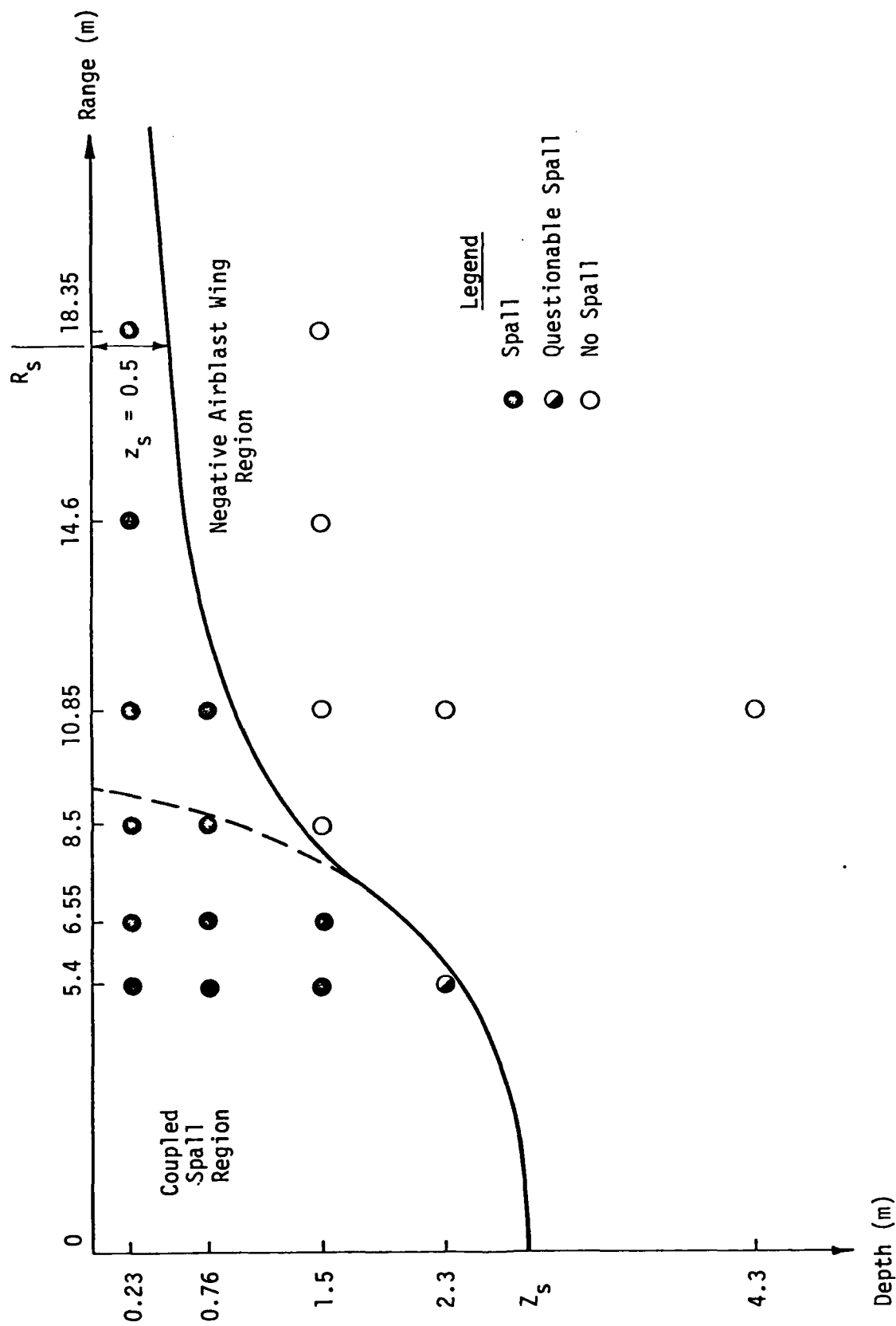


FIGURE 6.2
Estimated Extent of Spall, PHG I-07

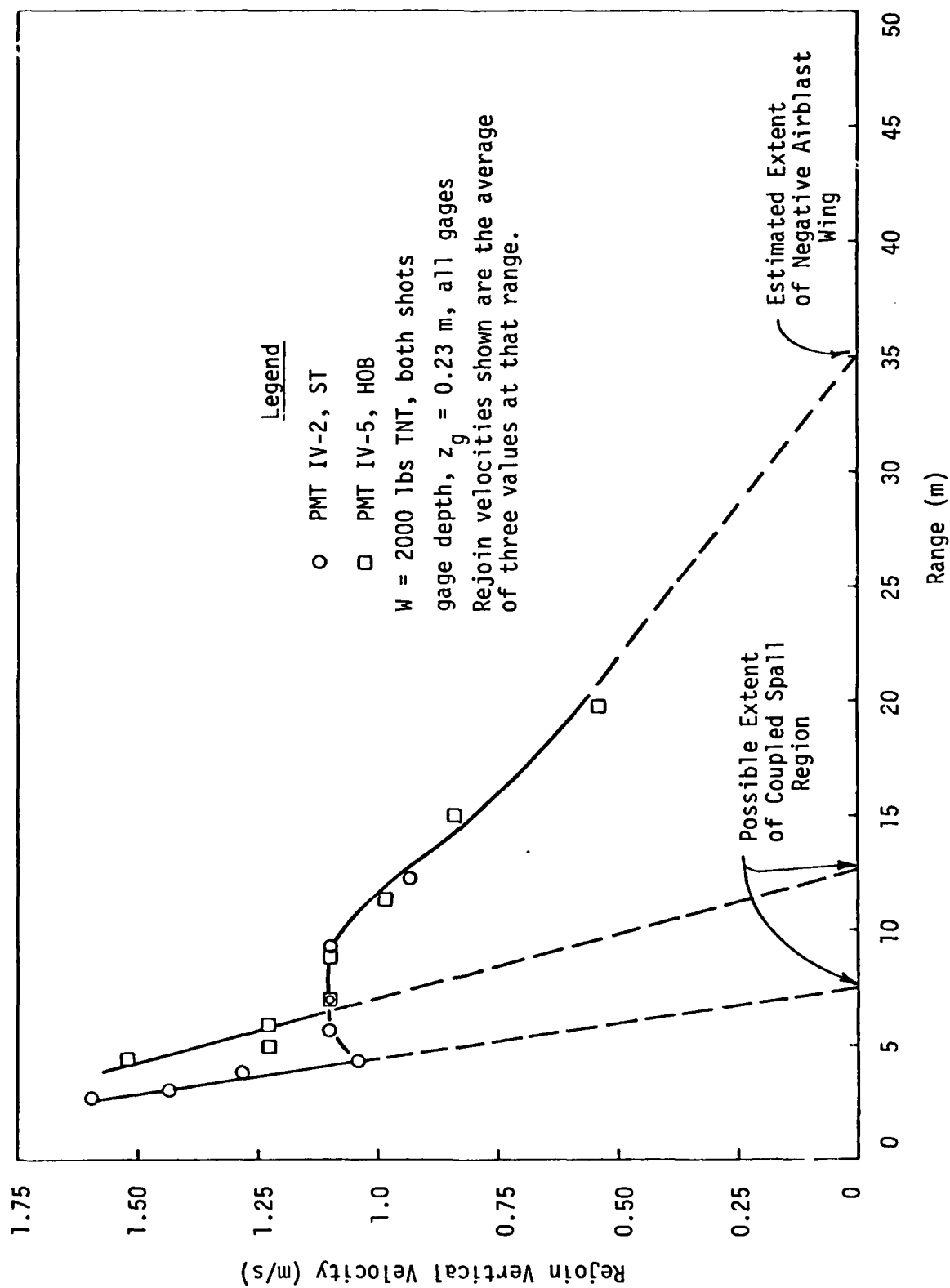


FIGURE 6.3

Typical Vertical Velocity Rejoin Amplitude, PRE-MINE THROW IV

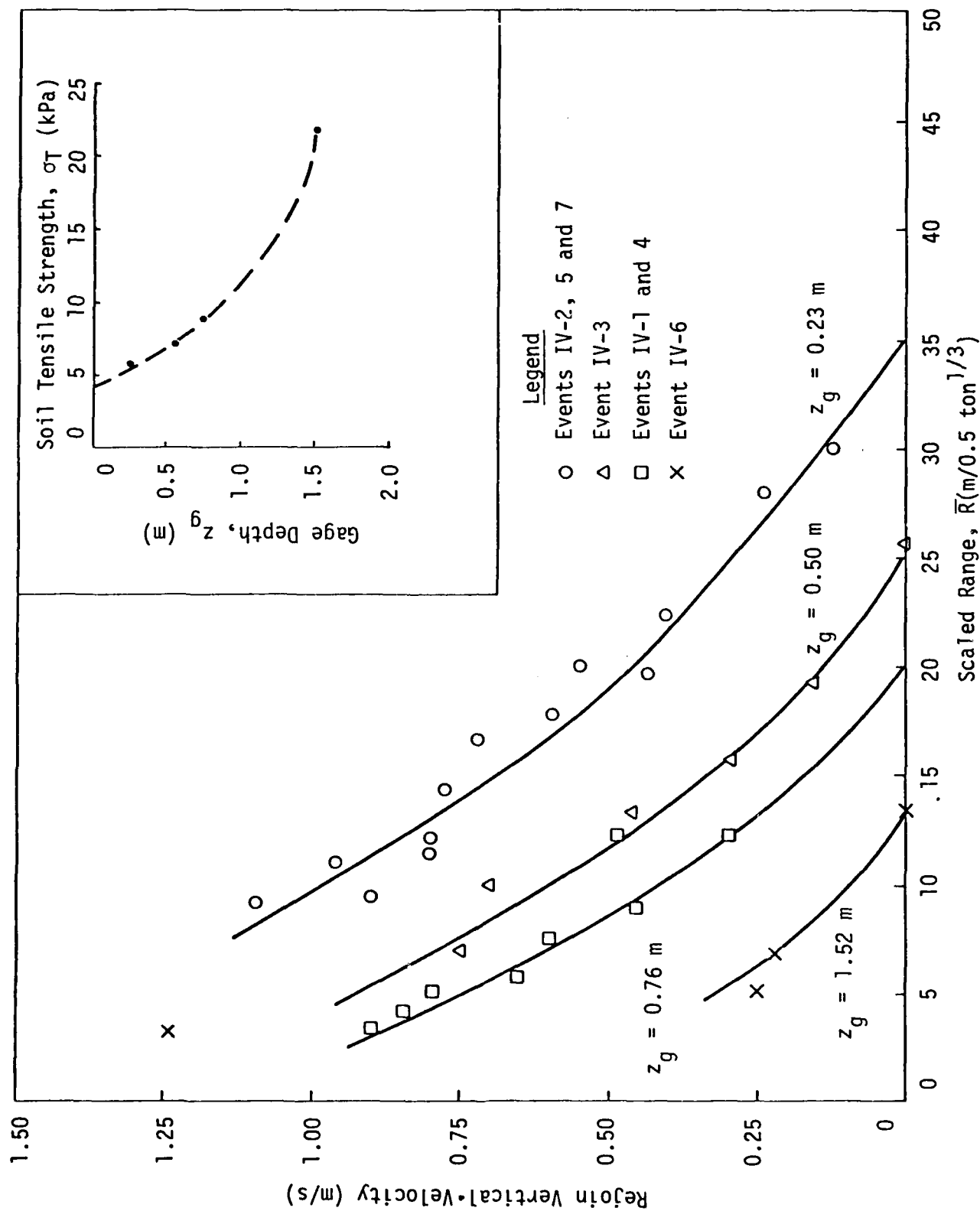


FIGURE 6.4

Summary of Vertical Velocity Rejoin Amplitude Versus Scaled Range, PRE-MINE THROW IV

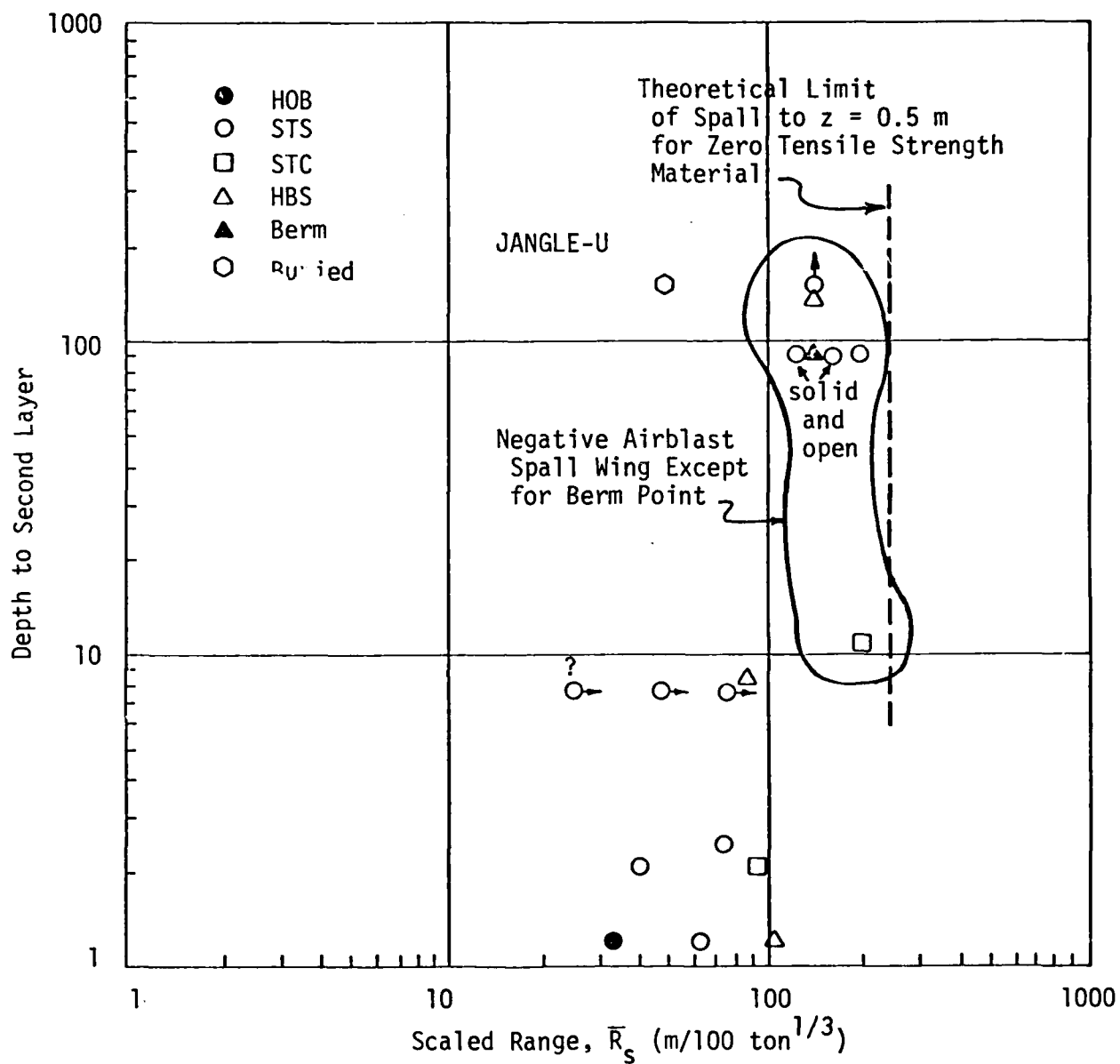


FIGURE 6.5

Scaled Maximum Radius of Spall at $z = 0.5$ m Versus Depth to Second Layer

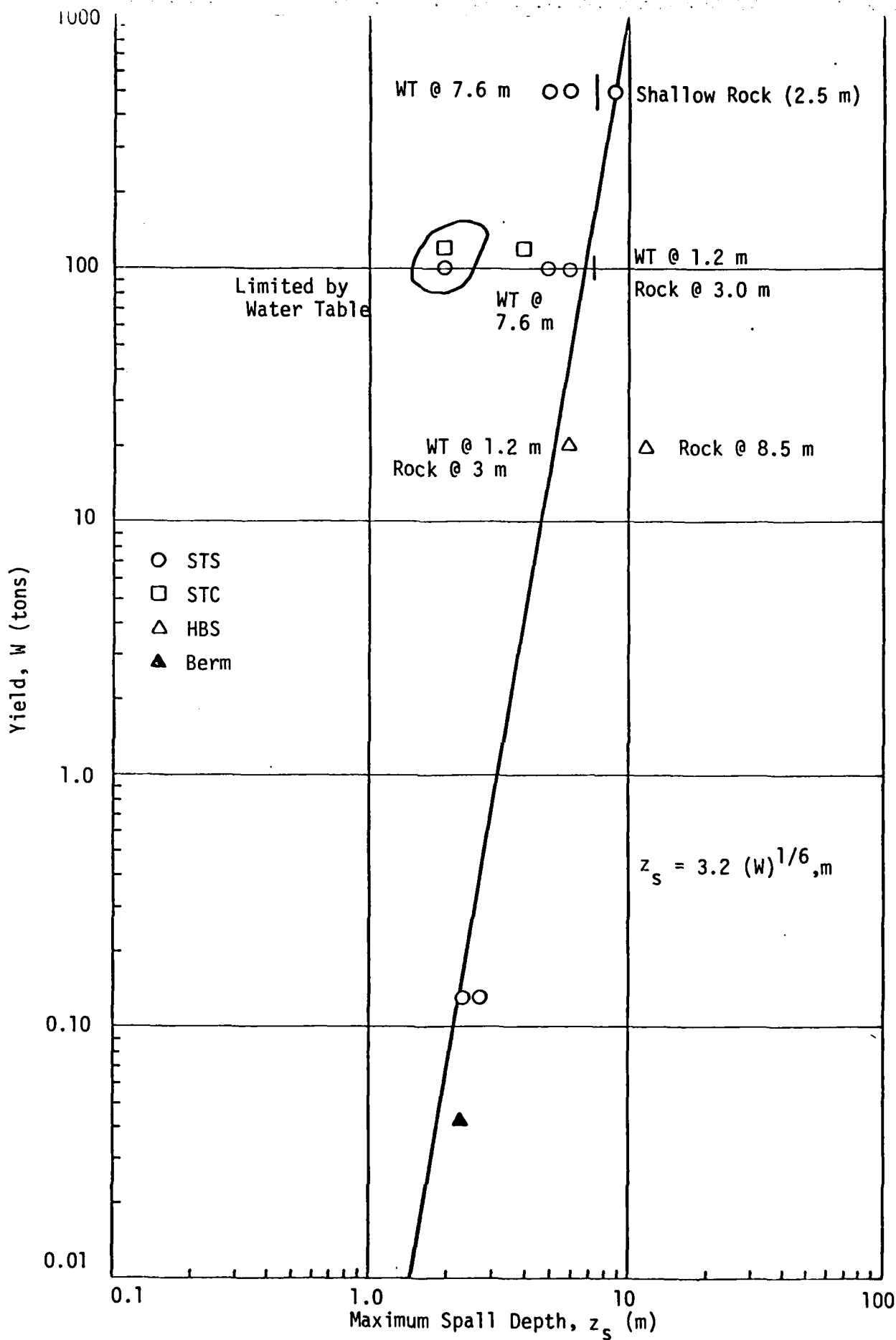


FIGURE 6.7

Maximum Depth of Spall Versus Yield

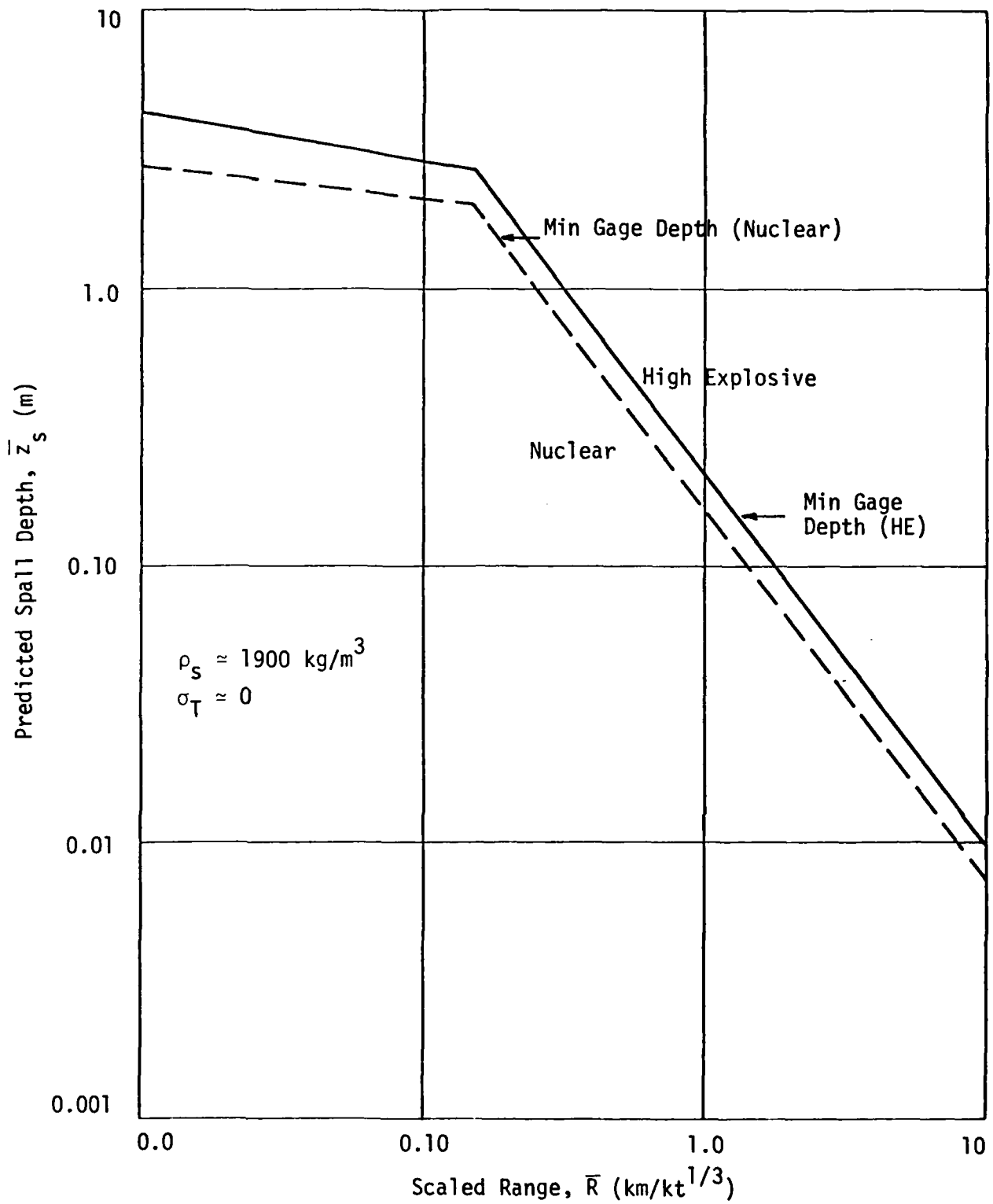


FIGURE 7.1

Spall Depth in the Negative Airblast Wing Region

3-8

DT